Mechanisms of femtosecond laser-cornea interaction in keratoplasty

Valeria Nuzzo

Thèse

présentée pour obtenir le titre de

Docteur de l'École Polytechnique

Spécialité: Physique

par

Valeria Nuzzo

Mechanisms of femtosecond laser-cornea interaction in keratoplasty

soutenue le 1er février 2008 devant le Jury composé de

Isabelle Brunette	rapporteur, présidente du jury
Nicolas Château	
Benoît C. Forget	
Jean-Marc Legeais	
Holger Lubatschowski	rapporteur
Gérard Mourou	
Karsten Plamann	directeur de thèse
Marie-Claire Schanne-Klein	

préparée au

Laboratoire d'Optique Appliquée UMR 7605

A Stefania e Mariella

Remerciements

Ce jour, où j'aurais écrit les remerciements, me semblait très loin, voire utopique, quand, après avoir travaillé pendant deux ans et demi dans une société privée en tant qu'ingénieur, j'ai voulu faire une thèse. Chose un peu insolite dans un système éducatif assez normatif, mais finalement pas impossible, grâce à un brin de chance et à la persévérance de Karsten et moi dans la recherche d'une allocation de recherche. Le choix de quitter le connu pour l'inconnu n'a pas été facile, mais aujourd'hui je suis très contente de l'avoir fait car cette thèse a représenté pour moi une expérience exceptionnelle, stimulante et enrichissante. J'ai pris beaucoup de plaisir à essayer de comprendre de plus près les lois d'interaction entre la nature et la technologie, ainsi qu'a découvrir le monde des chercheurs, si varié.

Mes collaborateurs et collègues au Laboratore d'Optique Appliquée et à l'Hôtel Dieu ont contribué avec leurs compétences, leur disponibilité et leur accueil chaleureux à rendre les trois années de mon doctorat très constructives d'un point de vue scientifique et humainement agréables. Pour cela, je tiens à les remercier.

Je ne peux que commencer par exprimer ma plus grande gratitude à Karsten Plamann, mon directeur de thèse. Je lui suis reconnaissante de la confiance qu'il m'a accordée, de la qualité de son encadrement, franche et rigoureuse, de sa capacité à me conseiller aux moments opportuns et de son soutien pendant la rédaction de cette thèse.

Je remercie également :

Gerard Mourou pour m'avoir accueillie au sein du LOA et avoir permis que cette allocation de recherche me soit attribuée ;

les membres du Jury, en particulier Isabelle Brunette et Holger Lubatschowski, pour leurs remarques précieuses sur mon manuscrit et l'intérêt qu'ils ont montré envers mon travail ;

Jean-Marc Legeais, pour m'avoir accueillie au Laboratoire Biotechnologie et Œil (LBO) de

l'Hôpital Hôtel Dieu de Paris, pour sa disponibilité et la pertinence de ses suggestions ainsi que Michèle Savoldelli, qui, avec beaucoup de passion, m'a fait découvrir le monde de la cornée de très près. Je la remercie pour sa patience et pour la très grande qualité du travail fourni. Jean-Marc et Michèle ont joué un rôle clé en apportant une importante valeur ajoutée à mon travail de thèse ;

M. Rosso, directeur de l'École doctorale de l'École Polytechnique, et toute son équipe, accueillante et compétante ;

David Donate et Florent Aptel pour leur apport médical à mon travail, le Pr. Pouliquen pour son soutien, ainsi que Françoise Dagonet et le secrétariat du LBO pour leur disponibilité et leur sympathie ;

ceux qui m'ont soutenue pendant l'écriture du manuscrit et la préparation de la soutenance, ainsi que les nombreux relecteurs de mes chapitres de thèse et les auditeurs des répétitions orales, je pense surtout à Ciro, Davide, Christoph, Alexandre, Evangelos, Gilles, Rahul, Florent et Donald ;

les équipes techniques, en particulier Thierry, Marc, Charly, Mikael, Alain, Fatima, Pierre et Arnaud, qui ont contribué à l'avancement et la réussite de ce projet, en étant toujours très efficaces et patients, ainsi que Dolores, Cathy, Sandrine, Patricia, Régis, Octavie et Valérie, pour leur aide au secrétariat ;

Alain, qui m'a encouragée pendant les derniers mois et qui m'a acceptée comme voisine de bureau (le calme pour favoriser la concentration, l'espace pour éparpiller les papiers et les tablettes de chocolat ont été des éléments essentiels pour la rédaction de la thèse), Fatima qui avait son bureau toujours ouvert et Charly grâce à qui je ne devrais plus perdre de clé.

Cela a été un plaisir de travailler avec Olivier Albert, dont j'ai beaucoup apprécié les conseils scientifiques et les remarques qui m'ont permis d'améliorer la présentation de mes travaux de thèse. Je suis également reconnaissante à Michele Merano, qui a su me transmettre une partie de son savoir-faire pendant les expériences effectuées ensemble.

Je garderai un bon souvenir des cafés commentés en italien avec Laura ou Alessandro ; des trajets en RER avec Thomas, que je devais toujours attendre avec le risque de louper le train ; des trois ans de partage de bureau avec Guillaume ; des premières expériences réalisées avec Pedro.

Je souhaite remercier également Sébastien Jan pour m'avoir fortement encourgée dans mon

envie de faire un doctorat et mes anciens collègues d'ICADE, Fabienne, Isabelle, Magalie, Nasr et Gérard, qui m'ont soutenue dans cette démarche, même s'ils auraient aimé que je reste travailler avec eux.

Un merci à Mauricette Ortu, dont les enseignements de français m'ont été si précieux.

Un ringraziamento particolare va a Christophe, che mi ha incoraggiata, aiutata e "sopportata" durante questi tre anni.

Enfin, je remercie d'avance tous les lecteurs qui s'intéresseront à ce travail et à sa suite.

Abstract

The objective of the present research work has been to study the femtosecond laser-tissue interaction in order to define optimal conditions for performing keratoplasty of pathological corneas by femtosecond laser. This is the first thesis on the subject accomplished at the Laboratoire d'Optique Appliquée (Ecole Polytechnique, ENSTA, CNRS in Palaiseau) and it has been carried out in close collaboration with the Laboratoire Biotechnologie et Œil (Université Paris Descartes, EA 4063, Hospital Hôtel Dieu de Paris).
The femtosecond laser is currently used in refractive surgery for cutting tissue and recently it has been introduced for substituting traditional mechanical instruments for corneal transplant or keratoplasty, which consists in replacing a pathological cornea of a patient with a healthy cornea from a donor. Approximately 100 000 procedures are performed per year worldwide. Leading indications for keratoplasty involve opacification of corneal tissue due to a dysfunction of the endothelial cells. The cornea becomes permeable and looses its transparency. The oedema degree increases progressively and, if not interrupted by transplantation, it can cause total opacification of the cornea and a drastic decrease of the visual acuity. Traditional techniques for keratoplasty present a high risk of rejection, insufficient visual recovery and/or a risk of failure because technically delicate. In this context, femtosecond lasers represent a safe, accurate, and reliable surgical tool. However, clinical systems commercially available are very successful in cutting transparent corneal tissue (donor) but present technical limitations when inducing dissection in pathological corneas (receiver).
At the interface between the physics and the ophthalmology, this research work has allowed to assess the potential and the limitations of the present clinical systems and it has brought solutions for optimizing the laser-tissue interaction, also indicating directions for the development of a further high performing system.
This research work received the "Fondation Dalloz - Institut de France" Prize 2007 and the "La Recherche" Prize 2008.

Contents

Introduction

Scientific context

The advent of ultrashort pulsed lasers has represented a major breakthrough in corneal surgery. The first clinical application of femtosecond lasers in ophthalmology has been their use in refractive surgery over the last decade. The most common technique for correcting ametropia is called LASIK (laser in situ keratomileusis). It consists of three main steps: first a hinged flap is cut and folded back, revealing the corneal stroma. In the second step, an excimer laser remodels the stromal layer tissue in order to correct focusing errors of the eye. Finally, the flap is unfolded back. Traditionally, the flap is created by a mechanical microkeratome equipped with a metal blade. Imperfect cutting related to the use of a microkeratome may lead to various intraoperative and/or postoperative complications. Femtosecond lasers have proven to be a useful and potential tool in tissue dissection and tend to replace traditional handled surgical blades. Advantages in using a femtosecond laser include a greater accuracy in flap size, shape, and thickness and therefore, a lower probability of complications. Since they represent a safe, reliable and flexible tool, although costly alternative, femtosecond systems are now currently employed in LASIK procedures.

Recently, the applications of ultrashort pulsed lasers have extended to corneal transplantation or keratoplasty. Leading indications for keratoplasty involve opacification of corneal tissue due to a dysfunction of the endothelial cells. Approximately 100 000 procedures are performed per year worldwide. Different transplantation techniques are currently performed, which are divided into full-thickness penetrating and partial lamellar keratoplasties. In penetrating keratoplasty, a full-thickness cornel button is replaced. It is the less technically demanding and the most common transplantation procedure. However, it presents a risk of rejection and involves a button anesthesia due to the 360^o tissue denervation of the sensitive nerves which run mostly

in the anterior layers of the cornea. Recovery of vision may also be slow and not satisfactory because astigmatism and other optical aberrations are often induced by sutures and interface imperfections of the dissected tissue, thus reducing the connection of the donor button and the recipient bed. Part of these problems may significantly be reduced by partial corneal transplantation. Anterior lamellar and posterior lamellar keratoplasty are performed by selectively replacing either the anterior layer or the posterior layer of the cornea in patients with localized corneal disease; the Descemet's stripping automated endothelial keratoplasty (DSAEK) is a relatively new surgical technique which involves the replacement of the endothelium through a limbal incision. It presents further clinical advantages compared to traditional lamellar techniques. However, it is a very delicate surgery which presents a risk of failure even when performed by experienced surgeons.
Femtosecond lasers ensure cutting with accuracy and reproducibility, and matching between the donor graft and the recipient eye, regardless of the type of keratoplasty performed. This leads to reduced astigmatism and a rapid visual recovery. Clinical systems commercially available are successful in dissection protocols of transparent corneas, however they present technical limitations when inducing dissection in pathological corneal tissue. The laser beam experiences scattering and optical aberrations when propagating through edematous tissue. The highly ordered arrangement of corneal layers is broken and variations in the refractive index are not negligible as in transparent corneas. Moreover, posterior surgery requires to focus at high depths in the cornea, which introduces additional spherical aberrations which contribute to beam broadening. These effects, resulting in attenuation of the laser energy into the bulk of the tissue, are not taken quantitatively into account by daily femtosecond laser system. The quality of the cutting decreases in the volume of the cornea, thus prohibiting them from being routinely employed in keratoplasty.
In this context, a new laser system efficient in cutting pathological corneas safely, and enabling localized dissection or total removing of the diseased tissue, would represent a real advancement. It would allow performing "customized" and possibly sutureless keratoplasties.

Objectives

The objective of the present research work is to define optimal conditions for performing keratoplasty of pathological corneas by femtosecond lasers. The project has been executed by covering the following phases:

- the investigation of the interaction mechanisms of laser with healthy and pathological corneal tissue in the femtosecond regime. The purpose was to identify side effects and evaluate their dependance on laser parameters;
- the *in situ* analysis and quantification of the optical properties of pathological corneas. This required the development of an *in situ* method for optical measurements;
- the determination of the optimal laser parameters when dissecting opaque corneal tissue;
- the elaboration of strategies for adapting the laser parameters to the tissue properties.

The project has included the development of an experimental set-up for performing corneal surgery by a femtosecond laser.
This is the first thesis on the subject accomplished at the Laboratoire d'Optique Appliquée.
The work has been carried out in close collaboration with the Laboratoire Biotechnologie et Œil[1].

Organisation

The dissertation is composed of two main parts. First, a literature review on the subject is provided. The second part focuses on the experiments.
Chapter 1 provides a description of the anatomy of the cornea and its optical properties. In particular, I review the different theories advanced for explaining corneal transparency, and modification of the optical properties in pathological opaque corneas.
Chapter 2 briefly introduces principles and techniques for generating ultrashort laser pulses, including detailed description of the two laser systems used in our experiments. Finally, I present the state of the art in applications of femtosecond lasers in corneal surgery and compare clinical systems on the market.
Chapter 3 considers the nonlinear mechanisms which govern the interaction of ultrashort pulsed lasers with transparent materials. Special emphasis is on phenomena observed in the corneal tissue, when exposed to an infrared femtosecond irradiation: laser-induced optical breakdown,

[1]Université René Descartes - Paris V, EA 4063, Hospital Hôtel Dieu, 1 place du parvis Notre Dame, 75181 Paris cedex 4, France

chemical alteration due to low-density plasmas, self-focusing, and second harmonic generation.
In *Chapter 4*, I describe the experimental set-up that we have developed and summarize characteristics of the clinical system that we used in our experiments. Sample preparation is also detailed.
In *Chapter 5*, I present our study on the interaction mechanisms of femtosecond pulses with corneal tissue as function of various parameters: corneal optical properties, pulse energy, numerical aperture of the focusing optics, laser systems. All experiments have been performed on human corneal grafts delivered by the *Banque Française des Yeux* for scientific use. Using a histological and ultrastructural examination of the irradiated corneal tissue, we compare tissue which underwent keratoplasty by a clinical system with tissue dissected by our experimental approach. The parameters outside of which undesirable effects become significant are evaluated. In edematous cornea, the laser beam is attenuated during propagation and the real energy delivered to the tissue at a determined depth is *a priori* unknown. In this case, side effects are more likely to be produced.
In *Chapter 6* we propose an *in situ* and nondestructive method for quantifying the attenuation of the laser beam into the volume of pathological corneas. It is based on the acquisition of the backscattered second harmonic generation. We estimate the contribution of the spherical aberration and the scattering of the beam broadening, when focusing the laser into the bulk of the tissue. Thereby, we determine the optimal numerical aperture for corneal surgery. Finally, incisions performed with optimized laser parameters, with respect to the performances of our experimental set-up, are shown.
Chapter 7 summarizes the work contained in this thesis and gives an outlook on possible further investigations and improvements of the existing clinical systems.

Chapter 1

The cornea

In this chapter, I summarize the composition and structure of the cornea as well as its function. The optical properties of the corneal tissue are then described. Finally, I elucidate the basis for the transparency of normal healthy corneas and the structural changes related to pathological opacification of the cornea.

1.1 The human eye

The eye is a complex organ, which serves the important function of detecting light and give the sense of sight. Vision is the most used human sense to gather information from our environment. The eyeball has approximately an axial length of 23 mm and horizontal and vertical dimensions of 24 mm. Figure 1.1 displays a section of the anatomy of the eye. The outer layer maintains the shape of the eye and consists of the cornea and the sclera, which are connective tissues composed essentially of collagen. Whereas the sclera has a typical white color, the cornea is transparent or clear. After entering the eye through the cornea, light passes through the pupil which acts as a diaphragm; it then reaches the crystalline lens and focuses on the retina where it is converted into neuronal signals. The cornea is responsible for most of the optical power of the eye and the crystalline lens fine-tunes the focus. Inside the eye there are two fluid-filled sections separated by the lens: the anterior segment, including the cornea, the angle structures, and

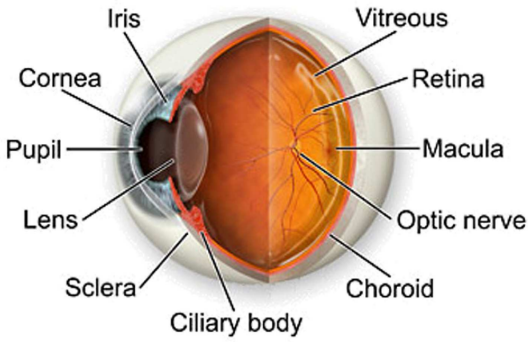

Figure 1.1: Section of the anatomy of the eye (from www.jirehdesign.com)

the iris, and a clear, watery substance called aqueous humor; the posterior segment containing a clear, gel-like material called the vitreous humor; the retina, and the optic nerve.

1.2 The anatomy of the cornea

The cornea is a transparent and avascular ocular tissue. It is exposed to the external environment as it forms the outer shell of the eyeball covering the iris and the anterior chamber. Its major functions are refracting and transmitting light to the lens, the retina and the choroid as well as protecting the inner components of the eye against physical injury and potential harmful substances.

The cornea has a convex and aspherical shape. Its anterior surface curvature is steeper in the center and flattens towards the periphery. Its horizontal dimensions are 11 to 12 mm, whereas its vertical dimensions are 9 to 10 mm. Its thickness varies from 0.5 mm at the center to 0.7 mm at the periphery. The refractive power of the cornea is 40 to 44 dioptries and accounts for about two-thirds of the total refractive power of the eye. Therefore, small changes in the corneal shape or thickness can result in important visual distortions and refractive errors. Transparency is also a unique characteristic of the corneal tissue, which is necessary to maintain its optical properties. This is ensured by the highly ordered stratified structure of the tissue coupled to small variations in the refractive index of the cornea.

The structure of the cornea has been studied by scanning electron microscopy, transmission electron microscopy and, more recently, synchrotron X-ray diffraction. This last technique does not require sample preparation including fixing, dehydration or staining, and therefore better respects the physiological hydration of the cornea.
The human cornea is composed of five layers, which are the epithelium, Bowman's membrane, the stroma, Descemet's membrane and the endothelium. The anterior layer is covered by a tear film and the posterior layer is bathed in the aqueous humor [35, 70, 71, 81, 90]. A histological section of a human cornea is shown in figure 7.1.
The epithelium has five to seven layers of cells for a total thickness of 50 to 52 μm and specialized metabolic characteristics that allow its survival over an avascular tissue. It is self-renewing and presents the ability to respond to wound healing. The function of light refraction proper

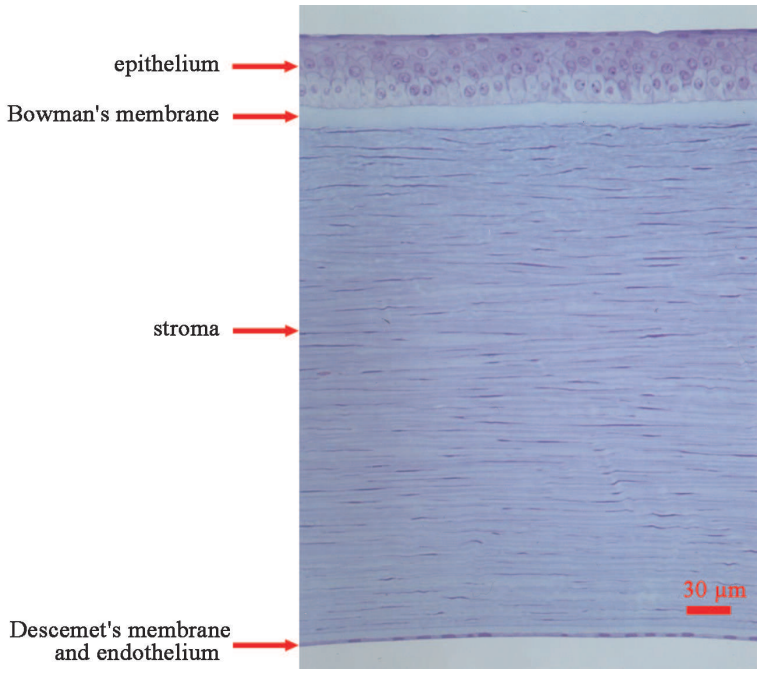

Figure 1.2: Histological section of a human cornea [from Michèle Savoldelli, Hôpital Hôtel Dieu de Paris]

to cornea is brought about by its perfectly smooth and wet surface and its regular thickness. Loss of the smoothness of the epithelial surface results in degradation of the optical image and blurred vision. Another important physiological function of the epithelium is to protect the deeper layers of the cornea from external biological and chemical attacks and to prevent the penetration of the tear liquid into the stroma which could be responsible for edema and inflam-

mation.

The basement membrane is the inner surface of the epithelium. It provides anchorage to the adjacent Bowman's membrane and stroma. Bowman's layer is a 8-12 μm acellular membrane formed of a random arrangement of collagen fibers and proteins like proteoglycans. It exists in primates, including humans, but is thin or nonexistent in many mammals. The physiological role of Bowman's layer remains still unclear, but it is believed that the network of fibrils ensures adhesion between epithelial cells and stromal matrix and contributes to the smoothness of the corneal surface.

The stroma constitutes about 90 % of the corneal thickness. The structure and properties of the stroma are responsible for important characteristics of the cornea, such as transparency and mechanical strength. The stromal tissue is formed by cells which occupy only 2 to 3 % of the total volume, and by an extracellular matrix whose main components are collagen, water, proteoglycans, glycosaminoglycans, and other proteins, which can absorb water in amounts equivalent to 1 000 times their volume. Collagen itself is a strongly hydrophilic protein and constitutes about 90 % of the stromal volume. In the stroma, collagen forms fibrils, which get organized in fibers. These last are in turn arranged in lamellae, generating a hierarchic structure. The basilar unit of collagen fibrils is the tropocollagen (TC) molecule, which is 1.5 nm in diameter, and 300 nm long. It consists of three polypeptide chains associated in a triple-helix structure with a periodicity of 8.6 nm, as shown in figure 1.3. Six TC molecules self-assemble around a com-

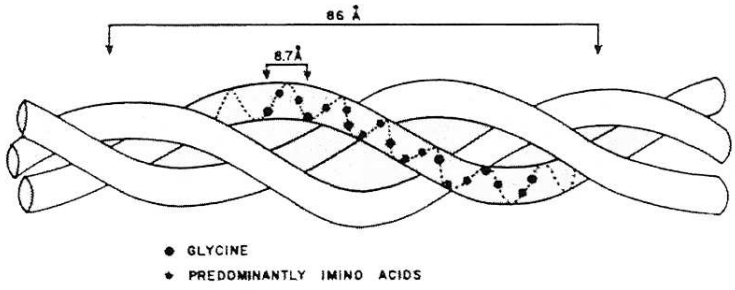

Figure 1.3: Schematic drawing of the tropocollagen (TC) molecule (modified from [118])

mon center in a nearly hexagonal manner to form fibrils, which in turn settle down with lateral and end-to-end binds in order to compose fibers with uniform diameter. Spaced at a regular distance, the fibers pack into layers. X-ray diffraction measurements yielded a fibril diameter close to 31 nm and a center-to-center distance of 62 nm [38, 97], whereas other investigators reported values of 24-26 nm for the diameter and 64-67 nm for the distance [14] using transmis-

sion electron microscopy. Since TC molecules within the fibril are staggered by approximately one quarter of their length, fibrils display a band structure in which regions with gaps and regions with overlaps of TC molecules alternate, as schematized in figure 1.4. Surrounded by

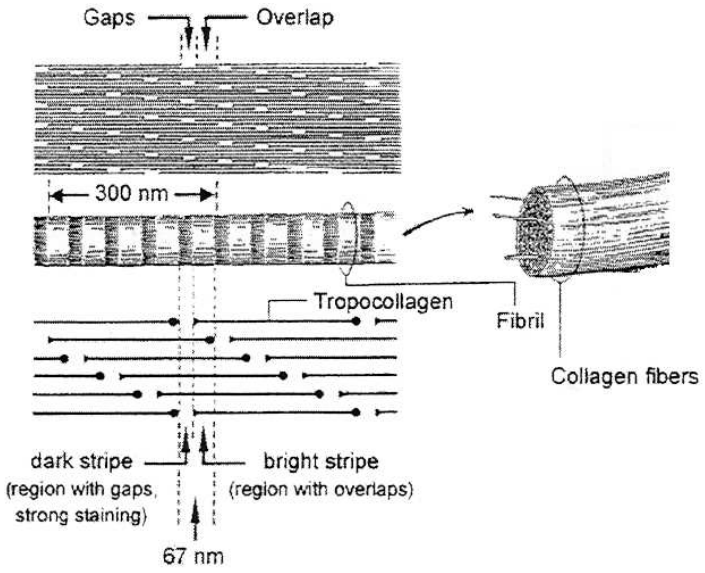

Figure 1.4: Spatial organization of collagen from the molecular level to the fiber level (modified from [118])

a ground substance consisting largely of proteins and nonfibrillar collagens, fibers associate with a regular distance of about 41 nm to form layers or lamellae. In the center of the cornea, the human stroma contains over 300 stacked thick lamellae. Thickness of each lamella is 1 to 2 μm (figure 1.5). Adjacent lamellae lay at different angles, between 0° and 90°, with preferred orientations in the inferior-superior and nasal-temporal directions, and run uninterrupted from limbus to limbus. Different collagens are present in the lamellar stroma: corneal fibers consist essentially of type I collagen; however, they also contain a significant proportion of type V collagen. The latter, within a type I fibril, limits the ultimate diameter that fibrils can reach, which may contribute to explain transparency. Type VI and XII filaments bind collagen fibers in the shape of fibril network. They ensure the regularity of the stromal structure, essential to maintain the corneal optical transparency at visible wavelengths. After the collagens, the second major group of extracellular proteins in the stroma is proteoglycans, which are molecules composed of a core protein joined to one or more polysaccharide chains called glycosaminoglycans. Proteoglycans are also considered responsible for maintaining the relative position of the fibrils and restricting their growth. The extracellular matrix is secreted by cellular components, the kera-

tocytes, which are elongated cells laying between stromal lamellae and parallel to the corneal surface. Keratocytes are thought to contribute to the stability of the corneal shape and regular organization.
Descemet's membrane is located between the stroma and the endothelium and constitutes a protective barrier. In adult humans it is 8 to 10 μm thick and is mostly composed of collagen.
The endothelium is the inner part of the cornea. It is composed of a single layer of cells, 4 to 6 μm thick, uniformly arranged, with a density of about 3500 cells/mm^2. The endothelium has two important physiological functions: the barrier and the pump function. Adjacent cells are linked so that they constitute a leaky barrier to aqueous humor permitting the transport of nutrients to the cornea while preventing the fluid from flowing into the stroma. Acting as an ionic pump, the endothelium regulates hydration of the cornea and maintains it at low levels. A failing endothelium leads to a stromal swelling and a consequential loss of the corneal transparency. It is therefore critical to avoid damaging endothelial cells during any surgery, yet in some cases a possible loss of cells may cause the remaining cells to enlarge until they cover the defective area.

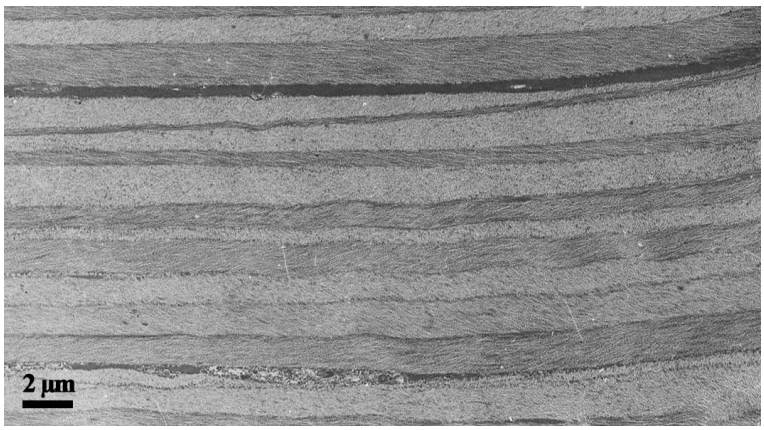

Figure 1.5: TEM micrograph of corneal stroma showing the lamellar organization. Lamellae are parallel to the corneal surface and lay at different angles [from Michèle Savoldelli, Hôpital Hôtel Dieu de Paris]

1.3 Optical properties of the cornea

1.3.1 Refractive index

X-ray diffraction experiments performed by Leonard *et al.* [60] have unambiguously demonstrated that there is a difference in the refractive indices of the collagen fibrils and of the extracellular matrix. Since the fibrils cannot be separated from the ground substance, it is difficult to measure directly the respective indices of refraction. Nevertheless, X-ray diffraction techniques give information about the volume of the compounds and enable estimating the total refractive index using the Gladstone-Dale law of mixture which applies to composite materials. The total refractive index of a composite material n_{tot}, can be expressed as the partial sum of the refractive indices of its components, n_1, n_2, ..., n_N, weighted by the volume fraction of each component, f_1, f_2, ..., f_N:

$$n_{tot} = n_1 f_1 + n_2 f_2 + ... + n_N f_N \quad . \tag{1.1}$$

For a human cornea, Leonard *et al.* calculated a refractive index of 1.41 for fibrils and of 1.36 for extrafibrillar material and a fibril volume fraction of 0.22. By applying the Gladstone-Dale law, this set of values leads to a refractive index of the stroma of 1.37 in agreement with measurements provided by Maurice in a previous study [69].

1.3.2 Birefringence

Corneal tissue shows birefringent properties which can be separated into intrinsic birefringence and form birefringence ([7], review). The former is due to the structure of collagen fibers composed of molecules longitudinally elongated. Light linearly polarized along the axis of the fibril travels at a slow velocity from light polarized perpendicularly. Form birefringence is attributed to the anisotropy of the stroma, characterized by a lamellar organization of the collagen fibrils. Each lamella may be considered as a thin linear retarder with its slow axis oriented along the fibril direction; corneal birefringence would represents the cumulative action of the lamellae of the entire stroma. A different approach has likened the cornea to a curved biaxial crystal with its fastest principal axis perpendicular to the surface. In many clinical situations (surgery

or diagnostic), light is incident nearly perpendicular to the surface, the perpendicular axis has little influence on the polarization of the state, and corneal birefringence is governed by the two principal axes that lie tangential to the surface.
The birefringent properties of the corneal tissue has been observed by measuring the cross-polarized transmission for a rabbit cornea as the incident polarization direction is rotated through 360^o [25]. Results are presented in figure 1.6 and reflect the behavior of a birefringent material except that the minimum transmission is higher than zero.

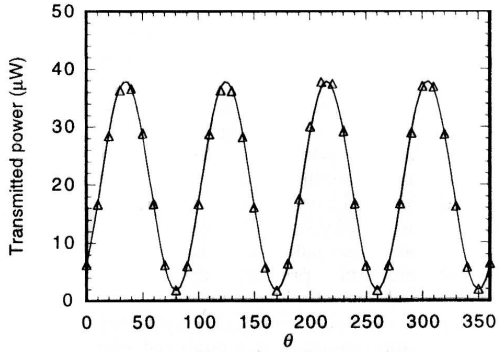

Figure 1.6: Cross-polarized transmission power through a rabbit cornea, recorded as the incident polarization is rotated through 360°. The solid line represents a fit of the data [25]

1.3.3 Optical absorption

Optical absorption in a tissue takes place when the frequency of the incident light corresponds to energy transitions of the molecules which compose the tissue. Figure 7.2 shows the absorption of proteins, DNA, melanin, hemoglobin and water, which are the main tissue components, as a function of the wavelength.
The optical transmission of the cornea is essentially governed by the absorption properties of water and proteins. In the wavelength range of 400 to 780 nm, the most important chromophores are melanin and hemoglobin that are absent from the cornea. Hence, light is transmitted by the corneal tissue, which is why this spectral range is called the visible region of the optical spectrum. In the ultraviolet region, proteins display significant absorption and in the infrared both proteins and water contribute to the absorption of the light, with certain transmission windows between 1 and 2 μm.

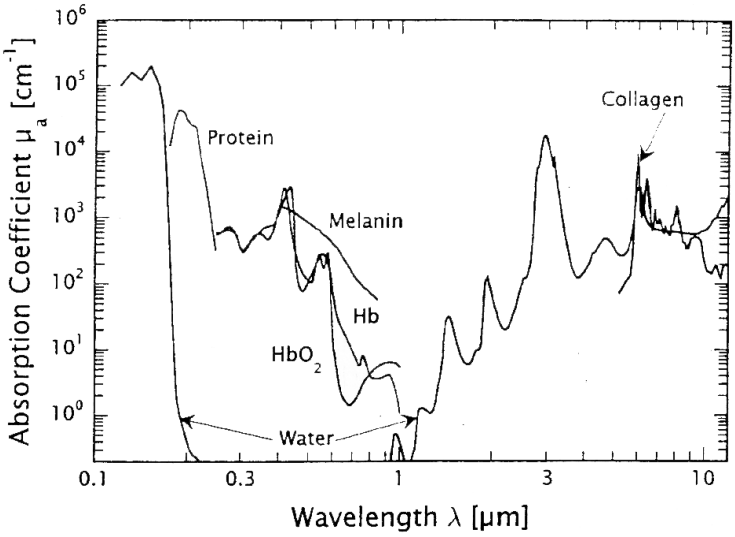

Figure 1.7: Optical absorption coefficients of principal tissue chromophores in the 0.1-12 μm spectral region [118]

1.3.4 Transparency of healthy corneas

The characteristic property of the cornea of neither absorbing nor appreciably scattering visible light is referred to as transparency. This remarkable property distinguishes the cornea from the other human connective tissues. In the previous section we have seen that the corneal tissue does not absorb light in the 400-780 nm wavelength range. The reasons why light is not scattered either are still not fully understood, although it has been a subject of interest for many decades. However, a number of different theories have been put forward.

The simplest model is based on the assumption that the refractive index of the cornea is uniform, therefore, the light is not scattered when propagating through the tissue. This theory is generally rejected as it contradicts results evidencing a difference in the refractive indices of the fibrils and of the ground substance in which they are embedded. Maurice [69] first proposed that the secret of the corneal transparency may lay rather in the regular arrangement of the collagen fibrils in the corneal tissue. He showed that if collagen fibrils acted as independent scatterers, almost 90 % of the incident light would be scattered. Hence, he suggested that if fibrils are arranged in the form of a perfect crystalline-like hexagonal lattice, correlations in their relative positions lead to destructive interferences of light scattered in all direction other than the forward direction. However, electron microscopy and X-ray diffraction investigations

failed to demonstrate crystalline order. Moreover, a perfect crystal-like structure would produce a total transparency, which is not observed as the cornea is visible in slit lamps. Later research showed that lattice structure is not essential to account for transparency. Feuk [26] formulated a theory based on a long range order model with small, random displacements from the ideal lattice organization. Nevertheless, further investigations, based on the Fourier analysis of the corneal structure, were consistent with a short range order rather than a long range order found in crystals [36]. Hart and Farrell [41] computed a distribution function expressing a probability of correlation between fibrils from electron micrographs of corneal stroma. They found that the position of pairs of collagen fibers remains correlated only over distances equivalent to the spacing between two neighboring fibers at most (figure 7.3a). This translates to a short-range correlation of about 200 nm. They made a precise mathematical summation of the fields scattered by such a partially ordered array. The calculated corneal scattering was in accordance with that found experimentally. With a similar but simpler mathematical model, Benedeck [3] demonstrated the Bragg diffraction principle. He advanced that scattering of light is produced only by those fluctuations in the refractive index whose Fourier components are larger than one-half of the light wavelength in the medium. In transparent cornea, scattering is then reduced by the densely packed structure of the stroma with low fluctuations in the density of the fibers.
In summary, even though there is still no universally accepted explanation to the corneal transparency, all theories recognize that three factors are determinant [25]:

1. each individual fibril has a very small scattering cross-section;
2. despite fibril scattering inefficiency, the large number of fibrils requires that the waves scattered by different fibrils must interfere destructively with one other in all directions but the forward one;
3. the cornea is thin, approximately 0.5 mm in humans.

1.3.5 Optical scattering of opaque corneas

Corneal transparency is partially dependent on the ability of the cornea to maintain a constant rate of hydration. When the endothelial cell density falls below a critical density (200 to 400 cells/cm^2), following trauma, inflammation or dystrophy, the endothelium fails to regulate the corneal hydration [35, 81]. As a consequence, edema gradually develops, which may mildly or

strongly deteriorate the vision, leading eventually to blindness. Edema are associated with a swelling of the stroma in the posterior direction and with an increase of the corneal thickness. Subsequently, the tissue becomes opaque and the incident light is scattered. Even though many complex models exist describing the attenuation of the light irradiance propagating through a scattering tissue, we limit our study to the Beer-Lambert law, whereby the transmitted irradiance I_t can be expressed as

$$I_t = I_0 e^{-\alpha_s z} \tag{1.2}$$

where I_0 is the incident irradiance, α_s is the scattering attenuation coefficient and z is the thickness in the direction of the light path. In the case of a corneal lamella, which consists of parallel fibrils, $\alpha_s = \rho\sigma_s$, where ρ is the number of fibrils per unit area in a cross section and σ_s is the scattering cross section. This last indicates the scattering capability and is related to its cross-sectional area σ_g through the scattering efficiency Q_s by the relation $\sigma_s = Q_s\sigma_g$. The scattering coefficient α_s is defined as the probability of photon scattering per unit length in a medium. The reciprocal of α_s is referred to as the scattering mean free path l. It measures how deep a light can penetrate according to the relation

$$l = \frac{1}{\alpha_s} \quad . \tag{1.3}$$

The loss of transparency in a swollen cornea is often associated to a perturbation of the order in the position of the fibrils forming the collagen matrix [36]. Electron micrographs have revealed that in swollen corneas fibril density is decreased to a point that some regions of the collagen are completely devoid of fibrils (figure 7.3b). Benedek [3] called these defective regions "lakes" in the assumption that they contain excess fluid. Lakes have dimensions comparable to the wavelength of light and introduce fluctuations in the refractive index over a length scale that is equivalent or larger than half the wavelength of the light. They therefore may act as scattering centers [3, 49].
Meek *et al.* [72] explored theoretically the influence of different parameters on the loss of the light transmission by the cornea. In figure 1.9, the transmission of the light is plotted against the wavelength as function of individual parameters. The graphs clearly demonstrate that light scattering is increased when:

1. the fibril diameter increases. Reducing the diameter has an opposite effect, which means the transmission is augmented, however very thin fibrils would not ensure mechanical strength;

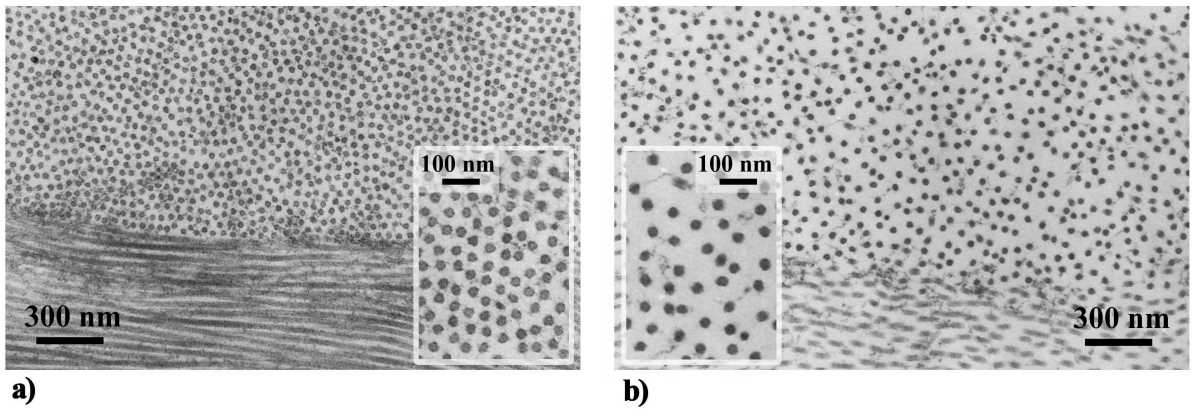

Figure 1.8: Comparison of a transparent cornea characterized by a short range order (a) with an edematous cornea in which the regular arrangement of the fibers is perturbed (b) [from Michèle Savoldelli, Hôpital Hôtel Dieu de Paris]

2. the corneal thickness is increased;

3. the mismatch in the refractive indices of the collagen fibrils and the extracellular matrix is increased.

All these factors reflect either a disorder in the organization of the fibrils in the corneal collagen or an increased scattering efficiency for fibrils. Additionally, recent investigations suggested that keratocytes contain a special protein cell, which is responsible for matching the refractive index of the cellular cytoplasm to that of the surrounding matrix in healthy corneas. When keratocytes are affected by a disorder, they do not ensure this function anymore and can become efficient scatterers [75].
Scattering of the light by spherical particles of any size can be modeled by the Mie theory. It takes into account the reflecting or absorbing properties of the particle material and enables to define the characteristic scattering cross-section. The Mie theory can be reduced to the Rayleigh theory if the spherical particle is much smaller than the wavelength [114]. In this approximation, the scattering cross-section is inversely related to the forth power of the wavelength of the incident light. In swollen corneas, the exact nature of the scattering centers has not yet been determined and scatterers are probably not spherical, therefore a quantitative theoretical model is difficult to derive. However, it could be proved that the modified structure of the collagen fibrils adds a term to the total scattering cross section which varies as the inverse square of the

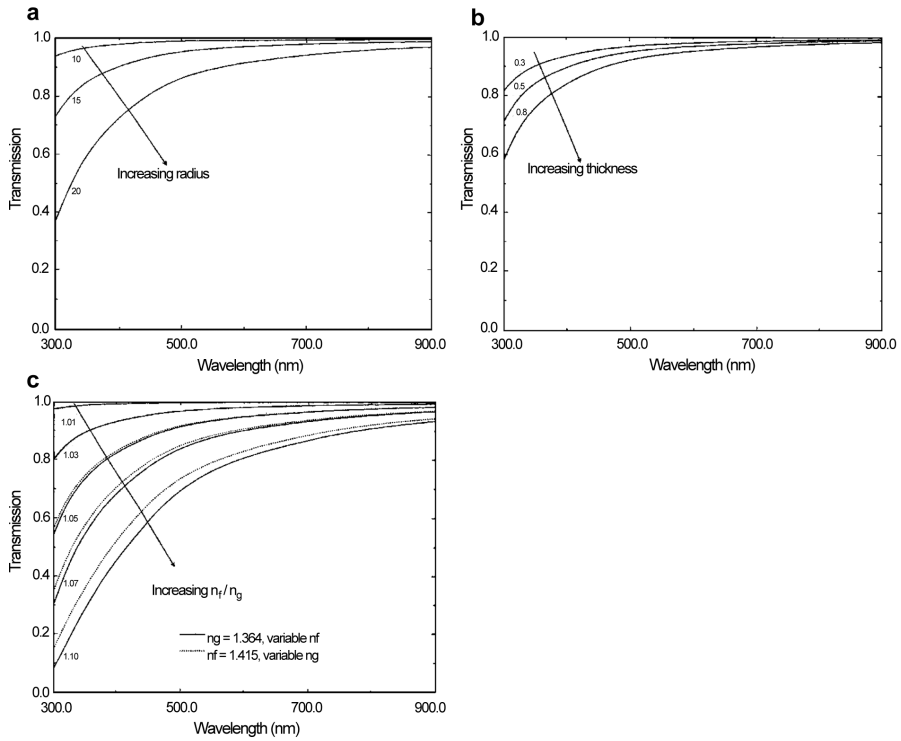

Figure 1.9: Theoretical effects of varying individual parameters of light transmission by cornea [72]

light wavelength, so that

$$\sigma = \sigma_{normal} + \frac{B}{\lambda^2} \tag{1.4}$$

where σ_{normal} is the scattering cross section for normal corneas, which is proportional to $1/\lambda^3$, and B is a constant that increases as the cornea swells [91].

Chapter 2

Ultrafast lasers and their application in corneal surgery

The 1980s - 1990s were marked by important technological improvements in the field of ultrashort lasers:

- in 1986, Moulton [76] discovered a new laser material, the titanium-sapphire, which is a sapphire crystal doped with titanium ions (Al_2O_3). It is characterized by a large spectral gain bandwidth enabling the generation of ultrashort pulses, and a good thermal conductivity reducing thermal effects even for high laser powers. Its nonlinear optical properties allow the generation of pulses *via* Kerr-lens mode-locking [104];
- Strickland and Mourou [107] introduced an amplification technique for the generation of high energetic laser pulses, called the chirped pulse amplification (CPA);
- in parallel, the progress in high-power diode laser technology enabled to generate pulses directly by pumping rare-earth-doped glasses.

These developments led to the successive replacement of dye lasers by more efficient ultrafast laser sources: Ti:sapphire lasers, which are nowadays mostly employed as laboratory systems, and diode-pumped-solid-state femtosecond lasers [45, 58]. Despite their slightly less spectacular performance with respect to pulse duration and energy, these latter are more adapted to

medical applications. Indeed, a surgical laser device needs to be turnkey, extremely reliable, easy to maintain, compact and affordable. Diode-pumped solid state lasers meet these requirements.
In particular, the characteristics of neodymium or ytterbium doped glass lasers were soon considered interesting for applications in ophthalmic surgery, like corneal dissection [53]. Femtosecond lasers are nowadays commonly employed in refractive surgery and tend to replace conventional techniques in cornea transplantation, due to their safety and reproducibility.
In this chapter, the characteristics and technology of ultrashort pulsed lasers are briefly introduced. The laser systems used in the experiments are also described. In the second section, I present current applications of ultrafast lasers in corneal surgery and I review recent experimental and clinical findings. Finally, a short overview of femtosecond laser systems commercially available is provided.

2.1 Ultrashort lasers

2.1.1 Ultrashort pulses

The time dependence of the complex electric field $\mathcal{E}$ of a light pulse generated by a laser can be written as [102]

$$\mathcal{E}(t) = E_0 e^{-\Gamma t^2} e^{-i\omega_0 t} \quad . \tag{2.1}$$

It results from the product of a carrier wave oscillating at an angular frequency of ω_0 corresponding to the central wavelength of the pulse and an envelope $A(t) = E_0 e^{-\Gamma t^2}$, assumed to have a Gaussian shape. The temporal intensity associated to this pulse is given by

$$I(t) = \frac{2}{\eta_0} \cdot |\mathcal{E}(t)|^2 = I_0 e^{-2\Gamma t^2} \tag{2.2}$$

where $\eta_0 = \sqrt{\mu_0/\varepsilon_0} = 377\ \Omega$ is the impedance of free space and $I_0 = 2E_0^2/\eta_0$ is the peak intensity. The Γ parameter is related to the pulse temporal width by the following relations

- at the $1/e^2$ intensity: $\Delta t_{\frac{1}{e^2}} = \dfrac{2}{\sqrt{\Gamma}}$

- at the full width at half maximum intensity: $\Delta t_{\frac{1}{2}} = \sqrt{\frac{2\ln 2}{\Gamma}}$.

By assuming the following Fourier transform convention

$$\mathcal{E}(\omega) = \mathcal{F}[\mathcal{E}(t)] = \int_{-\infty}^{+\infty} \mathcal{E}(t) e^{i\omega t} dt \tag{2.3}$$

$$\mathcal{E}(t) = \mathcal{F}^{-1}[\mathcal{E}(\omega)] = \frac{1}{2\pi} \int_{-\infty}^{+\infty} \mathcal{E}(\omega) e^{-i\omega t} d\omega \tag{2.4}$$

the Fourier transform of $\mathcal{E}(t)$ can be expressed as

$$\begin{aligned} \mathcal{E}(\omega) &= \frac{E_0}{2\pi} \mathcal{F}[e^{-\Gamma t^2}] \otimes \mathcal{F}[e^{-i\omega_0 t}] && \text{(2.5a)} \\ &= \frac{E_0}{2\pi} \tau\sqrt{2\pi}(e^{-\Gamma t^2}) \otimes 2\pi\delta(\omega - \omega_0) && \text{(2.5b)} \\ &= E_0 \tau\sqrt{2\pi} \left(e^{-\frac{(\omega-\omega_0)^2}{4\Gamma}} \right) && \text{(2.5c)} \end{aligned}$$

where the convolution theorem has been used. The Fourier transform of a Gaussian pulse in time is a Gaussian spectrum in frequency. The spectral intensity is therefore given by

$$I(\omega) = \frac{2}{\eta_0} \cdot |\mathcal{E}(\omega)|^2 = 2\pi\tau^2 I_0 e^{-\frac{(\omega-\omega_0)^2}{2\Gamma}} \tag{2.6}$$

and the bandwidths are expressed by

- at the $1/e^2$ intensity: $\Delta\omega_{\frac{1}{e^2}} = 4\sqrt{\Gamma}$
- at the full width at half maximum intensity: $\Delta\omega_{\frac{1}{2}} = \sqrt{8\ln 2}\sqrt{\Gamma}$.

Hence, for a Gaussian pulse, the time-bandwidth product, that is the product of FWHM in time and frequency domain, satisfies the inequality

$$\Delta t \Delta\omega \geq 4\ln 2 \quad . \tag{2.7}$$

If the pulse verifies the identity, it is called Fourier transform-limited, which means that the shortest possible duration corresponding to its spectrum is obtained.

Relation 2.7 implies that a very short pulse has a broad spectrum. It is therefore necessary to take into account that pulses are subjected to dispersion when travelling through optical materials. The propagation time delay of the spectral components of the pulse is defined by the relation

$$T(\omega) = \frac{d\phi(\omega)}{d\omega} \tag{2.8}$$

where $\phi(\omega)$ stands for the spectral phase, defined as the phase of the electric field in the frequency domain. When expressing $\phi(\omega)$ as a Taylor series

$$\begin{aligned} \phi(\omega) &= \phi_0 + \left(\frac{d\phi}{d\omega}\right)_{\omega_0}(\omega-\omega_0) + \frac{1}{2}\left(\frac{d^2\phi}{d\omega^2}\right)_{\omega_0}(\omega-\omega_0)^2 + & \text{(2.9a)} \\ &\quad + \frac{1}{6}\left(\frac{d^3\phi}{d\omega^3}\right)_{\omega_0}(\omega-\omega_0)^3 + \ldots & \text{(2.9b)} \\ \phi(\omega) &= \phi_0 + \phi^{(1)}(\omega-\omega_0) + \frac{1}{2}\phi^{(2)}(\omega-\omega_0)^2 + \frac{1}{6}\phi^{(3)}(\omega-\omega_0)^3 + \ldots & \text{(2.9c)} \end{aligned}$$

the following relation can be obtained

$$T(\omega) = \phi^{(1)} + \phi^{(2)}(\omega-\omega_0) + \frac{1}{2}\phi^{(3)}(\omega-\omega_0)^2 + \ldots \tag{2.10}$$

In particular, $\phi^{(1)}$ represents a constant delay in the pulse propagation and does not modify the pulse characteristics; $\phi^{(2)}$ is called the group velocity dispersion and introduces a time delay varying linearly with the frequency, which stretches the pulse duration.

2.1.2 Femtosecond laser chains

The peak intensity of a laser pulse is expressed in W/cm^2 and can be estimated by

$$I = \frac{E}{\Delta t \times S} \tag{2.11}$$

where E is the pules energy, Δt is the pulse duration and S is the surface of the beam.
Femtosecond pulses are created in a laser cavity, where they typically gain only a few nanojoules of energy. High peak intensities are obtained by amplification using the CPA technique. The principle is to temporally stretch out the pulses to a much longer duration by means of a strongly

dispersive element, before amplification. Reducing the intensity enables avoiding nonlinear effects and optical damage during amplification. After being amplified, pulses are recompressed to their initial duration (figure 7.4).

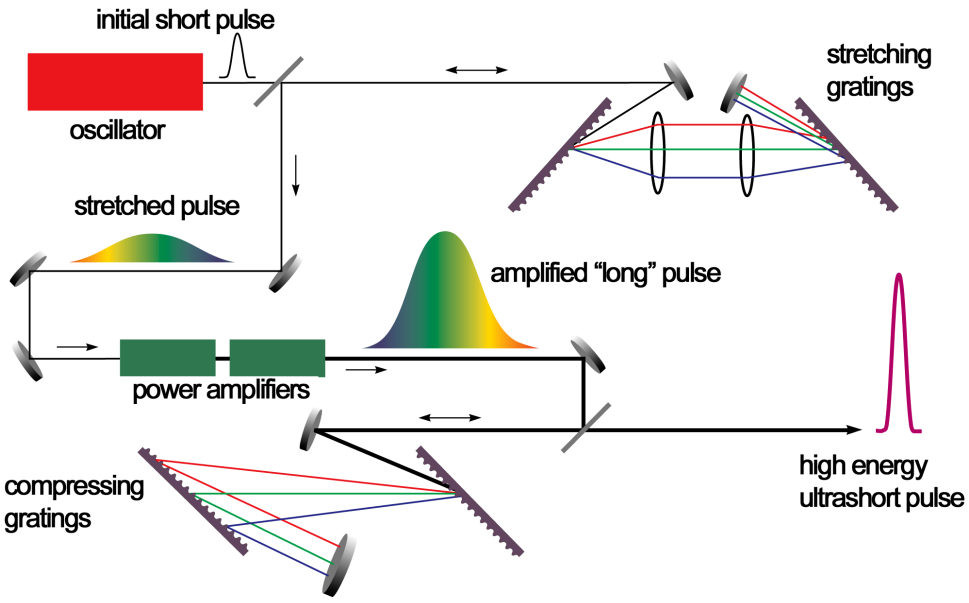

Figure 2.1: Chirped pulse amplification (modified from www.llnl.gov/str/pdfs/09_95.2.pdf)

Oscillator

The longitudinal modes existing in a laser resonator oscillate independently if there are no relations between the phase of the modes. The resulting laser operates in a free multimode regime and there is a competition between the different modes to be amplified by stimulated emission. If these modes are added *in phase* by constructive interference, wave packets are formed and a short pulse is generated. In order to obtain ultrashort pulses, many modes are required to interfere and the gain medium is needed to have a large emission bandwidth. Passive mode-locking is the most frequently used technique to hold the modes *in phase*. It is based on the principle of selectively modulating laser losses, in order to favor the pulsed regime. Passive mode-locking can be achieved by inserting into the cavity a semiconductor saturable absorber mirror or SESAM. It incorporates a saturable absorbing medium, whose optical absorption is

constant at low intensities, but saturates and decreases to lower values as the intensity rises. In this configuration weaker pulses are rejected and only the most energetic pulse propagates in the cavity. The active medium can also generate passive mode-locking by acting as a Kerr-lens which focuses the beam and increases its intensity. The pulsed operation is favored. Furthermore, a hard aperture may be used to attenuate the continuous wave as the spatial distributions of the cw and pulsed modes differ. A set of chirped mirrors or a pair of prisms are added in order to compensate for the beam group velocity dispersion (figure 2.2). The shortest pules duration that has been presently obtained is of the order of 5 fs [24].

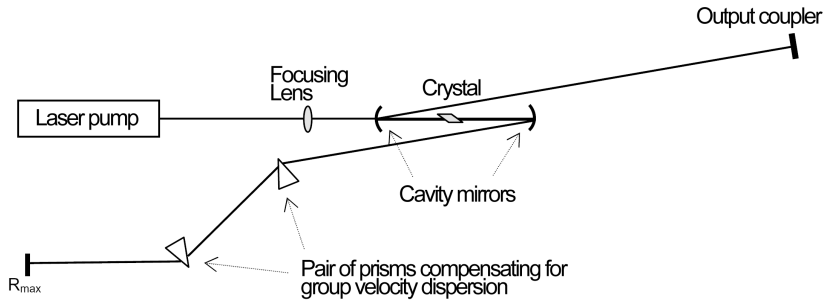

Figure 2.2: Schematic diagram of a self-mode-locked Ti:Sapphire oscillator

Pulse stretcher and compressor

Before being amplified, a pulse needs to be temporally stretched. The principle is to modify the optical path of the individual frequencies composing the spectrum of the pulse by means of dispersive optical elements. The duration of the incoming pulses is typically stretched from a few femtoseconds to a few hundreds picoseconds. Introducing a combination of gratings and lenses into the system induces a positive dispersion causing lower frequencies travelling faster than higher frequencies. The initial short pulse is therefore broadened or chirped. After being amplified, the pulse is recompressed back to its original duration by travelling through a conjugate dispersion line with opposite group velocity dispersion [87, 120]. The compressor has also the role of compensating for the beam dispersion associated to the propagation in the amplification chain.

Regenerative and multipass amplifier

Common approaches to pulse amplification are the regenerative and the multipass technique. The regenerative amplifier is a resonator in which the pulse travels several times through the gain medium, building up its energy at each roundtrip until gain saturation is obtained. The injection and ejection of the pulse are regulated by an optical switch composed of one or more polarizers coupled to a Pockels cell. Each pass introduces losses and dispersion, however the beam has typically a very good spatial quality, since it consists of a single mode amplified in a laser cavity. A schematic drawing of a regenerative amplifier is presented in figure 2.3a.
The multipass amplification device includes a set of mirrors which allows the beam to pass through the gain medium at different angles, as illustrated in figure 2.3b. Compared to the regenerative amplification technique, in the multipass amplifier the beam experiences less dispersion and losses because of the reduced number of optical elements and passes. However, care has to be taken in order to maintain its spatial quality as aberrations are caused by the tilt of the optical axis of the beam relative to the surface of the gain medium.

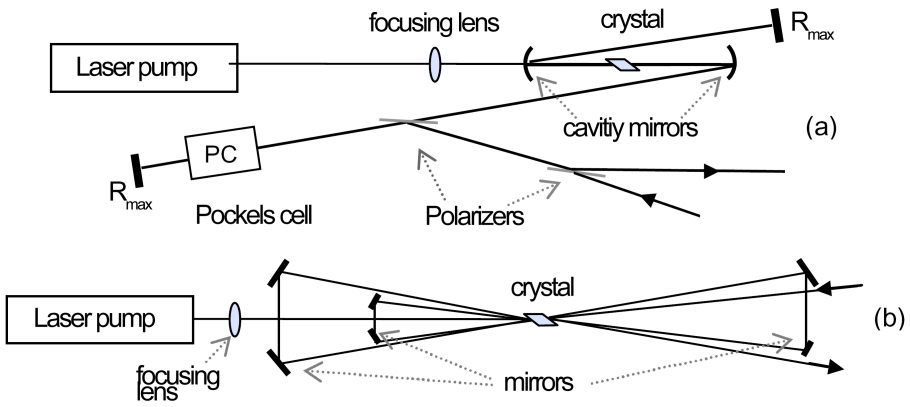

Figure 2.3: Schematic diagram of a regenerative amplifier (a) and a multipass amplifier (b)

2.1.3 Laboratory femtosecond lasers

Neodymium:glass laser

The neodymium:glass femtosecond laser described in this section corresponds to the laser used to perform the experiments at the Laboratoire Biotechnologie et Œil. The experimental set-up is described in chapter 4.

The laser consists of a passively mode-locked diode pumped neodymium doped glass (Nd:glass) oscillator, whose output is amplified by a CPA system with a regenerative amplifier. Figure 7.5 shows a picture of the laboratory Nd:glass laser. The main elements of the system are indicated by numbered labels and specified in the figure caption.

The system includes a Nd:glass oscillator [46]. Neodymium doped glass presents a relatively broad emission bandwidth of 22 nm, an emission cross section of 4×10^{-20} cm^2, an absorption band at 808 nm enabling diode laser pumping, and it can be relatively easily manufactured. On the other hand, its thermal conductivity is low, in the order of 1 Wm^{-1}K^{-1} [18]. This last characteristic requires to design thin glasses to evacuate the heat and to pump at low powers in order to avoid thermal damage. The gain medium is inserted in a z-fold cavity and is pumped by a single-stripe diode laser with a power between 1 and 1.2 W. The pulse propagates in the cavity with a solitonlike shape. The soliton is formed as a result of negative group velocity dispersion, properly introduced by a chirped mirror, and self-phase modulation, experienced by the pulse during propagation through the Nd:glass medium [58]. It is then kept stable by a semiconductor saturable absorber mirror [55]. Inserting a knife-edge into the laser beam path contributes to select the pulsed mode over the continuous one. Output pulses have a duration shorter than 100 fs, a central wavelength of 1.064 μm, an average power of about 20 mW, and are delivered at a repetition rate of 80 MHz.

Before entering the regenerative amplification system, pulses are stretched propagating twice through a transmission grating. The beam path between the stretcher and amplifier is controlled by changing its polarization. The beam first reaches a Glan prism that allows *p*-polarized light to pass and rejects *s*-polarized light, then it travels through a Faraday rotator and a $\lambda/2$ wave plate, which both rotate its polarization. In the forward direction, the polarization is unchanged and the beam is injected into the regenerative amplifier, where it is amplified by means of a diode pumped Nd:glass, as used in the oscillator. After amplification, it passes again through the Faraday rotator and the $\lambda/2$ wave plate and is rejected by the Glan prism because of its polarization, which in the backward direction has experienced a 90° rotation. The amplified

pulsed light is therefore separated from the injection beam line and is sent to the compressor composed of the same transmission grating as the stretcher.
Pulses leaving the compression system have a duration of about 500 fs, a repetition rate variable from 1 to 10 kHz, a central wavelength of 1.06 μm, and a maximum average energy of about 6 μJ (at 10 kHz). The pulse peak-to-peak stability is of about 1%.

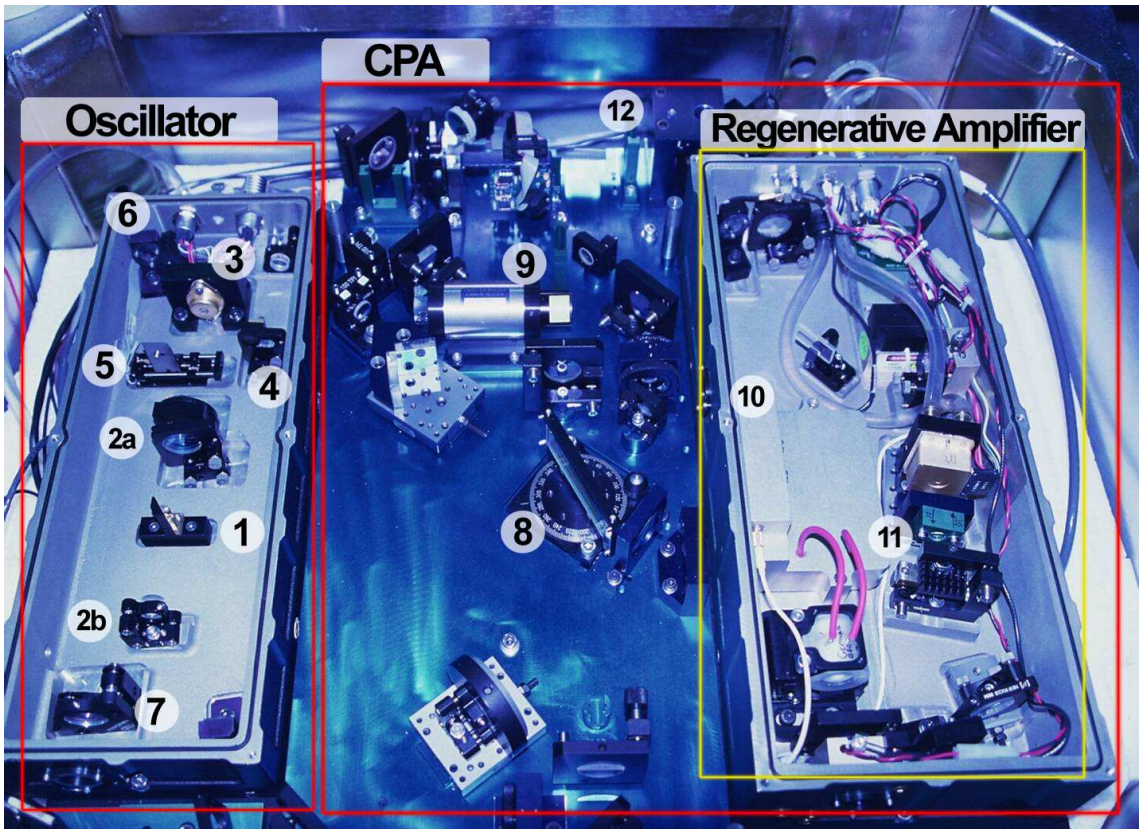

Figure 2.4: Picture of the laboratory Nd:glass laser, installed at the Laboratoire Biotechnologie et Œil. The main elements are labelled as follows: 1) Nd:silicate; 2a and 2b) cavity mirrors; 3) pump diode; 4) semiconductor saturable absorber mirror; 5) knife-edge; 6) chirped mirror; 7) output coupler; 8) grating; 9) Faraday isolator; 10) amplifier entry; 11) Nd:silicate; 12) exit of the laser

Ti:Sapphire laser

The Ti:Sapphire femtosecond laser described in this section corresponds to the laser used to perform experiments at the Laboratoire d'Optique Appliquée.
The oscillator is a Mira[1] Ti:Sapphire Kerr-lens mode-locked oscillator pumped by an Argon laser. It delivers pulses with a sub-100 fs duration, at a repetition rate of 80 MHz, a central wavelength of 805 nm, and an average power up to 64 mW. Pulses are stretched and recompressed after amplification in a CPA system by means of a grating. As in the case of the Nd:silicate laser, the beam path from the stretcher to the amplifier and from the amplifier to the compressor is regulated by a Faraday isolator. Pulse energy is increased in a regenerative amplifier, whose gain medium is a Ti:sapphire crystal pumped by a frequency-doubled yttrium lithium fluoride (YLF) laser. Following compression, pulses have a duration of 170 ± 20 fs, a central wavelength of 800 nm, a maximum pulse energy of 200 ± 20 μJ, and are delivered at a repetition rate of 1 kHz.

2.2 Clinical laser systems and surgical applications

2.2.1 Corneal surgery by femtosecond lasers

Corneal surgery has greatly profited from the technological improvements that pulsed lasers have known over the last decades. Femtosecond lasers enable obtaining very fine disruptive effects in tissue. Compared to nanosecond lasers used for other ophthalmic applications, the reduction of the pulse duration allows reducing the quantity of the energy to be delivered to the tissue for disruption, with strongly diminished mechanical and thermal collateral damages. Therefore, ultrashort pulsed lasers have widely replaced conventional techniques for tissue dissection, because of their precision, safety and predictability.
The first clinical (and commercially available) application of femtosecond laser systems in ophthalmology has concerned refractive surgery, to correct ametropia. Refractive errors typically treated by surgery are myopia and hyperopia. Myopia is a condition of the eye whereby the image is focused in front of the retina resulting in a blurred distance vision. It occurs when

[1] Coherent Inc.

the eyeball is too long or the cornea curvature is too strong. The opposite defect of myopia is hyperopia, which exists when light from a distant object comes into focus behind the retina, because of a too short eye or a too weak refractive power of the cornea or the lens.
In 1989, Pallikaris *et al.* [85] developed a surgical technique called the laser in situ keratomileusis (LASIK) which combines the use of an excimer laser and a mechanical microkeratome in order to modify the shape of the cornea. In the traditional LASIK surgery, the so-called microkeratome, which is a mechanical device, is employed for cutting a corneal flap with a thickness of approximately 150 μm. This layer is created with a portion of the cornea left uncut to provide a hinge (figure 7.6). The flap is then folded back on the hinge exposing the middle portion of the cornea. In a second step, the excimer laser is used to reshape the center of the cornea by removing a certain quantity of stroma. The amount of tissue removed is dependent upon the degree of myopia or hyperopia that is being corrected. Finally, the flap is repositioned over the stromal area fitting without sutures by means of adhesion forces. Since then, the technique has been

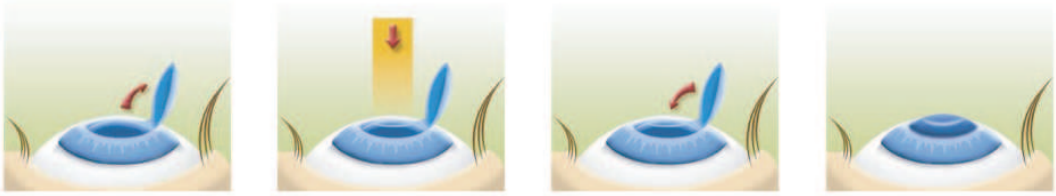

Figure 2.5: LASIK procedure steps (from www.ophtalis.tm.fr)

greatly improved with the introduction of automated and more sophisticated microkeratomes. However, complications may still occur in the creation of the flap with the mechanical instruments, which are delicate to manipulate. These include buttonholing or tearing of the flap, incomplete flap, free cap rather than hinged flap, and thinner or thicker flaps than expected. These problems have been partially or completely overcome by replacing the microkeratome with the femtosecond pulsed laser in cutting the superficial cornel flap. Since first laboratory experiments [53,64,67], fs-LASIK has been widely developed and it represents today a worldwide popular surgical procedure. A growing number of studies agree in stating that advantages in using a femtosecond laser include more precise positioning of the flap, more accurate thickness of the flap, and a lower probability of intraoperative complications [4, 57, 83, 106]. Additional works have shown improved astigmatism neutrality and lower wavefront aberrations [22, 113]. When using a femtosecond laser, depending on the laser system, the cut of the corneal layer

is achieved by applying successive beam spots in small adjacent zones, or a single-pass raster pattern, or a spiral pattern from the periphery to the center of the cornea at a fixed depth. This operation is followed by a movement of the spots along the circumference of the flap in order to incise through the anterior stroma up to the tissue surface.
A cornea requiring a refractive correction is a transparent material and the femtosecond laser interaction with transparent tissues in the ultashort pulsed regime has been widely investigated in both laboratory and clinical studies. From a physical point of view, we believe that the key parameter for a safe, precise and successful procedure is represented by the choice of a proper radiant exposure of the laser, when focused into the bulk of the cornea. As detailed in chapter 3, in the femtosecond regime optical breakdown inducing disruption of collagen fibers occurs at a determined fluence. Pulses with a radiant exposure lower than the threshold will not cause any cut, whereas pulses much more energetic than required may induce unwanted secondary effects. By taking into account the threshold value of the radiant exposure, which has been determined in different studies [34, 79, 109, 116, 118], commercial femtosecond lasers are pre-programmed to deliver the correct energy required for proper collagen disruption in transparent corneas.
Recently, ultrafast lasers are increasingly used to perform keratoplasty, which is also referred to as cornea transplantation. The common manual or semi-automated surgical techniques for total grafting or penetrating keratoplasty are critical and not always reproducible considering the depth of the incisions and the difficulty in dimensioning the donor graft to match exactly the geometry of the corneal disc to be replaced in the recipient eye. The flexibility and the precision of the femtosecond lasers ensure connection between the donor and the recipient corneas. In addition, commercial femtosecond lasers offer a wide variety of cut patterns, which may favor wound healing. They include top hat, mushroom and Z- shapes (figure 7.7). The potential of ultrafast lasers to cut corneal tissue in transplant procedures was first assessed in experimental studies. Trephination of corneal tissue [73], inverse mushroom [99], and top hat-shaped [105] penetrating keratoplasties were successfully achieved when using clinical systems. Two recent interventional case series have reported neither interoperative nor postoperative complications when performing penetrating keratoplasty in patients with various corneal diseases [9,44]. Partial thickness transplantation can also be carried out. Posterior lamellar keratoplasty consists in grafting only the posterior part of the cornea, including the endothelium, Descemet's layer, and a layer of stroma of variable thickness. This is a quite delicate surgery where a major advantage of the femtosecond laser over mechanical techniques consists in performing precise lamellar incisions in the volume of the cornea, preserving the anterior layers and reducing the risk of irregular cuts, perforations and tears.

Figure 2.6: Keratoplasty cut patterns: top hat, mushroom and Z-shaped (from left to right)

The feasibility of fs laser posterior lamellar keratoplasty was evaluated in *in vitro* studies. Tissue dissection was overall efficiently obtained and light and scanning electron microscopy displayed relatively smooth cut surfaces, yet tissue bridges remained [96, 100, 103]. However, when treating opaque corneas, energies up to three to four times the threshold energy for disruption of healthy corneal tissue were required.

2.2.2 Commercially available femtosecond laser systems

Four femtosecond laser devices are available today for corneal surgery (figure 7.8):

- Intralase FS60, produced by the US company AMO (Advanced Medical Optics, Inc.). Its main characteristics are: wavelength 1,05 μm, repetition rate 60 kHZ, applanation lens flat. A keratoplasty unit is available.
- Femtec, designed by the German company 20/10 Perfect Vision®. It is characterized by a Nd:glass laser medium, a repetition rate of 40 kHZ and a curved applanation lens.
- Da Vinci, manufactured by the company Ziemer Ophtalmic Systems (Ziemer Group Corporate Structure), installed in Switzerland. It is the only laser system delivering pulses at a repetition rate of approximately 1 MHz.
- VisuMax, recently commercialized by Carl Zeiss Meditec, Inc. It operates at a repetition rate of 100 kHz.

All systems incorporate a diode-pumped femtosecond laser (solid-state or fiber laser in the case of the VisuMax). They deliver pulses at an energy of a few μJ and a few nJ in the case of the Da Vinci, in the near-infrared wavelength range, with a duration between 400 and 800 fs. The main

Figure 2.7: Commercially available femtosecond lasers (trademarks and model designations are protected)

difference between the four devices consists in the repetition rate and/or the shape of the applanation lens. The repetition rate influences the laser-tissue interaction process. When operating at the MHz regime, temperature accumulation effects may occur [116]. However, no clinical studies exist reporting differences in the post-operative visual acuity or related long-term complications.

The confidentiality on technical characteristics prevents access to complete specifications, such as the focused spot size or numerical aperture, or the spots separation. These data would allow to fully characterize the system and determine the key parameters in the laser-tissue interaction.

Chapter 3

Interaction of femtosecond lasers with corneal tissue

The physical mechanisms which rule the interaction of the light with the tissue differ strongly depending on the laser operation regime. This allows a variety of surgical applications. The key parameters defining the specific modes of interaction of the laser with the tissue are the wavelength and the duration of the exposure, characterizing the energy deposition time. The interplay between these factors induces mechanical, thermal and/or chemical modifications and may result in hemostatic effects, molecular denaturation, structural changes, tissue removal or cutting.

In the context of ophthalmological surgery, interaction times from 10 ms to 100 ms are still considered quasi-continuous. They are commonly achieved by using argon lasers, which are focused on spot sizes of 30-100 μm^2. This leads to irradiances up to 10^5 W/cm^2 which are characteristic for photocoagulation, a thermal process associated to protein denaturation due to an increased temperature of the tissue [6, 119]. Laser photocoagulation is a technique widely employed for the treatment of retinal disorders affecting blood vessels [61, 74, 77]. Long, short, and ultrashort regimes refer to pulse durations from the nanosecond to the femtosecond range. The transition from one regime to the other is gradual; however, pulses lasting from one femtosecond to a few picoseconds may be considered ultrashort. When properly focused on a target, ultrashort pulses create irradiances in the order of 10^{13} W/cm^2, which locally generate electric fields comparable to the atomic and intramolecular Coulomb electric field. Pulse widths

in the order of a nanosecond are considered long. Short regime is in between these categories. The energy conversion process of long, short, and ultrashort pulses into tissue has been the subject of many investigations ([116, 118] reviews). The physical mechanism governing the laser-tissue interaction is called laser-induced plasma-mediated ablation, or laser-induced optical breakdown. It relies on the nonlinear absorption in the target achieved when a material specific radiant exposure is exceeded. Reducing the pulse duration from the nanosecond to the femtosecond scale diminishes the threshold for plasma formation and strongly minimizes thermal and mechanical effects [62, 109]. Ultrashort pulsed lasers enable achieving well confined and fine cutting effects and are therefore very interesting for microsurgery of ocular transparent media [63, 78].

In the fs regime, below fluence values causing permanent modification of the material, other nonlinear optical effects can be observed. The collagen matrix constituting the cornea displays strong nonlinear optical susceptibilities permitting the generation of frequency-doubled light under the action of short laser pulses. This phenomenon is called second harmonic generation (SHG); it occurs in materials characterized by a nonlinear polarization and a non-centrosymmetric molecular organization at the focal volume. Its intensity grows with the square of the incident intensity. In 1971, Fine *et al.* [27] first reported second harmonic generation (SHG) emitted in the visible region when collagen is irradiated by near-infrared light. To date, SHG in tissues has mostly been exploited in microscopy for high penetration depth imaging of tissue structures and functionalities and, as long as tissue is concerned, to resolve the organization of collagen fibers in corneal stroma and sclera. Compared to TW/cm^2 irradiances necessary for the disruption mechanism, SHG can be produced at MW to GW/cm^2 irradiances.

In the first part of this chapter, I provide a description of the mechanisms that govern the laser-tissue interaction with special emphasis on processes involved in our experiments. I first focus on the nonlinear ionization of the material followed by optical breakdown in short and ultrashort regimes, which leads to tissue ablation or disruption. I further explore how self-focusing phenomena arise from the nonlinear intensity-dependent index of refraction, when tissue is exposed to ultrashort pulses. In the following section, second harmonic generation in collagen is described, followed by a brief presentation of applications of SHG for understanding the structure and the activity of biological tissues.

3.1 Origin of nonlinearities

Optical nonlinear phenomena manifest the properties of some materials to develop a nonlinear polarization in the presence of an external electric field. They occur when the system response depends nonlinearly upon the strength of the applied optical field.
The real field $\mathbf{E}$[1] associated to a quasi-monochromatic wave of central frequency ω can be written as

$$\mathbf{E} = (\mathbf{E}_\omega e^{-i\omega t} + \bar{\mathbf{E}}_\omega e^{i\omega t}) = (\mathcal{E} + \bar{\mathcal{E}}) \tag{3.1}$$

where the spatial variation of the field is taken into account by means of the relation

$$\mathbf{E}_\omega = A_\omega e^{i\mathbf{k}\cdot\,\mathbf{r}} \tag{3.2}$$

A_ω being the amplitude, $\mathbf{k}$ the wave function associated to the electric field, and $\mathbf{r}$ the position at which it is calculated. In the linear regime, applying $\mathbf{E}$ to a material produces a polarization according to

$$\mathbf{P}_L = \varepsilon_0 \widetilde{\chi}^{(1)} \mathbf{E} \tag{3.3}$$

where ε_0 is the permittivity of free space and $\widetilde{\chi}^{(1)}$ is the first order susceptibility tensor. The spatial and temporal dependency of $\mathbf{P}_L$ and $\mathbf{E}$ have not been made explicit for clarity.
Focusing a pulsed laser beam into the bulk of a material produces very high peak intensities, which can correspond to electric fields comparable to the atomic internal fields. In these conditions, the linear approximation is no longer valid. The produced polarization $\mathbf{P}$ can be written as

$$\begin{aligned} \mathbf{P} &= \mathbf{P}_L + \mathbf{P}_{NL} = \mathbf{P}^{(1)} + \mathbf{P}_{NL} && \text{(3.4a)} \\ &= (\mathbf{P}_\omega e^{-i\omega t} + \bar{\mathbf{P}_\omega} e^{i\omega t}) \quad . && \text{(3.4b)} \end{aligned}$$

$\mathbf{P}_\omega$ is the contribution to the polarization at the frequency ω of the incident electric field. $\mathbf{P}_{NL}$, the nonlinear polarization has the form

$$\begin{aligned} \mathbf{P}_{NL} &= \mathbf{P}^{(2)} + \mathbf{P}^{(3)} + ... + \mathbf{P}^{(n)} && \text{(3.5a)} \\ &= \varepsilon_0 (\widetilde{\chi}^{(2)} \mathbf{E}\mathbf{E} + \widetilde{\chi}^{(3)} \mathbf{E}\mathbf{E}\mathbf{E} + ... + \widetilde{\chi}^{(n)} \mathbf{E}^n) && \text{(3.5b)} \end{aligned}$$

[1] Bold letters in this text are used to indicate a vector

where $\widetilde{\chi}^{(n)}$ represents the n_{th}-order nonlinear susceptibility tensor and $\mathbf{P}^{(n)}$ is the n_{th}-order nonlinear polarization, which is proportional to $\mathbf{E}^n$. The magnitude of $\widetilde{\chi}^{(n)}$ quickly decreases as the order n increases. For gas and condensed matter $\widetilde{\chi}^{(n+1)}/\widetilde{\chi}^{(n)}$ is of the order of $1/E_{at}$, where E_{at} is the atomic binding electric field ($\sim 10^8$ V/cm) [8].
We restrict our investigation to the observation of second- and third-order nonlinear polarizations.

3.2 Laser-induced optical breakdown

3.2.1 Nonlinear ionization

Theoretical models of the ultrashort pulsed laser-tissue interaction are based on the Drude model and the assumption that the cornea is a transparent material which behaves like a dielectric. A free electron is generated when the energy absorbed is higher than the energy quantity necessary to excite the electron from the valence to the conduction band. In transparent materials, for the considered wavelengths one single photon is not energetic enough to overcome the band gap, and energy deposition is possible only *via* nonlinear absorption. This means that the absorption probability is a nonlinear function of the laser intensity. Moreover, in ultrashort regimes, the oscillation energy of the electrons due to the electric laser field needs to be taken into account, and the band gap energy has to be replaced by the effective ionization potential

$$\tilde{\Delta} = \Delta + \frac{e^2 E^2}{4m\omega^2} \tag{3.6}$$

where ω and E are the frequency and the amplitude of the electric laser field, e and m are the charge and the reduced mass of the electron, which is given by the mass of the electron in the conduction band and the mass of the hole in the valence band. Δ is the band gap energy [56]. *A priori* two competing nonlinear mechanisms contribute to the creation of free electrons: multiphoton ionization (MPI) and tunnel ionization [56], followed by avalanche ionization. MPI corresponds to a simultaneous absorption of k photons by an electron in order to be promoted from the valence to the conduction band, as represented in figure 3.1. The probability for multiphoton absorption is proportional to the laser intensity raised to the power k, I^k [51]. Since it has been shown that the optical breakdown threshold in cornea is comparable to that

in water [16], the band gap energy for cornea is considered to be close to the value in water of 6.5 eV [80]. The photon energies at wavelengths of 800 nm and 1.06 μm, which are typical of research and clinical lasers for plasma-mediated ablation in transparent materials, are 1.56 eV and 1.17 eV, respectively, thus requiring the addition of respectively five and six photons to promote an electron to the conduction band. In tunneling photoionization, the electric field of the laser lowers the potential barrier which binds one electron to its parent atom. If the field is very strong, the potential barrier can be sufficiently decreased to allow the electron escaping from the atom, as shown in figure 3.1. The transition from the MPI to the tunneling regime depends on the field strength and the frequency of the electromagnetic field, and is defined by the Keldysh parameter [56]

$$\gamma = \frac{\omega}{e}\sqrt{\frac{mcn\varepsilon_0\Delta}{I}} = \frac{\omega}{\omega_t} \tag{3.7}$$

where c is the velocity of the light in free space, n is the material refractive index, and I is the laser intensity. The parameter $1/\omega_t$ corresponds to the tunneling time through the atomic potential barrier, inversely proportional to the strength of the electromagnetic field. For values $\gamma \leqslant 1$, obtained with low frequencies and large field strengths, the predominant photoionization effect is tunneling, while for values $\gamma \geqslant 1$, characteristic of optical frequencies and moderate fields strengths, the ionization is driven essentially by multiphoton ionization. However, for optical breakdown to occur, high field strength are required, leading to values $\gamma < 1$, even at optical frequencies. At $\lambda = 800$ nm, the transition irradiance to pass from the multiphoton to

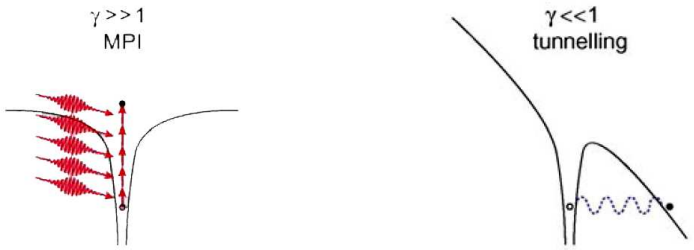

Figure 3.1: Schematic diagram of the photoionization mechanisms for different values of the Keldysh parameter γ (modified from [98])

tunneling ionization is of the order of 10^{13} W/cm^2, which corresponds to the typical parameters used for femtosecond corneal surgery. Therefore, in this case the ionization process should be the result of a combination of the two mechanisms.

Once free electrons are created under the action of the electric field, they can increase their energy *via* the "inverse Bremsstrahlung" process. They absorb photons through a collision with a third particle, which ensures the conservation of the energy and the momentum. After a certain number of inverse Bremsstrahlung events, they have enough kinetic energy to elevate an electron to the conduction band through impact ionization. The result is two electrons near the conduction band minimum, which can subsequently absorb energy and collisionally bring electrons from the valence to the conduction band. This process is called "avalanche ionization" or "cascade ionization" (figure 7.9).
As long as the material is irradiated, the free electron density ρ varies according to

$$\frac{d\rho}{dt} = \eta_{photo} + \eta_{casc}\rho - \eta_{diff}\rho - \eta_{rec}\rho^2 \quad . \tag{3.8}$$

η_{photo}, η_{casc}, η_{diff}, and η_{rec} correspond to the photoionization, cascade ionization, diffusion, and recombination rates, respectively. Hence, the first term refers to the creation of free electrons by photoionization (either tunneling or multiphoton ionization). The second and third terms represent the contribution of the avalanche ionization and the loss due to diffusion, respectively, which are proportional to the number of free electrons already produced. The fourth term expresses losses due to recombination, which is proportional to ρ^2, as two particles are considered in recombination (an electron-hole pair) [82]. At femtosecond timescales, diffusion and recombination rates can be neglected because of the short pulse duration.

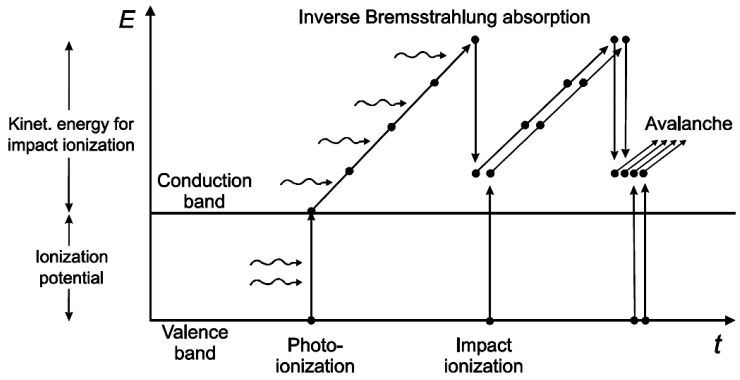

Figure 3.2: Schematic drawing of plasma formation by an interplay of photoionization and impact ionization. Recurring sequences of inverse Bremsstrahlung absorption events lead to an avalanche growth of free electron *via* impact ionization (modified from [116])

3.2.2 Critical free-electron density

From a theoretical point of view, the optical breakdown may be defined as the irradiance I_{th} sufficient to produce a critical free electron density beyond which the plasma becomes totally reflective. A free-electron plasma density ρ is characterized by a frequency defined as

$$\omega_p = \sqrt{\frac{\rho e^2}{\varepsilon_0 m}} \tag{3.9}$$

and called plasma frequency. The associated complex refractive index is given by

$$n = \sqrt{\varepsilon(\omega)} = n' + i\kappa = \sqrt{1 - \frac{\omega_p^2}{\omega^2\left(1 + i\frac{\nu}{\omega}\right)}} \tag{3.10}$$

where $\varepsilon(\omega)$ is the dielectric complex function of the plasma, n' and κ are the real and imaginary parts of the refractive index, respectively, and ν is the electron collision frequency. For a collisionless plasma ($\nu << \omega$), the index of refraction vanishes when the plasma frequency approaches the laser optical frequency. In this configuration, the plasma causes total reflection of the laser light. According to equation 3.9, the critical free electron density is given by

$$\rho_{cr} = w^2 \frac{m\varepsilon_0}{e^2} \quad . \tag{3.11}$$

At $\lambda = 1.06\,\mu$m, the critical free electron density amounts to about 10^{21} cm^{-3} [82].

3.2.3 Laser-induced ablation and disruption

A detailed review of the femtosecond laser-induced optical breakdown causing disruption in tissue has been published by Vogel *et al.* [116].
In the "long pulse" regime, optical breakdown in tissue leads to ablation. It originates from the Latin *ablatum*, which means "taken away". In the nanosecond regime, depending on the wavelength, material removal is obtained by interplay of photochemical decomposition, which leads to chemical bond breaking, and photomechanical and photothermal mechanisms resulting in vaporization of the tissue and ejection of molecular fragments [118]. In ophthalmology,

photoablation is mostly exploited in the treatment of ocular diseases related to refractive errors. Excimer lasers at UV wavelengths are generally employed.

With pulses lasting more than a few picoseconds, energy deposition occurs at timescales comparable to acoustic and thermal relaxation times. During the pulse delivery, the created plasma first expands at supersonic velocity due to its high temperature and pressure, then slows down to the speed of the sound, emitting a shock wave. Further expansion of the plasma, due to increasing pressure and temperature, results in the creation of a cavitation bubble which expands out of the focal volume until collapse, producing damages around the plasma generation region [29, 52, 117]. Different studies have shown that the threshold fluence for optical breakdown in transparent materials scales as $\sqrt{\tau}$ for pulse duration > 10 ps, yet threshold values were not in total agreement, probably due to different experimental conditions [59, 110, 112]. For picosecond pulses, seed free electrons for ionization are believed to be provided by thermionic emission [89]. Once the irradiance is sufficient to create a seed electron, the cascade ionization starts and very rapidly the critical free electron density is reached. Therefore, the onset of the cascade ionization depends on the probability to produce a free electron in the focal volume. Moreover, the threshold is lowered by the presence of impurities in the material, thus contributing to the statistical behavior of the breakdown threshold [31, 118].

Unlike in the nanosecond and picosecond regimes, femtosecond breakdown has a deterministic behavior, occurring at a determined irradiance and radiant exposure [19, 20]. In the femtosecond regime, the free electrons transfer their energy to the tissue by locally elevating the temperature. However, the thermal diffusion is too slow to dissipate the laser energy during the pulse duration and the temperature rise stays confined in the focal volume. Similar considerations apply to the mechanical interaction. The elevation of the temperature creates a highly localized tensile stress. Whenever it exceeds the critical tension for mechanical breakdown, a cavitation bubble is formed resulting in tissue disruption. Due to the short pulse duration, the stress-confinement condition is also fulfilled for ultrashort pulses. In this configuration, collateral effects are strongly reduced and the process is generally called non-thermal. Furthermore, when the tissue is irradiated by femtosecond pulses, because of the reduced interaction time, a higher irradiance is required to induce optical breakdown compared to nanosecond pulses. This condition favors the generation of seed electrons by multiphoton ionization which scales as I^k opposed to cascade ionization which scales as I and insures the production of free electrons for seeding the avalanche.

A pulse duration of 10 ps separates two regimes for the threshold irradiance and radiant exposure. Figure 3.3 represents the optical breakdown threshold dependance with the pulse duration

as calculated by Vogel *et al.* [116]. Below 10 ps, the threshold radiant exposure depends only weakly on the pulse duration, because the recombination does not play a significant role and only one set of electron needs to be created. It corresponds to a roughly constant energy density in the focal volume. On the contrary, the irradiance threshold increases when the pulse duration is reduced. Beyond 10 ps, irradiance stays approximately constant, as a minimum value is

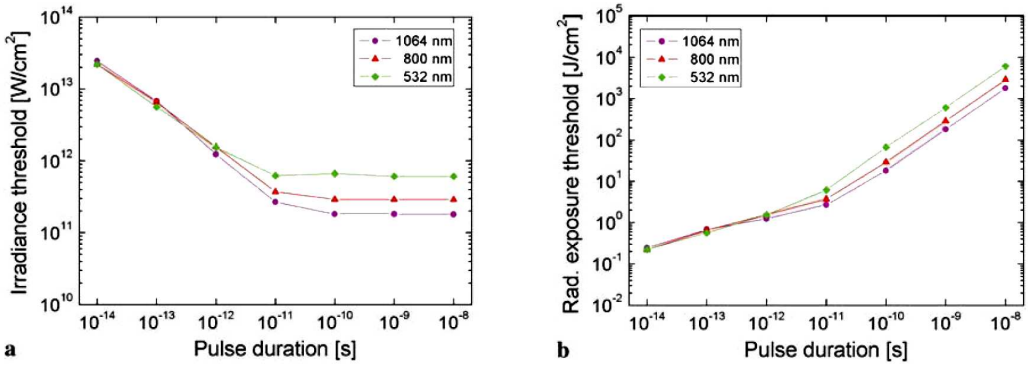

Figure 3.3: Calculated irradiance (a) and radiant exposure (b) threshold for producing the critical free electron density of 10^{21} cm^{-3} for optical breakdown [116]

necessary to produce a seed electron for cascade ionization. As a consequence of the constant irradiance threshold, the radiant exposure augments with pulse duration, also compensating the electron recombination process, which plays a role at these timescales.

Whether photoionization or cascade ionization dominates the optical breakdown in the femtosecond regime is still under discussion. Stuart *el al.* [110] proposed a theoretical model based on electron production *via* multiphoton ionization, Joule heating and avalanche ionization. It matched results obtained from experiments performed on fused silica with nanosecond to femtosecond pulses. Lenzner *el al.* [59] experimentally showed that in the femtosecond regime, depending on the size of the band gap, the predominant effect for free electron generation is either multiphoton ionization (in barium aluminium borosilicate) or collision ionization (in fused silica). An important factor which may influence numerical results is that while strong-field ionization is a quasi-instantaneous process, impact ionization requires several inverse Bremsstrahlung events before an electron has increased its kinetic energy enough to shift a second electron from the valence band to the conduction band. Kaiser *et al.* [54] developed a model in which the time constraint in cascade ionization is analyzed in detail. Numerical simulation showed that multiphoton ionization is the predominant mechanism of free-electron generation in dielectrics irradiated by femtosecond pulses. On the contrary, Joglekar *et al.* [50]

performed experiments showing that the cascade ionization is responsible for plasma creation. However, time constraints were not taken into account.
Below the threshold for optical breakdown, low density plasma are generated. They likely produce chemical effects, which alter the tissue: changes of the water molecules may liberate reactive oxygen species which can affect organic molecules. A chemical analysis of the gas bubbles content induced by fs laser plasma formation was performed by Heisterkamp *et al.* [43] and photodissociation of water molecules was observed.

3.3 Self-focusing

A complete description of current knowledge on the self-focusing process is provided by Marburger [68]. A detailed review on femtosecond self-focusing has been published by Couairon and Mysyrowicz [12] and by Chin *et al.* [11].

3.3.1 Nonlinear index of refraction

The predominantly deterministic and non-thermal nature of the femtosecond interaction process may be altered by the beam self-focusing and plasma defocusing likely occurring at high intensities in the focal volume, due to dynamic variations in the refractive index.
Considering an isotropic material and a moderate laser intensity (up to about 10^{12} W/cm^2), orders higher than the third order can be neglected in the development of the nonlinear polarization. In the scalar approximation, the contribution to the polarization at the frequency ω of the incident electric field, P_ω, introduced in equations 3.4 and 7.4, can be expressed as

$$P_\omega = \varepsilon_0(\chi^{(1)} + \frac{3}{4}\chi^{(3)}|E|^2)E \quad . \tag{3.12}$$

Substituting expression 3.12 into the wave equation, the following relation can be obtained

$$n^2 - 1 = \chi^{(1)} + \frac{3}{4}\chi^{(3)}|E|^2 \tag{3.13}$$

which leads to

$$n = \sqrt{1+\chi^{(1)}+\frac{3}{4}\chi^{(3)}|E|^2} \tag{3.14a}$$

$$\cong n_0+\frac{3}{4}\frac{\chi^{(3)}|E|^2}{2n_0} \tag{3.14b}$$

where n_0 represents the usual, weak-field refractive index.
Expressing the electric field in terms of the laser intensity gives

$$n = n_0+\Delta n = n_0+n_2 I \tag{3.15}$$

where the laser intensity is

$$I = \frac{1}{2}\varepsilon_0 c n_0 |E|^2 \tag{3.16}$$

and the nonlinear refractive index is given by

$$n_2 = \frac{3}{4}\frac{\chi^{(3)}}{\varepsilon_0 c n_0^2} \quad . \tag{3.17}$$

The total refractive index is therefore intensity dependent. Considering a laser pulse with a transverse Gaussian distribution in intensity travelling in a nonlinear optical material, if $n_2 > 0$, which is the case for many materials, the total refractive index is higher in the center of the beam compared to the wings and the medium is turned into a series of convex lenses. As a consequence, the central part of the beam propagates more slowly than the periphery part, the wavefront is curved forward and the beam focuses until it collapses (figure 3.4a).
Relation 3.12 does not strictly apply to cornea, which is a non-centrosymmetric and birefringent material. However, in our work, we consider that the nonlinear refractive index of the cornea is of the order of the nonlinear refractive index of water.

3.3.2 Critical power for self-focusing

In the absence of self focusing, laser light experiences diffraction during propagation. The characteristic diffraction angle, for a Gaussian beam with $1/e^2$ diameter d, at a wavelength λ,

is given by

$$\theta_d = \frac{0.61\lambda}{n_0 d} \quad . \tag{3.18}$$

Supposing that self-focusing occurs at a focusing distance f, the angle $\theta_{sf} = d/2f$, representing the limit angle for total reflection of a self-guided beam, is related to the nonlinear change δn of the refractive index by

$$\theta_{sf} = \sqrt{\frac{\delta n}{n_0}} = \sqrt{\frac{2n_2 I}{n_0}} \quad . \tag{3.19}$$

Therefore, self-focusing overcomes the diffraction experienced by the beam during propagation, eventually leading to collapse, only when

$$\sqrt{\frac{2n_2 I}{n_0}} \geq \frac{0.61\lambda}{n_0 d} \tag{3.20}$$

which implies that the incident peak power P of a continuous wave Gaussian laser beam has to exceed the critical power P_{cr} defined by [8]

$$P_{cr} = \frac{\pi}{4} d^2 I = \frac{\pi (0.61)^2 \lambda^2}{8 n_0 n_2} = \frac{\alpha \lambda^2}{8\pi n_0 n_2} \quad . \tag{3.21}$$

The α coefficient may slightly vary depending on the shape of the beam. For a Gaussian beam it amounts to 3.77. This equation strictly applies to monochromatic waves. Nevertheless, it is also used as a reference for ultrashort pulses, whose propagation is modified by other physical effects as group velocity dispersion, which delays the onset of self-focusing by redistributing the pulse along the temporal axis. Following this consideration, time should be taken into account as an additional parameter. Since no expression for non-monochromatic pulses exists, it is common to compare the peak power - energy divided by the pulse duration - to P_{cr}.

At values of $P > P_{cr}$, the laser intensity increases upon propagation until it is high enough to generate a plasma of electron density ρ. New free electrons continue to be generated and the plasma becomes highly absorbing, leading to a consequent decrease in the refractive index of the beam core

$$\Delta n = -\frac{\rho}{2\rho_{cr}} \quad . \tag{3.22}$$

Hence, the plasma acts as a divergent lens which defocuses the laser beam preventing it from collapsing (figure 3.4b). Once defocused, the beam may still contain enough power to undergo a new focusing-defocusing cycle. The repetition of this scenario sustains a self-guided propa-

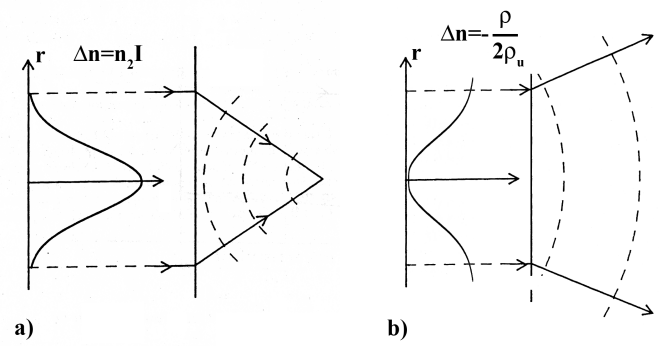

Figure 3.4: Intensity dependency of the refractive index leading to self-focusing of the beam for $\Delta n > 0$ (a); defocusing of the beam for $\Delta n < 0$ (b)

gation in the form of a filament, as illustrated in figure 7.10. Other physical processes may be responsible for beam defocusing in condensed matter, like group velocity dispersion, saturation of n_2, and non linear losses due to photoionization.
In femtsecond corneal surgery, self-focusing effects may permanently damage the tissue and it is of utmost important to choose the appropriate set of laser parameters to avoid reaching the critical power for self-focusing.

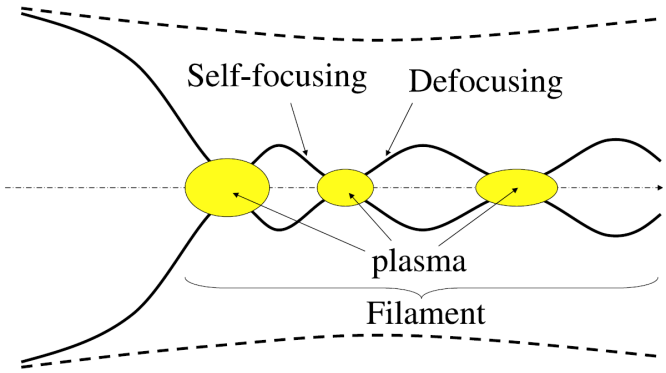

Figure 3.5: Schematic drawing of the focusing-defocusing cycles undergone by the intense core (solid curves) of a laser beam. The dashed lines indicate the root mean square radius of the full beam [12]

3.4 Second harmonic generation

At irradiances lower than the breakdown threshold, due to the nonlinear properties of biological tissue, other nonlinear phenomena can occur. These are for instance second harmonic generation (SHG), two-photon emission (TPE), and third harmonic generation (THG). TPE is based on the nonlinear excitation of fluorophores. It is a resonant process involving the absorption of two photons *via* a virtual state whose combined energy is sufficient to promote an electron to a real excited molecular vibronic state. Relaxation to the ground state includes two steps: a vibrational relaxation to the lowest vibrational energy level in the excited state, followed by the emission of a photon with energy slightly less than the combined incident photon energies, which consists in a radiative process referred to as fluorescence. The decay time is of the order of picoseconds or longer and fluorescence is not a coherent mechanism. On the contrary, SHG and THG are nonresonant processes, in which two and three photons, respectively, of the same energy "coalesce" to a virtual state to create a photon with energy exactly twice or threefold the energy of the incidents photons.
Since TPE is negligible at our excitation wavelength, and THG is less efficient, we restrict our description to the second harmonic generation.
A detailed study of the second harmonic generation process is provided, for example, by Boyd [8] and Shen [101] in their books about nonlinear optics.

3.4.1 Nonlinear response of tissue

The nature of the nonlinearity depends on the structure of the material, which is required to be non-centrosymmetric for SHG to occur. A dielectric material, under the action of an intense light field, can be modelled by a set of anharmonic oscillators. In this configuration, the Lorentz model of the atom, which considers the atom as a harmonic oscillator, needs to be extended by allowing a nonlinear term in the force exerted on the electron. Here, we assume that the atom possesses only one resonance frequency, accordingly to its classical description. When an electromagnetic wave $\mathbf{E}$ is applied to a non-centrosymmetric system, electrons are slightly shifted from the equilibrium position, inducing a polarization

$$\mathbf{P} = N\mathbf{p} \tag{3.23}$$

where **p** is the electric dipole moment produced by the displacement **x** of the electron and N is the electric dipole density. In the scalar-field approximation, the displacement of the electron is described by the following equation

$$\frac{d^2x}{dt^2} + a\frac{dx}{dt} + \omega_0^2 x + bx^2 = -\frac{e}{m}E(t) \tag{3.24}$$

where $-e$ and m are the charge and the mass of the electron, respectively, $a(dx/dt)$ is a damping term and the third and fourth terms on the left side of the equality can be represented by

$$F = -m\omega_0^2 x - mbx^2 \tag{3.25}$$

where F stands for the harmonic and anharmonic restoring force, b being the parameter that characterizes the nonlinearity of the response. Assuming that the applied electric field is of the form

$$E(t) = E(\omega)e^{i(kz-\omega t)} + E(-\omega)e^{-i(kz-\omega t)} \tag{3.26}$$

no exact solution exists to equation 3.24 and a perturbation method is typically used. We replace $E(t)$ by $\zeta E(t)$, where ζ is a parameter that ranges between zero and one and that will be set equal to one in calculations. The expansion parameter ζ characterizes the strength of the perturbation. Therefore, we seek a solution in the form of a power series expansion in the strength ζ of the perturbation, namely a solution of the form

$$x(t) = \zeta x^{(1)}(t) + \zeta^2 x^{(2)}(t) + \zeta^3 x^{(3)}(t) + ... \tag{3.27}$$

The first-order steady-state solution is then given by

$$x^{(1)}(t) = x^{(1)}(\omega)e^{i(kz-\omega t)} + x^{(1)}(-\omega)e^{-i(kz-\omega t)} \quad . \tag{3.28}$$

The amplitude $x^{(1)}(\omega)$ has the form

$$x^{(1)}(\omega) = -\frac{e}{m}\frac{E(\omega)}{[\omega_0^2 - \omega^2 - ia\omega]} \tag{3.29}$$

and the first-order polarization becomes

$$P^{(1)}(\omega) = -Nex^{(1)}(\omega) = \frac{Ne^2}{m}\frac{E(\omega)}{[\omega_0^2 - \omega^2 - ia\omega]} = \varepsilon_0\chi^{(1)}(\omega)E(\omega) \quad . \tag{3.30}$$

$\chi^{(1)}$ represents the linear or the first-order susceptibility. Introducing $x^{(1)}(t)$ in the 3.24 leads to second order solutions at the frequencies 2ω, -2ω and 0, respectively

$$x^{(2)}(2\omega) = -b\frac{e^2}{m^2}\frac{E(\omega)^2}{[\omega_0^2-\omega^2-ia\omega]^2[\omega_0^2-4\omega^2-2ia\omega]} \tag{3.31a}$$

$$x^{(2)}(-2\omega) = -b\frac{e^2}{m^2}\frac{E^2(\omega)}{[\omega_0^2-\omega^2-ia\omega]^2[\omega_0^2-4\omega^2+2ia\omega]} \tag{3.31b}$$

$$x^{(2)}(0) = -2b\frac{e^2}{m^2}\frac{E^2(\omega)}{\omega_0^2[\omega_0^2-\omega^2-ia\omega]^2[\omega_0^2-\omega^2+ia\omega]^2} \quad . \tag{3.31c}$$

In particular, the term $x^{(2)}(2\omega)$ expresses the amplitude of the component of nonlinear polarization oscillating at the frequency 2ω, which describes the second harmonic generation. The polarisation related to the SHG is given by

$$P^{(2)}(2\omega) = Nb\frac{e^3}{m^2}\frac{E^2(\omega)}{[\omega_0^2-\omega^2-ia\omega]^2[\omega_0^2-4\omega^2-2ia\omega]} \tag{3.32a}$$

$$= \varepsilon_0\chi^{(2)}(\omega,\omega)E(\omega)E(\omega) \tag{3.32b}$$

where

$$\chi^{(2)} = \frac{Nb}{\varepsilon_0}\frac{e^3}{m^2}\frac{1}{[\omega_0^2-\omega^2-ia\omega]^2[\omega_0^2-4\omega^2-2ia\omega]} \tag{3.33}$$

is the second order nonlinear susceptibility.
The condition $\chi^{(2)} \neq 0$ is fulfilled only in non-centrosymmetric materials. Indeed, in the presence of an inversion symmetry, $\mathbf{P}^{(2)} \rightarrow -\mathbf{P}^{(2)}$, $\mathbf{E}^{(2)} \rightarrow -\mathbf{E}^{(2)}$, but $\tilde{\chi}^{(2)} \rightarrow \tilde{\chi}^{(2)}$ because of the inversion properties. Therefore,

$$-\mathbf{P}^{(2)} = \varepsilon_0\tilde{\chi}^{(2)}(-\mathbf{E}^{(2)})(-\mathbf{E}^{(2)}) = \mathbf{P}^{(2)} \tag{3.34}$$

can be true only if $\tilde{\chi}^{(2)} = 0$.
Relations 3.32 show that the second harmonic generation is proportional to the square of the incident electric field. In a cartesian reference frame the components of the polarization are expressed as

$$P_i^{(2)}(2\omega) = \varepsilon_0\sum_{jk}\chi_{ijk}^{(2)}(\omega,\omega)E_j(\omega)E_k(\omega) \quad . \tag{3.35}$$

$\chi_{ijk}^{(2)}(\omega,\omega)$ is a third-order tensor composed of 27 terms which can be simplified by symmetry considerations depending on the properties of the material system.

3.4.2 Physical mechanism of frequency doubling

Second harmonic generation is a nonresonant process and can be interpreted as the annihilation of two photons of frequency ω to form a photon of frequency 2ω simultaneously in a single quantum mechanical process. It is a phase-sensitive mechanism which requires the phase-matching condition to be verified, namely it is efficient if $E(\omega)$ and $E(2\omega)$ are *in phase* along their propagation in the material.
In order to express the SHG phase-matching condition, we introduce the wave vector mismatch

$$\Delta k = k_\omega + k_\omega - k_{2\omega} = 2k_\omega - k_{2\omega} \tag{3.36}$$

where $k_\omega = n_\omega/c$ and $k_{2\omega} = n_{2\omega}2\omega/c$ represent the wave vector of the incident field and the field at a frequency 2ω, respectively. The relation

$$\Delta k = 0 \tag{3.37}$$

is known as the perfect collinear phase matching and is fulfilled when

$$n_\omega = n_{2\omega} \quad . \tag{3.38}$$

Assuming an electric field propagating in the z direction which interacts with a nonlinear material, the individual dipoles radiate a wave at a frequency 2ω. The harmonic field obtained at each point z_0 results from the sum of all the 2ω waves generated at $z < z_0$, whose phase is twice the incident field phase and is determined by the index of refraction at the fundamental frequency. The resulting 2ω wave propagates in the forward direction at a phase velocity determined by the refractive index at the harmonic frequency. Whenever relation 3.38 is not satisfied, the fields emitted by each dipole are not properly phased and they interfere partially or even destructively (figure 3.6).
Perfect phase matching conditions can be achieved in isotropic materials with anomalous dispersion near an absorption feature where the index of refraction decreases when increasing frequency, or in birefringent materials. The latter is the most common case. In uniaxial birefringent crystals, at each direction of propagation and at a given frequency, two refractive indices exist: the ordinary one n_o, which does not depend on the direction of propagation of the optical radiation and the extraordinary one n_e which depends on the propagation. In these materials, it is therefore possible to find a direction which satisfies $n_\omega = n_{2\omega}$.

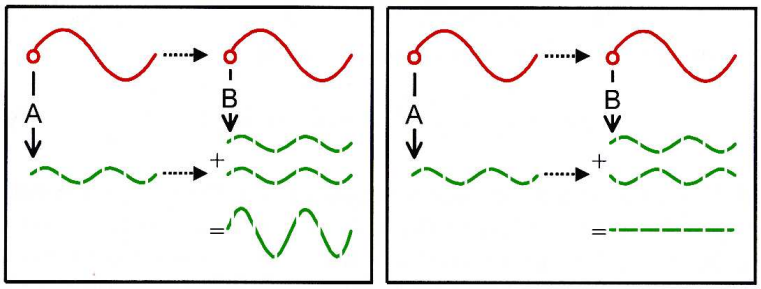

Figure 3.6: Schematic representation of phase matching. The solid-red line represents the laser and the dashed-green line the SHG in two points, A et B. When the laser wave and the harmonic wave propagate in phase from A to B, the SHG waves in B add constructively (a). On the contrary, when the phase velocities of the laser and the harmonic waves are different, SHG emission interfere destructively (b)

3.4.3 Second harmonic generation in collagen

The corneal stroma is a non-centrosymmetric material organized in lamellae of collagen constituted by well-arranged corneal fibers, which, in turn, consist of fibrils. Within the fibrils singular collagen molecules have no symmetry, however optical SHG averages molecular properties over dimensions of order a wavelength of light, so that local asymmetries disappear. Following these considerations, collagen molecules can be considered to have cylindrical symmetry about their long axes. Moreover, the polarity of individual molecular chains implies an effective symmetry for the SHG of C_∞, according to the classification of the piezoelectric properties of biological macromolecules given by Fukada *et al.* [30]. The nonlinear polarization $\mathbf{P}_{NL}$ induced by the electric field $\mathbf{E}$ is described by

$$\mathbf{P}_{NL} = \tilde{\alpha}\mathbf{E} + \tilde{\beta}\mathbf{E}\mathbf{E} + \tilde{\gamma}\mathbf{E}\mathbf{E}\mathbf{E} \tag{3.39}$$

where $\tilde{\alpha}$, is the polarizability matrix and $\tilde{\beta}$ and $\tilde{\gamma}$ are the first and second-order hyperpolarizability matrices. The $\tilde{\alpha}$, $\tilde{\beta}$, and $\tilde{\gamma}$ nomenclature has been traditionally used as the molecular equivalent to the various order nonlinear susceptibility tensors $\tilde{\chi}^{(n)}$. If we denote the z axis as the "long" axis and the x and y axes as two orthogonal axes forming a plane perpendicular to the fiber, the components of the harmonic polarization $\mathbf{P}(2\omega)$, induced by the electric field $\mathbf{E}(\omega)$,

are given by

$$\begin{bmatrix} P_x \\ P_y \\ P_z \end{bmatrix} = 2 \begin{bmatrix} 0 & 0 & 0 & d_{14} & d_{15} & 0 \\ 0 & 0 & 0 & d_{24} & d_{25} & 0 \\ d_{31} & d_{32} & d_{33} & 0 & 0 & 0 \end{bmatrix} = \begin{bmatrix} E_x^2 \\ E_y^2 \\ E_z^2 \\ 2E_yE_z \\ 2E_xE_z \\ 2E_xE_y \end{bmatrix} \tag{3.40}$$

where the coefficients d_{il} represent a contracted notation of the β_{ijk} coefficients of the $\tilde{\beta}$ matrix, according to the prescription

jk:	*xx*	*yy*	*zz*	*yz,zy*	*xy,yx*
l:	1	2	3	4	5

.

Equation 3.40 can be reduced to the form

$$P_z(2\omega) = \beta_3 E_z^2(\omega) + \beta_1 [E_x^2(\omega) + E_y^2(\omega)] \tag{3.41a}$$

$$P_x(2\omega) = 2\beta_1 E_x(\omega) E_z(\omega) \tag{3.41b}$$

$$P_y(2\omega) = 2\beta_1 E_y(\omega) E_z(\omega) \tag{3.41c}$$

where

$$\beta_3 = \beta_{zzz} \tag{3.42}$$

and

$$\beta_1 = \beta_{zxx} = \beta_{zyy} = \beta_{xzx} = \beta_{yzy} \quad . \tag{3.43}$$

The simplification of the $\tilde{\beta}$ matrix results from the C_∞ symmetry, the application to an optical field, the formal equivalence of the C_∞ tensor to the hyperpolarizability tensor, and the assumed validity of the Kleinman symmetry. This last stipulates that the elements in the nonlinear matrix, which are connected by permutation of indices, are equal if harmonic frequencies are far from the resonant electronic transitions of the material system. Assuming that all the collagen molecules are aligned, equations 3.41 describe well the SHG of an isolated fibril, considering that

$$\beta_{fiber} = N\beta_{molecule} \tag{3.44}$$

where N is the number of the molecules comprising the fibril.
Roth and Freund [93, 94] described theoretically second harmonic generation in collagen and

performed experiments on rat-tail tendons with the set-up shown in figure 3.7. The detection arm could be rotated about the tendon axis. By measuring the scattered second harmonic generation as function of the scattering angle, they showed that the signal was composed of a coherent part and an incoherent part. The former term confirms the existence of a microscopic polar order of tendons, which, in further studies, was attributed to a coherent network composed of fine filament-like structures and intense polar patches on or near the tendon surface [28]. The study

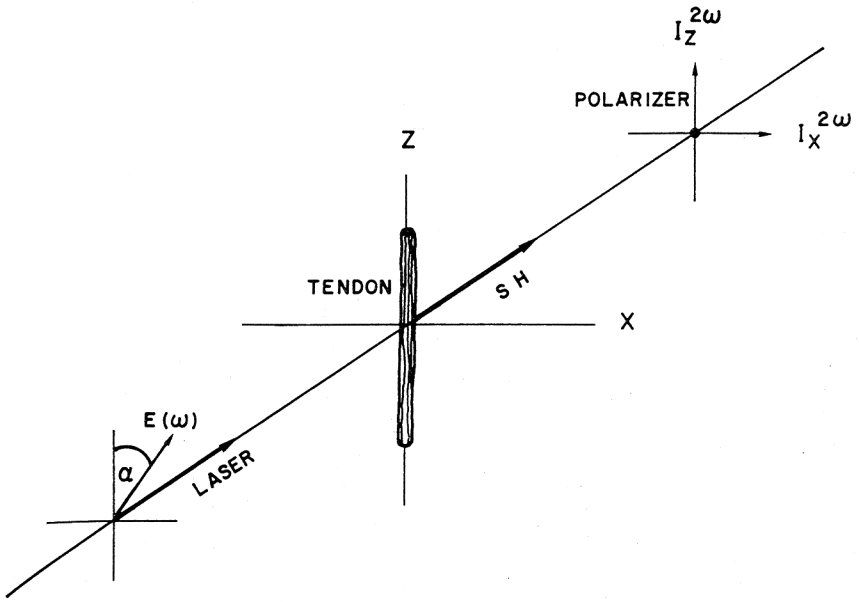

Figure 3.7: Set-up for second harmonic generation in collagen from experiments performed by Roth and Freund [93, 94]. The detection arm could be rotated about the Z axis.

of the incoherent part was based on the following parameters

1. as evidenced by electron microscopy, the polar direction of fibrils changes up and down throughout the tendon, therefore, in summing the second harmonic contributions from different fibrils it has to be summed the SH intensities rather than field amplitudes;

2. optical birefringent effects need to be taken into account when describing the laser field;

3. at the location of the fibril the incident field consists of two orthogonal components oriented along the Z and X axes, with unit amplitude and propagating in the Y direction, which are

$$E_Z(\omega) = \cos\alpha \tag{3.45a}$$
$$E_X(\omega) = e^{i\delta}\sin\alpha \quad . \tag{3.45b}$$

XYZ represents the reference frame of the tendon, whereas the fibril reference frame is xyz. The z axis, which is the fibril axis, makes the polar angle θ and the azimuthal angle ϕ relative to the XYZ frame. Here, α denotes the angle that the incident laser polarization makes with the Z-tendon axis, and must not be confused with components of the polarizability matrix introduced previously. The term $e^{i\delta}$ expresses the fact that, because of the birefringence, the two components of the light travel with different phase velocity. Following this approach, they calculated the components of the field $E_x(\omega)$, $E_y(\omega)$ and $E_z(\omega)$ in the fibril reference frame from equations 3.45 and the corresponding components of the nonlinear polarization $P_j(2\omega)$, according to equations 3.41. Based on the relation $I = |P_j(2\omega)|^2$, they deduced the SH intensity of a single fibril with arbitrary location and orientation, and averaged this over all fibril locations and orientations, weighting each orientation by an appropriate distribution function. For the case of a perfectly ordered array of fibrils composing the tendon ($\theta = 0$), they found that a linearly polarized beam at an angle α with respect to the Z-(tendon) axis produces a SHG intensity for which the harmonic is polarized parallel, $I_Z^{2\omega}(\alpha)$, and normal, $I_X^{2\omega}(\alpha)$, to the Z axis

$$I_Z^{2\omega}(\alpha) = \beta_3^2\cos^4\alpha + \beta_1^2\sin^4\alpha \tag{3.46}$$

and

$$I_X^{2\omega}(\alpha) = \beta_1^2\sin^2 2\alpha \quad . \tag{3.47}$$

Equations are plotted in figure 3.8b and are in a reasonably good agreement with experiments presented in figure 3.8a, obtained for tendons from rats of different ages.

These theoretical expressions may be used to describe the second harmonic generation in the cornea. Indeed, corneal tissue is formed of fibers which, by analogy with perfectly ordered tendons, consist of fibrils that are regularly organized around a common axis. Collagen fibers are packed in layers or lamellae and run parallel to each other in the same lamella; adjacent lamellae are arranged at approximately right angles. One can assume that fibers axes are aligned in the Z-direction and in the X-direction from one layer to the next and that the angles of the light polarization are α and $90-\alpha$ respectively. From figure 3.8b it can be noticed that the corresponding SGH intensity in the two directions has the same amount for both configurations.

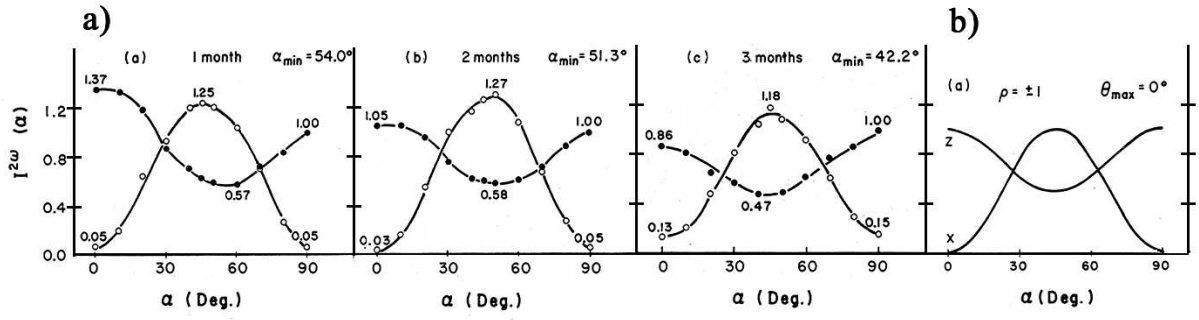

Figure 3.8: (a) Experimental measures of $I_Z^{2\omega}(\alpha)$ filled circles, and $I_X^{2\omega}(\alpha)$, open circles, for different rat ages, performed by Roth and Freund. The data are normalized to $I_X^{2\omega}(90^o) = 1$. (b) Calculated $I^{2\omega}$ curves for a perfectly ordered tendon ($\theta_{max} = 0$), where $\rho = \beta_3/\beta_1$ [93]

3.4.4 Application of SHG in biology

Nonlinear mechanisms such as SHG, TPE, and THG are mostly employed in high-resolution imaging. High light intensities for a nonlinear response of the material are only achieved in the focal volume. Hence, varying the depth of the focal volume through the sample allows to obtain a 3D image. Multiphoton excitation fluorescence microscopy was first demonstrated by Denk *et al.* [15]. With the advent of ultrafast laser pulses, SHG and TPE imaging has become a powerful form of microscopy because of the greatly reduced out-of-plane photobleaching and phototoxicity due to the focal volume localized excitation. Moreover, infrared wavelengths, at which the Ti:sapphire and solid state lasers operate, are less damaging to most living cells and tissues than UV light because fewer molecules absorb in the IR domain. In particular, SHG microscopy has the additional advantages over the TPE technique that the in-plane photobleaching is avoided, as it does not involve photon absorption, and that staining techniques are not required, although sometimes used to increase the signal strength and selectivity.

The feasibility of a simultaneous multichannel nonlinear imaging was proved by Gauderon *et al.* [33], who combined TPE and SHG microscopy. Reflection TPE and transmission SHG images of the same area of a biological specimen were obtained simultaneously in time with a resolution for both close to the theoretical Rayleigh criterion. An experimental configuration, based also on a double detection of SHG and TPE emissions, was adopted by Zoumi *et al.* [123] for investigating the dependance of the nonlinear mechanisms on the excitation wavelength, when irradiating a three-dimensional organotypic tissue model. By tuning a Ti-Sapphire

laser between 730 and 880 nm, it was demonstrated that increasing the excitation wavelength reduces the TPE signals, which approaches zero for $\lambda > 750$ nm, whereas SHG is still present for excitation wavelength in the near infrared region. Furthermore, spectral analysis of images of collagen alone and collagen plus cells indicated that SH is mainly generated by collagen. By measuring SHG and THG generated from chicken skin, muscle and fat tissue, Guo *et al.* [37] demonstrated that the intensity of the harmonic signal depends on the tissue structure: the SHG signal was higher for the skin than the muscle and the fat tissue. This result is consistent with the fact that skin as well as muscle have more collagen, characterized by an asymmetric structural response, whereas fat is composed of fewer asymmetric molecules. Additional studies, in which various collagenous tissues were imaged with micrometric resolution, revealed more precisely that SHG emissions arise from fibrillar collagen - type I - whereas nonfibrillar collagen - type IV - shows no or weak SHG signals [13, 108]. These findings may be attributed to two main factors. First, SHG efficiency in collagen I may result from coherent effects due to the high order of collagen fibers as opposed to collagen IV which presents a nearly isotropic microscopical organization [122]. Second, the chirality of molecules, characterizing collagen I and disappearing in collagen IV probably due to interruptions in the helical structure, enhances the SHG process [86]. By imaging living cells stained with both achiral and chiral dyes, Campagnola *et al.* [10] also proved that the chirality intensifies the SH signal in biological materials. Studies based on nonlinear imaging address the cornea more specifically and focus on the organization of collagen fibers, closely linked to the property of transparency, on the metabolism of cells, which plays an important role during wound healing, and on the imaging of corneal tissue following laser plasma-mediated ablation. TPE and SHG images of rabbit corneas and porcine corneas confirmed that collagen fibers are highly organized in lamellae, predominantly parallel to the corneal surface, as stated by previous electron microscopy and X-ray diffraction works, with the advantage that cell structures and collagen lamellae can be selectively resolved [39, 121]. Piston *et al.* [88] investigated the metabolism of corneal tissue by two-photon microscopy. Images of the epithelium, the stroma and the endothelium from rabbit corneas revealed that nicotinamides, which are molecules related to the metabolism in cells, are responsible for autofluorescence. Therefore, monitoring changes in the autofluorescence intensity over time informs about the metabolic activity in cornea. SHG imaging was utilized by Han *et al.* [40] to evaluate the efficacy of femtosecond laser surgery on porcine corneas. Laser-induced intrastromal cavities could be images non-invasively at high resolution and strong contrast. However, two different lasers were used for the surgery and the SHG microscopy, which prevented from real-time monitoring.

Chapter 4

Experimental set-up and sample preparation

4.1 Experimental set-up

In our study we investigated the laser-tissue interaction by performing mainly two types of experiments:

- dissections of corneal tissue while varying a large panel of parameters. For this purpose, an experimental set-up and a clinical laser system have been used;
- *in situ* generation of nonlinear emissions from collagen in a backscattering detection configuration.

We performed a series of keratoplasty cutting procedures with a commercialy available clinical laser (Intralase FS60, IntraLase Corp, Irvine, CA). The system includes a diode-pumped solid state laser, which delivers pulses with duration of about 200 fs and energies < 3 μJ, at a repetition rate of 60 kHz and a central wavelength of 1.05 μm.
Other experiments were performed with a set-up consisting of

- a Nd:glass laser, delivering pulses with duration of about 500 fs, at a repetition rate of 10 kHz, a central wavelength of 1.06 μm, and a maximum energy of 6 μJ. The output power is varied by a computer controlled attenuator. It has similar characteristics to the clinical laser, however, our set-up allows more flexibility what the experimental geometry and the parameters are concerned.

or

- a Ti:Sapphire laser delivering pulses with duration of about 150 fs, at a repetition rate of 1 kHz, a central wavelength of 800 nm, and a maximum energy of 20 μJ. The output power is changed by a polarizing cube preceded by a half wave retardation plate and measured by a joulemeter[1] or a powermeter[2] .

In both cases, a computer controlled shutter blocks the beam when requested. A detailed description of the laser systems has been provided in chapter 2.
A schematic drawing of the experimental set-up is shown in figure 8.1. The laser beam is linearly polarized, passes trough a set of mirrors and reaches a beam expander[3] of expansion ratio 6x. It is then reflected by a dichroic mirror[4] and overfills the back aperture of the optics which focus it into the sample. The dichroic mirror is designed for transmission between 410 and 700 nm and reflection between 750 and 1080 nm. A transmittance spectrum is presented in figure 4.2. Focusing optics are mounted on a specific holder or an optical inverted microscope[5] inserted into the beam path. An achromatic doublet lens and different microscope objectives were used in our experiments, covering a range of numerical apertures (NA) from 0.15 to 0.75 (table 4.1). Focusing units have an optical transmission between 50% and 80% depending on the wavelength. Design data were available only for the achromat and numerical calculations computed with an optical design code[6] showed that it produces a point spread function (PSF) corresponding to $NA = 0.15$ reasonably close to a well corrected system (Strehl ratio ~ 0.7). For the microscope objectives, no design data were available and the Strehl ratios were estimated from experimental measurements.

[1] Nova, Ophir Photonics
[2] Gentec, SOLO PE
[3] Melles Griot, 09LBZ103
[4] Melles Griot, 03MHG007
[5] Olympus IX70
[6] ZEMAX EE, Optical Design Program, ZEMAX Development Corporation, 1999-2007, USA

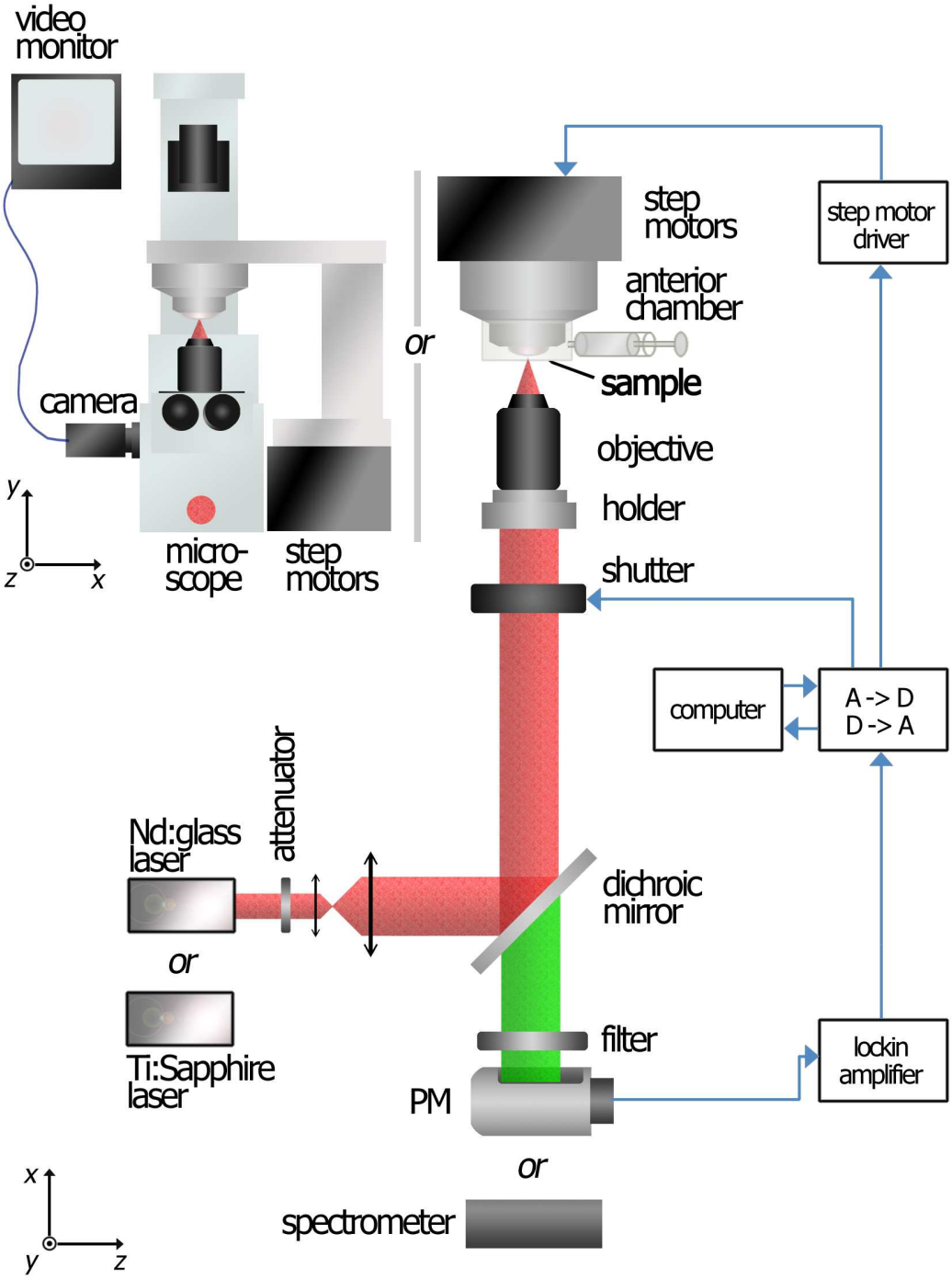

Figure 4.1: Schematic drawing of the experimental set-up

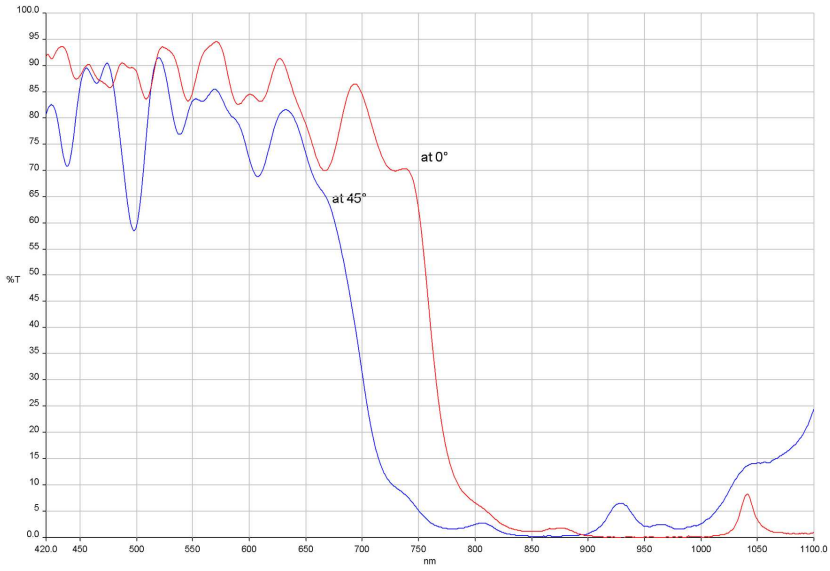

Figure 4.2: Transmittance spectrum of the dichroic mirror

Focusing optics	Coverslip correction	NA	Airy radius $\lambda = 1.06\ \mu$m	Airy radius $\lambda = 800$ nm
Melles Griot laser-grade precision-optimised achromat LAL013, $f = 50mm$	-	0.15	4.31 μm	3.25 μm
microscope objective Olympus UP-LFL 10x	-	0.3	2.15 μm	1.62 μm
microscope objective Olympus UP-LFL 20x	170 μm	0.5	1.29 μm	0.98 μm
microscope objective Olympus UPFL 40x	170 μm	0.75	0.86 μm	0.65 μm
microscope objective Zeiss LD Plan-Neofluar 20x/corr[a]	0-0.15 mm	0.4	1.61 μm	1.22 μm
microscope objective Zeiss LD Plan-Neofluar 40x/corr[a]	0-0.15 mm	0.6	1.08 μm	0.81 μm

[a]Optics specifically designed to correct spherical aberrations at different depths

Table 4.1: Overview: technical characteristics of the focusing optics.

The cornea is mounted onto an artificial chamber[7] specifically conceived to respect the natural curvature of the tissue and reproduce the living environment of the eye (figure 4.3a). Filling the chamber with a bicarbonate-buffered saline (BBS) solution allows applying a pressure to the cornea and to keep it hydrated. The sample can be positioned in three dimensions by step motors with sub-micrometric resolution and a variable displacement speed. For dissection experiments with the optical microscope added to the set-up, the *in situ* configuration can be preserved (figure 4.3b). In order to visualize the specimen, a chamber in plexiglass is used and

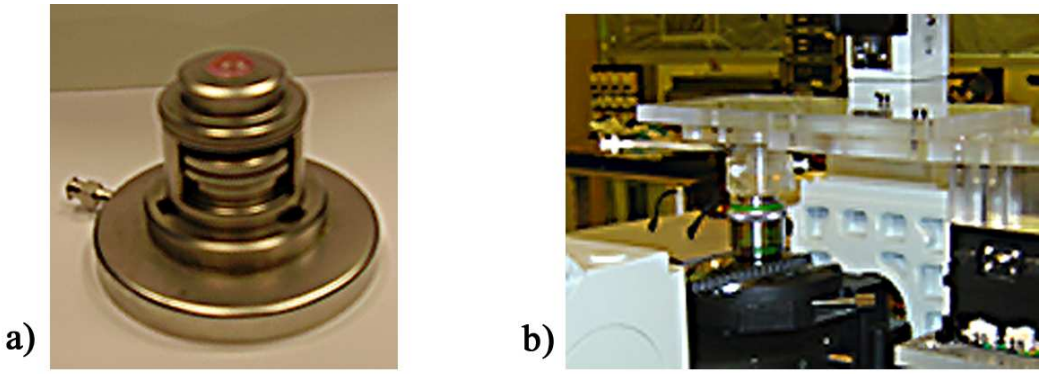

Figure 4.3: Artificial chamber used for *in situ* experiments (a). When inserting a microscope into the beam path, a chamber in plexiglass is preferred (b).

a camera[8] is mounted on the side of the microscope with a video port.
When performing experiments in the backscattering geometry, photons due to the nonlinear emission are detected by a spectrometer[9] or a photomultiplier[10], positioned behind the dichroic beam splitter. The spectrometer covers a wavelength range from 200 to 1100 nm, whereas the spectral response of the photomultiplier is from 185 to 930 nm. The electronic output of the photomultiplier is filtered by a lock-in amplifier[11] tuned to the laser repetition rate. Backscattered light can be filtered placing filters between the dichroic mirror and the photomultiplier. For part of the experiments concerning the nonlinear emission of the cornea, we used two band-pass filters[12].

[7] Moria, Antony, France
[8] Sony, Exwave HAD
[9] get-Spec 2048 COOL
[10] Hamamatsu R636-10
[11] SR830, Stanford Research
[12] Thorlabs, FGB37-BG40, optimized for filtering between 340 and 600 nm; Thorlabs, green colored transmission filter

Positioning of the sample, detection of the nonlinear emission, and acquisition of signals *via* an analog-to-digital interface[13] are controlled by LabView[14] programs.

Considerations on signal detection efficiency

Concerning the detection of nonlinear optical emission, a relation between the signal detected by the lock-in amplifier and the input energy can be established as follows. In the time-domain, the incident power on the photomultiplier is given by

$$P_{PM}(t) = E_{NL}\Delta_T(t) \tag{4.1}$$

where

$$\Delta_T(t) = \sum_{-\infty}^{\infty} \delta(t - kT) \tag{4.2}$$

is a Dirac comb, E_{NL} is the energy contained into the fraction of the backscattered nonlinear photons emitted by the tissue and collected by the photomultiplier and T is the laser frequency repetition rate. The output voltage converted by the transimpedance amplifier[15] from the photomultiplier current can be expressed as

$$U(t) = \eta_{PM}E_{NL}\Delta_T(t) \otimes \frac{1}{\tau}\left(\Theta(t)e^{-\frac{t}{\tau}}\right) \tag{4.3}$$

with

$$\Theta(t) = \begin{cases} 0, & t \leq 0 \\ 1, & t > 0 \end{cases} \tag{4.4}$$

being the Heaviside step function, τ the photomultiplier time response, and η_{PM} the efficiency factor of the photomultiplier. For $T >> \tau$, which may be safely assumed, the average power is given by

$$\langle U \rangle = \eta_{PM}E_{NL}\frac{1}{\tau}\frac{1}{T}\int_0^T e^{-\frac{t}{\tau}}dt \approx \eta_{PM}E_{NL}\frac{1}{\tau}\frac{1}{T}\int_0^{+\infty} e^{-\frac{t}{\tau}}dt = \eta_{PM}E_{NL}\frac{1}{T} = \eta_{PM}\langle P_{PM}\rangle \tag{4.5}$$

[13] National Instrument BNC-2110
[14] National Instruments, Version 7.1
[15] Hamamatsu C6271

where $\langle P_{PM} \rangle$ stands for the lossless average power of the PM.
We assume the unitary convention for the Fourier transform

$$U(\omega) = \mathcal{F}[U(t)] = \frac{1}{\sqrt{2\pi}} \int_{-\infty}^{+\infty} U(t) e^{-i\omega t} dt \tag{4.6}$$

$$U(t) = \mathcal{F}^{-1}[U(\omega)] = \frac{1}{\sqrt{2\pi}} \int_{-\infty}^{+\infty} U(\omega) e^{i\omega t} d\omega \quad . \tag{4.7}$$

In the frequency-domain, $U(\omega)$ is expressed by

$$U(\omega) = \mathcal{F}[U(t)] = \eta_{PM} E_{NL} \sqrt{2\pi} \left(\mathcal{F}[\Delta_T(t)] \cdot \mathcal{F} \left[\frac{1}{\tau} \Theta(t) e^{-\frac{\tau}{T}} \right] \right) \tag{4.8a}$$

$$= \eta_{PM} E_{NL} \sqrt{2\pi} \left(\frac{1}{T} \Delta_{\frac{2\pi}{T}}(\omega) \right) \left(\frac{1}{\tau\sqrt{2\pi}} \frac{1}{\frac{1}{\tau} + i\omega} \right) \tag{4.8b}$$

where the convolution theorem has been used.
In the time-domain, the reconstructed signal is given by a Fourier series according to

$$U_{tot}(t) = \frac{1}{\sqrt{2\pi}} \int_{-\infty}^{+\infty} U(\omega) e^{i\omega t} dt \tag{4.9a}$$

$$= \eta_{PM} E_{NL} \frac{1}{T} \int_{-\infty}^{+\infty} \Delta_{\frac{2\pi}{T}}(\omega) \frac{1}{1 + i\omega t} e^{i\omega t} dt \tag{4.9b}$$

$$= \eta_{PM} E_{NL} \frac{1}{T} \sum_{k=-\infty}^{+\infty} \frac{1}{1 + ik2\pi \frac{\tau}{T}} e^{ik\frac{2\pi}{T}t} \quad . \tag{4.9c}$$

The lock-in amplifier measures the first harmonic (k=1) given by

$$U_1(t) = \eta_{PM} E_{NL} \frac{1}{T} \left(\frac{1}{1 + i2\pi \frac{\tau}{T}} e^{i\frac{2\pi}{T}t} + \frac{1}{1 - i2\pi \frac{\tau}{T}} e^{-i\frac{2\pi}{T}t} \right) \tag{4.10}$$

The signal amplitude is expressed as

$$\widehat{U}_1 = \eta_{PM} E_{NL} \frac{1}{T} \left| \frac{2}{1 + i2\pi \frac{\tau}{T}} \right| \tag{4.11a}$$

$$= \eta_{PM} E_{NL} \frac{1}{T} \underbrace{\left(\frac{1}{\sqrt{1 + \left(2\pi \frac{\tau}{T}\right)^2}} \right)}_{\eta_{LA}} \tag{4.11b}$$

where we define η_{LA} as the lock-in amplifier efficiency factor. The signal amplitude displayed corresponds to the root mean square (RMS) value, which is then given by

$$\widehat{U}_{RMS} = \frac{1}{\sqrt{2}} \eta_{PM} \eta_{LA} \frac{1}{T} E_{NL} \quad . \tag{4.12}$$

Considering the following parameters

- the laser beam is focused into the material with a microscope objective,
- the signal travels back through the dichroic beamsplitter and two filters, between the focusing optics and the photomultiplier,
- the nonlinear signal is represented by second harmonic emission, as shown in chapter 6

we can establish a relation between the SHG signal amplitude measured by the lock-in amplifier and the incident energy, according to

$$\widehat{U}_{RMS} = \frac{1}{\sqrt{2}} \eta_{PM} \cdot \eta_{LA} \cdot \eta_F \cdot \eta_{MD} \cdot \eta_{Obj} \cdot \eta_{sol} \cdot \eta_{SHG} \cdot \frac{1}{T} E_i \tag{4.13}$$

where η_F, η_{MD}, and η_{Obj} represent the transmission of the two filters, of the dichroic mirror, and of the objective, respectively. η_{sol}, η_{SHG} and E_i express the photon fraction collected by the solid angle of the objective, the SHG conversion efficiency, and the incident energy, respectively.

Experimentally, for a $NA = 0.5$ objective and an incident energy of 100 nJ, we measured a maximum signal in the order of 0.1 mV. Numerically, we have

$$\eta_{PM} = 0.3\frac{V}{\mu A} \times 62\frac{mA}{W} = 18.6 \times 10^3 \frac{V}{W}$$

$$\eta_{LA} = 1$$

$$\eta_F \eta_{MD} \eta_{Obj} = 0.4 \times 0.94 \times 0.5 = 0.19$$

$$\eta_{sol} = \frac{1}{4\pi} 2\pi(1 - \cos(\arcsin 0.5)) = 0.07$$

where η_{PM}, η_F, and η_{MD} can be deduced from the corresponding data sheets, η_{LA} can be calculated from relation 8.11b, and η_{Obj} is determined experimentally. Inserting the numerical values into relation 8.13 gives

$$0.1 \times 10^{-3} = \frac{1}{\sqrt{2}} \times (18.6 \times 10^3) \times 1 \times 0.19 \times 0.07 \times \eta_{SHG} \times (10 \times 10^3) \times (100 \times 10^{-9})$$

we therefore obtain

$$\eta_{SHG} = 5.7 \times 10^{-4} \quad .$$

We point out that this value represents the SHG conversion efficiency with respect to our experiments and has not to be considered as an absolute value. It worth recalling that our measurements refer to a backscattered detection geometry, an integration time in the order 0.5 s and a focusing depth between 50 and 100 μm into the cornea. In this configuration, the conversion efficiency is particularly sensitive to the scattering properties of the tissue and the collected signal includes contributions from a microscopic layer of the excited tissue, which may lead to overestimation.

4.2 Sample preparation

All experiments were performed on human corneas obtained from the *Banque Française des Yeux*[16] (French Eye Bank) (figure 8.2). The corneo-scleral buttons were recovered from one to

[16]Division of Paris, France

two weeks after enucleation and stored in CorneaMax(R)[17] solution at room temperature until experiments. Buttons for research purpose are rejected from the BFY, since they are unsuitable

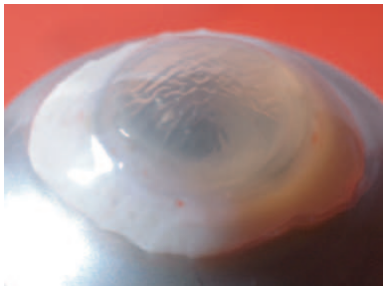

Figure 4.4: Human cornea corneo-scleral buttons obtained from the Banque Française des Yeux

for transplantation, generally because of a defective endothelium, which normally ensures the regulation of the corneal hydration. As a consequence, bathing them in the solution promotes swelling, thus reproducing corneal edema.

Before the laser experiments we removed the epithelium with a methylcellulose spear once samples were mounted on the artificial chamber. The epithelial layer of corneas from eye-bank eyes may present irregularities on the surface due to manipulation, which may cause distorsion of the laser beam when focused into the bulk of the corneal tissue.

Following incisions procedures, samples were systematically prepared for analysis by optical and transmission electron microscopy. After laser irradiation, 1 hour waiting time allowed complete resorption of the cavitation bubbles. The corneas were then fixed for 2 hours in 2.5 % glutaraldehyde in 0.1 M cacodylate buffer (pH 7.3), washed with the same buffer solution, after fixing in 0.1% osmium tetroxide and dehydrating in alcohol with graded concentrations, and finally embedded in LX 112 resin. Subsequent semithin and ultrathin sections were obtained using an ultramicrotome[18]. Semithin sections were stained with toluidine blue and analyzed by optical microscopy[19], while ultrathin sections were colored by uranyl acetate and lead citrate solutions and examined with a transmission electron microscope[20].

[17] Eurobio, Courtaboeuf, France
[18] Reichert OmU2
[19] Zeiss Phomi2
[20] Philips CM10, resolution 0.5 nm

Chapter 5

Femtosecond laser corneal surgery

5.1 Introduction

Ultrafast lasers are currently used in LASIK (laser in situ keratomileusis) procedures for cutting the superficial layer of the cornea prior to tissue reshaping by the excimer laser. Recently, ultrafast lasers have been introduced in keratoplasty, representing a second major advancement in corneal surgery. The use of the femtosecond laser can considerably reduce the risk of complications due to its precision, safety and predictability compared to mechanical microkeratomes. Numerous studies have demonstrated the feasibility of femtosecond keratoplasties of various shapes [73,99,105]. However, while clinical systems successfully cut transparent donor corneas, their performances may not be sufficient when treating edematous or other pathological corneas. In fact, the pre-programmed dissection routines do not take into account that optical properties of pathological corneas are altered and in this case additional phenomena contribute to the laser-tissue interaction. As a consequence, in clinical practice, surgeons have to adopt different strategies in order to achieve complete dissection of opaque corneal tissue, such as completing the surgery with mechanical instruments, using the maximum energy available on the system, or even performing a double-passage laser procedure.

The aim of this chapter is to provide a systematic study concerning fs laser photodisruption of corneal tissue investigated at a microscopic scale. We explore a large panel of parameters: laser source, optical properties of the cornea, laser energy, numerical aperture of focusing

optics, shapes of incisions. We examine their influence on tissue disruption by optical and transmission electron microscopy. (For simplicity, at times we will use the terms "clinical dissection or incision" and "experimental dissection or incision" as abbreviations for dissection or incision performed with the clinical system and the experimental set-up, respectively).
I first present a preliminary study of histological and ultrastructural modifications induced by a clinical femtosecond laser to opaque corneal tissue following three different keratoplasty cut procedures.
Photodisruption produced by our experimental approach is then investigated and we demonstrate that side effects may occur when the laser parameters are not chosen as a function of the modified optical properties of the tissue. We begin with examining histological and ultrastructural analysis of perforating incisions performed at constant energy in clear human corneas. Secondly, incisions in edematous corneas are shown to illustrate the attenuation of the radiant exposure in the volume and to relate the quality of the incisions to the pulse energy, numerical aperture, and incision depth. Finally, lamellar dissection performed at varying numerical apertures enables showing side effects which we ascribe to self-focusing.
Ultrastructural observation of clinical and experimental dissection has also allowed to put into evidence an additional side effect related to the use of an applanation lens used to flatten the cornea during the laser delivery.

5.2 Dissection with the clinical laser system

In this section, we evaluate the performances of a clinical system in three different keratoplasty cut procedures on edematous corneas: top hat-shaped, Z-shaped and posterior lamellar keratoplasties.

5.2.1 Methods

We performed six keratoplasties - top hat-shaped ($n = 2$), Z-shaped ($n = 2$), and posterior lamellar ($n = 2$) - in edematous corneas with the clinical femtosecond laser system Intralase FS60[1]. For details on sample preparation, one should refer to chapter 4, whereas technical specifica-

[1] IntraLase Corp, Irvine, CA, USA

tions about the laser system are provided in chapter 2. Nominal pulse energies were chosen to be 2.62 μJ for the top-hat shaped protocol and at 2.92 μJ for the two others. The former value corresponds approximately to the energy recommended by the laser manufacturer when treating pathological corneas. The latter value is the maximum energy that the system can deliver. Data about the focusing optics are not available, therefore it is not possible to precisely translate these values into the equivalent threshold radiant exposure. However, we can assume that the energy threshold is ≤ 1.5 μJ, which is the value used for performing LASIK in transparent corneas. Laser paths were slightly modified from the standard protocols, so that the button and the rim of the cut cornea stayed attached in two points, for the purpose of facilitating the histological and ultrastuctural observation of the incisions. Exposition times were comprised between 30 and 90 seconds. Details on parameters used in the three procedures are presented in tables 5.1. A standard cone flattened the corneas as provided for in the fs laser surgery procedure.

Top hat-shaped penetrating keratoplasty cut					
Lamellar cut		Anterior side cut		Posterior side cut	
Depth in cornea	400 μm	Posterior depth	370 μm	Anterior depth	430 μm
Outer diameter	7.0 mm	Diameter	7.1 mm	Posterior depth	1000 μm
Inner diameter	6.0 mm	Energy	2.62 μJ	Diameter	5.9 mm
Energy	2.62 μJ	Side cut angle	90^o	Energy	2.62 μJ
				Side cut angle	90^o
Z-shaped penetrating keratoplasty cut					
Lamellar cut		Anterior side cut		Posterior side cut	
Depth in cornea	100 μm	Posterior depth	70 μm	Anterior depth	130 μm
Outer diameter	8.2 mm	Diameter	6.9 mm	Posterior depth	1000 μm
Inner diameter	7.4 mm	Energy	2.92 μJ	Diameter	8.7 mm
Energy	2.92 μJ	Side cut angle	30^o	Energy	2.92 μJ
				Side cut angle	30^o
Posterior lamellar keratoplasty cut					
Lamellar cut		Anterior side cut		Posterior side cut	
Depth in cornea	400 μm	The laser delivery was		Anterior depth	370 μm
Outer diameter	8.2 mm	stopped before the anterior		Posterior depth	1000 μm
Inner diameter	0 mm	side cut was performed		Diameter	8 mm
Energy	2.92 μJ			Energy	2.92 μJ
				Side cut angle	90^o

Table 5.1: Protocols of top hat, Z-shaped and posterior lamellar keratoplasty cut performed on human cornea from eye-bank eye with a clinical femtosecond laser

The thicknesses of the cornea which underwent top hat-shaped, Z-shaped, and posterior lamellar keratoplasty cut were measured after the removal of the epithelium by pachymetry. They amounted to 710 ± 10 μm, 700 ± 10 μm, and 880 ± 20 μm, respectively, where the indicated error stands for the standard deviation. The difference between the corneal thicknesses in various groups was not found to be statistically significant. These measured values are typical for corneas in which the degree of organization of the collagen fibers is decreased and the amount of interstitial fluid is increased. In these conditions, the transparency of the tissue is reduced, namely its optical properties are modified.

5.2.2 Results

Figure 9.1 shows thin sections of top hat, Z-shaped and posterior lamellar cuts obtained with the clinical laser. Keratoplasty is transfixing when using top hat and Z-shaped protocols (figure 9.1a and 9.1b). The cornea which underwent posterior lamellar keratoplasty presents a difference between the vertical (posterior to anterior) and the horizontal (parallel to lamellae) incisions (figure 9.1c). The horizontal incision is formed by elongated cavities between collagen lamellae, which alternate with tissue bridges. The vertical cut shows disrupted collagen fibers and it does not reach Descemet's membrane. Figures 9.2, 5.3 and 5.4 illustrate details of the top hat, Z-shaped, and posterior lamellar incisions, respectively, at different depths into the cornea. Ultrastructural investigation confirms the above findings. Z and top hat-shaped keratoplasty were perforating, while incisions obtained by using the posterior lamellar procedure are discontinuous in the lamellar plane due to the presence of tissue collagen strands extending between the adjacent cavities. Dissection is not transfixing in the vertical plane. High magnification of collagen fibers and lamellae shows that the organization of collagen fibers is preserved, without thermal impact in any of the three cases. However, one can notice that nanometric debris are created and deposited on the edges of the incisions (figure 9.2b,c and 5.3a,c). The amount of this debris appears to be more important in the anterior stroma than in the posterior stroma. When observing the ultrathin sections of the tissue cut following the top hat and Z procedures, a difference in their distribution becomes evident. In the anterior stroma, it frequently forms typically a 3.0 ± 0.5 μm thick layer, adjacent to the incision, consisting in a disorganized area composed of cellular and collagen fibrils fragments or amorphous material (9.2b and 5.3a). The ends of the underlying collagen fibrils are well visible. Figure 9.2d is remarkable as the proper incision can be easily recognized and disordered material deposited on the left border

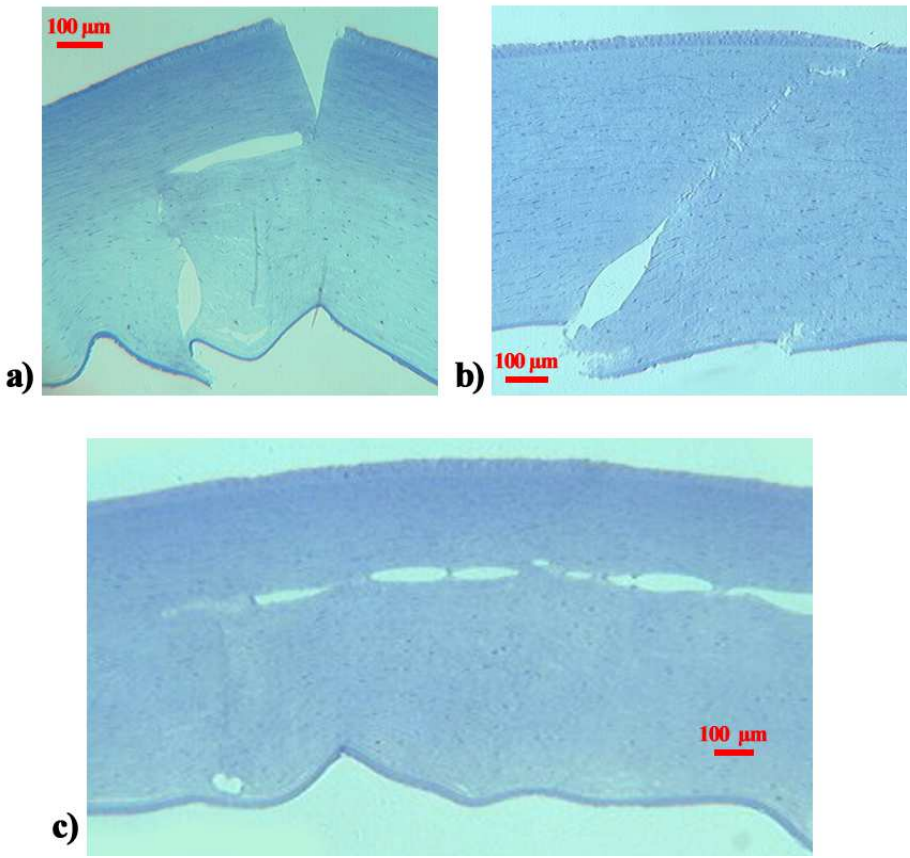

Figure 5.1: Histological sections of corneas from eye-bank eye, which underwent a top hat (a), Z-shaped (b), posterior lamellar (c) keratoplasty cut performed at energies of 2.62 μJ, 2.92 μJ, and 2.92 μJ, respectively

seems to originate from the opposite side. In the posterior stroma, the debris assemble to form a pseudo-membrane, nanometric in thickness, which runs along the border of the incision (figure 9.2c and 5.3c). A similar ultrastructural feature was found when analyzing lamellar incisions induced by posterior lamellar keratoplasty. A pseudo-membrane settled on the edges of the cavities (5.4b). In some sections small dark particles with dimensions up to micrometric size were visible, which do not appear ultrastructurally normal (figure 9.2d). These are glass debris produced by laser machining of the applanation lens used to flatten the cornea during surgery. These findings are detailed in section 5.6.

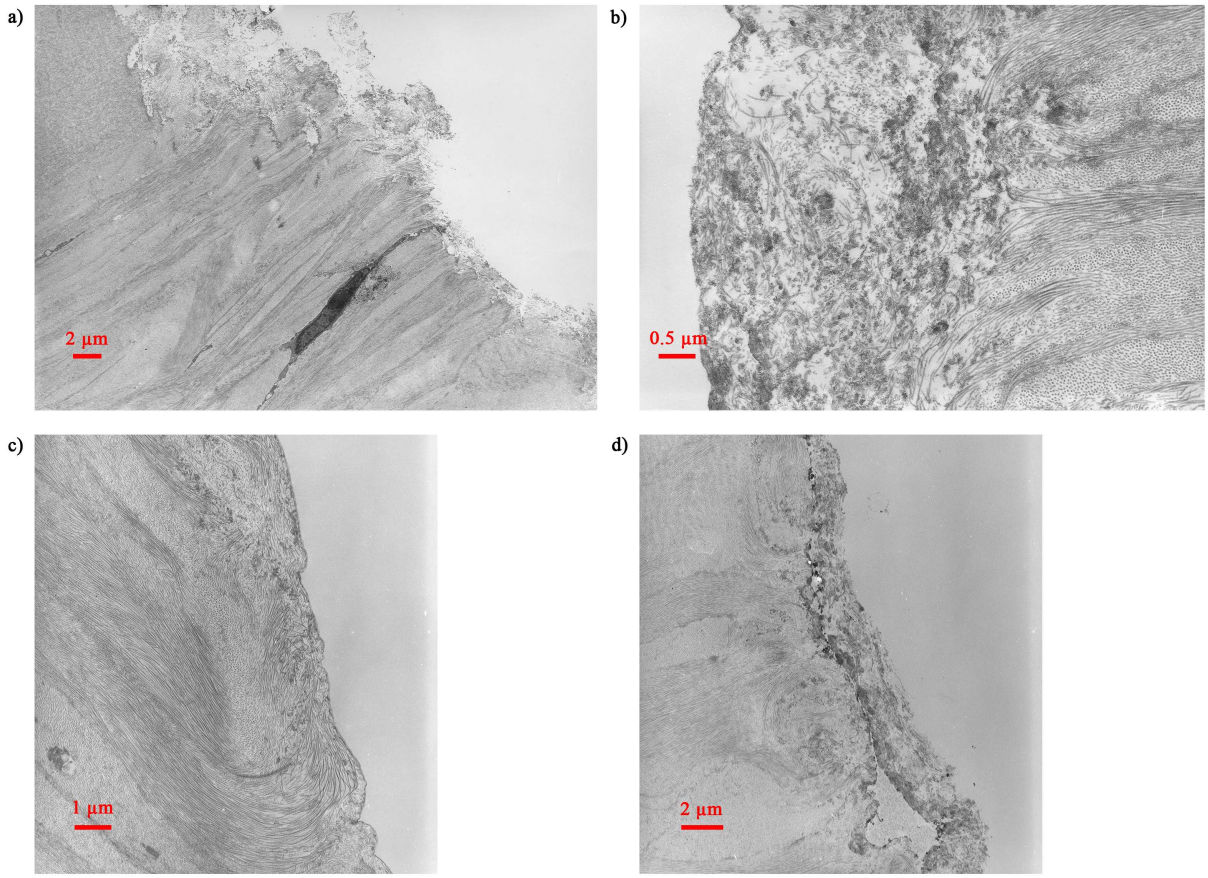

Figure 5.2: Ultrastructural section of a cornea from eye-bank eye, which underwent a top hat-shaped keratoplasty cut performed at an energy of 2.62 μJ. a) Bowman's membrane and the underlying collagen fibers. b) Detail of an incision in the anterior stroma. c) Collagen lamellae in the posterior stroma. d) Collagen fibers in the anterior-middle stroma

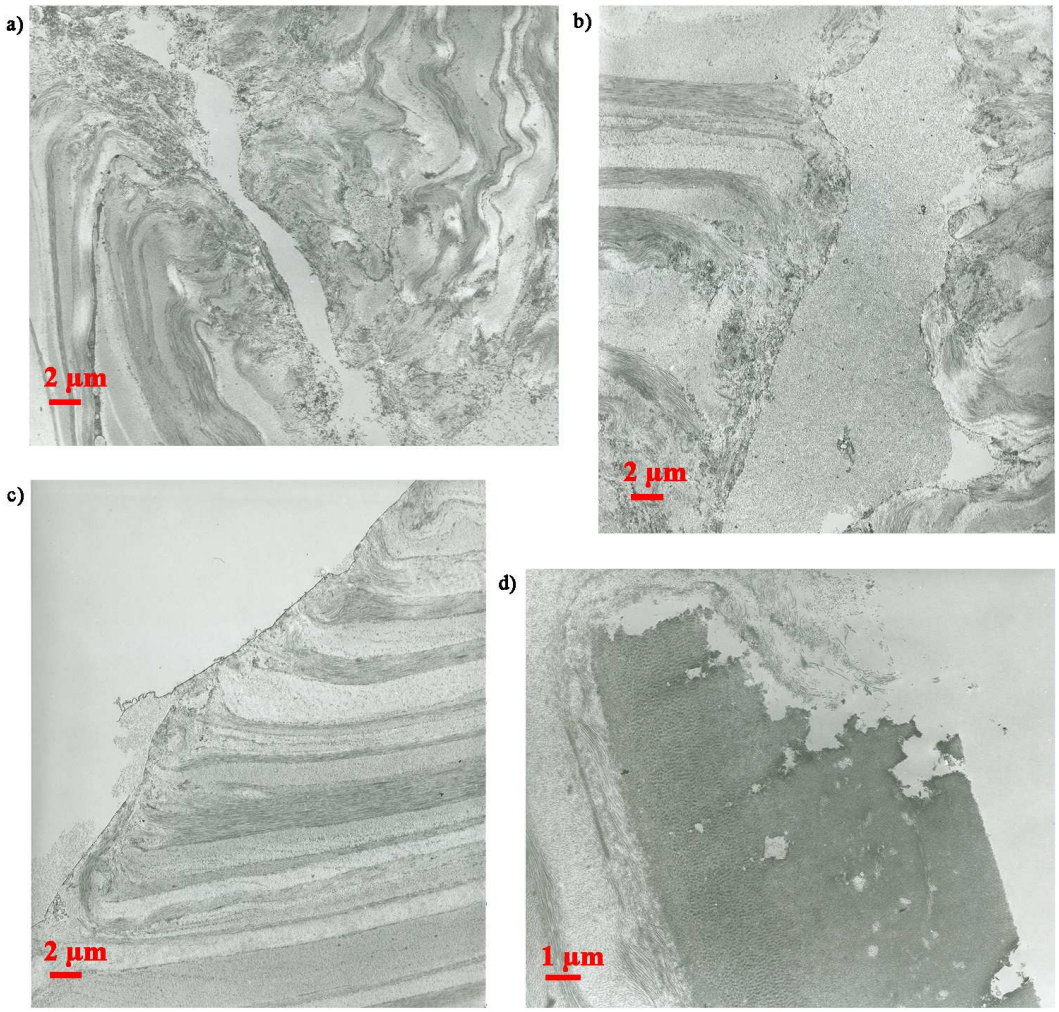

Figure 5.3: Ultrastructural section of a cornea from eye-bank eye, which underwent a Z-shaped keratoplasty cut performed at an energy of 2.92 μJ. a) Collagen lamellae in the anterior stroma at a deepness of about 100 μJ. b) Detail of the disrupted fibers in the anterior-middle stroma at a deepness of about 250 μJ. c) Collagen lamellae in the posterior stroma. d) Descemet's membrane.

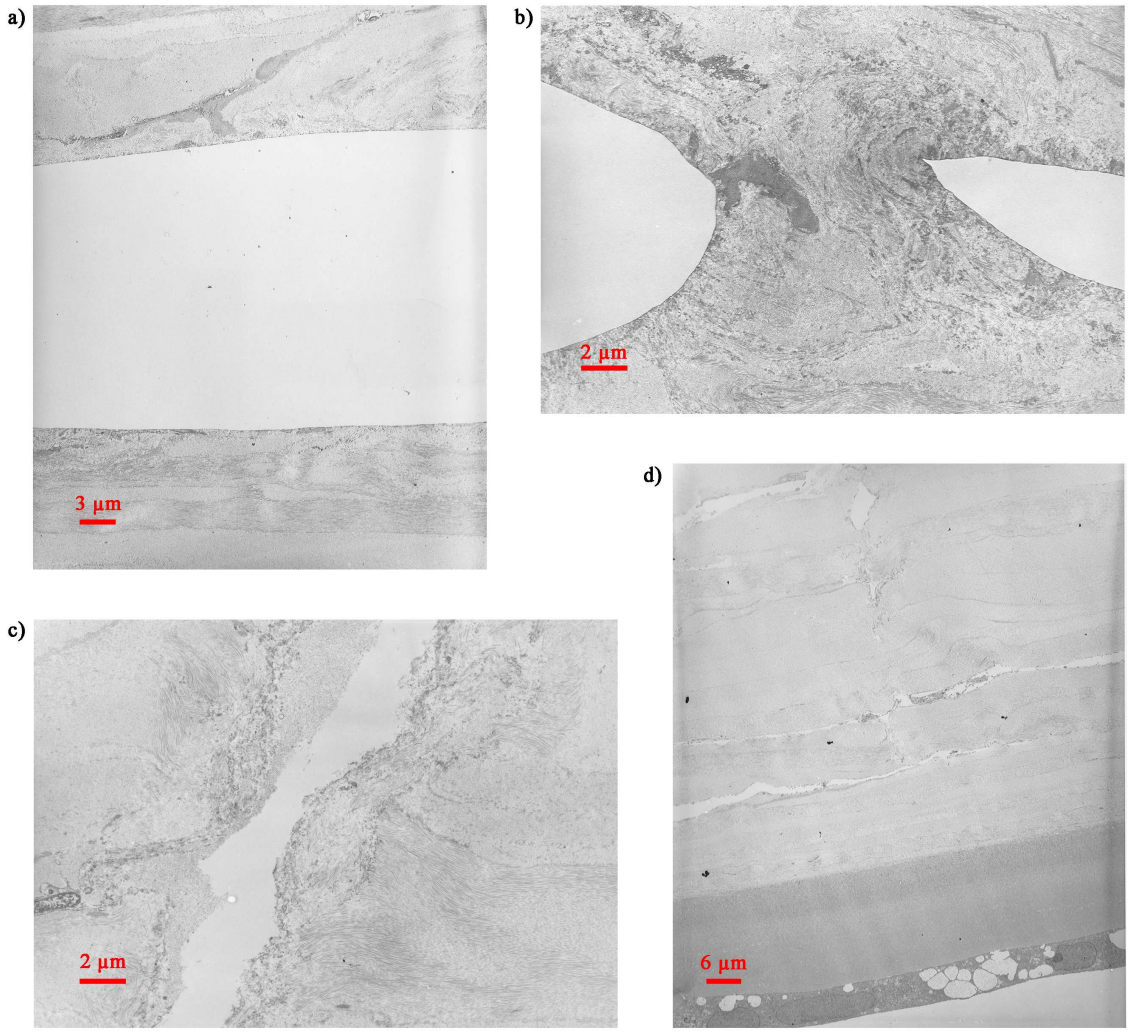

Figure 5.4: Ultrastructural section of a cornea from eye-bank eye, which underwent a posterior lamellar keratoplasty cut performed at an energy of 2.92 μJ. a) Lamellar cavity oriented parallel to the corneal surface, b) Remaining tissue bridge in the lamellar cavity. c) Collagen lamellae in the middle stroma. d) Posterior stroma and Descemet's membrane.

5.3 Dissections with the experimental laser system

In this section, we examine edematous tissue dissection obtained with our experimental set-up, which includes a femtosecond laser whose characteristics are similar to the laser source of clinical systems. It is also more flexible, thus allowing exploring different parameters and their influence on the laser-tissue interaction. The following experiments were performed:

- *posterior-to-anterior dissections on clear corneas at different energies and focusing conditions;*
- *posterior-to-anterior dissections on edematous corneas at different energies and focusing conditions;*
- *lamellar dissection on edematous corneas at different energies and focusing conditions.*

5.3.1 Experimental threshold determination

Following theoretical and experimental data from the literature, for pulse durations used in this study the radiant exposure threshold is expected to be just under 2 J/cm^2 [34, 79, 109, 116, 118]. In the literature, different conventions are adopted in order to define a theoretical value for the threshold radiant exposure. Amongst them are

1. pulse energy divided by the surface encircled by the $1/e^2$ beam radius for a Gaussian beam, which at the focal plane is given by [95]

$$w = 0.32\frac{\lambda}{n\sin\theta} \tag{5.1}$$

2. total pulse energy divided by the surface corresponding to the Airy radius, which is expressed as

$$r = 0.61\frac{\lambda}{n\sin\theta} \tag{5.2}$$

   where $n\sin\theta$ is the *NA* of the focusing optics [95];

3. average irradiance contained in the Airy disk;

4. peak irradiance value of the Gaussian distribution;

5. peak irradiance value of the Airy pattern.

In our work, we use the second convention for defining the theoretical value. The last two conventions are rarely adopted when reporting experimental results, however, it is worth pointing out that to be able to compare measured to theoretically predicted data, the peak value of the beam profile would have to be used. In the case of a diffraction limited beam, this value is about four times higher than the value averaged over the Airy radius.
Experimentally, we adopt as breakdown criterion the formation of consistent and regular bubbles close to the surface of the tissue, regardless of local sample irregularities. We assume that at the surface, the laser beam is not deformed neither affected by scattering. In the present study the lowest numerical aperture used for laser dissections was $NA = 0.15$, obtained with an achromatic doublet lens (Melles Griot, LAL013, f = 50 mm). At this NA, a value of 2 J/cm^2 translates to theoretical threshold pulse energy of 1.2 μJ when assuming a diffraction limited beam. We observed bubble formation on the surface of the cornea at pulse energies of 2.0 ± 0.2 μJ. The quotient of these values delivers an experimental minimal Strehl ratio of 0.6, which agrees well with the result of the numerical calculation mentioned in chapter 4. For the focusing optics with $NA = 0.3$, 0.5, and 0.75 (objectives Olympus UPLFL 10x, 20x, and 40x, respectively), experimental thresholds were observed at 288 ± 30 nJ, 130 ± 20 nJ, and 60 ± 6 nJ, respectively, when working close to the surface. They were determined by gradually decreasing the energy until no more bubbles were observed at the corneal surface in the optical microscope supporting the focusing optics. The measured values correspond to Strehl ratios of 0.6 ± 0.1, 0.46 ± 0.05, and 0.44 ± 0.05, respectively (table 5.2). We note that these values represent lower boundaries for the real Strehl ratios. The deviation from ideal values may be attributed to a non uniform wavefront at the back pupil of the objectives - to which high numerical aperture optics are particularly sensitive - and to aberrations intrinsic to the experimental set-up, rather than the optical elements themselves.

5.3.2 Methods

Incisions in the posterior-anterior direction and in the lamellar plane were induced with the experimental set-up on clear corneas, which were exceptionally recovered few hours after enu-

Focusing optics	*NA*	λ	Theoretical threshold energy	Experimental threshold energy (average value ± standard deviation)	Strehl ratio in cornea (experimental)
achromat $f = 50$ mm	0.15	1.06 μm	1.2 μJ	2.0±0.2 μJ	$\geq 0.6 \pm 0.1$
objective 10x Olympus UPLFL	0.3	800 nm	166 nJ	288±30 nJ	$\geq 0.6 \pm 0.1$
objective 20x Olympus UPLFL	0.5	800 nm	59 nJ	130±20 nJ	$\geq 0.46 \pm 0.05$
objective 40x Olympus UPLFL	0.75	800 nm	26 nJ	60±6 nJ	$\geq 0.44 \pm 0.05$

Table 5.2: Threshold energies for the focusing optics used in our experiments

cleation, and on edematous corneas (details on sample preparation are reported in chapter 4). The Nd:glass and the Ti:Sapphire lasers were used.
Incisions in the posterior-anterior direction were obtained by scanning the sample under the beam. The laser was focused throughout the entire thickness of the cornea from the posterior towards the anterior region. Lamellar cuts were instead obtained by scanning the sample in the lamellar plane. The selected scanning velocity provided a 2 μm spot separation. In order to produce planar incisions, adjacent cuts were performed at a constant distance of 2 μm. Details of the parameters used are presented in table 5.3

5.3.3 Results

Experiments on clear corneas

Figure 9.3a shows a histological section of a transfixing cut performed at $NA = 0.15$ in fresh corneal tissue, which was free of edema, at 3 μJ, slightly above the threshold. It can be observed that the laser produced a regular incision with constant good quality across the depth of the cornea. This has to be compared to figure 9.3b which depicts a laser incision induced in the cornea by 5 μJ pulses. Although this energy corresponds to only about 2.5 times the experimental threshold energy, the resulting incision is considerably larger. Irregular residual cavities remain present in the corneal tissue with dimensions up to several tens of microns. The strong dependence of the incisions quality on laser energy is confirmed by an ultrastructural

Experiments on clear corneas				
	Posterior-anterior incisions			
Laser wavelength	1.06 μm		800 nm	
Numerical aperture	0.15		0.75	
Energy	3 μJ	5 μJ	140 nJ	250 nJ
Posterior depth	1000 μm			
Anterior depth	-300 μm			
Length of the incision plane	1.5 mm			

Experiments on edematous corneas					
	Post.-ant. incisions		Lamellar incisions		
Laser wavelength	800 nm				
Numerical aperture	0.3	0.5	0.3	0.5	0.75
Energy	500 nJ	170 nJ	900 nJ	450 nJ	150 nJ
Posterior depth	1000 μm		-		
Anterior depth	-300 μm		-		
Lamellar depth	-		150 μm		
Length of the incision plane	1.5 mm				

Table 5.3: Protocols of the posterior-anterior incisions and lamellar cuts performed on human cornea from eye-bank eye with the experimental set-up

examination of the tissue: figure 9.3c and 9.3d show TEM pictures of the incision performed in the anterior stroma at 3 μJ (left) and 5 μJ (right), respectively. At 3 μJ, the region presenting disorder in the collagen fibers at the edges of the cut extends only to micrometer depths in the tissue. In comparison, in the 5 μJ incision, the perturbation of the collagen structure is more pronounced, and disordering and delamination effects are visible at the borders of the incision. From figure 5.6a and 5.6b it can be remarked that comparable secondary effects may occur as well at high numerical apertures when using an objective with $NA = 0.75$. The incision on the right was made at a moderate pulse energy of 140 nJ, which corresponds to about twice the experimental surface threshold. The cut is of good quality throughout the corneal depth. The incision on the left was obtained with pulse energies of 250 nJ - about four times the threshold - and shows in some places severe degradations of the tissue in the vicinity of the incision. However, in spite of the remaining side effects, the quality of the incisions obtained using $NA = 0.75$ is, in both investigated cases, much better than $NA = 0.15$.

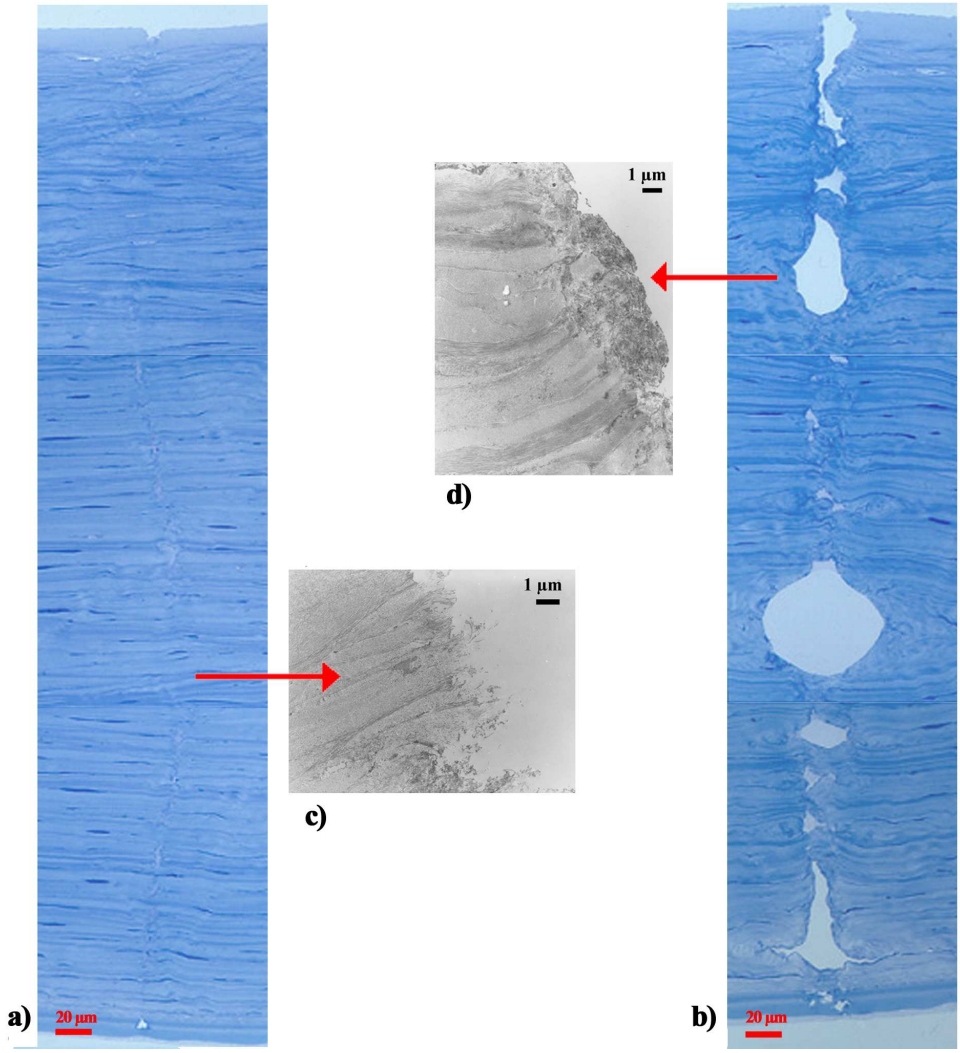

Figure 5.5: a-b) Histological section of a laser incision performed at $NA = 0.15$ and in a clear cornea at a constant energy of 3 μJ and 5 μJ, respectively; c-d) TEM micrographs detailing fibers in the anterior stroma disrupted at 3 μJ and 5 μJ, respectively [17]

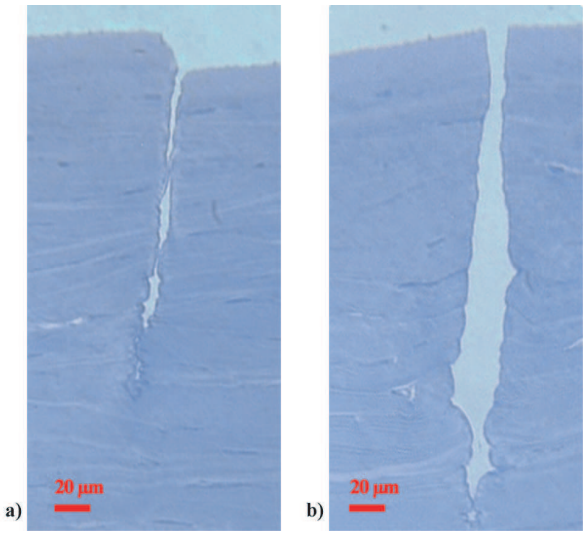

Figure 5.6: Histological section of a laser incision obtained with $NA = 0.75$, in a clear cornea at a constant energy of 140 nJ (b) and 250 nJ (a)

Experiments on edematous cornea at varying numerical apertures

Figure 9.4 shows thin and ultrathin sections of incisions made in the same pathological cornea with numerical apertures of 0.3 (a-c) and 0.5 (d-f), and at constant energies of 500 nJ and 170 nJ, corresponding to roughly two times the threshold. It can be noticed that in edematous tissue, incisions performed at constant energies are of good quality in the anterior stroma but they are not penetrating. From the TEM micrographs, one can observe that in the anterior stroma collagen fibers are properly disrupted and no secondary effects are visible. However, in the posterior stroma for a keratoplasty cut at $NA = 0.3$ and in the middle stroma for a keratoplasty cut at $NA = 0.5$, the incision becomes irregular and eventually ends at depths of about 500 μm ($NA = 0.3$) and 280 μm ($NA = 0.5$). Where the threshold for optical breakdown is not reached, a slight blackening of the tissue can be observed, which can be attributed to chemical alteration of the tissue occurring at radiant exposures slightly lower than the threshold.
As both incisions have been performed at different numerical apertures with equivalent parameters, a comparison of the maximum incision lengths allows a primary evaluation of the influence of spherical aberration which occurs when the beam is focused from air into the volume of the cornea. At a numerical aperture of $NA = 0.3$, the influence of spherical aberrations is reduced and the beam attenuation is mainly due to light scattering in the cornea. In this case,

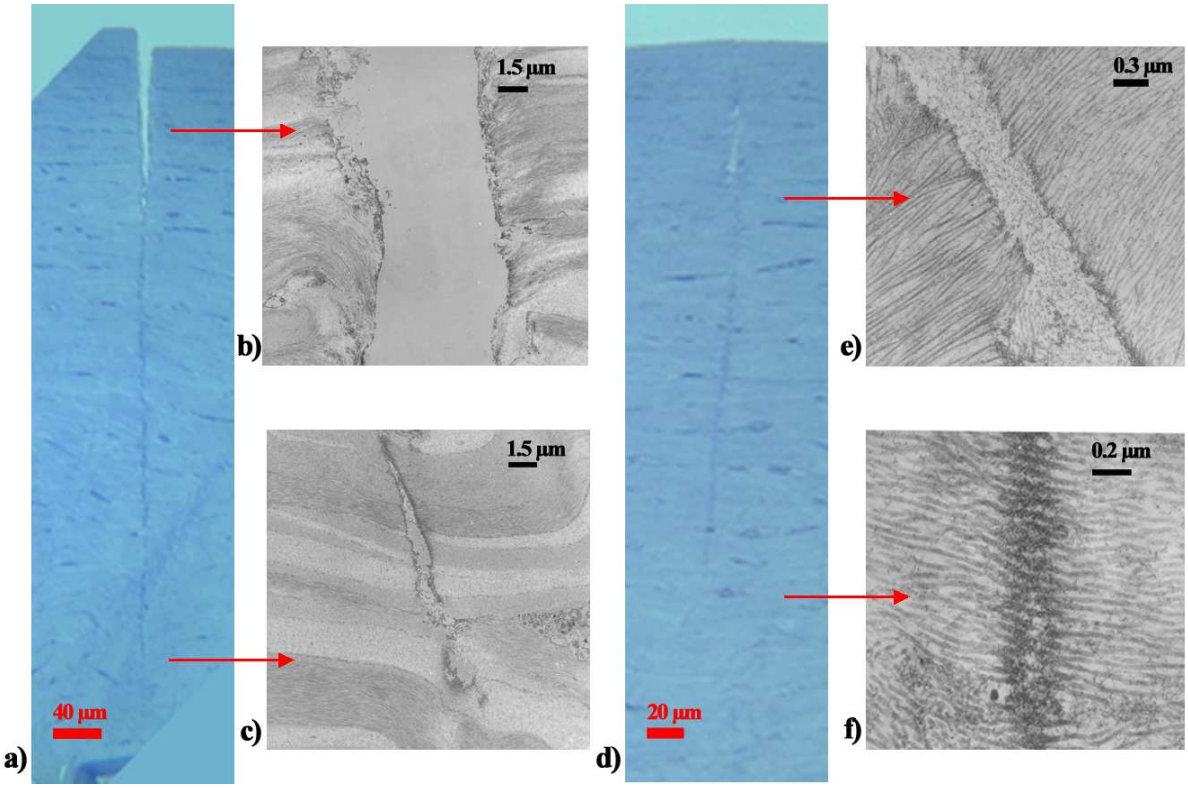

Figure 5.7: a,d) Histological section of laser incisions in an edematous cornea performed at $NA = 0.3$ and $NA = 0.5$ and constant energies of 500 nJ and 170 nJ respectively; b-c, e-f) TEM micrographs of the collagen in the anterior stroma (b,e) and at the end of the incision (c,f)

slightly augmenting the pulse energy enables performing transfixing incisions in mildly edematous corneas. In the case of $NA = 0.5$, the maximum incision length is decreased to less than 300 μm, the contribution of the spherical aberration to the energy beam attenuation is stronger than for $NA = 0.3$ and transfixing incisions in this cornea using this objective would require very high pulse energies. The influence of optical aberrations on the beam broadening is examined in more detail in chapter 6.

Lamellar incisions at varying numerical aperture

In addition to the above experiments, lamellar incisions were performed in the anterior stroma of edematous cornea, thus allowing the observation of possible tissue alteration, as in this ge-

ometry cuts are perpendicular to the laser beam propagation axes. Figures 9.5a,b and 9.5a,c illustrate histological sections of incisions induced at 150 μm from the corneal surface with $NA = 0.3$ and 0.5 at energies of 900 nJ and 450 nJ, respectively, which correspond to about 3 times the threshold experimentally determined. The quality of the incisions improves greatly with increasing numerical aperture. Tissue modifications are still visible in the histological sections for $NA = 0.3$ and, to a smaller extent, for $NA = 0.5$. Figure 9.5a,d presents the histological section of the incision performed at $NA = 0.75$ at a pulse energy of 150 nJ (about 2.5 times the experimental threshold), showing little secondary effects. The general tendency of these observations is confirmed by ultrastructural imaging using TEM (figure 9.5e-g), which shows streak formation and residual cavities. The strength of this effect diminishes with increasing numerical aperture, but it remains present even at $NA = 0.75$.

5.4 Discussion

A primary evaluation of the quality of cuts induced by the laser system consists in identifying the presence of tissue bridges or possible secondary effects (thermal or mechanical effects). Keratoplasty cuts performed in edematous corneas with the clinical laser result in incisions comparable to those obtained with our experimental set-up at a *NA* of 0.3 or 0.5. Experiments were performed alternatively at $\lambda = 800$ nm and $\lambda = 1.06$ μm, however this should not much affect laser-tissue interaction, as it has been shown that the wavelength dependance of femtosecond breakdown in the IR region is weak [116]. This assumption can also be justified considering that at 800 nm the increase of the threshold due to stronger scattering is compensated by the lower plasma defocusing due to the tighter focus. This last phenomenon is presented in section 5.5. Examination of thin and ultrathin sections reveals that tissue dissection is not penetrating, which we ascribe to the broadening and the attenuation of the laser radiation, due to spherical aberrations and scattering that the beam experiences during propagation through opaque tissue. The incomplete cut in the graft button which underwent the posterior lamellar keratoplasty is consistent with its higher measured thickness compared to the two other corneas, indicating a strong edema. At high magnification, we observed creation of debris, which deposit on the borders of the incision or stand between the two edges. Two types of debris appear to exist: debris formed of collagen fibrils and of a heterogeneous substance. These fragments can be the result of mechanical effects, even though the conversion efficiency of light energy into mechan-

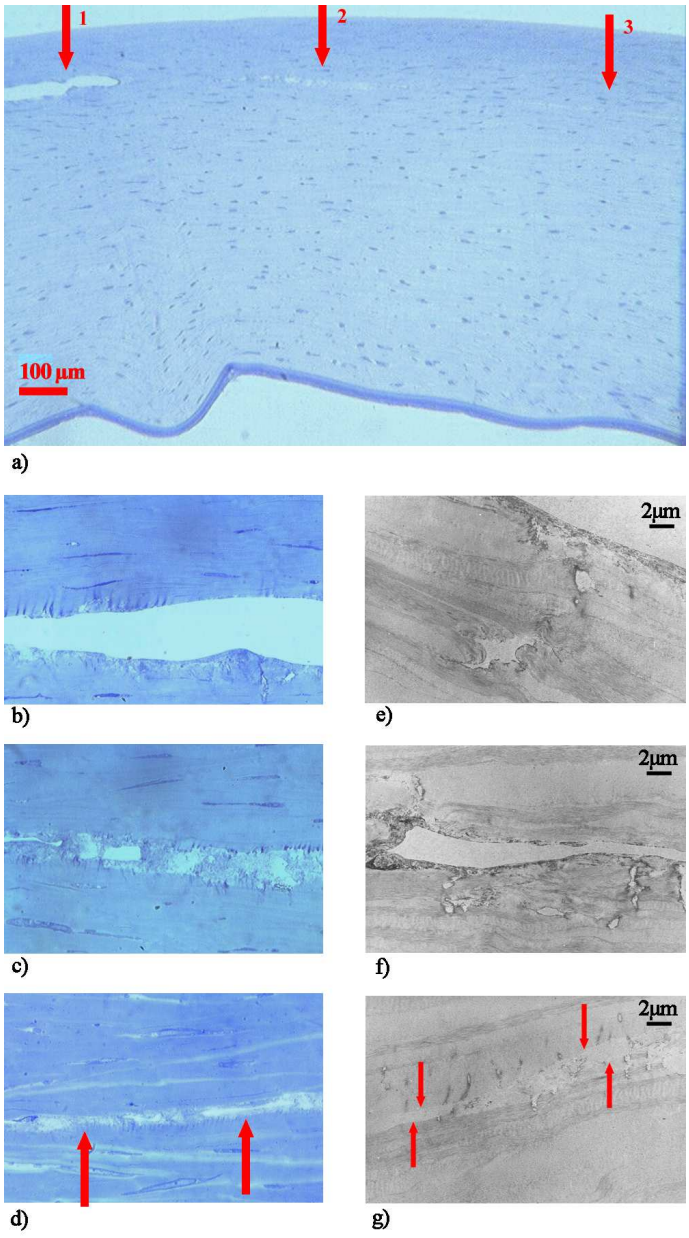

Figure 5.8: Histological sections of lamellar laser incisions induced at 150 μm from the corneal surface with NA = 0.3 (a1,b), 0.5 (a2,c), and 0.75 (a3,d) at energies of 900 nJ, 450 nJ, and 150 nJ respectively; e,f,g) Detail of the lamellar incisions from TEM at $NA = 0.3$, 0.5 and 0.75 respectively

ical energy is strongly reduced in the femtosecond regime [115]. We observed that a higher quantity of debris was generated in the anterior stroma than in the posterior stroma, which we ascribe again to the extinction of the irradiation source when focused at important depths in the cornea. At irradiances larger than the threshold as in the anterior stroma, the optical breakdown starts before the femtosecond pulse reaches the beam waist [2]. This effect enlarges the size of breakdown region and leads to stronger disruption effects in the the anterior lamellae compared to the posterior layers. Incisions in the lamellar plane preserve the organization of collagen fibers with diminished mechanically induced side effects, as laser impacts form cavities, which separate collagen lamellae rather than disrupt fibers. This can also explain why the debris are principally found in the vertical plane, whereas in the lamellar plane, they organize like a nanometric pseudo-membrane lining the incision, as found in previous studies [100, 103].
The experiments concerning perforating femtosecond laser incisions in clear corneal tissue, at threshold radiant exposure and above, show also significant histological differences. The laser cuts induced close to the threshold exhibited only localized disorganization of the stroma, whereas the incisions induced at higher energies presented a strong disorder of the stroma. These side effects were reduced, but not suppressed by tightly focusing the beam. At low *NA*s, the distribution of the energy at the focal volume is influenced by nonlinear effects, such as self-focusing and plasma defocusing, thus reducing the spatial confinement.
Clinically, incisions realized with too high energies might induce inflammatory reactions and possible vascularization followed by fibrose, with consequences on the healing process [47].
When the laser energy is not controlled, other phenomena may occur producing chemical permanent modification of the tissue. Vogel *et al.* [116] attributed chemical effects to the generation of low-density plasma in the bulk of biological materials, causing photodissociation of water molecules and creating reactive oxygen species. Heisterkamp *et al.* [43] confirmed the presence of oxygen and hydrogen by means of a chemical analysis of the components of the laser-induced bubbles during optical breakdown. In our experiments, similar chemical changes are observed when performing vertical and lamellar incisions. The series of lamellar incisions reveal the formation of "filaments" along the axis of the laser beam and close to the breakdown region, with periodical dark staining of the tissue. Similar features were observed in tissue which underwent fs laser procedures with a clinical system. The expected reduction of secondary effects with increasing numerical aperture and optimized energy was confirmed. Further details about experimental streak formation and complementary numerical simulations are exposed in the following section.
In short, optical and TEM investigation of tissue dissection by clinical procedures demonstrated

that tissue bridges remain in thicker corneas and that cellular and collagenous nanometric debris are created by the laser. In the anterior stroma, they rather form a layer of a few microns thickness, which stands on the terminated disrupted collagen fibres, in the posterior stroma they organize like a pseudo-membrane running along the edges of the incision. Therefore, low energies do not cut completely the tissue and too high energies create significant amounts of debris. Similar findings were obtained when performing incisions using our experimental system. We demonstrate that the augmented energies in clear and edematous corneas may result in unwanted side effects, like high disrupted regions or chemical alteration of the tissue. These effects were reduced but not suppressed when tightly focusing.
Event though in keratoplasty cuts performed by the femtosecond laser the ultrastructure of the disrupted collagen fibers is preserved and many previous studies have shown that fs keratoplasty is a safe and predictable procedure, it remains extremely important to choose the appropriate energy, since too high energies may lead to reversible or irreversible collateral effects.

5.5 Self-focusing effects

Lamellar incisions displayed above exhibit dark streaks or even tissue disruption below and above the focal plane. In this section, we investigate the possible underling mechanisms.
Under high magnification, details of material alteration become visible. TEM micrographs of ultrathin sections show that the streaks, visible below and above lamellar incisions, are characterized by a periodic structure, as displayed in figure 9.6. This feature was recurrent in a series of 5 corneas analyzed in this respect. Figure 5.10 shows the average period of this structure for each cornea, measured from TEM photographs. The parameters which varied among experiments were specimen, excitation wavelength, numerical aperture, and energy. We have chosen to classify results as a function of the *NA*. We notice that the period ranges between 0.29 ± 0.02 μm and 0.47 ± 0.07 μm. They have therefore sub-wavelength dimensions. Material modifications have been reported in previous studies in fused silica and tissue, however, to best of our knowledge, this kind of periodical structure has not be observed before. This is probably due to analysis at a lower resolution [43, 111].
Darkening of the tissue is produced by a local increase of the laser irradiance and we put forward different hypothesis in order to interpreting the above findings.

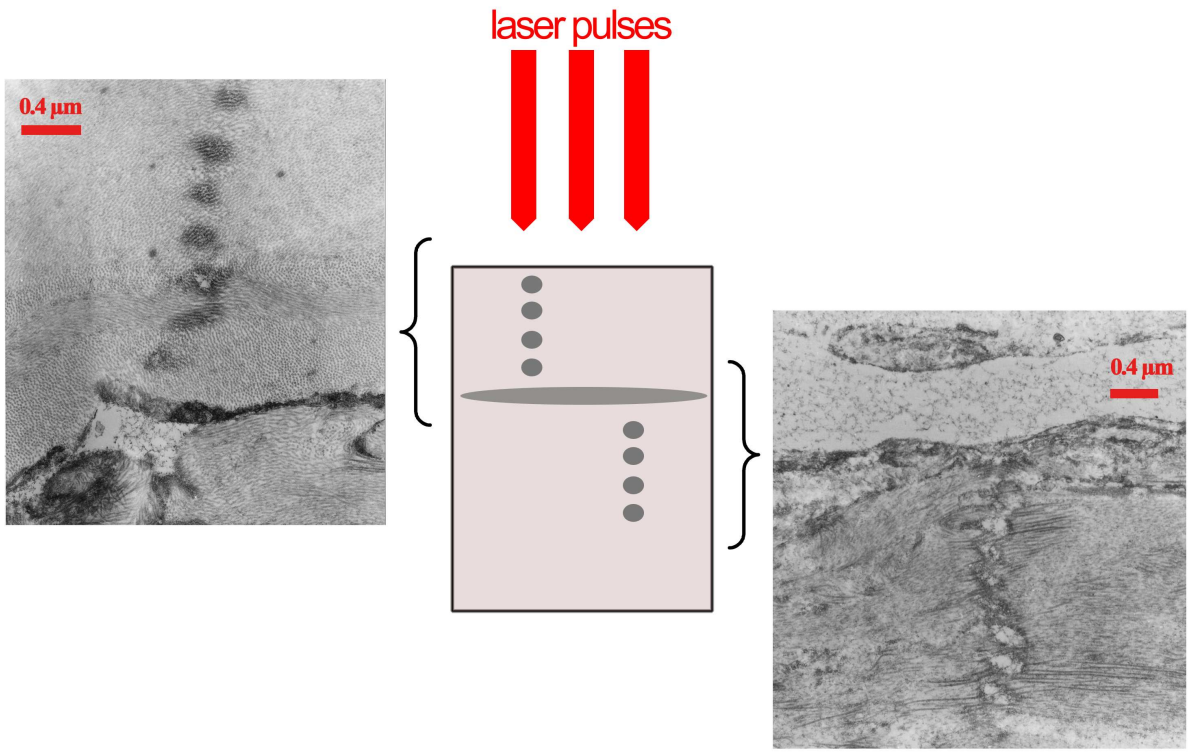

Figure 5.9: TEM photographs of a periodic structure below and above the lamellar plane in which the incision was performed

Comparison to features of the point spread function

Irradiance peaks may correspond to the light distribution in the focal volume. Light distribution arises from Fraunhofer diffraction on the aperture of a lens which in our case is represented by the objective pupil.
For notation, we refer to figure 5.11. In the plane $(u, \nu = 0)$ perpendicular to the focal plane, the irradiance distribution is described by a first order Bessel function, also called Airy pattern, according to

$$I(u, \nu = 0) = I_0 \left(\frac{\sin u/4}{u/4} \right) \tag{5.3}$$

where I_0 is the peak intensity. The distribution presents minima and maxima along the optic axis and could explain the irradiance peaks (figure 5.12). The first maximum of intensity on the

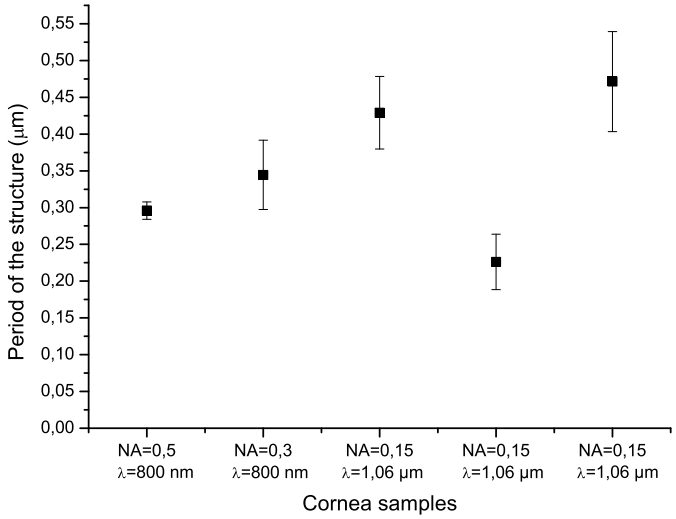

Figure 5.10: Average structure period of 5 corneas which underwent lamellar dissection. Values are classified as function of the focusing optics *NA* and were measured from TEM photographs

optic axis is given by

$$\frac{u}{6} = \frac{3\pi z}{\lambda} \cdot \left(\frac{a}{f}\right)^2 = \frac{\pi z}{3\lambda} \cdot (\tan(\arcsin NA))^2 = \pi \tag{5.4}$$

which would correspond to a a distance z from the focal point of 130λ, 30λ, and 9λ at $NA = 0.15$, 0.3 and 0.5, respectively. These values are far from being comparable to the periods measured in our experiments. Moreover, according to equation 5.3, the values of the intensity maxima decrease as one moves away from the focal plane. This would correspond to reduced effects on tissue, which is not in agreement with TEM micrographs presented in figure 9.6. In fact, we can observe that laser impacts on collagen do not depend on the distance from the lamellar incision.

Comparison to features produced by self-focusing effects

Tissue streaks are probably due to the increase of the intensity-dependant refractive index, related to the Kerr effect, which causes self-focusing, followed by plasma defocusing.

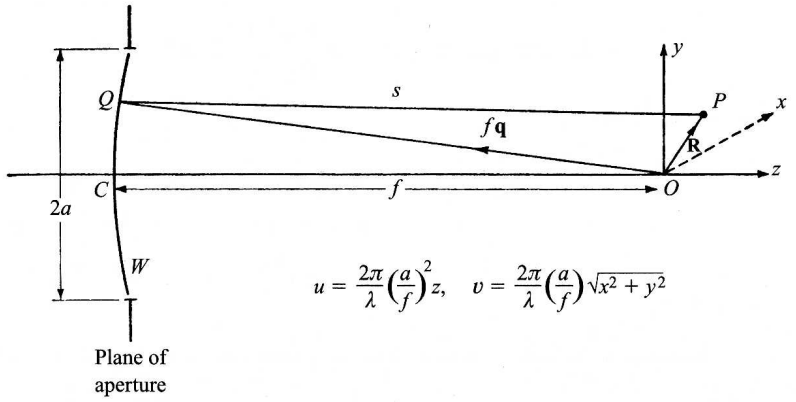

Figure 5.11: Fraunhofer diffraction on a circular aperture: notation (from [5])

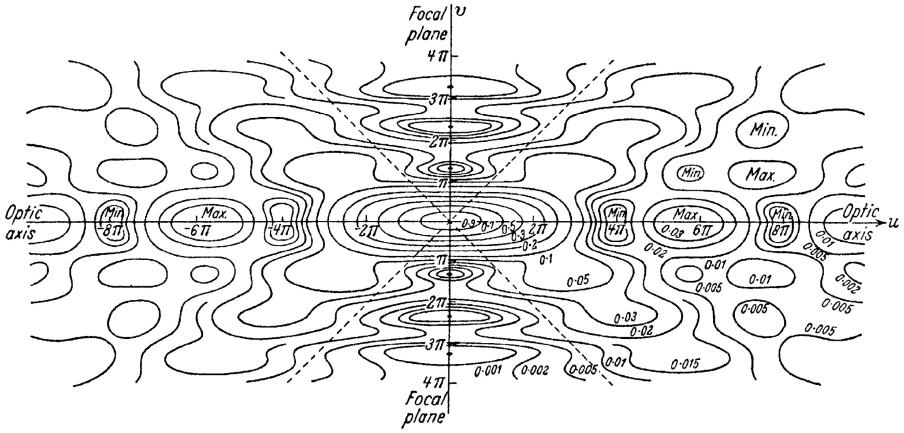

Figure 5.12: Isophotes (contour lines for equal irradiances) in the focal region of a diffraction-limited microscope objective used to focus a plane wave. The dashed lines represent the boundary of the geometrical focus (from [5])

From equation 7.7 and considering the approximation $n_2^{cornea} \approx n_2^{water} = 1.2 \times 10^{-16}\ cm^2$/W where n_2 stands for the nonlinear refractive index, we obtain the following values for the critical power for self-focusing to occur

$$\begin{cases} P_{cr}^{cornea} \approx 10.2\ MW, & \lambda = 1.06\ \mu m \\ P_{cr}^{cornea} \approx 5.8\ MW, & \lambda = 800\ nm \end{cases} . \tag{5.5}$$

Based on our experimental conditions, and considering the theoretical and experimental energy values, presented in table 5.2, we calculated the respectively peak power in order to induce optical breakdown (table 5.4). Lamellar incisions were performed at fourfold the threshold radiant

	λ=1.06 μm, τ=500 fs, $NA = 0.15$	λ=800 nm, τ=150 fs, $NA = 0.3$	λ=800 nm, τ=150 fs, $NA = 0.5$
P_{th} (corresponding to the theoretical energy for OB)	2.3 MW	1.1 MW	0.4 MW
P_{ex} (corresponding to the experimental energy for OB)	4 MW	1.3 MW	0.8 MW
$P_{ex\cdot 4}$ (corresponding to four times the threshold)	14 MW	5.2 MW	3.2 MW

Table 5.4: Calculated values at different experimental conditions of the peak powers corresponding to the theoretical and experimental energies for optical breakdown and four times the threshold energy as used when performing incisions at 150 μm

exposure and at a depth of approximately 150 μm. Even though the laser beam undergoes attenuation and pulse duration is stretched by dispersion in the optics and the tissue, we estimate that we are still in a regime corresponding to a peak power higher than P_{cr}^{cornea}. Based on the considerations regarding the laser attenuation in edematous corneas, which are introduced in chapter 6, we evaluate that for an edematous cornea (with a typical penetration length of $\approx 300\ \mu$m), the energy at 150 μm is attenuated by a factor of about 0.6, which would support our estimation.
The nonlinear interaction of the beam with the cornea at the focus volume can be modelled numerically[2]. Arnold [1] proposes a numerical code which takes into the account the vectorial character of the electric field and the nonparaxial approximation for tight focusing. A (3+1) dimension Schrödinger equation is therefore derived to describe the spatial and temporal

[2]Simulations were provided by Cord Arnold, Department of Biomedical Optics - Medicine Laser, Laser Zentrum Hannover, Germany

nonlinear propagation of the laser pulse in a dielectric media. In a low *NA* focusing regime ($NA \leq 0.5$), equations may be solved by neglecting the nonparaxial term. In parallel, a multirate equation model introduced by Rethfeld [92] is used to calculate the generation of free electrons in dielectrics. Simulations were performed for a model substance assumed to be water. Diffraction-limited Gaussian pulses of duration 500 fs at center wavelength $\lambda = 800$ nm were assumed. In our experiments pulse duration was approximately 170 fs at the output of the laser, therefore, in order to take into account the group velocity dispersion that the beam experiences when travelling through the focusing units, numerical simulations were performed for a pulse duration of 500 fs.
The breakdown criterion was the generation of a plasma of density $\rho_{cr} = 10^{21}$ cm^{-3}. The threshold irradiance was then determined when the plasma reached ρ_{cr} at one point. Numerical,

Numerical aperture	0.3	0.5	0.75
Energy corresponding to 2 J/cm^2 (total energy divided by the Airy disk surface) (nJ)[a]	166	59	26
Experimental threshold energy at the surface (nJ)	288	130	60
Numerical threshold energy (nJ)	300	18.14	7.61
Energy corresponding to 1.3 J/cm^2 (total energy corresponding to the peak value of the Airy pattern) (nJ)	45	16	7

[a]Threshold irradiance for optical breakdown from the literature [34, 79, 109, 116, 118]

Table 5.5: Comparison of the energy values at the optical breakdown, measured experimentally in the cornea with values computed numerically in water. Theoretical values are also reported

experimental and theoretical values of the energy are presented in table 5.5.
We analyze the results concerning the energy as follows

- as detailed in section 5.3, the experimental threshold energy corresponds to consistent and regular bubble formation at the surface of the tissue, regardless of local sample irregularities. Its value corresponds to about twice the theoretical threshold, as we expected;

- for a numerical aperture of 0.3, it also compares well to numerical calculation. For higher numerical apertures, the simulations predict a rapidly decreasing threshold energy as the tighter focusing attenuates defocusing effects. The values converge towards those corresponding to an ideal, nondeformed Airy disk (row 4 of table 5.5). The experimental

values do not quite follow this extreme reduction in threshold energy as the experimental conditions very probably did not produce "ideal" point spread function.

The plasma distribution and the fluence at the optical breakdown are plotted in figure 5.13 (top and bottom respectively). Contour plots are provided for various *NA*s, in the plane $(x-z)$ perpendicular to the focal plane. We notice that in a low numerical aperture regime, plasma density is spatially highly asymmetric. Its highest value is obtained before the beam reaches the focus located at $z=0$ and it takes the shape of a "tail" as long as it propagates in the focal volume.
The first half of the pulse is dominated by multiphoton or tunneling ionization increasing the electron density. The generated plasma becomes highly absorbing and leads to a negative refractive index spatially in the central part of the pulse. This effect defocuses the pulse and decreases the number of electrons generated [2]. Thereby, low-density plasmas are created. The asymmetry tends to diminish when focusing more tightly. Indeed, since plasma defocusing competes with spatial focusing, at high *NA*s a higher density of free electrons is required to be generated for defocusing the beam.
These simulations account for dark streaks in the tissue below the focal plane. However, they still not explain staining observed above the lamellar incisions, neither the periodicity of the structures.
This may be at least in part attributed to the modelling parameters used. In fact, simulations were performed in water and the laser pulses were considered diffraction-limited. This configuration neglects the structure and the optical nonlinear properties of the cornea as well as beam broadening induced by optical aberrations.
Tissue which underwent lamellar dissection exhibits dark streaks or disruption near the focal volume and along the beam optical axis. These laser effects are characterized by a periodic structure. We believe that this unwanted tissue alteration is attributable to peak irradiances due to self-focusing, although previous studies have not reported a sub-wavelength periodic feature. Numerical simulations of plasma generation in the focal volume provided first elements allowing interpretation. We propose that further simulations are performed, taking into account the beam propagation through a nonlinear model material with parameters closer to tissue properties. Additional experiments should also be performed in order to understand the dependance of the structure period with the numerical aperture, pulse duration and wavelength.

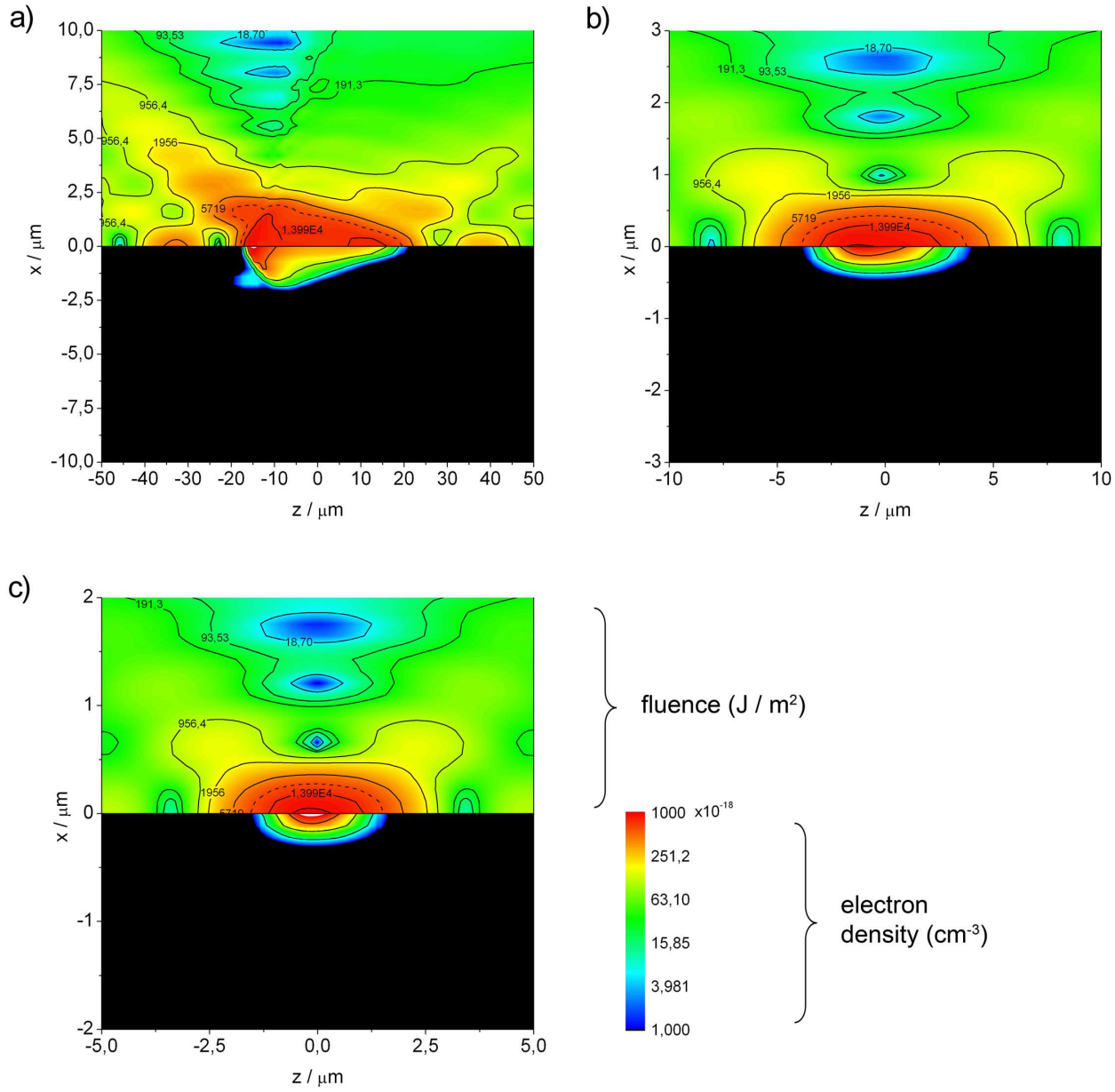

Figure 5.13: Contour plots for the electron density (bottom) and the fluence (top) at $NA = 0.3$ (a), $NA = 0.5$ (b), $NA = 0.75$ (c) in the $x - z$ plane, at the optical breakdown. Pulses propagate from left and the focus is located in $z = 0$. Electron density scale applies to all three plots (provided by Cord Arnold, Laser Zentrum Hannover)

5.6 Deposit of glass fragments during keratoplasty

In figure 5.14 shown in section 5.2, we have observed black solid particles and we intend to elucidate their nature and composition. For that purpose, we performed additional dissection experiments varying the energy values and the shapes of the clinical procedures and compare results obtained with our experimental set-up. The nature of the particles was determined with the EELS technique. The applanation lenses provided for the clinical laser procedures were examined by SEM and 3D images were reconstructed from the SEM micrographs.

5.6.1 Methods

We performed two series of experiments using the clinical laser and the laboratory set-up. With the Intralase system, following the standard protocols proposed, we performed three penetrating keratoplasties with a depth into glass set by default at 50 μm: one mushroom-shaped, at an nominal energy of 2.62 μJ, and an anterior diameter of 7.1 mm; one top hat-shaped, at an energy of 2.62 μJ, and an anterior diameter of 7.1 mm; one straight circular shaped, at an energy of 2.92 μJ, and a diameter of 8 mm. Energies higher than 2 μJ were used as suggested by the laser manufacturer for treating oedematous corneas. A cone flattened the corneas during the laser delivery. The "depth into glass" parameter is defined as the length over which the laser interacts with the glass of the applanation cone in contact with the cornea. Additionally, we performed three penetrating keratoplasties with the same parameters but stopping the laser delivery at the lens-epithelium interface, and one posterior lamellar keratoplasty at a nominal energy of 2.92 μJ. In parallel, we induced keratoplasty cuts in four corneas with the laboratory set-up. The laser beam was focused into the tissue by means of an achromatic doublet lens at a $NA = 0.15$ (Melles Griot, LAL013). The cornea was flattened with a standard glass coverslip. We expressly focused the laser from the endothelium until the corneal surface and through the coverslip. Following a straight circular geometry, transfixing incisions were performed in the cornea at an energy of 4 ± 0.4 μJ, corresponding to a radiant exposure which was twice the threshold that we measured in our experiments.

In addition to systematic histological and ultrastructural study of corneal tissue following laser keratoplasty cuts, thin sections were analyzed by the energy electron loss spectroscopy tech-

nique (EELS), in order to verify the presence of specific chemical elements [23]. EELS consists in the analysis of a sample through the interaction with an electron beam. When the electron beam is passing through the material, the electrons may suffer inelastic scattering. They are then deflected and they lose energy. Phonon, plasmon, inter-band and inner-shell excitations may result from these collisions. The analysis of the resulting transmitted beam gives the required data on the composition of the material, while the energy loss peaks are specific for each element. It is thus possible to determine the chemical nature of these particles by comparing the experimental data to a library of fingerprints.
Applanation lenses used during laser keratoplasty were observed by optical microscopy and scanning electron microscopy (SEM) following coating with gold of a thickness of about 10-20 nm in a sputter coater. SEM analysis was performed on a JEOL microscope[3], and images were processed with a 3D reconstruction software[4].

5.6.2 Results

From histological sections of corneal tissue cut by the clinical laser during a mushroom-shaped keratoplasty procedure at a energy of 2.57 μJ, it can be noticed that in some areas of the anterior stroma at different depths dark particles are visible, which can be clearly distinguished from collagen or keratocytes (figure 5.14a). They lay on the edges of the disrupted tissue or between the collagen lamellae. Comparable foreign bodies accumulated on the epithelium and Bowman's membrane close to the incision (figure 5.14b). The same kind of particles was observed when top hat and straight circular surgeries were performed and when posterior-to-anterior incisions were obtained with the laboratory system. TEM micrographs of two different sections of Bowman's membrane were compared, when the tissue had undergone a clinical laser treatment (figure 5.15a), and when it was cut by the laboratory device (figure 5.15b). In both cases, black particles can be discerned, whereas the white spots represent breaking of the resin occurred during preparation of the sample sections. This may be due to the presence of these solid fragments. From TEM micrographs it results that the quantity of particles varies from one section to another, and that they have a distribution of shapes and sizes up to micrometric dimensions. We measured the surface of 200 particles from a sample of TEM micrographs and estimated the third dimension for calculation of the corresponding volume. We constructed a

[3]Jeol 5910-LV, Tokyo, Japan
[4]MeX, Alicona, Graz, Austria

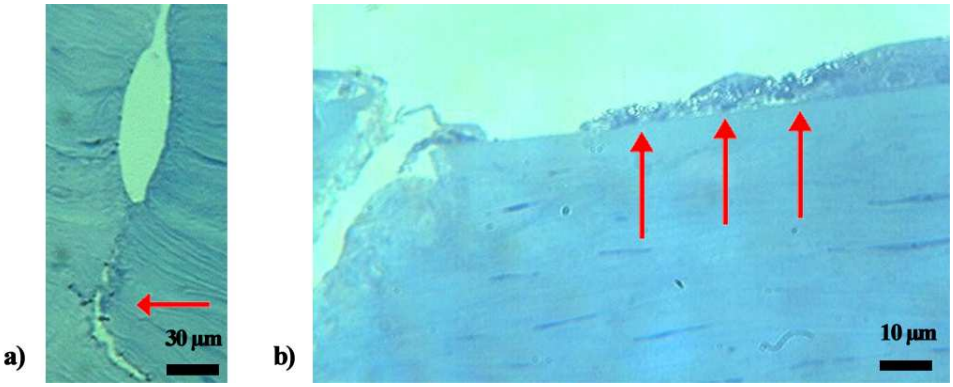

Figure 5.14: Histological sections of corneal tissue after mushroom-shaped keratoplasty cut performed with a clinical femtosecond laser at an energy of 2.57 μJ. Solid particles deposit on the epithelium (a) and along the incision edges in the anterior stroma (b)

histogram of the distribution by plotting the volume on the x-axis and the number of particles on the y-axis (figure 5.15c). It can be noticed that almost 50% of the particles have a volume smaller than 0.002 μm^3. No clear relation could be established between the quantity and size of the fragments with the energies used. By contrast, no abnormal substance was found when the tissue had undergone posterior lamellar keratoplasty and penetrating keratoplasty cuts during which the laser delivery was stopped at the lens-cornea interface.
The chemical composition of these fragments was identified using the EELS technique[5]. The presence and shape of the silicon (Si) and the oxygen (O) edges were detected when the electronic probe was located on the particles, with peak intensities at electron energy losses of about 107 eV and 135 eV respectively (figure 5.16). Even though tissue normally contains oxygen, the identification of silicon clearly indicates that the fragments are composed of silica (SiO_2). Accordingly, we did not detect silicon signals when the probe was located in the space in between the particles. In parallel, an unused applanation lens and the ones used during penetrating femtosecond keratoplasty cuts were examined by optical microscopy (figure 9.8). It can be clearly seen that, after a keratoplasty cut procedure, the surface of the lens, which was in contact with the epithelium during the surgery, is not smooth; the laser beam has micromachined the glass. The coverslip used in the laboratory experiments exhibited the same type of laser damages. By analyzing the surface of the applanation lens with scanning electron microscopy, we could measure the width of the structures machined by the laser: 7.0 ± 1.5 μm for the circular

[5]These measurements were performed in collaboration with Fréderic Pailloux and Thierry Cabioc'h from the Laboratoire de Physique des Matériaux, Université de Poitiers

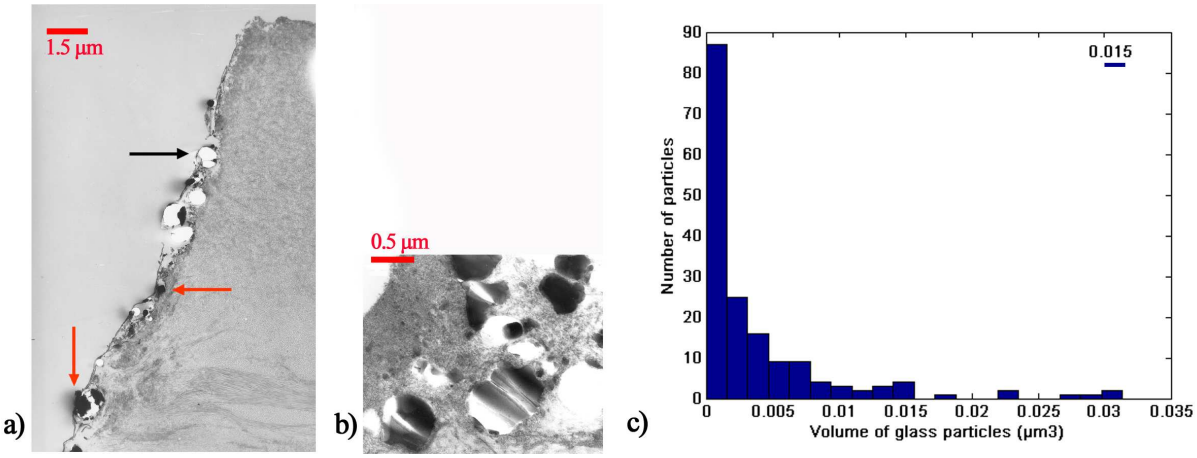

Figure 5.15: Ultrastructural sections of Bowman's membrane after penetrating keratoplasty cut performed with a clinical femtosecond laser (a) and a laboratory laser system (b). Similar black bodies are generated which correspond to solid particles (red arrows), whereas the white spots (black arrow) represent breaking of the resin occurred during preparation of the sample sections. From a sample of ultrathin section, the volume of 200 particles was measured and plotted into a histogram (c).

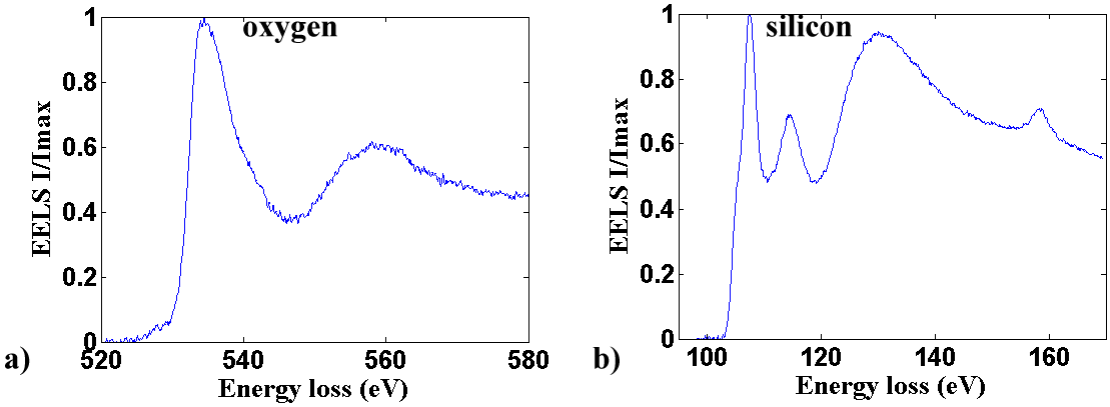

Figure 5.16: Oxygen-edge (a) and Silicon-edge (b) recorded with the EELS technique when the electron probe was on a solid particle, revealing that the particle are composed of silicon dioxide (provided by Fréderic Pailloux and Thierry Cabioc'h, Laboratoire de Physique des Matériaux, Université de Poitiers)

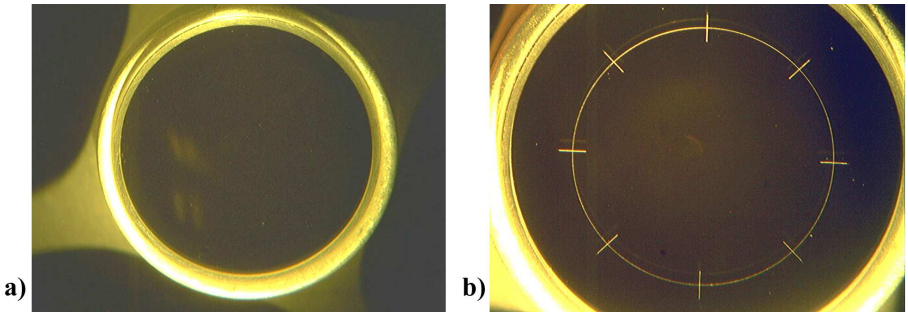

Figure 5.17: Optical micrographs of an unused cone (a) and an applanation lens after clinical femtosecond laser keratoplasty cut (b). The glass lens in contact with the epithelium was clearly machined by the laser

structure and 18 ± 2 μm for the radial structure corresponding to the suture marks (figure 5.18). We processed data from SEM with a 3D reconstruction software and obtained 3D images of

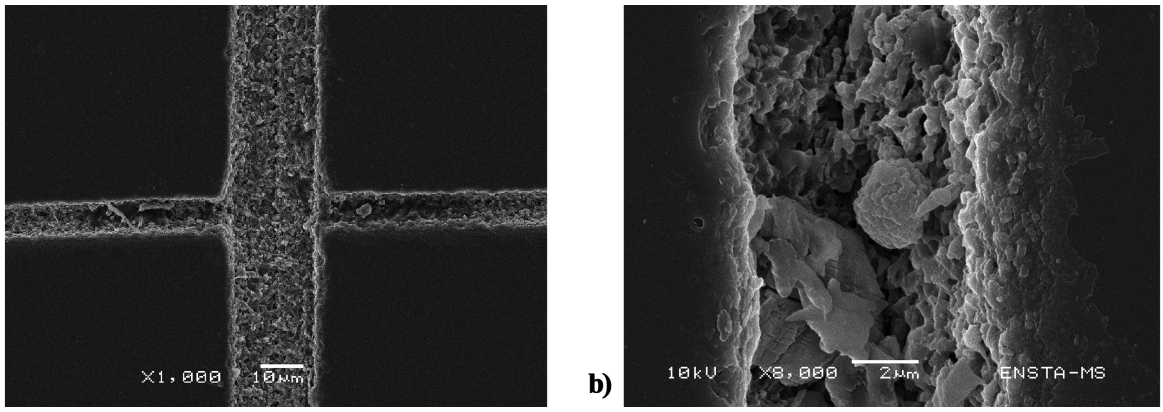

Figure 5.18: SEM micrographs of an applanation cone after clinical femtosecond laser keratoplasty cut: intersection of the circular and the radial structures (a) and detail at a higher magnification of the radial mark (b) (provided by Bertrand Reynier, Unité de Mécanique, ENSTA, Palaiseau)

structures written on the lens (figure 5.19a)[6]. The profiles of the groove features were extrapolated (figure 5.19b), thus permitting to determine the depth, which varied from 5 μm to 7 μm in the circular features. We determined an average profile and calculated the volume of glass lacking in the applanation lens. For a keratoplasty cut at a diameter of 8 mm, the volume amounts to

[6]These results were obtained in collaboration Bertrand Reynier from the Unité de Mécanique, ENSTA, Paris.

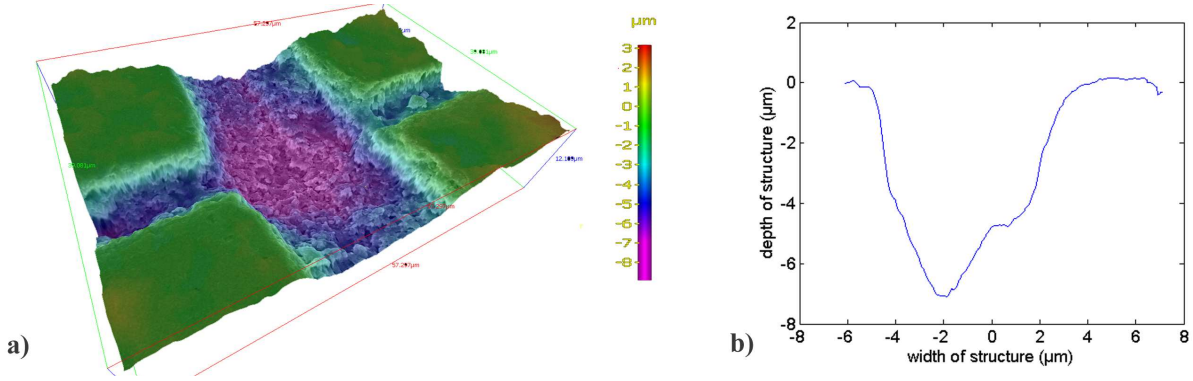

Figure 5.19: 3D reconstruction from SEM micrographs of laser machined structures at the surface of an applanation cone after clinical femtoseconds laser keratoplasty cut (a). The profile of structures can be extrapolated giving access to an estimation of the volume of the removed glass fragments (b) (provided by Bertrand Reynier, Unité de Mécanique, ENSTA, Palaiseau)

$(1.1 \pm 0.2) \times 10^6$ μm^3. By analyzing the sample at high magnification and evaluating a certain number of profiles, we could also observe that the inner edge of the circular feature is always smoother than the outer edge. This information coupled to the deepness variations suggests that the laser beam is slightly tilted, at least for high diameters. This causes astigmatism, thus contributing to beam broadening. This finding may also be interesting in the context of studies examining the influence of optical aberrations on the quality of corneal surgery.

5.6.3 Discussion

The identification of silicon detected by the EELS clearly indicates that the dark particles found in TEM are composed of silica (SiO_2). Judging from the optical and SEM observation of the surface lens in contact with the epithelium during keratoplasty, we believe that they originate from the applanation lens. Silica is a dielectric and transparent material, which has an energy threshold comparable to the one of cornea [34, 79, 109, 116, 118]. Therefore, energies used to induce disruption in corneal tissue also induce optical breakdown in the applanation lens and we believe that the machining of the glass by the laser is caused by this process. Moreover, keratoplasty on oedematous corneas requires the use of higher energies than in the case of surgery on transparent corneas, as shown in the previous sections. Hence, the surface in the glass in which optical breakdown occurs is increased and particles are more likely created [2, 116]. The

tracks machined by the laser beam on the lens coincide well with the circular incision and the radial marks to assist the suture placement in penetrating keratoplasty procedures. However, the maximum measured depth of glass machined was 8 μm by analyzing the profile tracks, and does not correspond to the "depth in glass" parameter fixed at 50 μm. The discrepancy between the observed and nominal depths of the machined structures in the glass may be due to tolerances in the calibration of the system. When performing posterior lamellar keratoplasty or penetrating keratoplasty without applanation lens machining, we did not found black particles with TEM or silicon signals with EELS. Glass fragments were created when using both the laboratory and the commercial laser. No other glass tool was used during the two procedures.

It was beyond the scope of the present study to evaluate the biological effects the deposited particles may have in living tissue. To date, no complications related to microscopic glass fragments present into corneal tissue have been reported. Glass is usually considered to be biologically inert. However, it seems pertinent to suggest that the presence of these particles may influence the corneal inflammatory response and wound healing process. In other tissues than cornea, such as subcutaneous connective tissue, small bioactive glass particles with a comparable size may activate the cellular inflammatory response, mediated by macrophages and multinucleated giant cells [66]. In clinical studies, some authors have described diffuse lamellar keratitis after laser in situ keratomileusis [48, 65]. The etiologic factors remain unknown, but it has been suggested that a previously inert inciting agent could cause a delayed toxic or inflammatory response of the cornea several months after surgery [48]. Confocal microscopic examination of one patient with lamellar keratitis showed a large number of activated keratocytes in the flap interface, particulate debris of variable size distributed throughout the interface, and scattered inflammatory cells [65]. However, the exact chemical composition of these particles was not known. The impact of the glass particles on keratocytes functions during the corneal wound healing process, such as cell proliferation and migration, and collagen deposition or polymerization, is also unknown.

Further investigation should concern *in vivo* studies to evaluate the impact of glass fragments in corneal tissue. Particularly, only studies comparing wound healing and clinical outcome after femtosecond assisted keratoplasty with and without applanation lens machining may evaluate the clinical impact of this novel finding. In the absence of data on the biological tolerance of glass particles, it would certainly be preferable to avoid glass deposit into cornea. Our study shows that this unexpected effect can be easily avoided by cutting the laser delivery off when the beam is focused at the lens-cornea interface. We therefore suggest stopping the procedure at the lens-cornea interface or modifying the "depth into glass" parameter, thus prohibiting the

laser to machine the applanation lens.
When performing penetrating surgery, SiO_2 particles are produced. They originate from the applanation lens during the laser machining process at the interface cornea-lens. These particles may remain in the tissue. No related complications have been reported up to now, however, it would preferable to avoid this secondary effect, by modifying the pre-programmed laser parameters or improving the existing commercial systems.

Chapter 6

In situ evaluation and correction of laser energy density attenuation in opaque corneas

6.1 Introduction

Aside from refractive surgery, in which the ultrafast laser creates a standard flap in a transparent cornea regardless of the degree of the correction, indications for keratoplasty are often associated to disorders which involve opacities of the corneal tissue. In the preceding chapter we have shown that the modified optical properties of the cornea, due to a loss of transparency, need to be taken into account when delivering the laser beam. Using inappropriate laser parameters may lead to unwanted secondary effects. Depending on the pathology, opacities can be localized or can affect the whole cornea to a mild or severe degree and clinical femtosecond devices propose procedures with various shapes and recommendations concerning the energy values. However, no system determines the parameters from a quantitative evaluation of the optical properties proper to the cornea to be treated and the choice of the protocol details depends mostly on the experience of the surgeons. In this context, a system designed to perform automated keratoplasty would represent a very attractive tool for ophthalmic surgery. It would completely define keratoplasty protocols according to the pathology of the cornea and would

provide postoperative evaluation facilities.
In the present chapter, the interaction mechanisms of femtosecond pulses with opaque tissue below the threshold for optical breakdown are first investigated. We chose to perform the experiments adopting an in situ *configuration and using the surgical laser. An* in situ *geometry is based on the detection of the emission propagating in the backward direction, which is possible when irradiating opaque tissue. Corneal edema are reproduced by letting the graft swell in a solution for a few days before the experiments. This modifies the highly ordered arrangement of collagen fibers ensuring the transparency of healthy corneas. As a consequence the tissue becomes scattering to different degrees.*
Using two different methods we determine the nature of the nonlinear backscattered emission produced when the laser beam is focused into the bulk of the cornea. The first method is the analysis of the signal spectrum. The second is the analysis of the dependance of the excitation laser intensity on the acquired signal intensity. The potential of the nonlinear emission from the tissue for imaging the cornea is further investigated.
We notice that, regardless of the laser application - in situ *imaging or surgery - such a system would still be limited by the extinction of the excitation source into the bulk of pathological corneas. It then becomes essential to evaluate the energy attenuation for optimized procedures and reduced side effects. We therefore propose a non-destructive method, based on the monitoring of the backscattered SHG for determining the laser penetration depth and we further use the measured value for performing dissections with the energy correction as function of the beam focusing depth. We finally evaluate the influence of optical aberrations on the precision of intraocular femtosecond and provide consideration about an optimal numerical apertures for surgery.*
The set-up used to perform the experiments presented below is described in chapter 4.

6.2 Identification of the nonlinear emission

When focusing a femtosecond laser beam into the cornea, at energies below the threshold for optical breakdown, a nonlinear emission can be generated. We analyze the signal detected in a backscattered configuration when exposing opaque corneal tissue at a 1.06 µm laser radiation. In a first step, we examine the spectrum of the backward emission. Secondly, we study the variation of the nonlinear emission when increasing the incident pulse energy.

6.2.1 Line spectrum of backward emission

We acquired the spectrum of the backscattered signal by focusing the laser beam with an achromat lens (Melles Griot, LAL013), at different depths into the cornea and an integrating time of 1000 ms. Figure 6.1 shows the spectrum which is typically obtained when the corneal tissue is exposed to the Nd:glass laser beam at a radiant exposure below the threshold for tissue disruption. The strong peak at around 1.06 μm corresponds to the laser line, while the peak at 530 nm matches the $\lambda/2$ condition, indicating that the nonlinear emission is represented by the second harmonic generation in the collagen matrix. The laser line corresponds to the residual transmission through the dichroic mirror and is visible because of the long integration time owing to the weakness of the backscattered SHG photons. During the experiments, this residual laser light is

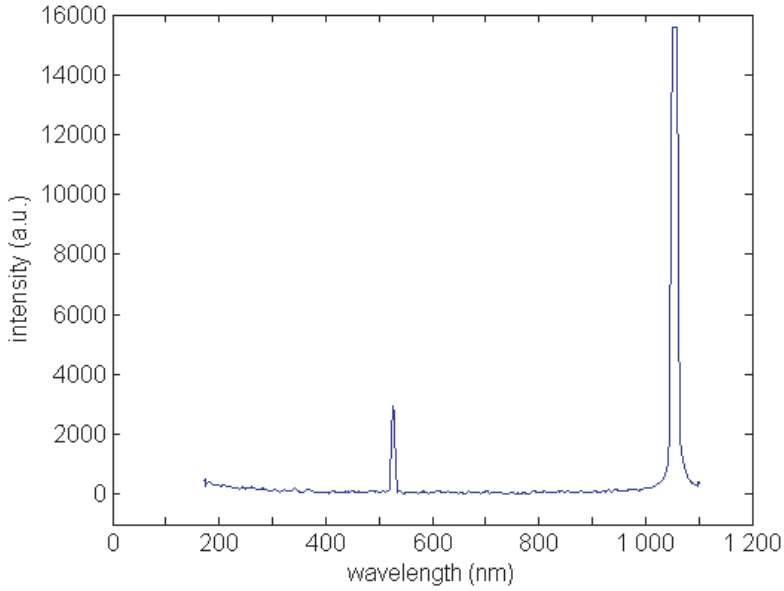

Figure 6.1: Spectrum of the backscattered optical signal emitted by human corneas when irradiated at 1.06 μm

filtered out by the spectral response of the photomultiplier coupled with appropriate bandpass filters.

Spectra were acquired at different locations in the tissue; only the intensity level was modified, notably when changing the depth of focus. This is explained considering that the corneas used for the experiments had lost their transparency following swelling *in vitro* and as a consequence

the laser energy was attenuated into the volume of the cornea. The latter phenomenon is shown in chapter 5.
No third harmonic generation (THG) signal could be observed, in contrast with findings reported by Guo *et al.* [37]. However, spectra measurements were performed in a transmission geometry and we believe that the backscattered configuration coupled to a weak conversion efficiency compared to SHG prevents detection of THG.
We remind that in chapter 4 we have calculated a SHG efficiency factor in the order of 10^{-4} with respect to our experimental system.

6.2.2 Dependance of the SHG on the incident light

For the purpose of investigating the SHG dependance on the laser intensity, we focused the laser beam with an achromat doublet (Melles Griot, LAL013) at a position in the cornea and gradually augmented the energy from 0 to 3 μJ. Backscattered photons were detected by the photomultiplier. Figure 6.2 displays the intensity of the nonlinear emission as a function of the incident beam power. The stars curve shows the total optical emission of the sample which is captured by the photomultiplier. Band pass filtering of the signal indicates that it is composed for the most part of the second harmonic, which follows a dependency of the square of the incoming power, resulting in a straight line in a double logarithmic plot. As the focus was kept stationary during the acquisition, the relation $I_{SH} \alpha I_{laser}^2$ is verified. At energies higher that 2 μJ, both of these signals diminish abruptly, indicating that the optical breakdown threshold is reached. According to Vogel *et al.* [116], no plasma emission exists in the wavelength range 300 nm$< \lambda <$900 nm, which corresponds to our spectral response window, when optical breakdown occurs into tissue at pulse duration in the femtosecond range. At the threshold, the temperature reached by the tissue at the focus volume is too low to produce plasma radiation in the 300-900 nm interval. Experiments on corneal tissue disruption, which have been presented in chapter 5, confirm that the threshold energy for plasma-induced ablation is 2.0 ± 0.2 μJ when using a $NA = 0.15$ achromat lens. This experimental value corresponds to radiant exposure of 3.3 J/cm^2. High pass filtered signal is represented by the residual laser light, traversing the dichroic mirror.
The signal was acquired at a fixed position in the cornea for the purpose of avoiding errors related to tissue inhomogeneities. Due to the integration time in the order of second, accumulation effects may occur. However, we checked that tissue did not suffer damage by verifying that

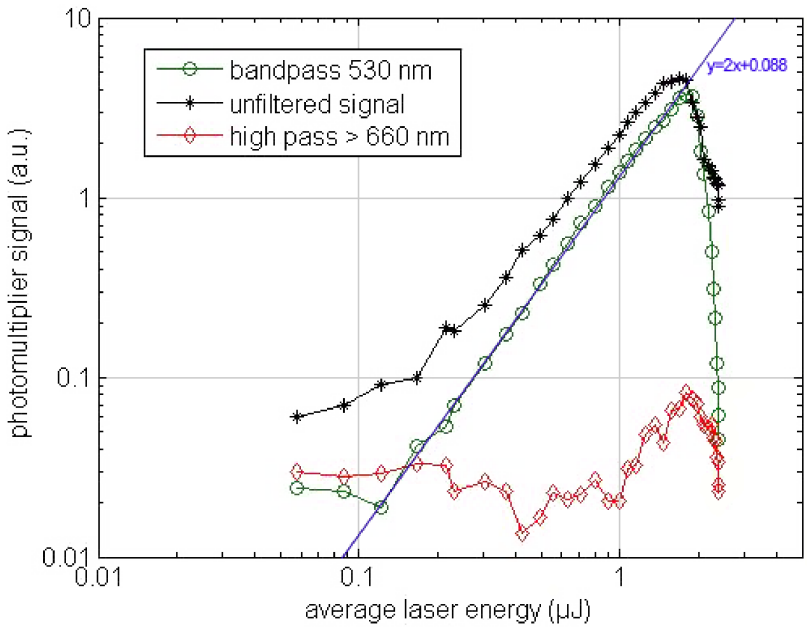

Figure 6.2: Intensity of optical emission versus average laser energy. The femtosecond laser stimulates second harmonic generation, which disappears when the region of optical breakdown is approached

two successive measures led to the same SHG measurement, meaning that tissue response was unaltered. In the case of possible chemical modification or disruption by optical breakdown, we would have obtained a decreased or modified signal.
The line spectrum of the backscattered emission shows that SHG occurs when corneal tissue is irradiated at 1.06 µm. This result is confirmed by the quadratic dependance of the detected nonlinear signal with the incident laser energy.

6.3 SHG imaging of cornea

In this section, the potentiality of SHG for imaging the cornea using the surgical laser system is evaluated. SH radiation is a priori *emitted in the forward direction, however the scattering properties of opaque tissue enable detecting signal in the backward direction for* in situ *experi-*

ments.

Images of the cornea were obtained with a microscope objective 20x, $NA = 0.5$ (Olympus, UP-LFL) by scanning the sample in the x-z plane (posterior-to-anterior plane), from the endothelium towards the epithelium at a fixed y-coordinate. Energies were set at half the measured experimental threshold to avoid optical breakdown. Figure 10.3 (left) shows a 2D image of a human cornea in the anterior-to-posterior plane, from the epithelium to the endothelium. Signal could be obtained throughout the depth of the sample, although the signal intensity decreased with increasing imaging depth due to the attenuation of the excitation beam. The principal anatomical

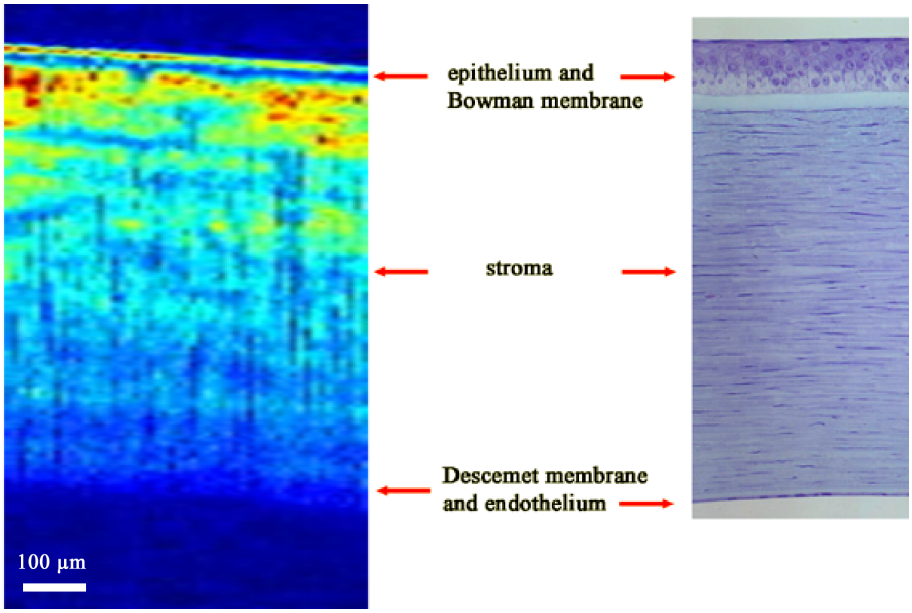

Figure 6.3: SHG image of a human cornea acquired *in situ* on the microsurgery experimental system. The main anatomy of the cornea is distinguished

structure of the cornea could be identified. One can notice that a dim stripe runs parallel to the lamellar plane, close to the surface. We believe that this effect is not an artifact, as it could be suppressed when expressly removing the epithelium before experiments, as illustrated in figure 6.4a. We reduced the laser spots separation from 4 μm to 2 μm in figure 6.4b. One can notice that no SH emission is generated from the epithelium, except from a superficial layer. This can be explained considering that the epithelium is mainly composed of cells rather than collagen, which is the main SHG source. Nevertheless, a weak SH signal is detected at the surface because the symmetry condition is broken. Bowman's and Descemet's membranes are not easily distinguished. The endothelium, which consists of one cell layer, is very difficult to preserve

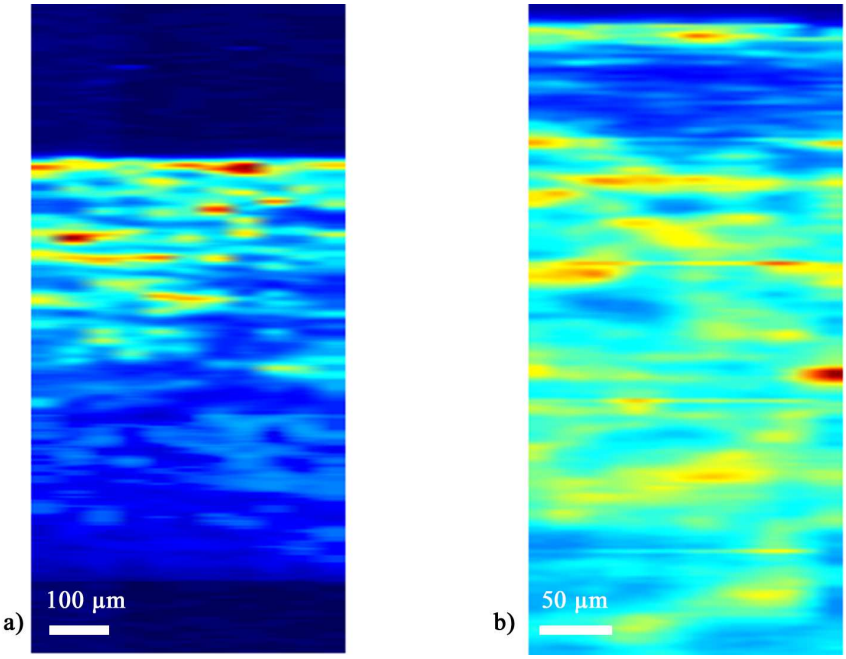

Figure 6.4: SHG image of a human cornea acquired *in situ* on the microsurgery experimental system before (b) and after (a) the removal of the epithelium

and has probably been removed during preparation.

Images also inform about the thickness of the cornea which amounts to 720 ± 30 μm, that is typical for less transparent corneas. The numerical value of the thickness was obtained by multiplying the difference between surface and rear surface positions by the projection factor of the focal volume into the cornea using a value of 1.37 for its refractive index.

Concerning the choice of the numerical aperture of the objective, the value of 0.5 proved to be optimal for generation and collection compared to other *NAs* available in our experiments. At moderate focusing and a constant radiant exposure, increasing the *NA* augments the collection solid angle. However, the focal volume is reduced and the number of nonlinear photons generated is decreased. Therefore, a compromise has to be found. At very high *NAs*, which are generally used for high resolution imaging, the collecting efficiency is even reduced. In this configuration, the excitation photons in the outer cone travel a longer distance and in turbid media probability for scattering is higher. Thus, fewer photons may be available for excitation [21, 84].

It has to be considered that, for our purpose, high resolution in not even required, as the main objective of SHG would be to assist for determining laser parameters for surgery and to pro-

vide a primary postoperative evaluation of the dissection rather than to produce high resolution images of the cornea. We believe that the main drawbacks of the system rather concern the data acquisition time and the attenuation of the excitation source when focused into the volume of opaque corneal tissue. Due to the 10 kHz repetition rate at which the laser operated and the backward detection configuration, a relatively weak SHG signal was captured. The SH emission was even weaker when generated by the posterior layers owing to attenuation. As a consequence, the signal had to be integrated for several minutes per image. The acquisition time could be dramatically decreased by using the laser beam emitted by the oscillator. At this point pulses are available at a repetition rate of 80 MHz, which would favor the SHG and permit to work in optimized laser conditions comparable to those found with many nonlinear microscopes. A second improvement would regard the correction of the attenuation related to the important working depths. In principle, a reduced radiant exposure can be compensated for by increasing the pulse energy sufficiently to ensure that the irradiance threshold for optical breakdown is reached in the volume of the cornea. However, at the intermediate numerical apertures of 0.3 - 0.5, typically used in clinical practice, pulse energies for optical breakdown correspond to peak powers of a few megawatts and are just below the critical energy for self-focusing, which may permanently damage the tissue as shown in chapter 5. To keep these effects at a low level, care has to be taken not to expose the tissue to too high energies. It is therefore necessary to evaluate the attenuation of the beam in the cornea prior to surgery in order to adjust the pulse energy to the depth of the treatment.
For the purpose of identifying the structure of the cornea, in situ *SHG imaging using the surgery laser set-up is possible. However, the system should be improved with respect to the data acquisition time and the laser beam excitation which occurs in opaque corneas.*

6.4 Evaluation of the laser beam attenuation

Attenuation of the radiant exposure in the tissue is chiefly attributed to scattering and spherical aberration:

- *edema and other irregularities which are present in the patient cornea broaden and attenuate the laser radiant exposure by light scattering;*
- *the greater working depth in the cornea combined with high numerical aperture focusing*

optics results in spherical aberrations which broaden the point spread function when focusing from air into the cornea as a medium with a higher refractive index;

- *irregularities of the corneal surface (for instance in case of keratoconus) are likely to cause additional optical aberrations resulting in a further broadening of the beam and a reduction of the radiant exposure.*

All the above mechanisms lead to larger spot sizes than would theoretically correspond to the numerical aperture of the focusing optics. This changes the irradiance distribution in the region of the beam focus and alters the breakdown threshold. As a consequence, laser precision is reduced and unwanted side effects are privileged.
We aim to evaluate the attenuation by measuring the laser penetration depth, as defined by the depth at which the irradiance drops to $1/e$ *of that delivered to the tissue surface. In a first step, we determine the laser penetration length by histology. We further propose a non-destructive method based on the acquisition of the backscattered second harmonic emission associated with the nonlinear optical properties of the tissue.*

6.4.1 Methods and results

Quantification of the laser beam attenuation by histology

For a systematic quantification of the laser beam attenuation, in a first step, the incisions length as a function of pulse energy was studied for the case of a typical edematous cornea. Dissections were induced using $NA = 0.15$ and pulse energies from 1 to 6 μJ in approximately 1 μJ steps. Figure 10.5a shows the histological section of the cornea after laser treatment. The laser incisions corresponding to the different energies are clearly visible and the incision length increases with increasing pulse energy. The relationship of maximum incision depth to pulse energy is plotted in figure 10.5b. As expected for the case of exponential attenuation of the beam, a logarithmic dependence of the incision length as a function of pulse energy is observed. A logarithmic regression yielded a $1/e$ penetration depth of 340 ± 30 μm for this particular cornea. This result should not be generalized: the penetration depth of the laser beam in edematous cornea varies considerably with the degree of the edema, from 200 μm to 480 μm, as measured in the following section. It is also slightly dependent on the position of the specimen.

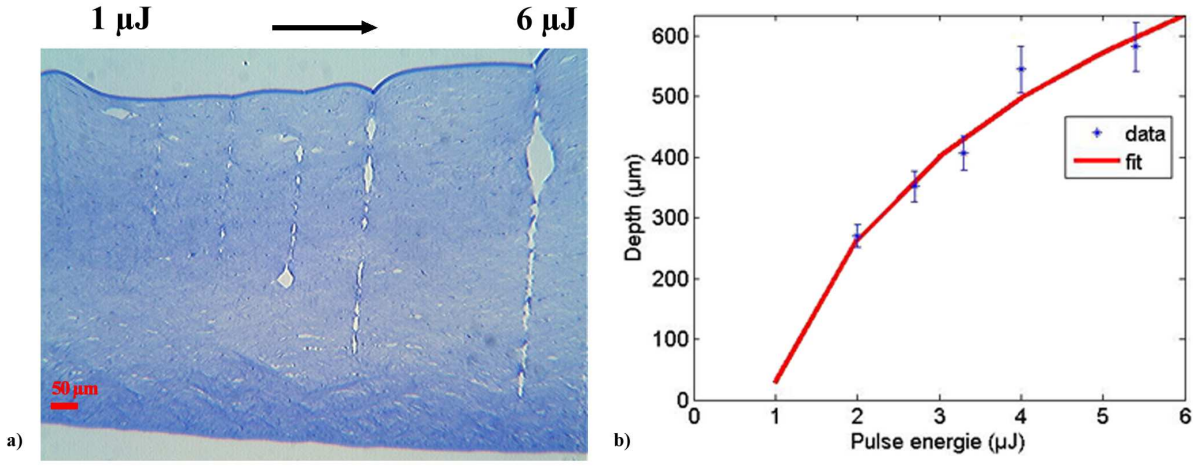

Figure 6.5: a) Histological section of laser incisions performed at energies of from 1 μJ to 6 μJ with a step of approximately 1 μJ at $NA = 0.15$; b) Penetration depth of the laser versus laser power. The red line represents the fitting curve expressed by $y = \ln(x/342\ \mu m)$

Non destructive optical evaluation of the laser beam attenuation by SHG detection

In order to evaluate the laser penetration depth *via* a non-destructive method, we monitored the backscattered SH emission, whose strength is proportional to the square of the incident radiant exposure. Experiments were performed at energies well below the threshold for optical breakdown. The focusing of the laser was achieved with a 20x objective, $NA = 0.5$ (Olympus, UPLFL), corresponding to a configuration used in clinical practice. The focal spot of the laser was scanned through the cornea in 10 μm steps along the optical axis from the endothelium towards the corneal surface while recording the generated second harmonic signal. The axial coordinates of the surface of the cornea were determined by measuring the position at which the peak in the SHG signal corresponding to the coverslip/cornea interface was observed. As corneas produced the SHG signal across their entire volume, their thickness was determined by measuring the position of the drop in the SHG signal at their rear surface, corrected by the projection factor of the focal volume into the cornea using a value of 1.37 for its refractive index.

Figure 10.2a presents a semi-logarithmic graph of the SH radiation versus the corneal depth typically obtained in our experiments. The signal is normalized with respect to the emission measured at the surface. At 100 ± 10 μm from the front and rear surfaces of the cornea, SHG

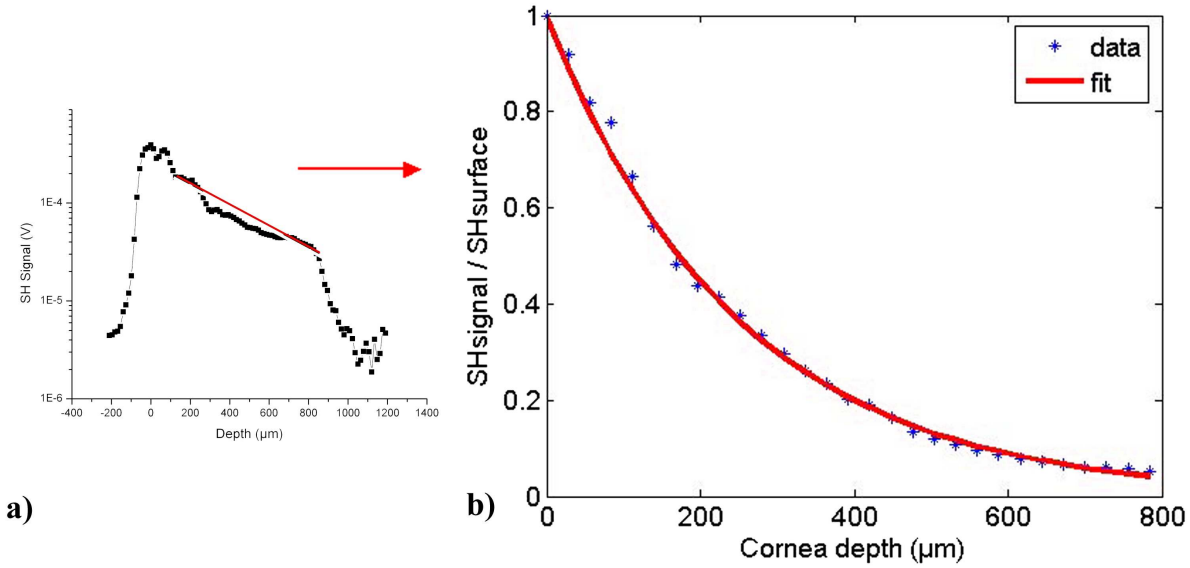

Figure 6.6: Attenuation of the backscattered SHG emission in an opaque cornea irradiated by a Nd:glass laser at a nondestructive energy in a logarithmic (a) and linear (b) representation

acquired from the endothelium towards the epithelium showed an approximately exponential attenuation when illuminating the sample at constant pulse energy below the ablation threshold, as shown in figure 10.2b. The variation of the SHG as a function of the depth coordinate z can be expressed by the relation

$$I_{SH} = [I_0 e^{-\frac{z}{l}}]^2 e^{-\mu z} \tag{6.1}$$

where I_0 is the incident laser intensity, l is the $1/e$ penetration depth of the laser in the cornea at the incident wavelength of 1.06 μm, and μ is the corneal attenuation coefficient for the frequency doubled light travelling back to the surface. In the present work, we assume the μ coefficient negligible and neglect the attenuation proper to the SHG light. We thereby assume that the exponential decrease of the SH emission as function of the depth is predominantly due to the attenuation or broadening of the point spread function. This approach relies on the assumption that in our backscattering geometry, multiply scattered SHG photons are detected on a large surface detector, the collective intensity of which does not depend much on the depth of the focal volume in the cornea where they are created. We also consider that the exponential behavior is valid far from the surface. By examining figure 10.2a, we notice when focusing close to the endothelium, the SH signal abruptly decreases since more photons are lost as they are created near the surface.

On a series of 10 corneas presenting edema of varying degree, measurements of the type illustrated in figure 10.2 were performed at different lateral coordinates. For a best fit of the exponential curve, we used a linear regression algorithm of the logarithm of the measured values from which we deduced the $1/e$ penetration lengths. Since pathological corneas are typically slightly inhomogeneous, the penetration depths may vary with the position on the cornea. By evaluating the SH emission at different positions it is possible to establish a 3D map of the local attenuation of the cornea. Figure 10.4 shows the attenuation of the SH signal in the volume of an individual cornea at different lateral coordinates. Due to important data acquisition time, we limited our measurements to 5 or 6 points per cornea. The average $1/e$ penetration lengths of

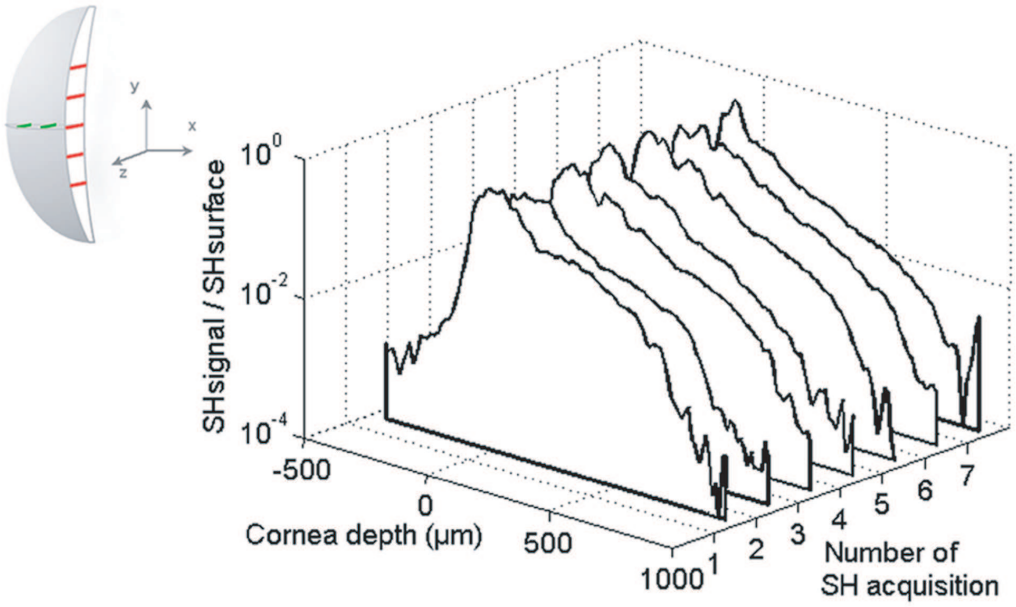

Figure 6.7: Attenuation of the backscattered SHG emission in the volume of an individual opaque cornea at different lateral coordinates

the entire group of edematous corneas tested are compiled in table 6.1. Depending on the degree of edema, the thickness of the corneas varied between 600 μm and 1100 μm and values between 200 μm and 470 μm were calculated for the laser penetration depths. The ratio of thickness to penetration depth varied from 1.8 for the weakly scattering cornea n^o 4 to 3.8 for the strongly scattering cornea n^o 2.

Cornea	1	2	3	4	5	6	7	8	9	10
Thickness (μm)	700	750	850	600	900	750	800	1100	1000	1000
Penetration length (μm)	205	210	299	313	326	337	359	381	388	476
Standard deviation (μm)	13	13	22	27	24	23	32	28	27	29

Table 6.1: Measure of the $1/e$ penetration depth of the laser in the volume of ten corneas

6.4.2 Discussion

An *a posteriori* histological analysis of corneal incisions obtained with varying pulse energies offers a straightforward but destructive means to quantify the laser beam penetration depth. To a good approximation, maximum incision depths showed logarithmic dependence on pulse energies. The corresponding Beer-Lambert exponential behavior for the laser energy and the calculated value of the beam penetration depth are consistent with the non-invasive attenuation measurements by second harmonic generation. Penetration depths between $l = 200$ μm and $l = 400$ μm could be measured in edematous cornea. We underline that the experimentally determined penetration depth l represents the combined effects of all processes contributing to radiant exposure reduction and we consider that

$$l \approx \frac{1}{\frac{1}{l_{sc}} + \frac{1}{l_{sa}}} \tag{6.2}$$

where l_{sc} and l_{sa} stand for the scattering and the spherical aberrations penetration depths, respectively. We therefore introduce the simplifying assumption that the irradiance decay with depth due to optical aberrations is associated to a penetration depth l_{sa} and follows an exponential decreasing behavior. From numerical calculations performed using an optical design program[1] it turned out that for the purpose of assessing the contributions of scattering and of focus enlargement by spherical aberrations to laser attenuation, our assumption is sufficient at $NA = 0.5$ (numerical simulations are presented in section 6.5). The irradiance reduction by spherical aberrations at a numerical aperture of 0.5 is roughly equivalent to the attenuation in an system presenting a $1/e$ optical penetration depth of 800 μm (this value is obtained using an exponential fit of the curves shown in section 6.5). By inserting into equation 10.2 the above experimental values, we estimate the penetration depth due to scattering and we obtain mini-

[1]ZEMAX EE, Optical Design Program, ZEMAX Development Corporation, 2007, USA

mal and maximal values of $l_{sc} \approx 270$ μm and $l_{sc} \approx 800$ μm. In the first case, optical scattering by the modified structure of the collagen matrix of the cornea is the most prominent process contributing to the attenuation of the radiant exposure. In the latter case, corneas can be considered weakly edematous and therefore relatively transparent; scattering and beam broadening due to spherical aberrations contribute equally. Corneas corresponding to even higher degrees of transparency did not produce sufficient backscattering to enable the determination of the optical penetration depth, which lets us believe that these corneas do not need a depth-dependent correction of the pulse energy for scattering at all.
In situ *monitoring of the backscattered nonlinear emission offers a nondestructive method for estimation of the laser energy attenuation. Assumptions made on the measurements of the SHG are supported by the quantitative evaluation of the source extinction by means of histological measurements. Further experiments determining the ratio of forward/backward propagating SHG may provide an additional verification of the method here proposed.*
The technique presented above would in principle allow constructing a 3D map of the optical properties of a cornea before keratoplasty; however, as in the case of the SHG imaging, the acquisition time should be reduced.

6.5 Correction of the laser beam attenuation

The values obtained for the laser penetration depth can be used to correct the energy reduction in the depth of opaque corneal tissue. However, simply increasing the beam energy during dissection procedures may not be sufficient to achieve incisions of good quality throughout the thickness of the cornea. Indeed, depending on the NA of the focusing units, spherical aberration may strongly contribute to the degradation of the beam into the volume of the tissue.
We therefore intend to elucidate the influence of the NA on spherical aberrations induced by great working depths.
Additional incisions are shown, performed with compensation of the energy attenuation based on the experimental and numerical results obtained for the penetration depth and the contribution of optical aberrations.

6.5.1 Methods and results

Correction for spherical aberrations

We performed numerical simulations using the ZEMAX software in order to evaluate the beam focus degradation ascribed to spherical aberrations at different *NAs* as a function of the focusing depth. Based upon geometric ray tracing, ZEMAX allows the analysis of modeled optical systems. In particular, we computed wavefront aberrations in order to determine the Strehl ratio. For our simple optical system consisting of optics focusing the beam into the cornea, the geometric approximation appears to be adequate. Design data for the doublet lens were available in the ZEMAX catalogue, while the microscope objectives were modelled by a paraxial element corresponding to their numerical aperture. Thereby, we assume that their point spread function is reasonably close to the diffraction limit. The cornea was simulated as an isotropic material with a refractive index of 1.37. The merit function was minimized by optimizing the wavefront at $\lambda = 1.06$ μm and the beam at the pupil entrance of the system was considered as a uniform illumination. The Strehl ratio in ZEMAX can be computed employing two approaches. The first technique consists in calculating the diffraction PSF (point spread function) and the Strehl ratio using the direct integration of "Huygens wavelets" method. A grid of rays is launched through the optical system and each ray represents a particular amplitude and phase wavelet. The diffraction intensity at any point of the image is given by the interference of all these wavelets radiated. The second method, which we call the RMS approach, uses the following relation

$$S = e^{-(2\pi\sigma)^2} \tag{6.3}$$

where σ is the RMS value of the wavefront error. Equation 6.3 represents an approximation which is only valid for Strehl ratios higher than about 0.10. This explains discrepancies that can be observed at low ratios when comparing values calculated with the two methods.
Figure 10.6 shows the Strehl ratio computed with the RMS approach as function of the focal plane depth into the sample. The $1/e$ penetration depths measured from the Strehl ratio curves, and peak to valley and RMS wavefront aberrations calculated with the Huygens method at a depth of 500 μm are presented in table 6.2. We point out that these values represent an evaluation and they underestimate the total aberration that the beam experiences during propagation since only the working depth is here considered and aberrations introduced by irregularities on the surface and local changes in the refractive index are not taken into account.

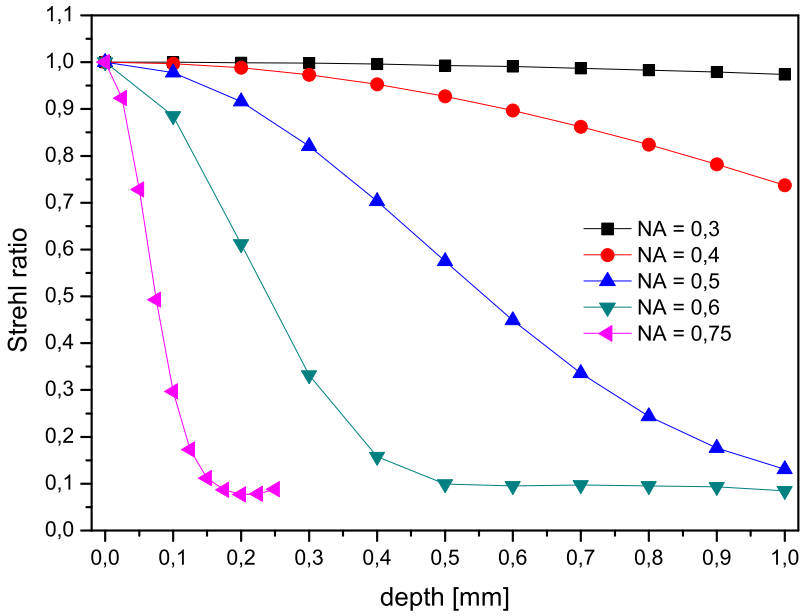

Figure 6.8: Variations of the the Strehl ratio at different numerical apertures as function of the focusing depth in a material with a refractive index of 1.37, modelling the cornea. Values are obtained using the RMS method

Numerical aperture	0.3	0.4	0.5	0.6	0.75
$1/e$ penetration depth (μm)	>1000	>1000	620	300	90
peak to valley wavefront aberration	0.048λ	0.164λ	0.450λ	1.088λ	3.776λ
RMS wavefront aberration	0.014λ	0.047λ	0.127λ	0.298λ	0.953λ

Table 6.2: $1/e$ penetration depths measured from the Strehl ratio curves, and peak to valley and RMS wavefront aberrations calculated at a depth of 500 μm as function of the *NAs*

One can immediately notice that for low numerical apertures spherical aberrations can be neglected. Considering a maximum thickness of about 1 mm for an edematous cornea, the contribution to the beam attenuation becomes significant for $NA > 0.5$.
In parallel, we performed additional experiments in which we used two microscope objectives specifically designed to correct spherical aberrations at a given focusing depth in the sample (Zeiss LD Plan-Neofluar 20x, $NA = 0.4$ and 40x, $NA = 0.6$). Fig 10.7a and 10.7b show incisions performed at $NA = 0.6$ and $NA = 0.4$, respectively, in a strongly edematous cornea. In both series of experiments, we used energies of four times the surface threshold. In table 6.3, the correction depth in the volume of the tissue and the yielded incision lengths are tabulated.

$NA = 0.6$				
correction depth (μm)	0	300	450	640
yielded incision length (μm)	250	295	320	220
$NA = 0.4$				
correction depth (μm)	0	200	400	600
yielded incision length (μm)	425	420	435	360

Table 6.3: Incision length obtained when focusing the beam into a cornea using microscope objectives with correction of spherical aberration at a given depth

When performing dissections at $NA = 0.6$, from comparing the second to the first incision we notice that correcting for an increased depth in the sample results in an increased incision length until a maximum depth. We believe that moving the corrected plane too far from the interaction region in scattering tissues as it has been done for the forth incision decreases the beam quality and the overall incision length is reduced. A similar tendency is observed at $NA = 0.4$ when correcting at a depth of 600 μm, whereas changing the correction length between the surface and 400 μm does not change significantly the quality of the beam. These findings confirm that spherical aberrations play a relevant role for large *NAs*. We obtained comparable results on a series of three corneas.
Experimental results were supported by a numerical simulation in which we estimate the maximum incision length as function of the Strehl ratio and the penetration depth. As stated above, we suppose that the extinction of the radiant exposure follows an exponential decay for both scattering and spherical aberrations according to

$$I(z) \approx I_0 e^{-\frac{z}{l}} = I_0 e^{-\left(\frac{1}{l_{sc}}+\frac{1}{l_{sa}}\right)z} \quad . \tag{6.4}$$

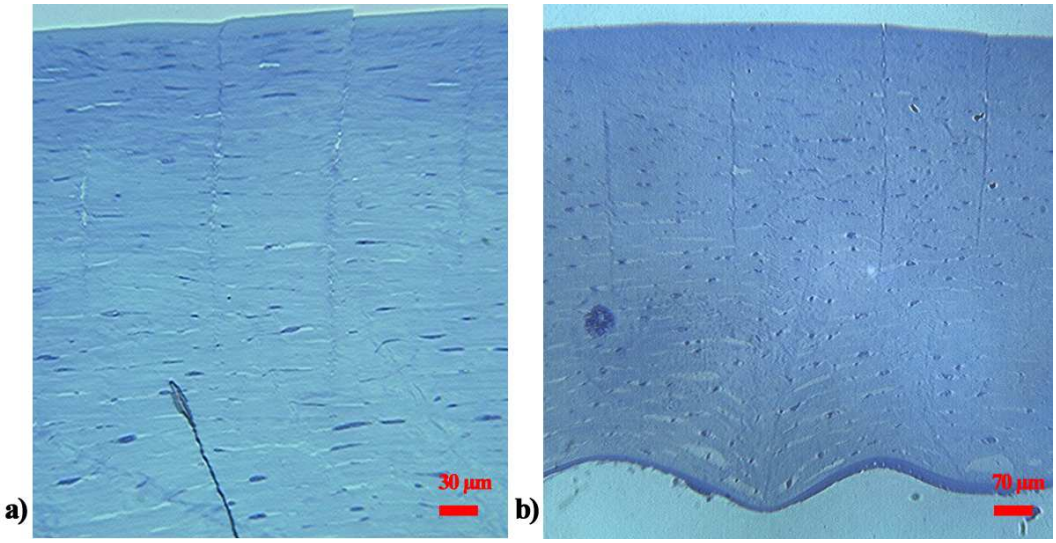

Figure 6.9: Histological section of laser incisions in an edematous cornea performed at $NA = 0.6$ (a) and $NA = 0.4$ (b) with correction of spherical aberrations at depths of 0, 300 μm, 450 μm, and 640 μm and 0, 200 μm, 400 μm, and 600 μm respectively (from left to right)

If we define z_0 the correction length of the objective, we obtain for the radiant exposure the relation

$$I(z) \approx I_0 e^{-\frac{z}{l_{sc}} - \frac{|z-z_0|}{l_{sa}}} \quad . \tag{6.5}$$

The optical breakdown occurs if the radiant exposure is slightly higher than the threshold I_{th}, which is expressed by

$$I_0 e^{-\frac{z}{l_{sc}} - \frac{|z-z_0|}{l_{sa}}} > I_{th} \tag{6.6}$$

or

$$\frac{z}{l_{sc}} + \frac{|\, z - z_0 \,|}{l_{sa}} < ln\left(\frac{I_0}{I_{th}}\right) \quad . \tag{6.7}$$

By suppressing the absolute value, we obtain

$$\begin{cases} z < z_0, & \dfrac{z}{l_{sc}} + \dfrac{z-z_0}{l_{sa}} < ln\left(\dfrac{I_0}{I_{th}}\right) \\ z > z_0, & \dfrac{z}{l_{sc}} - \dfrac{z-z_0}{l_{sa}} < ln\left(\dfrac{I_0}{I_{th}}\right) \end{cases} \tag{6.8}$$

and finally

$$\begin{cases} z < z_0, \quad z < \dfrac{ln\left(\dfrac{I_0}{I_{th}}\right) l_{sa} + z_0}{\left(\dfrac{l_{sa}}{l_{sc}} + 1\right)} \\ z > z_0, \quad z < \dfrac{ln\left(\dfrac{I_0}{I_{th}}\right) l_{sa} - z_0}{\left(\dfrac{l_{sa}}{l_{sc}} + 1\right)} \end{cases} . \tag{6.9}$$

In relation 10.7 many parameters can be varied and we have chosen to represent the spherical aberration penetration depth as function of the correction length. We consider two scenarios:

- we fixe $l_{sc} = 350$ μm and we plot a beam of line varying the spherical penetration depth l_{sa} from 300 to 700 μm with 100 μm intervals (figure 10.8);
- we fixe $l_{sa} = 500$ μm and we plot a beam of line varying the scattering penetration depth l_{sc} from 250 to 450 μm with 100 μm intervals (figure 10.9).

The experimental values are also reported on plots in figures 10.8 and 10.9. The stars correspond to one cornea; the circles represent an average value from two other corneas. The graphs have to be interpreted taking into account the following considerations:

- data are plotted for $I_0/I_{th} = 4$, as was the case in the experiments;
- the correction lengths have been multiplied by a factor $n_{glass}/n_{cornea} = 1.45/1.37 = 1.06$ as objectives are optimized for correction into glass;
- the maximum depth that can be corrected with respect to the the spherical aberrations is on the line $z = z_{max} = z_0$ (otherwise we would be able to correct for a higher depth in order to cut further into the cornea);
- the value of l_{sc} at $z = z_{max} = z_0$ can be deduced from equation 10.3;
- at $NA = 0.5$, from ZEMAX calculation we find $l_{sa} = 300$ μm. However, in figure 10.9 we have represented data for a higher value of l_{sa}. Experiments suggested that the maximum Strehl ratio of this particular objective is lower than one, therefore we consider that the point spread function degradation is less pronounced;

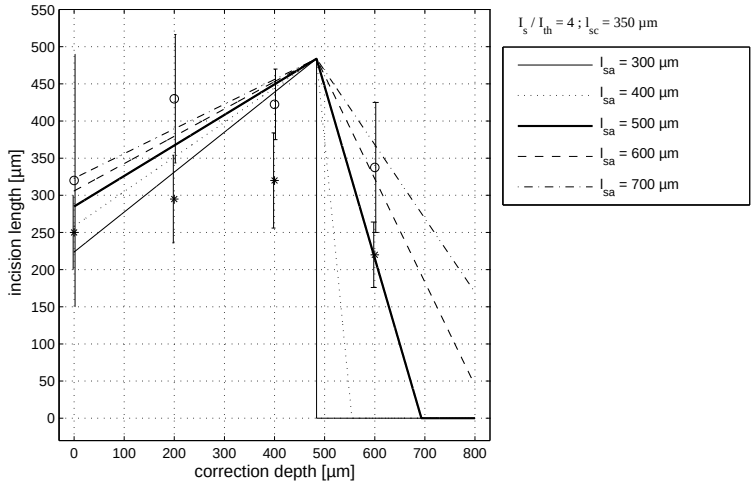

Figure 6.10: Maximum incision length as function of the correction depth adjusted on the microscope objective, with $l_{sc} = 350\ \mu$m and l_{sa} varying from 300 to 700 μm. The stars correspond to experimental values from one cornea; the circles represent an experimental average value from two other corneas

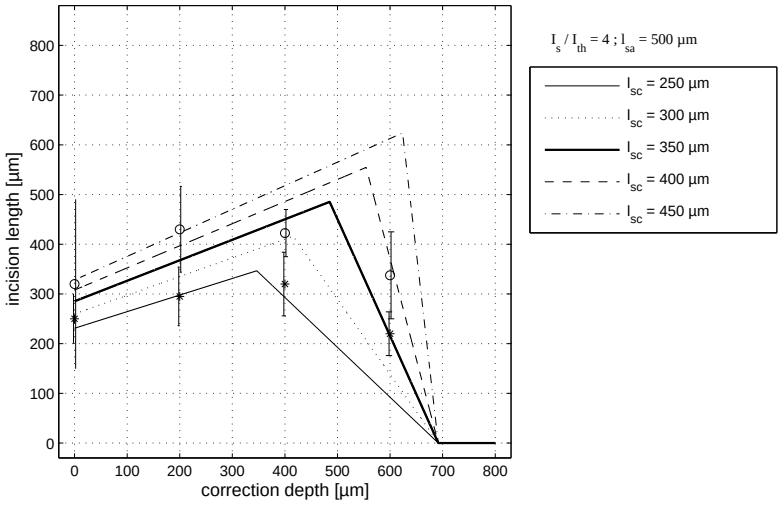

Figure 6.11: Maximum incision length as function of the correction depth adjusted on the microscope objective, with $l_{sa} = 500\ \mu$m and l_{sc} varying from 250 to 450 μm. The stars correspond to experimental values from one cornea; the circles represent an experimental average value from two other corneas

- $l_{sc} = 350\ \mu$m represents well an edematous cornea.

By analyzing figures 10.8 and 10.9, we notice that:

- at a given value of l_{sc}, l_{sa}, and I_0/I_{th}, a maximum correction depth can be determined. Correcting further does not increase the maximum incision length. This finding is in agreement with experimental results;
- this tendency is enhanced when $l_{sa} < l_{sc}$. The variation of l_{sa} does not influence the maximum incision length;
- at a fixed value of l_{sa}, the maximum incision length obviously increases with increasing l_{sc}.

Compensating for the laser beam attenuation

By using the *in situ* SHG monitoring as presented in the above section, we measured a penetration depth of $350 \pm 20\ \mu$m for a pathological cornea and we performed an incision in the sample by increasing the energy according to

$$E = E_{th} e^{\frac{z}{350\mu m}} \tag{6.10}$$

where E_{th} is the energy threshold at the surface. We used the achromatic doublet lens (Melles Griot, LAL013) at $\lambda = 1.06\ \mu$m. Pulse energies varied from 2 μJ at the surface to about 5 μJ in the volume corresponding to the maximum pulse energy available which was reached at a depth of about 320 μm. Even though nonlinear side effects are reduced and precision is enhanced at high numerical apertures, we induced laser dissections at $NA = 0.15$ for minimizing spherical aberrations, according to the above findings. From figure 10.10, it can be noticed that no unwanted side effects are visible in vicinity of the incision in the anterior stroma and that the incision is of uniform quality (except for a slightly extended ablation zone at the surface of the cornea). However, the maximal available energy in this particular experimental configuration limited the incision depth to about half of the cornea. It can in fact easily be calculated from relation 10.8 that for a cornea 800 μm thick, a transfixing incision would have required about ten times the energy corresponding to the threshold at the surface.

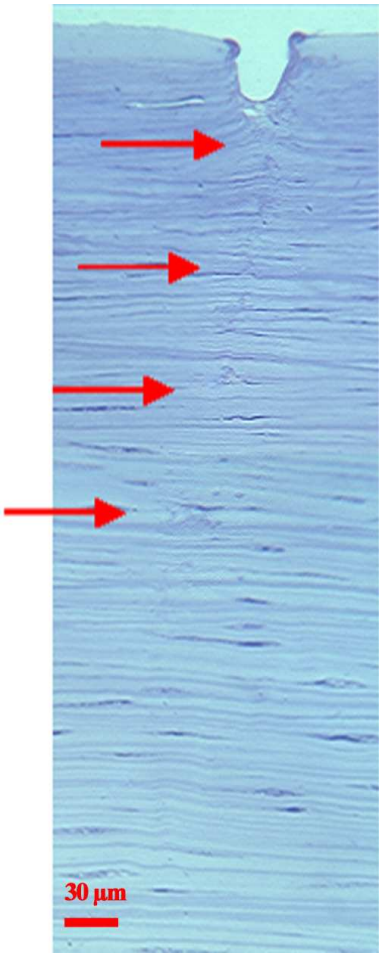

Figure 6.12: Incision in the anterior and middle stroma performed with $NA = 0.15$ and laser pulse energies varying from 2 μJ to 5 μJ

6.5.2 Discussion

We were able to demonstrate that laser dissection performed with energy correction in the volume of pathological cornea showed uniform good quality throughout the depth of the incision. The bowl-like shaped incision at the surface is probably due to an occasional increase of the pulse duration compared to optimal conditions. At this timescale, the ablation process at the surface is characterized by the production of an ablation plume consisting of water vapor and gaseous organic materials as well as water droplets and tissue fragments which are ejected outside the ablated tissue, leaving a lack of material [32, 118]. The cornea presented a penetration depth of about 350 μm. Because of the limited energy available in our set-up, incisions with correction were not transfixing. In experiments shown in section 6.4, we measured penetration depth well above 350 μm. Then, for strongly edematous corneas the energy necessary to induce perforating cuts can reach considerable levels and even standard clinical femtosecond laser systems are limited to low energies pulses. Moreover, when inducing tissue disruption at high numerical apertures, further beam broaden occurs due to optical aberrations. By performing experiments with correction for spherical aberration at a fixed depth, we have shown that aberrations can be corrected until a maximum optimal depth. This last can be lower than the total thickness of the cornea in strongly edematous tissue, in which the scattering contribution to the attenuation is significative. We have seen that the influence of the spherical aberration depends highly on the *NA* of the focusing optics and the question may arise what the "optimal" numerical aperture for femtosecond corneal surgery in the entire volume of the cornea should be. We have already observed, in the previous chapter, that intermediate numerical apertures allow considerably reducing the pulse energy compared to low apertures while improving the quality of the incision. Low numerical apertures ($NA < 0.3$) are not advisable for other reasons as well: for very strongly scattering tissue (sclera, skin, very strongly opacified cornea), the superficial radiant exposure may even be higher than in the focal plane, despite focusing into the bulk of the tissue. What high numerical apertures are concerned, an upper limit is more difficult to give. Focusing tightly ($NA \geq 0.75$) enables to reduce pulse energies to the nJ range. However, in this configuration small cavitation bubbles are created and laser repetition rates in the MHz range are required to avoid prohibitive durations of the clinical procedure. Drawbacks related to the use of very high numerical apertures are the need of well correcting for spherical aberrations by using adaptive optics and/or working in immersion, which might be arduous in clinical practice. Furthermore, the small field of view does not permit to use a beam scanning system for the entire surface of the cornea and does not allow a visual control of the operation

by the surgeon. Objectives without immersion typically reach maximum numerical apertures of $NA = 0.75$. At these high values, the influence of spherical aberration in the volume of the cornea is strong, the field of view is limited, the working distance is generally small and they are therefore not adapted for a use in surgery. Depending on the requirements of the actual system a compromise between small pulse energy, side effect reduction, bubble size, field of view, working distance and other constraints will have to be made. "Optimal" numerical apertures for a use in clinical practice will therefore probably lie in the range of $NA = 0.4$ to 0.6.

When performing perforating incisions in corneal tissue, the laser beam is focused at depths up to 800 µm, which corresponds to the thickness of a strongly edematous cornea. This may cause beam broadening due to spherical aberrations. In this section we have shown that spherical aberrations have to be taken into account when focusing at $NA > 0.5$. *Experiments performed with microscope objectives specifically designed to correct spherical aberrations at a given focusing depth confirmed this finding. They showed that the maximum incision length did not depend on the correction depth at* $NA = 0.4$. *On the contrary, at* $NA = 0.6$ *we could increase the incision length until a maximum value. However, this was obtained for an intermediate correction depth. In fact, at very high values of the correction depth, the incision length was decreased. Numerical computations, in which we studied the dependence of the incision length with the correction depth, the scattering and spherical aberration penetration depths, confirmed this tendency.*

Finally, when performing dissection with an increased energy accordingly to the penetration depth measured by SHG monitoring, an incision of good quality throughout the thickness of the cornea was obtained. However, the incision was not perforating due to the limited energy available on the laser system.

We deduce that compensation for the laser beam attenuation and correction of beam broadening for effective laser dissection in pathological cornea require important technological improvements.

Conclusion and outlook

This dissertation investigates laser-cornea interaction mechanisms in the femtosecond regime with respect to the use of femtosecond lasers system in keratoplasty. We have performed a series of experiments evaluating the performance and possible limitations of current systems and we have studied in detail different types of side effects which may occur. We have experimentally demonstrated an in situ *second harmonic diagnostic to determine the penetration depth of the incising laser beam in opaque cornea. In combination with numerical simulations this permitted us to quantify the contribution of scattering processes and optical aberrations to the interaction and to outline strategies for compensating these effects in view of optimal surgical results.*
Future work will focus on the minimization of losses in edematous tissue by local optimization (across the surgical area of interest) based on the second harmonic yield at desired surgical depths as well as aberration compensation and new laser technology.

Corneal transplant involves the replacement of a pathological opaque cornea by a healthy transparent cornea. Disruption of transparent tissue by femtosecond pulses has been investigated and applied to corneal surgery over the last two decades, and present-day clinical femtosecond laser systems work successfully in cutting (clear and healthy) donor corneas. The case of diseased, opaque corneal tissue presents challenges still unaddressed by existing systems due to its optical modifications. In the framework of the present thesis, a flexible experimental platform for femtosecond laser surgery has been developed permitting the modification of laser parameters and focusing optics as well as the detection of nonlinear emission created in the specimen by the surgical laser. In parallel, experiments were conducted on a clinical laser system for comparison. The experiments were exclusively performed on human cornea obtained under permission from the *Banque Française des Yeux* (French Eye Bank), for research purpose.

I briefly recall the issues I have addressed in the present work and the results we have obtained:

- in clear corneas, a determined constant energy produces an incision of good quality throughout the volume. In contrary, in pathological corneas the laser beam fluence attenuates depending on the transparency of the cornea. We have shown that in many cases, keratoplasty performed at a constant energy results in an incomplete cut in the posterior layers of the cornea or excessive tissue disruption in the anterior layers;

- when performing lamellar dissections (in the plane parallel to the corneal surface), as in the case of posterior lamellar keratoplasty, at energies higher than the optical breakdown threshold, our initial experiments showed streaks in the tissue above and below the lamellar incision along the axis of the laser propagation. This phenomenon was obtained at different numerical apertures and laser wavelengths. Analysis of tissue sections by transmission electron microscopy (TEM) revealed a repeating structure corresponding to dark staining and/or disrupted collagen fibers. The period of the structure had sub-wavelength dimension. Complementary numerical simulations allowed quantifying the plasma density created in the focal volume at the threshold irradiance for optical breakdown and the dependence of the threshold on numerical aperture. However, the exact cause of the observed periodic structure remains to be determined;

- independently of the laser system used, clinical or experimental, histological and ultrastructural investigation of the tissue revealed the presence of solid particles on the epithelium and in the anterior stroma when the cornea underwent penetrating surgery. The electron energy loss spectroscopy technique (EELS) revealed their composition as SiO_2. These particles originate from the applanation lens (or cover lens in the laboratory experiments) used to secure and flatten the cornea, and the track of the particles corresponds to the laser cutting path. Adjusting the laser parameters to minimize the cut safety margin or an alternative technological solution could address this problem.

The above observations emphasize the importance of operating at correct laser intensities. Operation in the opaque cornea presents a particular difficulty in this respect since the diseased collagen causes scattering and aberrations yet current systems fail to qualify these losses. Additional aberrations are produced by irregularities on the corneal surface. Currently one relies on

surgical judgment in selecting the laser energy for these cases. This involves the risk of using excessive energies in order to ensure a clean cut.

In this work, we have described a method to quantify the attenuation. When exposing the cornea to infrared radiation of intensities well below the damage threshold, second harmonic generation occurs. This nonlinear optical phenomenon scales as the square of the incident laser energy. Therefore, by *in situ* monitoring of the backscattered frequency-doubled light, one obtains the $1/e$ penetration length of the laser beam in the pathological tissue. In addition to presenting a nondestructive and easily measurable diagnostic, this approach has the added benefit of utilizing the surgical laser (at reduced intensity) for the measurement. Depending on the degree of edema, we found penetration depths ranging between 200 and 470 μm, which compares to a thickness range from about 550 μm (for healthy corneas) to more than one millimeter (for strongly edematous cornea).
While the attenuation is mostly due to optical scattering, part of it can be avoided by correcting for spherical aberrations. When not working with immersion liquids - an approach generally not considered practical in the case of a surgical laser - they depend strongly on the numerical aperture of the focusing units and the working depth. We experimentally and numerically quantified the influence of spherical aberrations as a function of the depth and proved that they are significant for $NA \geq 0.5$. Using microscope objectives specifically designed to correct spherical aberration at a given depth we have determined the maximum penetration depth, which can be reached using this correction. Based on our current results we suggest a numerical aperture between 0.4 and 0.6 as optimal for corneal surgery. This range represents a good compromise between cutting accuracy, reduced side effects and spherical aberrations, and ergonomics in clinical procedures.
Based on the measured value of penetration depths and the considerations with respect to aberrations, we could produce a uniform, high-quality incision at $NA = 0.15$ by adapting the energy to the depth of the treatment. However, for strongly scattering corneas the typical energy in current systems prevents transfixation, or complete penetration.

The work detailed in this thesis as well as known characteristics of the interaction suggest improvements of existing clinical systems:

- it is assessed from the literature that scattering phenomena in pathological corneal tissue scales as $1/\lambda^2$. Therefore, scattering can be dramatically reduced using a laser centered

at a wavelength higher than 1.06 μm, typical for clinical systems;

- optical aberrations can be quantified by *in situ* monitoring nonlinear optical emission and corrected by using adaptive optics.

The implementation of these improvements will be pursued at Laboratoire d'Optique Appliquée by the group *Optique - Photonique - Santé*. Specifically, work will transition to a femtosecond laser with a central wavelength at about 1.6 μm, for which scattering effects are strongly reduced and pathological corneas show enhanced transparency. Additionally, a deformable mirror will correct wavefront aberrations due to inhomogeneities of the cornea. The amount of the correction will be determined using a genetic algorithm to optimize the backscattered second-harmonic signal generated by the surgical laser and consequently will be adapted to the incision depth and sample properties quantified *in situ*.

RÉSUMÉ EN FRANÇAIS

Résumé

L'objectif du doctorat a été d'étudier l'interaction laser avec le tissu cornéen en régime femtoseconde et de déterminer les conditions optimales d'utilisation des lasers à impulsions ultracourtes pour la greffe de cornées pathologiques (kératoplastie). Il s'agit de la première thèse effectuée sur ce sujet au Laboratoire d'Optique Appliquée (École Polytechnique, ENSTA, CNRS, Palaiseau) et elle s'est déroulée en collaboration étroite avec le Laboratoire Biotechnologie et Œil (Université Paris Descartes, Hôpital Hôtel Dieu de Paris).
Environ 100.000 greffes sont réalisées par an dans le monde. La première cause de greffe de cornée est l'œdème, pathologie due à un disfonctionnement cellulaire ; le tissu devient perméable et perd ses propriétés de transparence. Le degré d'œdème progresse vite et, si non interrompu par une greffe, entraîne une opacification totale de la cornée et une baisse drastique de l'acuité visuelle. Les techniques traditionnelles chirurgicales de kératoplastie pratiquées par des instruments mécaniques présentent des complications post-opératoires, ainsi qu'un risque de rejet élevé ou un risque d'échec car elles sont délicates et difficiles et la technologie des lasers femtoseconde représente la seule alternative intéressante en remplacement des ces méthodes. Des systèmes à but clinique sont déjà présents sur le marché, cependant leurs performances sont réduites dans le cas du traitement de cornées fortement pathologiques, à cause d'effets optiques réduisant la qualité du faisceau laser au point d'interaction avec le tissu.
De nature parfaitement interdisciplinaire, ces travaux de recherche ont permis d'établir un bilan très complet du potentiel et des limites de l'application de la technologie laser actuelle à la greffe de cornées pathologiques. Ils ont apporté des solutions d'optimisation de l'interaction laser-tissu et ont ouvert la voie au développement d'une technologie future plus performante.
Ce projet de recherche a été recompensé par le Prix 2007 de la Fondation Dalloz de l'Institut de France et par le Prix "La Recherche" 2008.

Introduction

Contexte scientifique

Ces dernières années, le laser femtoseconde est devenu un outil chirurgical de plus en plus courant dans le domaine de la chirurgie cornéenne et tout particulièrement du LASIK (*laser in situ keratomileusis*). Il s'agit d'une méthode de chirurgie réfractive qui corrige les erreurs de focalisation et d'autres aberrations dans l'œil et qui comporte la découpe d'un volet cornéen superficiel. Les microkératomes mécaniques traditionnellement utilisés dans cette étape de découpe sont aujourd'hui largement remplacés par les lasers femtoseconde qui assurent une meilleure précision et fiabilité et réduisent les complications postopératoires grâce aux mécanismes particuliers de l'interaction laser-tissu dans le cas des impulsions ultra-brèves. Ainsi, malgré son coût, cette technologie s'impose progressivement en clinique. Récemment, les applications du laser femtoseconde en ophtalmologie se sont élargies à la greffe de cornée. Les indications de greffe comportent souvent l'opacification du tissu et aujourd'hui environ 100 000 greffes par an sont pratiquées dans le monde. Différentes techniques de greffe ou kératoplastie existent et elles se séparent en kératoplastie pénétrante de pleine épaisseur et kératoplastie partielle. Dans le premier cas, un disque de cornée dans toute son épaisseur est remplacé. Il s'agit de la technique la plus courante car la plus facile. Cependant, le risque de rejet est élevé, le greffon est anesthésié par dénervation des couches antérieures du tissu sur 360^o et des aberrations optiques importantes sont introduites dûes aux sutures et aux imperfections de découpe réduisant la correspondance entre le greffon du donneur et le lit du receveur. L'ampleur de ces problèmes est en partie réduite avec les techniques qui prévoient un remplacement partiel de couches postérieures de la cornée. De par leur technicité, ces chirurgies présentent un risque d'échec important même quand elles sont pratiquées par des chirurgiens expérimentés. L'utilisation d'un laser femtoseconde en remplacement des techniques manuelles permet le contrôle du diamètre, du centrage

et de la géométrie des greffons avec une meilleure adéquation entre le donneur et le receveur et il assure une découpe avec résolution et précision micrométriques. Les lasers femtoseconde actuels sont très performants dans la découpe de cornées saines mais se heurtent à plusieurs limitations techniques lorsque le tissu cornéen est pathologique. Par conséquent, la qualité de la découpe décroît rapidement. Ce phénomène est principalement dû au fait que des œdèmes et autres défauts présents dans la cornée engendrent une forte diffusion (et donc atténuation) du faisceau laser. De plus, la plus grande profondeur de l'intervention par rapport à la chirurgie réfractive favorise l'élargissement de la fonction d'appareil du fait des aberrations notamment sphériques et autres déformations du faisceau. L'apparition d'effets secondaires limite la compensation de cette baisse d'intensité par une simple augmentation de l'énergie. C'est la raison pour laquelle la greffe de la cornée ne rentre pas encore dans le cadre classique des applications des lasers femtoseconde. Les limites des systèmes actuels peuvent néanmoins être contournées par des solutions technologiques "sur mesure".

Objectif

L'objectif de mon travail de thèse a été de déterminer les conditions optimales d'utilisation des lasers femtoseconde pour la greffe de cornées pathologiques. Les principales étapes du projet ont été :

- le développement d'une plateforme expérimentale de chirurgie cornéenne par laser femtoseconde ;
- l'étude des mécanismes d'interaction du laser avec le tissu cornéen sain et pathologique en régime femtoseconde, afin d'identifier la nature et l'ampleur d'effets secondaires en fonction des paramètres laser ;
- le développement et l'implémentation d'une méthode de mesure optique *in situ* ;
- la détermination des paramètres optimaux, l'étude et la quantification des propriétés optiques du tissu pathologique et leur influence sur la dégradation du faisceau laser, la qualité et la reproductibilité de l'intervention chirurgicale ;
- l'élaboration de stratégies d'adaptation des paramètres laser au tissu.

Il s'agit de la première thése réalisée sur ce sujet au Laboratoire d'Optique Appliquée et elle a été effectuée en collaboration avec le Laboratoire Biotechnologie et Œil[2].

Plan

Le manuscrit se compose de quatre chapitres.
Dans le premier chapitre, j'introduis les notions pour comprendre les processus d'intéraction du laser avec la cornée, en régime femtoseconde. L'anatomie de la cornée et la technique des lasers à impulsions ultracourtes sont aussi présentées.
Le deuxième chapitre porte sur le développement et la caractérisation du dispositif expérimental.
Dans le troisième chapitre, je présente notre étude sur l'intéraction laser-cornée en fonction de différents paramètres. En effectuant des expériences sur des cornées de la *Banque Française des Yeux*, utilisées à but scientifique car non aptes à la greffe, nous montrons qu'une utilisation inappropriée de l'énergie lors de la découpe peut entrainer des effets secondaires.
Dans le quatrième chapitre, j'expose une méthode non-destructive de quantification des proprietés optiques des cornées pathologiques, basée sur la génération de seconde harmonique. La contribution des aberrations sphériques dans l'atténuation de la densité d'énergie dans les cornées opaques est aussi estimée. Pour finir, des incisions optimisées relativement à notre dispositif et effectuées dans un tissu pathologique sont présentées.
Les conclusions contiennent un résumé de l'étude, ainsi que des perspectives de travail.

[2]Université Paris Descartes, EA 4063, Hospital Hôtel Dieu, 1 place du parvis Notre Dame, 75181 Paris cedex 4, France

Chapter 7

Notions théoriques

7.1 La cornée

7.1.1 Anatomie

La cornée est la couche la plus extérieure de l'œil. Elle a un rôle de protection et constitue le premier élément réfractif de l'œil, comptant pour les 2/3 du dioptre oculaire. Elle mesure en moyenne, chez l'adulte, 11 mm de diamètre et son épaisseur diminue de la périphérie (environs 600 μm) vers le centre (environs 500 μm). La cornée est composée de plusieurs couches (figure 7.1) [35, 81] :

- l'épithélium, qui est formé de 5 à 7 couches de cellules. Il a un rôle de barrière et facilite la dispersion du film de larme à la surface de la cornée ;
- la membrane de Bowman. C'est une couche acellulaire de 8 à 14 μm d'épaisseur séparant l'épithélium du stroma. Elle est constituée de fibres de collagène réparties de façon non ordonnée dans une matrice de substance fondamentale. Cette membrane aurait un rôle d'échange des substances nutritionnelles, d'imperméabilité et de structure de soutien. Elle permettrait le caractère sphérique parfait de l'épithélium et l'ancrage de l'épithélium sur le stroma ;

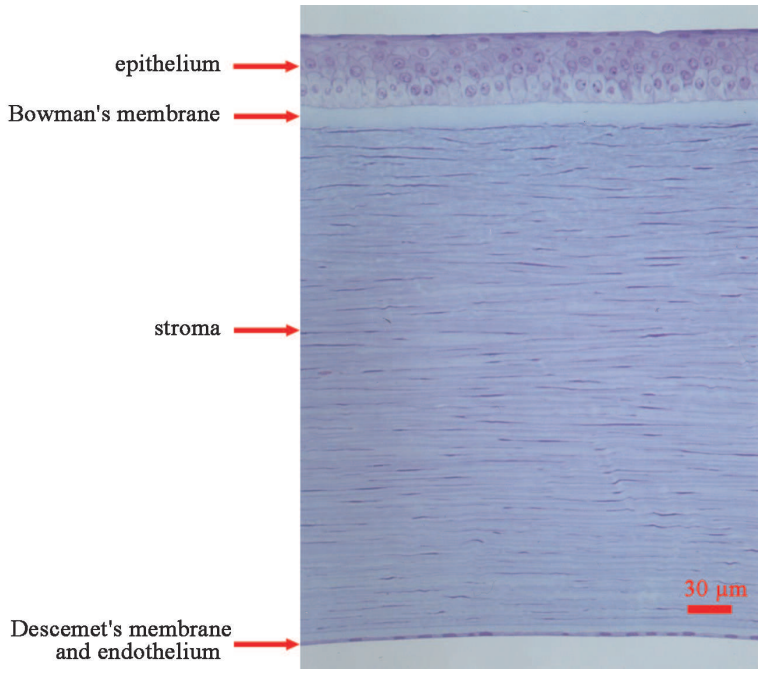

Figure 7.1: Section histologique d'une cornée humaine [Michèle Savoldelli, Hôpital Hôtel Dieu de Paris]

- le stroma cornéen, qui représente 90 % de l'épaisseur de la cornée. Il est constitué d'une matrice extracellulaire parsemée de cellules, les kératocytes, responsables de la sécrétion de la substance fondamentale. Les kératocytes ont une forme plate et sont disposés de façon parallèle aux lamelles de collagène. Ces dernières sont au nombre de 200 à 250, parfaitement empilées les unes sur les autres, et parallèles à la surface. Chaque lamelle mesure environ 2 μm d'épaisseur. Leur orientation est de préférence selon les directions inférieure-supérieure et nasale-temporale. Les lamelles sont constituées de fibres de collagène, elles-mêmes composées de fibrilles de collagène formées à leur tour de molécules de tropocollagène. Le diamètre d'une fibrille a été mesuré à 31-35 nm par diffraction-X [38, 97] et à 24-26 nm par microscopie électronique [14]. La distance inter-centre a été mesurée à 59-62 nm par diffraction X et à 64-67 nm par microscopie électronique. La molécule de collagène est constituée d'une triple hélice de 3 molécules de tropocollagène. On retrouve essentiellement du collagène de type I, mais des collagènes de type III, V, VI et XII, non-fibrillaires, auraient également été retrouvés. Le reste de la matrice extracellulaire est essentiellement constitué de protéoglycanes, molécules qui permettraient de réguler l'agencement des molécules de collagène et qui relieraient même directement les

fibrilles de collagènes (ponts inter-moléculaires) ;

- la membrane de Descemet, qui est la lame basale de l'endothélium cornéen, épaisse de 8 à 12 μm chez l'adulte ;

- l'endothélium. Il s'agit de la couche la plus postérieure de la cornée, directement en contact avec l'humeur aqueuse et dont les cellules assurent un triple rôle de synthèse, de barrière interne et de transport actif indispensable aux propriétés de déturgescence cornéenne. Limité en avant par la membrane de Descemet, l'endothélium est une couche unicellulaire formée de cellules plates, régulières, hexagonales, de 5 à 6 μm de hauteur et de 15 à 20 μm de largeur. Une défaillance de l'endothélium entraine un œdème cornéen.

7.1.2 Propriétés optiques

Des mesures en diffraction-X ont montré qu'il y a une différence dans l'indice de réfraction des fibrilles (n=1,41) et de la matrice extracellulaire (n=1,36). En tenant compte des fractions de volume des composants cornéens, l'indice total de réfraction de la cornée est évalué à 1,37 [60, 69].
La transmission optique de la cornée est régie par les propriétés d'absorption de ses composants, qui sont essentiellement l'eau et le collagène. La figure 7.2 montre que ces derniers n'absorbent pas dans le visible et présentent quelques fenêtres de transmission dans le proche infra-rouge [118]. La caractéristique de ne pas absorber dans le visible, couplée à celle de diffuser de façon négligeable la lumière, confère à la cornée sa propriété de transparence. Plusieurs théories ont essayé d'expliquer la transparence de la cornée. Le modèle le plus simple est bâti sur le principe d'un indice de réfraction complètement uniforme de la cornée, mais cela est en contradiction avec les mesures de diffraction-X. Maurice [69] a ensuite proposé que la transparence de la cornée serait due à un arrangement des fibres de collagène selon une structure cristalline, assurant des interférences destructives dans toutes les directions sauf à l'avant. Successivement, il a été montré par Hart et Farrell [41] qu'un ordre à courte distance des fibres de collagène (c.à.d. la distance centre-à-centre d'une paire de fibres est constante) couplé à leur petit diamètre par rapport à la longueur d'onde de la lumière visible est suffisant pour assurer la transparence. Bien que basées sur différentes hypothèses, toutes les théories arrivent à des conclusions très semblables quant à l'explication de la transparence cornéenne [25] :

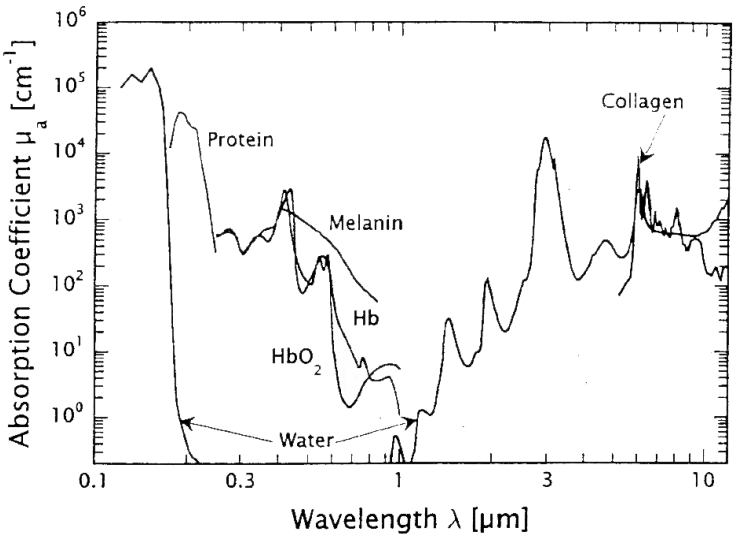

Figure 7.2: Coefficients d'absorption des principaux constituants tissulaires dans la region spectrale 0,1-12 μm [118]

- la diffusion de la lumière est provoquée par des fluctuations de densité spatiale supérieures à environ la moitié de la longueur d'onde du rayonnement incident ;
- les fibres présentent une section efficace de diffusion faible ;
- malgré cela, vu le nombre important de fibres composant la cornée, il est nécessaire que la lumière ne soit diffusée de façon constructive qu'à l'avant.

Lorsque l'endothélium cornéen ne maintient plus le taux d'hydratation constant dans le stroma, à la suite d'une inflammation, d'un trauma ou d'une dystrophie, un œdème se développe. Le tissu perd sa propriété de transparence et devient donc opaque, avec comme conséquence une baisse même drastique de la vision. Bien que des modèles très complexes aient décrit l'atténuation de la lumière dans un matériau diffusant, nous nous limitons dans notre étude à décrire cela par la simple loi de Beer-Lambert, selon laquelle l'intensité transmise est exprimée par

$$I_t = I_0 e^{-\alpha_s z} \tag{7.1}$$

où I_0 est l'intensité incidente, α_s est la section efficace de diffusion et z est la profondeur dans la direction de propagation. La perte de transparence du tissu cornéen est souvent associée à une perturbation dans l'organisation des fibres de collagène. La figure 7.3 permet de comparer

une cornée transparente avec une cornée œdémateuse. Dans cette dernière la densité des fibres

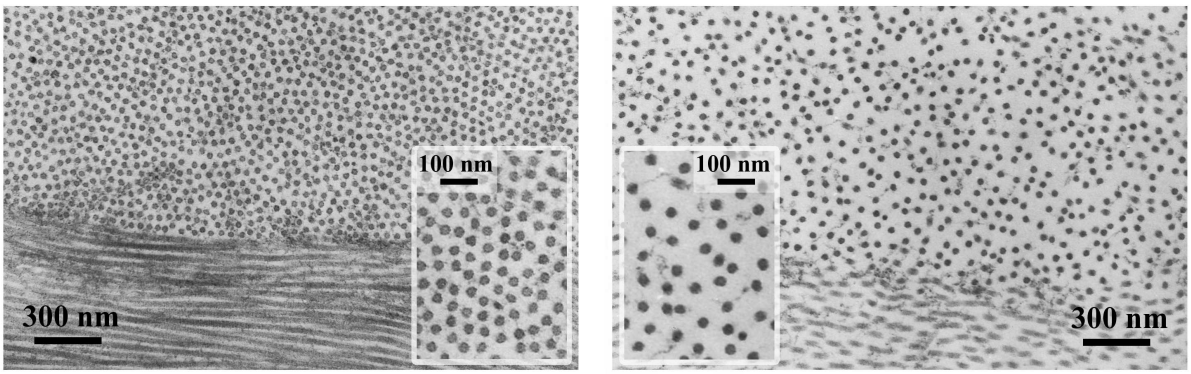

Figure 7.3: Comparaison d'une cornée transparente (a) avec une cornée œdémateuse (b) dans laquelle l'ordre des fibres de collagène est perdu (b) [Michèle Savoldelli, Hôpital Hôtel Dieu de Paris]

de collagène est diminuée à tel point que certaines régions sont complètement privées de fibres. Benedeck [3] a appelé ces régions " lacs ", puisqu'elles contiendraient du fluide en excès. Ces lacs introduisent des variations importantes de l'indice de réfraction qui font que la lumière est diffusée dans toutes les directions. La diffusion de la lumière par des particules sphériques est décrite par la théorie de Mie, qui prend également en compte les propriétés d'absorption et de réflexion du matériau et permet de définir la section efficace de diffusion. Lorsque les dimensions de la particule sont très inférieures à la longueur d'onde incidente, la théorie de Rayleigh est appliquée, selon laquelle la section efficace de diffusion est inversement proportionelle à λ^4 [114]. Dans la cornée opaque, la nature exacte des centres de diffusion n'a pas été identifiée et ces théories ne peuvent pas être appliquées directement. Cependant, il a été démontré que la section efficace de diffusion varie selon la relation suivante

$$\sigma = \sigma_{normal} + \frac{B}{\lambda^2} \tag{7.2}$$

où σ_{normal} est la section efficace de diffusion d'une cornée saine, proportionnelle à $1/\lambda^3$, et B est une constante qui augmente avec l'épaisseur de la cornée [91].

7.2 Les lasers ultrarapides et leurs applications en chirurgie ophtalmologique

Les années 80' et 90' sont marquées par des avancées technologiques significatives dans le domaine des lasers, qui permettent de remplacer les lasers à colorants par des sources d'impulsions ultra-rapides plus performantes. En 1986, Moulton [76] découvre un nouveau matériau laser, l'oxyde d'aluminium dopé aux ions titane, qui présente un spectre d'émission extrêmement large, favorisant la génération d'impulsions courtes, et une bonne conductivité thermique, limitant ainsi les effets thermiques, même à des fortes puissances. De plus, ses propriétés optiques permettent de générer des impulsions ultra-courtes par auto-blocage des modes par effet Kerr [104]. Ce nouveau matériau est rapidement associé à la technique d'amplification à dérive de fréquence, introduite par Strikland et Mourou [107], qui consiste à étirer temporellement des impulsions avant de les amplifier, puis à les re-comprimer à leur durée initiale, permettant ainsi d'obtenir des énergies très élevées. Parallèlement au développement et à l'expansion des lasers Ti:saphir, les progrès dans les technologies des diodes laser ont conduit à la mise en place de sources laser femtoseconde pompées par diode [45, 58]. Bien que leurs performances soient moins spectaculaires que dans le cas des lasers Ti:saphir en terme de durée d'impulsion et énergie maximum, leur coût modéré et leur compacité les rendent plus adaptées aux applications commerciales. En particulier, les lasers femtoseconde à base de verres phosphate ou silicate dopés aux ions terres rares, notamment le néodyme, ont attiré l'attention de scientifiques et de médecins pour des applications dans l'ophtalmologie [53, 64, 67]. Les lasers femtoseconde sont aujourd'hui couramment utilisés en chirurgie réfractive et tendent à remplacer les techniques traditionnelles de greffe de cornée grâce à leur fiabilité et leur reproductibilité.

7.2.1 Les chaines laser femtoseconde

Une chaine laser femtoseconde se compose des éléments suivants [102] :

- un oscillateur. Il s'agit d'une cavité laser dans laquelle les modes longitudinaux générés par le pompage du cristal interfèrent constructivement en phase afin de créer une impulsion de courte durée. La technique la plus courante pour cela est appelée blocage de mode passif. Ce dernier est obtenu soit par effet Kerr optique, phénomène non-linéaire

par lequel une lentille de Kerr s'établit dans le cristal en rendant le faisceau divergent, soit en introduisant un élément qui module les pertes, c'est-à-dire qui devient transparent avec les hautes intensités et favorise donc le régime impulsionnel, plus intense que le régime continu ;

- un étireur-compresseur, dans lequel des hautes intensités peuvent être obtenues par l'amplification à dérive de fréquence (CPA). Le principe consiste à allonger temporellement l'impulsion femtoseconde jusqu'à quelques centaines de picosecondes avant amplification. L'étirement de l'impulsion se fait à l'aide d'éléments dispersifs et évite les effets non-linéaires et l'endommagement optique pendant l'amplification. Après avoir été amplifiée, l'impulsion traverse à nouveau un réseau optique pour retrouver sa durée initiale (figure 7.4) ;

- un amplificateur, qui a pour but d'augmenter l'énergie de l'impulsion étirée. En particulier, l'amplificateur régénératif est un résonateur où l'impulsion est injectée et éjectée après amplification grâce à des polariseurs et par commutation d'une cellule de Pockels. L'impulsion est amplifiée en traversant plusieurs dizaines de fois le cristal.

L'intensité pic d'un laser femoseconde peut être exprimée, en W/cm^2, par la relation

$$I = \frac{E}{\Delta t \times S} \tag{7.3}$$

où E est l'énergie de l'impulsion, Δt est la durée de l'impulsion et S la surface du faisceau.

Dans nos expériences au Laboratoire d'Optique Appliquée et au Laboratoire Biotechnologie et Œil, nous avons utilisé deux sources laser :

- un laser néodyme:verre [46, 55, 58]. Le néodyme dopé au verre présente une largeur de bande d'émission d'environ 22 nm, une section efficace d'émission de 4×10^{-20} cm^2 et une absorption autour de 808 nm, permettant le pompage par diode laser et une facilité de fabrication. En revanche, la conductivité thermique est faible, de l'ordre de 1 Wm^{-1}K^{-1} [18], ce qui nécessite la réalisation de verres fins pour évacuer la chaleur et le pompage à basse puissance pour éviter l'endommagement thermique. Le laser se compose d'un oscillateur pompé par diode, d'un étireur-compresseur, dans lequel la durée de l'impulsion est modifiée par un réseau et d'un amplificateur régénératif avec Nd:verre

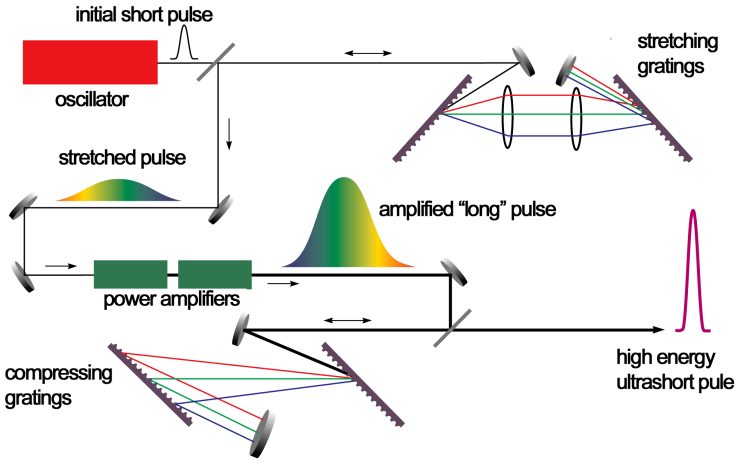

Figure 7.4: Amplification à dérive de fréquence (modifié de www.llnl.gov/str/pdfs/09_95.2.pdf)

pompé par diode comme dans le cas de l'oscillateur. L'ensemble des éléments constituant la chaine laser est décrit dans la figure 7.5. Le laser délivre des impulsions centrées autour d'une longueur d'onde de 1.06 μm, avec une durée approximative de 500 fs, un taux de répétition variable entre 1 et 10 kHz, une énergie max de 6 μJ (à 10 kHz), et une stabilité d'environ 1%.

- un laser Ti:saphir. Il inclut un oscillateur Mira[1] avec blocage de mode par effet Kerr pompé par un laser Argon, suivi d'un étireur-compresseur avec réseau et d'un amplificateur régénératif ayant comme milieu amplificateur un cristal Ti:saphir dopé par un laser YLF (yttrium lithium fluoride) doublé en fréquence. Le laser délivre des impulsions centrées autour d'une longueur d'onde de 800 nm, avec une durée approximative de 170 fs, un taux de répétition de 1 kHz, une énergie max de 200 nJ, et une stabilité d'environ 10%.

7.2.2 Applications chirurgicales et systèmes cliniques commercialisés

Les premières applications du laser femtoseconde en ophthalmologie ont été dans la chirurgie réfractive pour la correction de la myopie et l'hypermétropie [53, 64, 67]. En 1989, une technique chirurgicale pour modifier la courbure de la cornée et ainsi corriger les défauts réfrac-

[1] Coherent Inc.

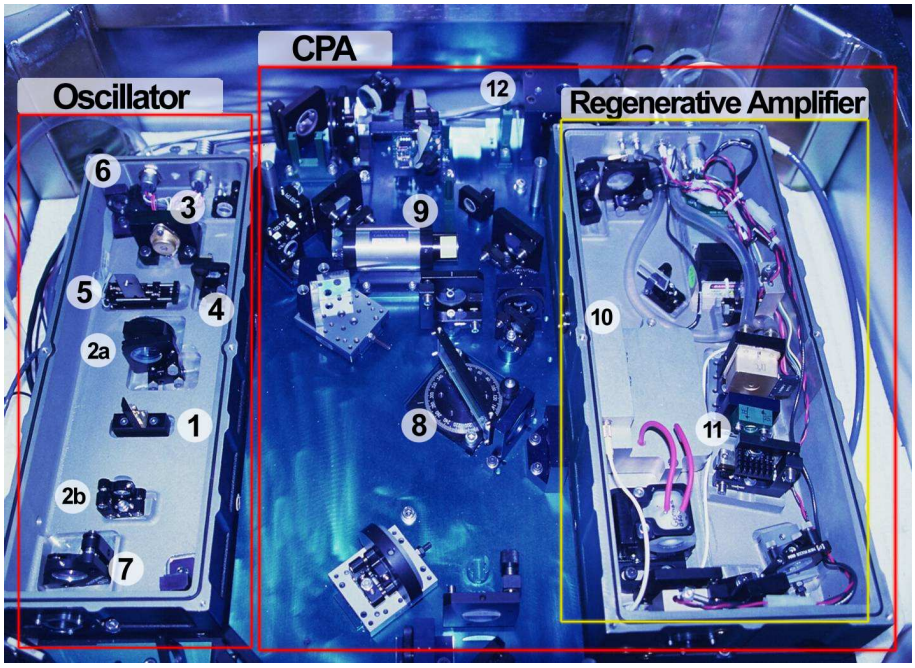

Figure 7.5: Photo du laser Nd:verre, installé au Laboratoire Biotechnologie et Œil. Les principaux éléments sont: 1) Nd:verre ; 2a et 2b) miroirs de la cavité ; 3) diode de pompe ; 4) absorbeur saturable ; 5) lame ; 6) miroir "chirpé" ; 7) miroir de sortie ; 8) reseau ; 9) isolateur de Faraday ; 10) entrée de l'amplificateur ; 11) Nd:verre ; 12) sortie du faisceau laser

tifs est introduite par Pallikaris *et al.* [85] : le LASIK (*laser in situ kiratomileusis*). Dans le LASIK traditionnel, un couteau mécanique, appelé le microkératome, coupe un volet superficiel d'environ 150 μm et un laser excimer vient ensuite remodeler la courbure de la cornée. Puis, le volet est repositionné (figure 7.6). Des complications opératoires peuvent avoir lieu, liées à l'utilisation du microkératome, comme une découpe incomplète ou trop importante, l'endommagement du volet, la création d'un volet trop fin ou trop épais. Ces problèmes ont été contournés en remplaçant le microkératome par le laser femtoseconde qui assure une précision de découpe [4, 57, 83, 106]. Des études cliniques ont montré que l'astigmatisme postopératoire est également réduit [22, 113]. Dernièrement, l'application du laser femtoseconde en ophtalmologie s'est élargie à la greffe de cornée ou kératoplastie. Comparé aux techniques manuelles ou semi-automatiques, le laser permet une meilleure complémentarité et donc une meilleure adhérence entre le greffon donneur et le lit du receveur [4, 57, 83, 106]. De plus, les systèmes commercialisés proposent différentes formes de découpe -les plus utilisées étant le chapeau, le z et le champignon- qui favorisent la cicatrisation (figure 7.7). Des études ré-

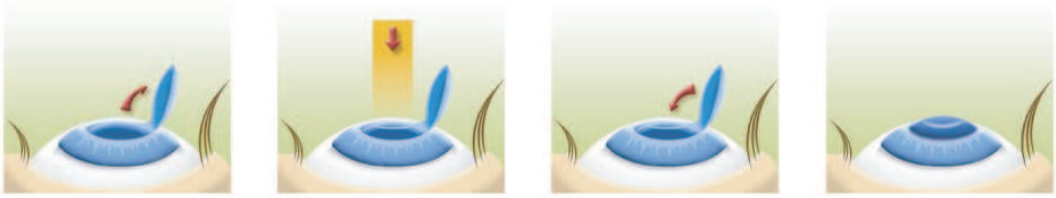

Figure 7.6: Étapes d'une procédure LASIK (from www.ophtalis.tm.fr)

Figure 7.7: Formes de découpe fréquemment utilisées en clinique: chapeau, champignon et z (de gauche à droite)

centes ont montré la faisabilité de la kératoplastie pénétrante ou partielle par laser femtoseconde [9,44,73,96,99,100,103,105]. Cependant, dans la découpe de cornées pathologiques, des énergies trois à quatre fois l'énergie seuil de disruption des cornées saines ont été utilisées. En effet, d'autres phénomènes ont lieu lorsque le faisceau interagit avec un tissu opaque, comme la diffusion et les aberrations optiques et, si l'énergie n'est pas contrôlée, des effets secondaires peuvent survenir, comme démontré dans la partie expérimentale.
Quatre lasers femtoseconde sont actuellement disponibles sur le marché (figure 7.8) :

- Intralase, produit par la société américaine Advanced Medical Optics. Ses principales caractéristiques sont : longueur d'onde 1,05 μm, taux de répétition 60 kHz, lentille d'applanation plate ;

- Femtec, commercialisé par la société allemande 20/10 Perfect Vision®. Il délivre des impulsions avec un taux de répétition de 40 kHz et présente une lentille d'applanation courbée ;

- Da Vinci, produit par la société Ziemer Ophtalmic Systems (Ziemer Group Corporate Structure), installée en Suisse. Il s'agit du seul système qui délivre des impulsions avec un taux de répétition approximatif d'1 kHz ;

- VisuMax, récemment introduit par la société Carl Zeiss Meditec, Inc. Il opère à un taux de répétition de 100 kHz.

Figure 7.8: Systèmes laser femtoseconde cliniques présents sur le marché

Tous les systèmes intègrent des lasers femtoseconde pompés par diode (laser à l'état solide ou fibré dans le cas de VisuMax). Ils délivrent des impulsions à des énergies de quelques μJ et quelques nJ dans la cas du Da Vinci, dans le proche-infrarouge, avec une durée comprise entre 400 et 800 fs. La principale différence entre les systèmes est représentée par le taux de répétition et/ou la forme de la lentille d'applanation. Le taux de répétition influence l'interaction laser-tissu. En effet, en régime MHz, des effets d'accumulation de température peuvent avoir lieu. Cependant, jusqu'à présent aucune étude n'a reporté des différences post-opératoires.

7.3 Interaction laser-tissu

Les mécanismes d'interaction du laser avec le tissu dépendent fortement de la durée de l'impulsion et de la longueur d'onde. En fonction de ces facteurs, des effets mécaniques, thermiques ou

chimiques sont produits, donnant lieu à une réaction hémostatique, une dénaturation moléculaire, des modifications structurales ou une découpe du tissu. En ophtalmologie, un temps d'interaction de 10 à 100 ms est considéré comme quasi-continu. Il est associé à des processus de photocoagulation pour la chirurgie de la rétine. Des durées d'impulsion de l'ordre de la nanoseconde, de la picoseconde et de la femtoseconde définissent respectivement les régimes long, court et ultracourt. En régime long, le processus d'interaction est appelé ablation. La vaporisation de la cible et la rupture de liens chimiques produisent l'enlèvement de matière. En régime court, la focalisation du laser induit la découpe du tissu avec de forts effets mécaniques et thermiques. En focalisant des impulsions qui durent quelques centaines de femtosecondes, on produit une ablation par création de plasma qui correspond à une disruption du tissu, avec les effets mécaniques et thermiques minimisés. À cette échelle de temps, des intensités de l'ordre de 10^{13} W/cm^2 peuvent être obtenues, générant ainsi des champs électriques comparables aux champs électriques qui assurent la cohésion des électrons aux atomes et aux molécules dont est constitué le milieu. En régime femtoseconde, à des plus faibles intensités, d'autres phénomènes nonlinéaires peuvent être observés, tels que la génération de seconde harmonique.
À la base de phénomènes non-linéaires, il y a la création d'une polarisation non-linéaire $\mathbf{P}_{NL}$, exprimée par :

$$\begin{aligned} \mathbf{P}_{NL} &= \mathbf{P}^{(2)} + \mathbf{P}^{(3)} + ... + \mathbf{P}^{(n)} && \text{(7.4a)} \\ &= \varepsilon_0(\widetilde{\chi}^{(2)}\mathbf{EE} + \widetilde{\chi}^{(3)}\mathbf{EEE} + ... + \widetilde{\chi}^{(n)}\mathbf{E}^n) && \text{(7.4b)} \end{aligned}$$

où $\widetilde{\chi}^{(n)}$ et $\mathbf{P}^{(n)}$ représentent respectivement le tenseur de susceptibilité non-linéaire d'ordre n et la polarisation non-linéaire d'ordre n, proportionnelle au champ électrique $\mathbf{E}^n$.

7.3.1 Photodisruption du tissu cornéen par laser femtoseconde

D'un point de vue théorique, la cornée est modélisée par un matériau diélectrique. Un électron libre est donc créé lorsque l'énergie absorbée est suffisante pour qu'il soit promu de la bande de valence vers la bande de conduction. Dans le cas des radiations émises dans le proche-infrarouge, qui produisent l'effet de photodisruption dans la cornée, un seul photon n'est pas assez énergétique et le dépôt d'énergie se fait par une absorption non-linéaire [98]. *A priori*, deux mécanismes contribuent à la formation d'électrons libres : l'absorption multiphotonique et l'effet tunnel suivi par l'effet avalanche (figure 7.9) [56]. Le premier phénomène décrit

une absorption simultanée de plusieurs photons pour que l'électron passe dans la bande de conduction. Dans l'effet tunnel, sous l'influence du champ électrique, la barrière de potentiel est diminuée et la probabilité qu'un électron atteigne la bande de conduction est augmentée. La densité d'énergie pour passer d'un régime multiphotonique à l'ionisation par effet tunnel est de l'ordre de 10^{13} W/cm^2, correspondant aux paramètres typiquement utilisés pour la chirurgie cornéenne par laser femtoseconde [116]. Les premiers électrons libres créés peuvent augmenter leur énergie sous l'action du champ électrique. En entrant en collision avec une tierce particule, ils peuvent absorber des photons et, par ionisation d'impact, transférer leur énergie en excès à un deuxième électron qui transite dans la bande de conduction. Ce dernier électron peut à son tour en créer d'autres : ce processus est appelé ionisation par avalanche. Théoriquement, le

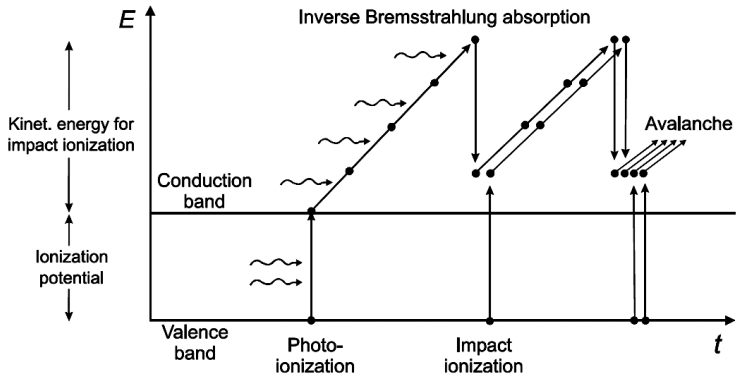

Figure 7.9: Schéma décrivant la formation d'un plasma par les effets de photoionisation et ionisation par avalanche (modifié de [116])

claquage optique est défini par une intensité I_{th} suffisante à produire une densité d'électrons ρ au delà de laquelle le plasma devient réfléchissant. Elle est donnée par

$$\rho_{cr} = w^2 \frac{m\varepsilon_0}{e^2} \tag{7.5}$$

À $\lambda = 1,06\,\mu$m, la densité d'électrons critique est de l'ordre de 10^{21} cm^{-3} [82]. Expérimentalement, le seuil de claquage optique est obtenu lorsqu'on crée dans le tissu une bulle de cavitation qui se traduit par une disruption du tissu. En régime femtoseconde, l'ablation par création de plasma est un phénomène déterministe [19, 20], qui, d'après la littérature, se produit à une intensité comprise entre 1 et 2 J/cm^2 [34, 79, 109, 116, 118]. L'irradiation laser génère dans le tissu une augmentation de température, suivi par une augmentation de pression. Cependant,

puisque la durée de l'impulsion est très courte, les interactions thermiques et mécaniques, liées à la propagation de la chaleur et de l'onde de choc, restent confinées au point focal. Cela réduit significativement les effets secondaires, comparés à la disruption par des impulsions picosecondes [116, 118].

7.3.2 Autofocalisation et défocalisation du faisceau

À des fortes intensités, on peut également générer un phénomène d'autofocalisation et défocalisation du faisceau [11, 12, 68].
Dans un milieu non-linéaire, l'indice de réfraction s'écrit

$$n = n_0 + \Delta n = n_0 + n_2 I \tag{7.6}$$

où n_0 et n_2 représentent respectivement l'indice de réfraction classique et non-linéaire. Cette relation montre que l'indice de réfraction varie en fonction de l'intensité incidente, qui a une distribution gaussienne. Par conséquent, l'onde va se propager plus vite au centre de l'impulsion, où l'indice est plus important que dans la périphérie, ce qui va focaliser le faisceau. Ce phénomène est appelé autofocalisation. Le plasma créé au milieu de l'impulsion va être très absorbant et, en agissant comme une lentille divergente, va à son tour défocaliser le faisceau laser. Plusieurs successions d'autofocalisation et défocalisation du faisceau produisent un filament laser, comme schématisé en figure 7.10. Ce processus se vérifie pour des valeurs de la

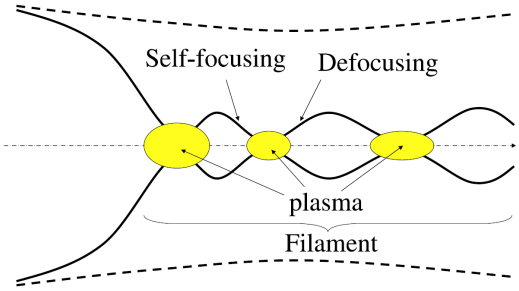

Figure 7.10: Schéma montrant des cycles successifs d'autofocalisation et défocalisation du faisceau laser produisant un filament [12]

puissance crête supérieures à une puissance critique P_{cr} définie par

$$P_{cr} = \frac{3.77\lambda^2}{8\pi n_0 n_2} \quad . \tag{7.7}$$

En chirurgie cornéenne, des effets de filamentation peuvent endommager de façon permanente le tissu [2].

7.3.3 Génération de seconde harmonique

La génération de seconde harmonique est un processus non-résonant qui peut être interprété comme l'annihilation de deux électrons à la fréquence ω pour former un photon à la fréquence 2ω [8, 101]. Lorsqu'une onde à ω interagit dans un milieu non centro-symétrique, elle génère une polarisation non linéaire de la forme

$$P(2\omega) = \varepsilon_0 \chi^{(2)}(\omega,\omega) E(\omega) E(\omega) \tag{7.8}$$

où $\varepsilon_0\chi^{(2)}(\omega,\omega)$ est la susceptibilité non-linéaire du second ordre. Cette polarisation va rayonner un champ à la fréquence 2ω. En général, ce rayonnement se produit de manière isotrope. Cependant, une direction peut être privilégiée : la direction pour laquelle on a adaptation de phase. En effet pour avoir un transfert d'énergie efficace de l'onde à ω vers l'onde à 2ω, on doit avoir simultanément conservation de l'énergie, $\omega + \omega = 2\omega$, et des moments, $k_\omega + k_\omega = k_{2\omega}$. Cette relation montre que l'onde oscillant à la fréquence 2ω est rayonnée efficacement dans la direction où l'accord de phase est minimisé. En effectuant des expériences sur des tendons de queue de rat, Roth et Freund [93] ont montré que, dans le collagène, l'émission de seconde harmonique se compose d'une partie cohérente et d'une partie incohérente. Le signal cohérent confirme l'existence d'un ordre polaire microscopique dans le tendon. Les composantes de l'intensité de SH, dans le système de référence du tendon (XYZ) varient en fonction de l'angle entre la polarisation du champ laser et l'axe du Z du tendon.
Dans la cornée, les fibres de collagène dans une lamelle sont alignées selon une direction unique et forment un angle de 90 degrés avec les fibres de la lamelle adjacente. Dans la figure 7.11, on remarque que les intensités de SH à α et $90 - \alpha$ ont la même valeur et ne vont donc pas s'annuler.

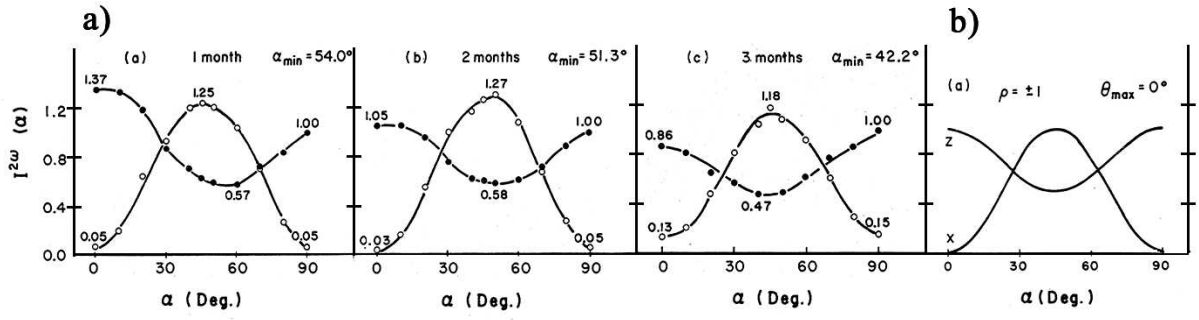

Figure 7.11: (a) Mesure expérimentale de $I_Z^{2\omega}(\alpha)$ points noirs, et $I_X^{2\omega}(\alpha)$, circles, pour des rats d'âge différent, realisées par Roth and Freund. Les données sont normalisées par rapport à $I_X^{2\omega}(90^o) = 1$. (b) Valeurs calculées d'$I^{2\omega}$ pour un tendon avec fibres ordonnées ($\theta_{max} = 0$), où $\rho = \beta_3/\beta_1$ [93]

La génération de seconde harmonique est principalement utilisée pour produire des images à haute résolution. L'imagerie de seconde harmonique présente l'avantage de ne pas endommager le tissu, car l'excitation est localisée au point focal. Des nombreuses études ont montré que la génération de l'émission de seconde harmonique dans un tissu est essentiellement dûe à la présence de collagène, alors que la contribution cellulaire est très faible. En particulier, l'efficacité de conversion de la SH est plus importante dans le collagène de type I que dans le collagène de type IV [10,13,86,108]. Cela s'expliquerait par le niveau d'organisation des fibres et par la chiralité des molécules caractérisant le collagène I. Des études plus spécifiques à la cornée ont pu donner des informations sur l'organisation fibrillaire du tissu cornéen [39, 121], directement liée à sa transparence, et sur l'activité métabolique [88].

Chapter 8

Dispositif expérimental et préparation des échantillons

8.1 Dispositif expérimental

Deux types d'expériences ont été effectués pour étudier l'interaction laser-tissu :

- incisions du tissu cornéen en variant plusieurs paramètres laser. Dans ce but, un dispositif expérimental a été monté ;
- détection *in situ* de l'émission non-linéaire retro-émise par la cornée.

Nous avons effectué des procédures de découpe de kératoplastie avec un système laser commercialisé (Intralase FS60, IntraLase Corp, Irvine, CA), qui inclut un laser solide pompé par diode délivrant des impulsions centrées autour de 1,05 μm, à un taux de répétition de 60 kHz, une durée d'environ 200 fs, une énergie < 3 μJ.
Les autres expériences ont été effectuées avec :

- un laser Nd:verre, délivrant des impulsions d'une durée d'environ 500 fs, à un taux de répétition de 10 kHz, une longueur d'onde centrale de 1,06 μm et une énergie max de

6 μJ. Il a des caractéristiques similaires aux lasers cliniques, mais il permet une flexibilité expérimentale ;

- un laser Ti:saphir délivrant des impulsions d'une durée d'environ 150 fs, à un taux de répétition de 1 kHz, une longueur d'onde centrale de 800 nm et une énergie max de 20 μJ.

Un schéma du dispositif expérimental est présenté en figure 8.1. Le faisceau laser, polarisé linéairement, est ajusté par un système télescopique pour remplir la pupille de l'objectif, qui le focalise sur l'échantillon. Dans le chemin, il est réfléchi par un miroir dichroïque, qui transmet entre 410 nm et 700 nm et réfléchit entre 750 nm et 1080 nm. Nous avons utilisé des optiques de focalisation avec une ouverture numérique de 0,15 à 0,75 (les données techniques correspondantes sont présentées dans le tableau 8.1). Elles sont montées dans un microscope inversé[1]

Optique de focalisation	Correction couvre-objet	ON	rayon d'Airy $\lambda = 1,06\ \mu$m	rayon d'Airy $\lambda = 800$ nm
achromat Melles Griot LAL013, $f = 50mm$	-	0,15	4,31 μm	3,25 μm
objectif de microscopie Olympus UPLFL 10x	-	0,3	2,15 μm	1,62 μm
objectif de microscopie Olympus UPLFL 20x	170 μm	0,5	1,29 μm	0,98 μm
objectif de microscopie Olympus UPFL 40x	170 μm	0,75	0,86 μm	0,65 μm
objectif de microscopie Zeiss LD Plan-Neofluar 20x/corr[a]	0-0,15 mm	0,4	1,61 μm	1,22 μm
microscope objectif Zeiss LD Plan-Neofluar 40x/corr[a]	0-0,15 mm	0,6	1,08 μm	0,81 μm

[a]Ces optiques sont conçues pour corriger les aberrations sphériques à une profondeur de focalisation donnée

Table 8.1: Caractéristiques techniques des optiques de focalisation

adapté, alors que l'échantillon est tenu par une chambre artificielle fixée à des moteurs pas à pas qui la déplacent dans les trois directions. En remplissant la chambre artificielle avec une solution saline, la courbure de la cornée est respectée et son environnement naturel est reproduit.

[1]Olympus IX70

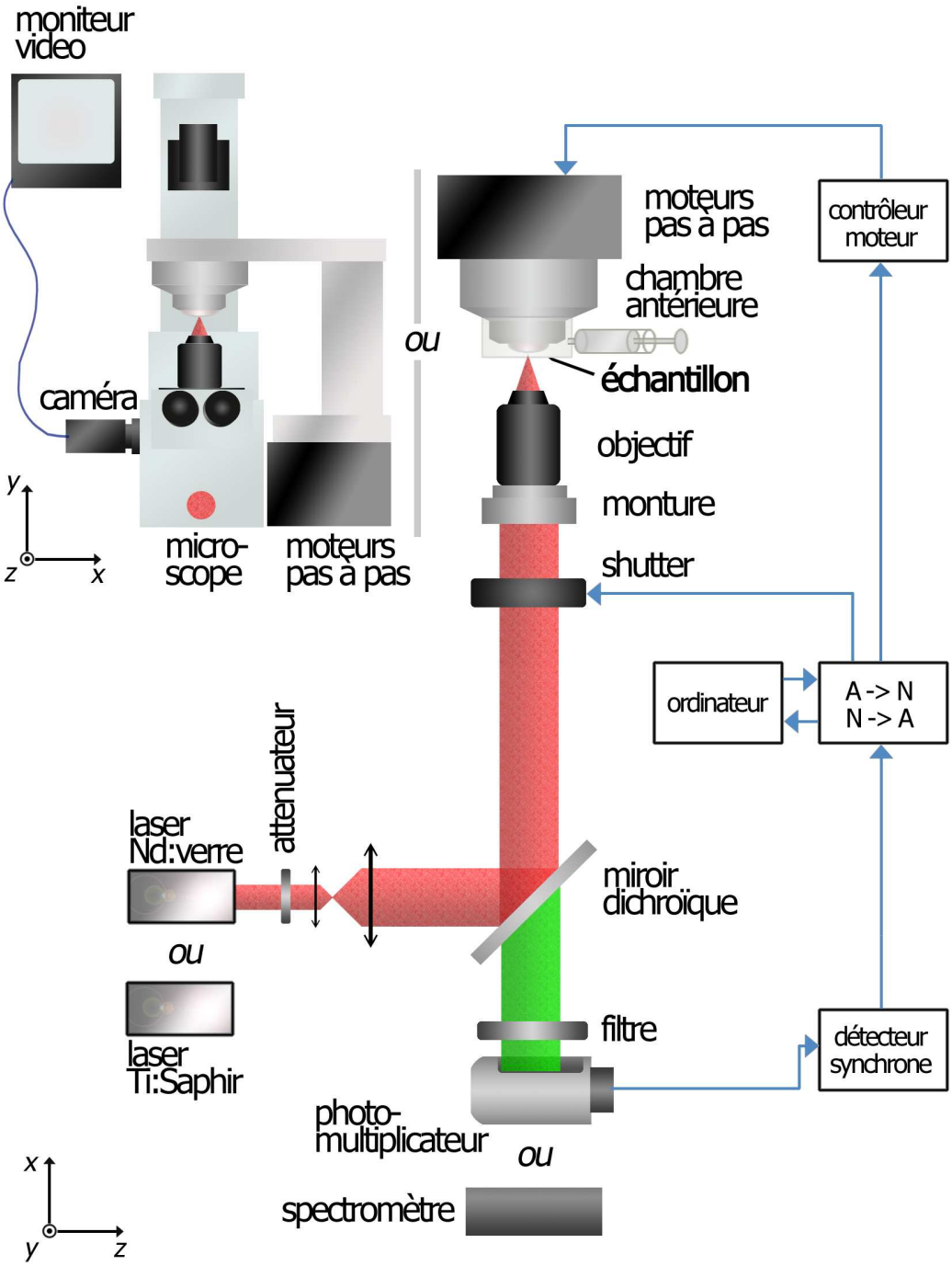

Figure 8.1: Schéma du dispositif expérimental

Pour les mesures de génération de seconde harmonique (GSH), les photons retro-émis sont détectés par un spectromètre[2] ou par un photomultiplicateur[3] couplé à un détecteur synchrone[4] et positionnés derrière le miroir dichroïque.
La puissance laser, le positionnement de l'échantillon et la détection du signal de SH sont contrôlés par ordinateur.

Considérations sur l'efficacité de la détection du signal de seconde harmonique

Concernant la détection de l'émission de SH, une relation entre le signal mesuré par le détecteur synchrone et l'énergie incidente peut être établie comme suit.
Dans le domaine temporel, la puissance atteignant le photomultiplicateur est donnée par

$$P_{PM}(t) = E_{NL}\Delta_T(t) \tag{8.1}$$

où

$$\Delta_T(t) = \sum_{-\infty}^{\infty} \delta(t - kT) \tag{8.2}$$

est le peigne de Dirac, E_{NL} est l'énergie contenue dans la fraction de photons non-linéaires retro-diffusés par le tissu et reçus par le photomultiplicateur et T est le taux de répétition du laser. Le voltage de sortie converti par l'amplificateur de transimpédance[5] du courant du photomultiplicateur peut être exprimé par

$$U(t) = \eta_{PM} E_{NL} \Delta_T(t) \otimes \frac{1}{\tau}\left(\Theta(t) e^{-\frac{t}{\tau}}\right) \tag{8.3}$$

où

$$\Theta(t) = \begin{cases} 0, & t \leq 0 \\ 1, & t > 0 \end{cases} \tag{8.4}$$

est la fonction escalier et τ et η_{PM} sont respectivement le temps de réponse et le facteur d'efficacité du photomultiplicateur. Pour $T >> \tau$, la puissance moyenne de sortie est donnée

[2] get-Spec 2048 COOL
[3] Hamamatsu R636-10
[4] SR830, Stanford Research
[5] Hamamatsu C6271

par

$$\langle U \rangle = \eta_{PM} E_{NL} \frac{1}{\tau} \frac{1}{T} \int_0^T e^{-\frac{t}{\tau}} dt \approx \eta_{PM} E_{NL} \frac{1}{\tau} \frac{1}{T} \int_0^{+\infty} e^{-\frac{t}{\tau}} dt = \eta_{PM} E_{NL} \frac{1}{T} = \eta_{PM} \langle P_{PM} \rangle \quad (8.5)$$

où $\langle P_{PM} \rangle$ représente la puissance moyenne du photomultiplicateur.
On assume la convention unitaire de la transformée de Fourier

$$U(\omega) = \mathcal{F}[U(t)] = \frac{1}{\sqrt{2\pi}} \int_{-\infty}^{+\infty} U(t) e^{-i\omega t} dt \quad (8.6)$$

$$U(t) = \mathcal{F}^{-1}[U(\omega)] = \frac{1}{\sqrt{2\pi}} \int_{-\infty}^{+\infty} U(\omega) e^{i\omega t} d\omega \quad . \quad (8.7)$$

Dans le domaine fréquentiel, $U(\omega)$ est exprimé par

$$\begin{aligned} U(\omega) = \mathcal{F}[U(t)] &= \eta_{PM} E_{NL} \sqrt{2\pi} \left(\mathcal{F}[\Delta_T(t)] \cdot \mathcal{F} \left[\frac{1}{\tau} \Theta(t) e^{-\frac{\tau}{T}} \right] \right) & (8.8a) \\ &= \eta_{PM} E_{NL} \sqrt{2\pi} \left(\frac{1}{T} \Delta_{\frac{2\pi}{T}}(\omega) \right) \left(\frac{1}{\tau\sqrt{2\pi}} \frac{1}{\frac{1}{\tau} + i\omega} \right) & (8.8b) \end{aligned}$$

où le théorème de convolution a été utilisé.
Dans le domaine temporel, le signal reconstruit est donné par une série de Fourier

$$\begin{aligned} U_{tot}(t) &= \frac{1}{\sqrt{2\pi}} \int_{-\infty}^{+\infty} U(\omega) e^{i\omega t} dt & (8.9a) \\ &= \eta_{PM} E_{NL} \frac{1}{T} \int_{-\infty}^{+\infty} \Delta_{\frac{2\pi}{T}}(\omega) \frac{1}{1 + i\omega t} e^{i\omega t} dt & (8.9b) \\ &= \eta_{PM} E_{NL} \frac{1}{T} \sum_{k=-\infty}^{+\infty} \frac{1}{1 + ik2\pi \frac{\tau}{T}} e^{ik\frac{2\pi}{T}t} \quad . & (8.9c) \end{aligned}$$

La première harmonique (k=1) mesurée par le détecteur synchrone est représentée par

$$U_1(t) = \eta_{PM} E_{NL} \frac{1}{T} \left(\frac{1}{1 + i2\pi \frac{\tau}{T}} e^{i\frac{2\pi}{T}t} + \frac{1}{1 - i2\pi \frac{\tau}{T}} e^{-i\frac{2\pi}{T}t} \right) \quad (8.10)$$

et l'amplitude du signal par

$$\widehat{U}_1 = \eta_{PM} E_{NL} \frac{1}{T} \left| \frac{2}{1 + i2\pi \frac{\tau}{T}} \right| \tag{8.11a}$$

$$= \eta_{PM} E_{NL} \frac{1}{T} \underbrace{\left(\frac{1}{\sqrt{1 + \left(2\pi \frac{\tau}{T}\right)^2}} \right)}_{\eta_{LA}} \tag{8.11b}$$

η_{LA} étant le facteur d'efficacité du détecteur synchrone. L'amplitude du signal affichée correspond à la valeur quadratique moyenne donnée par

$$\widehat{U}_{RMS} = \frac{1}{\sqrt{2}} \eta_{PM} \eta_{LA} \frac{1}{T} E_{NL} \quad . \tag{8.12}$$

Si l'on considère les paramètres suivants:

- le faisceau laser est focalisé dans l'échantillon par un objectif de microscopie,
- le signal optique, qui se propage entre l'objectif de focalisation et le photomultiplicateur, traverse le miroir dichroïque et deux filtres,
- le signal non-linéaire est représenté par la génération de seconde harmonique comme montré dans le dernier chapitre,

on peut établir une relation entre l'amplitude du signal de SH mesurée par le détecteur synchrone et l'énergie incidente, comme suit

$$\widehat{U}_{RMS} = \frac{1}{\sqrt{2}} \eta_{PM} \cdot \eta_{LA} \cdot \eta_F \cdot \eta_{MD} \cdot \eta_{Obj} \cdot \eta_{sol} \cdot \eta_{SHG} \cdot \frac{1}{T} E_i \tag{8.13}$$

où η_F, η_{MD}, et η_{Obj} représentent respectivement la transmission des deux filtres, du miroir dichroïque, et de l'objectif. η_{sol}, η_{SHG} et E_i correspondent respectivement à la fraction expérimentale de photons collectés par l'angle solide de l'objectif, au facteur de conversion de la SH

et à l'énergie incidente.
Expérimentalement, pour un objectif avec $ON = 0,5$ et une énergie incidente de 100 nJ, nous avons mesuré un signal maximum de l'ordre de 0,1 mV. Numériquement, nous avons

$$\eta_{PM} = 0,3\frac{V}{\mu A} \times 62\frac{mA}{W} = 18,6 \times 10^3 \frac{V}{W}$$

$$\eta_{LA} = 1$$

$$\eta_F \eta_{MD} \eta_{Obj} = 0,4 \times 0,94 \times 0,5 = 0,19$$

$$\eta_{sol} = \frac{1}{4\pi} 2\pi(1 - \cos(\arcsin 0.5)) = 0,07$$

où η_{PM}, η_F, and η_{MD} peuvent être déduits des fiches techniques correspondantes, η_{LA} peut être calculé par la relation 8.11b, et η_{Obj} est déterminé expérimentalement. En insérant les valeurs numériques dans la relation 8.13, on a

$$0,1 \times 10^{-3} = \frac{1}{\sqrt{2}} \times (18,6 \times 10^3) \times 1 \times 0,19 \times 0,07 \times \eta_{SHG} \times (10 \times 10^3) \times (100 \times 10^{-9})$$

et par la suite

$$\eta_{SHG} = 5,7 \times 10^{-4}$$

On fait remarquer que cette valeur représente le coefficient de conversion de la SH relativement à notre dispositif expérimental et ne doit pas être considérée comme étant une mesure absolue. On rappelle que nos expériences de SH ont lieu dans une configuration en rétrodiffusion, avec un temps d'intégration de 0,5 s et une profondeur de focalisation de 50 à 100 μm dans la cornée. Dans ce contexte, l'efficacité de conversion est particulièrement sensible aux propriétés de diffusion du tissu et le signal reçu inclut les contributions d'une couche microscopique du tissu excité, ce qui peut entrainer une surestimation.

8.2 Préparation des échantillons

Les expériences ont été effectuées sur des cornées de la Banque Française des Yeux[6], qui sont rejetées du circuit de greffe puisque elles présentent une mauvaise qualité endothéliale et sont donc utilisées à des fins scientifiques (figure 8.2). Les cornées ont été gardées dans une solu-

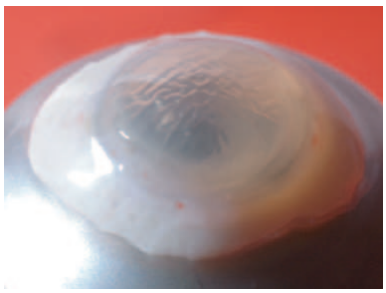

Figure 8.2: Greffon de cornée humaine obtenue par la Banque Française des Yeux

tion (CorneaMax)[7] pendant une à deux semaines après énucléation, ce qui a permis qu'elles s'épaississent et reproduisent l'œdème. Avant le traitement laser, l'épithélium a été enlevé pour réduire les irrégularités de surface et la cornée a été montée sur la chambre artificielle. Après les incisions laser, le tissu a été fixé chimiquement. Avec l'utilisation d'un ultramicrotome[8], des coupes semi-fines et fines ont été obtenues respectivement pour observation en microscopie optique[9] et électronique en transmission[10].

[6]Division of Paris, France
[7]Eurobio, Courtaboeuf, France
[8]Reichert OmU2
[9]Zeiss Phomi2
[10]Philips CM10, résolution 0.5 nm

Chapter 9

Chirurgie cornéenne par laser femtoseconde

9.1 Introduction

Les lasers femtoseconde sont couramment utilisés en chirurgie réfractive dans la découpe du volet superficiel dans la procédure de LASIK (laser in situ keratomileusis). Récemment, leur utilisation s'est élargie à la greffe de cornée, représentant une seconde avancée majeure en chirurgie ophtalmologique. L'utilisation du laser femtoseconde réduit considérablement les risques opératoires par rapport à celle du microkératome, grâce à sa précision et à sa reproductibilité. Plusieurs études ont montré la faisabilité de la kératoplastie par laser femtoseconde [73,99,105]. Cependant, si les systèmes cliniques sont très efficaces dans la découpe du tissu transparent, ils présentent des limitations techniques lorsqu'ils incisent le tissu opaque, car ils n'adaptent pas les paramètres laser aux modifications dues à l'œdème dans l'interaction avec le laser. Les chirurgiens sont donc obligés d'utiliser des solutions de secours, telles que compléter la découpe avec des instruments mécaniques, utiliser l'énergie maximum du système, faire des procédures à double passage.

Le but de ce chapitre est de fournir une étude systématique de la photodisruption du tissu cornéen par laser femtoseconde. Un large panel de paramètres est exploré : la source laser, les propriétés optiques de la cornée, l'énergie laser, l'ouverture numérique des optiques de fo-

calisation, la forme des incisions. Leur influence est estimée par une analyse histologique et ultrastructurale du tissu. (Par simplicité, on utilise les abréviations "dissection ou incision clinique ou expérimentale " pour indiquer respectivement les dissections ou incisions réalisées avec le système clinique ou le dispositif expérimental).
Dans une première partie, je présente l'étude en microscopie optique et électronique en transmission des découpes effectuées avec le système clinique. En suite, la photodisruption produite avec notre dispositif expérimental est examinée et nous démontrons que des effets secondaires peuvent avoir lieu lorsque les paramètres laser ne sont pas contrôlés.

9.2 Dissection du tissu cornéen avec le laser femtoseconde

9.2.1 Dissection avec le système laser clinique

Méthodes

Six découpes de kératoplastie ont été effectuées - chapeaux ($n = 2$), Z ($n = 2$) et lamellaire postérieure ($n = 2$) - dans des cornées œdémateuses avec le système clinique Intralase FS60. Les détails sur la préparation des échantillons et les spécifications techniques du laser sont fournis respectivement dans les deuxième et troisième chapitres. Une énergie de 2,62 μJ a été utilisée pour la découpe en chapeau et de 2,92 μJ pour les deux autres types. La première représente l'énergie recommandée par le fournisseur, la deuxième l'énergie maximale disponible sur le système. Les données concernant l'optique de focalisation ne sont pas disponibles, il n'est donc pas possible de calculer l'irradiance. Cependant, on peut considérer l'énergie seuil comme étant $\leq 1,5$ μJ, qui est utilisée pour la découpe du volet dans la procédure LASIK. Les protocoles de découpe, comme présentés par le système, sont décrits dans le tableau 9.1. Les épaisseurs des cornées traitées étaient comprises entre 700 et 900 μm qui sont des valeurs standard pour des cornées œdémateuses. Le cône d'applanation prévu a été utilisé pendant la découpe.

Découpe de kératoplastie transfixiante en chapeau					
Lamellar cut		Anterior side cut		Posterior side cut	
Depth in cornea	400 μm	Posterior depth	370 μm	Anterior depth	430 μm
Outer diameter	7.0 mm	Diameter	7.1 mm	Posterior depth	1000 μm
Inner diameter	6.0 mm	Energy	2.62 μJ	Diameter	5.9 mm
Energy	2.62 μJ	Side cut angle	90^o	Energy	2.62 μJ
				Side cut angle	90^o
Découpe de kératoplastie transfixiante en Z					
Lamellar cut		Anterior side cut		Posterior side cut	
Depth in cornea	100 μm	Posterior depth	70 μm	Anterior depth	130 μm
Outer diameter	8.2 mm	Diameter	6.9 mm	Posterior depth	1000 μm
Inner diameter	7.4 mm	Energy	2.92 μJ	Diameter	8.7 mm
Energy	2.92 μJ	Side cut angle	30^o	Energy	2.92 μJ
				Side cut angle	30^o
Découpe de kératoplastie postérieure lamellaire					
Lamellar cut		Anterior side cut		Posterior side cut	
Depth in cornea	400 μm	*Laser arrêté*		Anterior depth	370 μm
Outer diameter	8.2 mm	*avant la découpe*		Posterior depth	1000 μm
Inner diameter	0 mm	*antérieure*		Diameter	8 mm
Energy	2.92 μJ			Energy	2.92 μJ
				Side cut angle	90^o

Table 9.1: Protocoles de découpe de kératoplastie transfixiante sur des cornées de banque, comme présentés par le système

Resultats

La figure 9.1 montre une section histologique du tissu coupé par laser avec les procédures chapeau, Z et postérieure lamellaire. L'analyse histologique montre que les découpes sont transfixi-

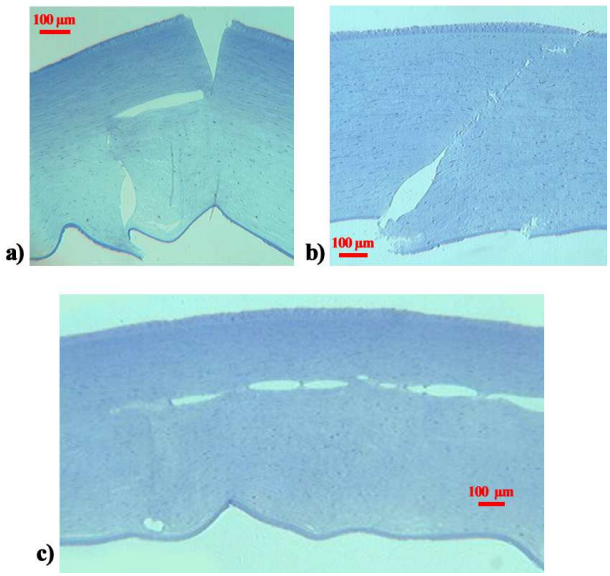

Figure 9.1: Sections histologiques de cornées de banque après les procédures chapeau (a), Z (b) et postérieure lamellaire (c) de kératoplastie

antes en chapeau et en Z (figure 9.1a et 9.1b). Sur la greffe lamellaire postérieure, on remarque une différence de qualité de découpe entre l'incision horizontale et l'incision verticale (figure 9.1c). L'incision horizontale est bien régulière mais présente des ponts tissulaires. L'incision verticale n'est pas visible jusqu'à la Descemet. L'étude en microscopie électronique en transmission confirme les résultats histologiques : les kératoplasties en Z et en chapeau sont transfixiantes et ne présentent pas de ponts tissulaires. Sur la kératoplastie lamellaire postérieure les incisions sont discontinues dans le plan lamellaire et non perforantes dans le plan vertical. La figure 9.2 donne un exemple de section ultrafine du tissu analysé par MET (détail de la découpe en chapeau à différentes profondeurs dans la cornée). Aucune découpe n'a induit d'effets thermiques. L'organisation ultrastructurale des fibrilles de collagène est respectée. On met en évidence des débris déposés sur les berges des incisions. Ce dépôt est constitué de microfibrilles de collagène et de matériaux plus denses et plus hétérogènes (figure 9.2b,c). La quantité de débris semble plus importante sur les incisions stromales antérieures que sur les

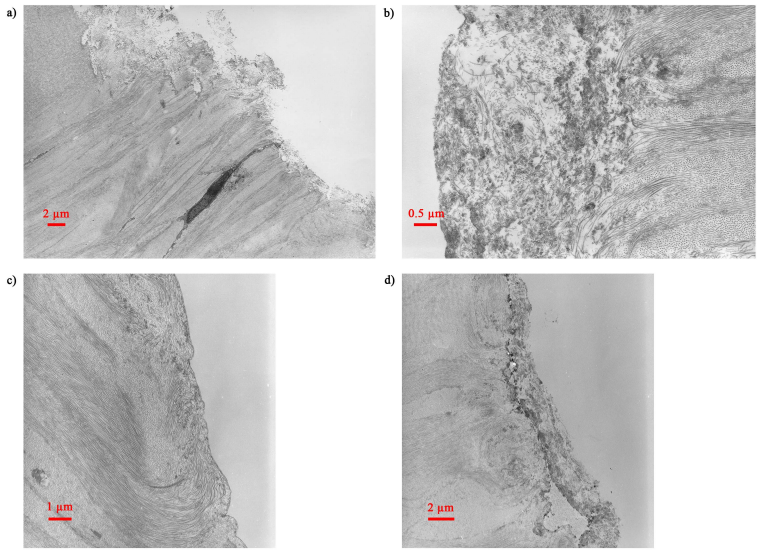

Figure 9.2: Coupe pour l'étude ultrastructurale d'une cornée de banque après découpe en chapeau effectuée à une énergie de 2,62 μJ. a) Membrane de Bowman. b) Stroma antérieur. c) Stroma postérieur. d) Stroma moyen

incisions du stroma profond. Dans le stroma antérieur, ces débris forment fréquemment une couche de l'ordre de quelques μm d'épaisseur, adjacente à l'incision proprement dite. Dans le stroma postérieur, ces débris forment une pseudo-membrane le long de l'incision, d'épaisseur nanométrique. Cette couche peut laisser croire à une modification de l'ultrastructure des berges. Sur la photo de la figure 9.2d, il est facile de faire la différence entre la vraie berge cornéenne et la couche de débris. Dans certains cas, des dépôts avec structure anormale ont été observés. Il s'agit de particules de verre liées à l'utilisation du cône d'applanation. Ce résultat est analysé dans la section 9.4.

9.2.2 Dissections avec le système laser expérimental

Méthodes

Nous avons réalisé des incisions dans le plan antérieur-postérieur et dans le plan lamellaire dans des cornées claires et dans des cornées œdémateuses, avec le système expérimental incluant le laser Nd:verre ou le laser Ti:saphir. Tous les protocoles expérimentaux sont présentés dans le

tableau 9.2. D'après la littérature, la valeur théorique du seuil de claquage optique et comprise

Expériences sur cornées claires				
	Incisions postérieures-antérieures			
Longueur d'onde	1.06 μm		800 nm	
Ouverture numérique	0.15		0.75	
Energie	3 μJ	5 μJ	140 nJ	250 nJ
Profondeur postérieure	1000 μm			
Profondeur antérieure	-300 μm			
Longueur du plan d'incision	1.5 mm			

Expériences sur cornées claires					
	Incisions post.-ant.		Incisions lamellaires		
Longueur d'onde	800 nm				
Ouverture numérique	0.3	0.5	0.3	0.5	0.75
Energie	500 nJ	170 nJ	900 nJ	450 nJ	150 nJ
Profondeur postérieure	1000 μm		-		
Profondeur antérieure	-300 μm		-		
Profondeur lamellaire	-		150 μm		
Longueur du plan d'incision	1.5 mm				

Table 9.2: Protocoles expérimentaux de découpe de cornées de banque

entre 1 et 2 J/cm^2 [34, 79, 109, 116, 118]. Dans notre étude, nous avons supposé la convention selon laquelle cette valeur est donnée par le rapport entre l'énergie incidente et la surface correspondante au rayon d'Airy. Expérimentalement, l'énergie seuil a été donnée par la valeur nécessaire à la formation de bulles de cavitation régulières à la surface de la cornée. Les énergies mesurées lors de nos expériences en fonction de l'ouverture numérique et les respectifs rapports de Strehl sont reportés dans le tableau 9.3

Resultats

La figure 9.3 montre des incisions induites dans une cornée humaine transparente à 3 μJ, proche du seuil et à 5 μJ, environ 2,5 fois le seuil, avec une ouverture numérique de 0,15. Il est facilement remarquable que lorsqu'on utilise une énergie trop forte, la largeur de l'incision devient importante, des cavités résiduelles se forment, couplées à un désordre des fibres de collagène de quelques microns. Des résultats comparables ont été obtenus en utilisant une $ON = 0,75$,

Optique	*NA*	λ	Seuil énergétique théorique	Seuil énergétique expérimental	Rapport de Strehl dans la cornée (expérimental)
achromat $f = 50$ mm	0.15	1.06 μm	1.2 μJ	2.0±0.2 μJ	$\geq 0.6 \pm 0.1$
objectif 10x Olympus UPLFL	0.3	800 nm	166 nJ	288±30 nJ	$\geq 0.6 \pm 0.1$
objectif 20x Olympus UPLFL	0.5	800 nm	59 nJ	130±20 nJ	$\geq 0.46 \pm 0.05$
objectif 40x Olympus UPLFL	0.75	800 nm	26 nJ	60±6 nJ	$\geq 0.44 \pm 0.05$

Table 9.3: Seuils d'énergie mesurés lors de nos expériences selon les optiques utilisées

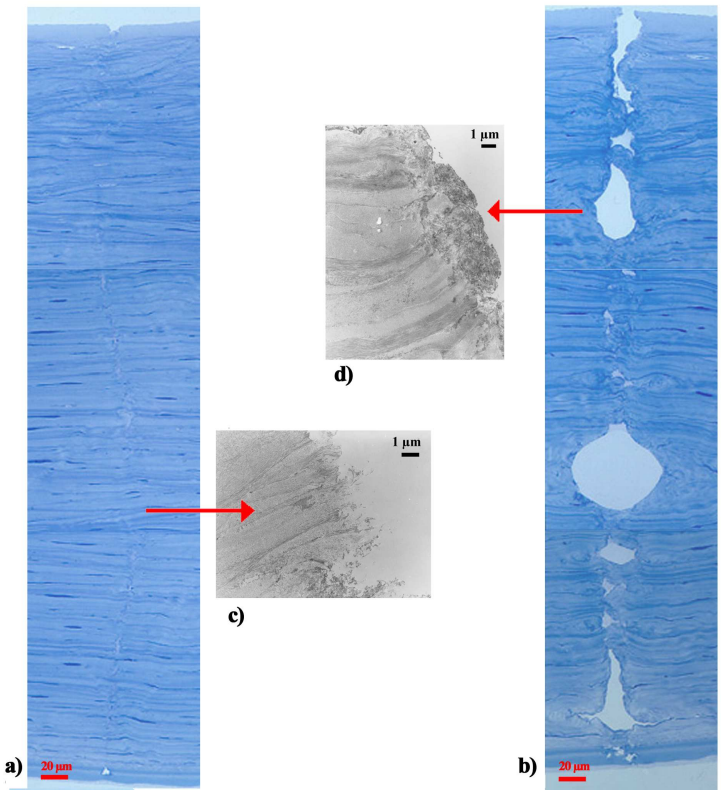

Figure 9.3: a-b) Section histologique d'une cornée dans laquelle on a effectué une incision à l'énergie seuil et à une énergie de 2,5 fois le seuil avec $ON = 0,15$, respectivement; c-d) Micrographes MET montrant les détails des fibres rompues dans le stroma antérieur (image extraite de [17])

bien qu'en mesure mineure.
En parallèle, des incisions ont été effectuées dans des cornées œdémateuses à une énergie constante correspondant à deux fois le seuil, à différentes ouvertures numériques (figure 9.4). En

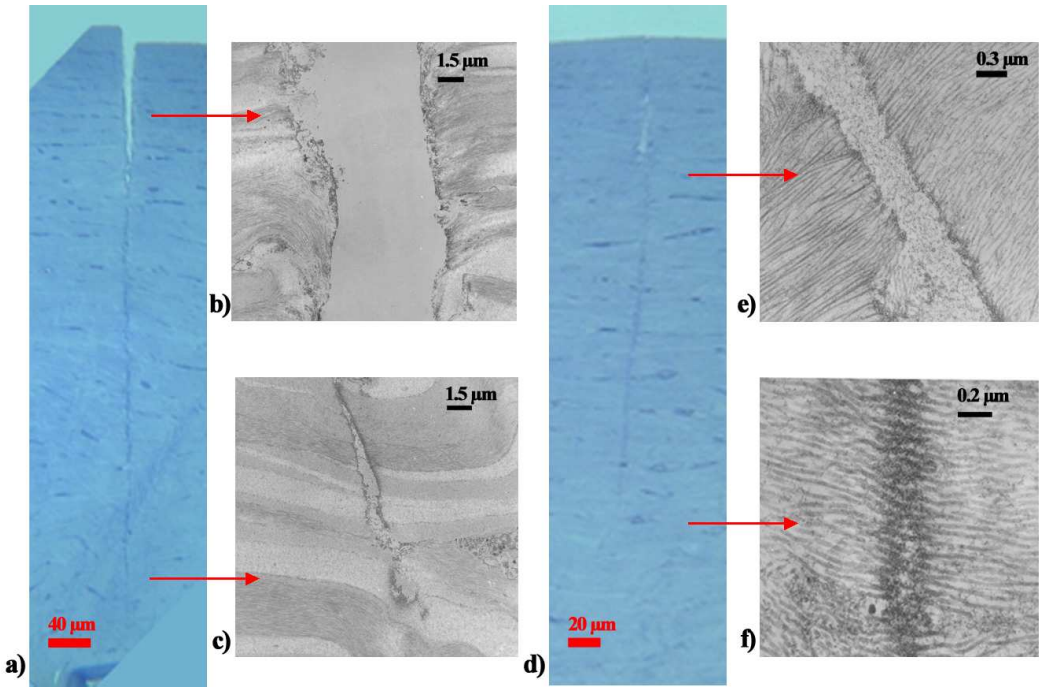

Figure 9.4: a,d) Section histologique du tissu opaque avec incision laser verticale obtenue à $ON = 0,3$ et $ON = 0,5$ et des énergies constantes; b-c, e-f) Images en MET du collagène dans la stroma antérieur (b,e) et vers la fin de l'incision (c,f)

les observant en microscopie optique et électronique en transmission, on remarque qu'elles sont non transfixiantes ou présentent une qualité de découpe inhomogène, entre le stroma postérieur et le stroma antérieur.
Enfin, des incisions lamellaires montrent qu'en augmentant l'ouverture numérique et en réduisant l'énergie, la finesse de découpe augmente. Cependant on remarque que des ponts tissulaires sont présents et qu'une modification du tissu a lieu dans l'axe de propagation du faisceau laser en dehors du plan de focalisation.

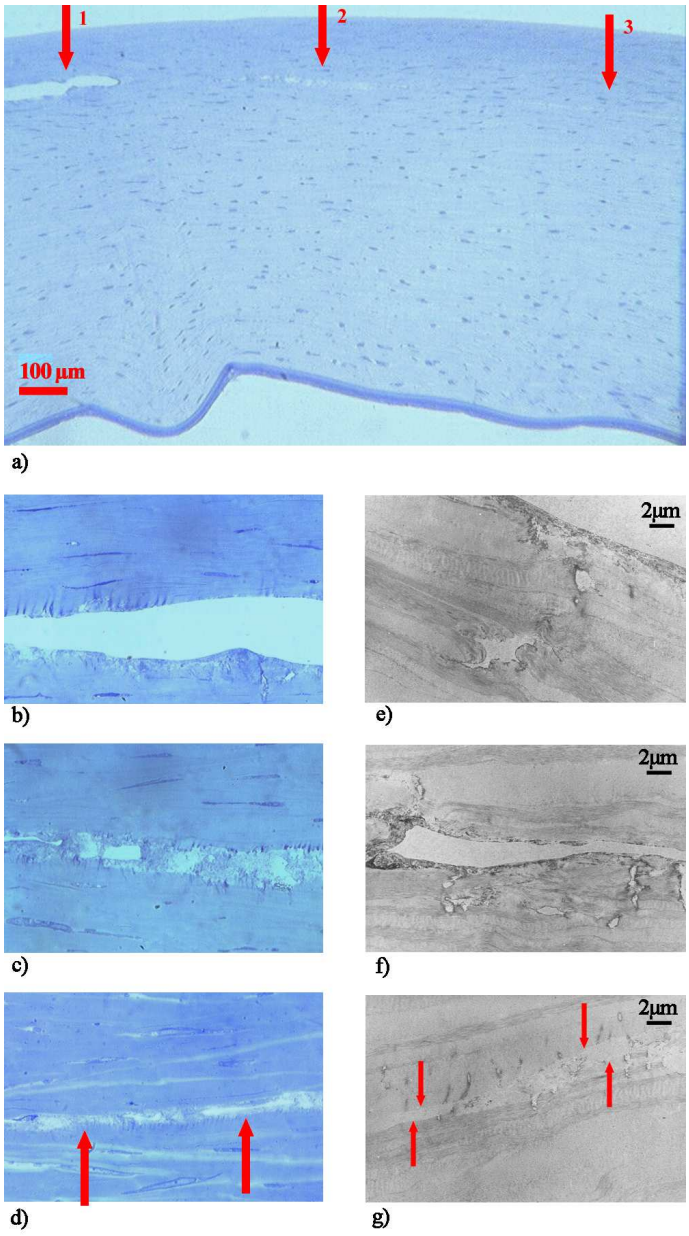

Figure 9.5: Section histologique de découpes lamellaires à 150 μm de la surface de la cornée avec $ON = 0,3$ (a1,b), 0,5 (a2,c), et 0,75 (a3,d) à des énergies supérieures au seuil; e,f,g) Images en MET des découpes lamellaires avec respectivement $ON = 0,3$, 0,5 et 0,75

9.2.3 Discussion

Une première évaluation de la qualité de découpe est donnée par la présence de ponts tissulaires et d'effets secondaires, mécaniques ou thermiques, sur le tissu.
Les incisions de kératoplastie effectuées avec le système clinique et celui expérimental présentent un même aspect histologique et ultrastructural, ce qui permet de valider notre dispositif. Dans les deux cas, on remarque que les incisions à énergie constante ne sont pas perforantes, dû à une atténuation de la densité d'énergie du laser dans le volume de la cornée. Cela est attribué essentiellement à la diffusion et aux aberrations sphériques que le faisceau subit lors de la propagation dans un tissu opaque. Nous avons mis en évidence que si l'énergie est trop importante, comme dans le stroma antérieur, des débris de collagène microscopiques sont formés. Cela s'explique par le fait que l'excès d'énergie élargit la région de claquage optique avec des effets de disruption à plus grande échelle [2, 116]. Cliniquement, ces débris peuvent déclencher des processus inflammatoires et ralentir le processus de cicatrisation [47].
Dans les sections de tissu coupé dans le plan lamellaire, il a été observé que des modifications sont produites en dehors de la zone de focalisation du faisceau. Vogel *et al.* [116] a reporté que des plasmas à basse densité peuvent générer des effets chimiques. Ils seraient dûs à la photodissociation de molécules d'eau en éléments oxydant le tissu [42].

9.3 Effets d'autofocalisation

Dans la section précédente, des images en microscopie électronique en transmission ont mis en évidence que des modifications permanentes du tissu peuvent se produire, lors de la découpe lamellaire, sous forme de noircissement ou encore de disruption du tissu en dehors du plan focal, comme montré dans la figure 9.6. Il est facilement observé que ces modifications présentent une structure périodique, la période étant comprise entre $0,29 \pm 0,02$ μm et $0,47 \pm 0,07$ μm. Ces valeurs ont été mesurées sur une série de 5 cornées. Les changements apportés au tissu sont dûs à des augmentations locales de la densité d'énergie qui pourraient être attribuées à un phénomène d'autofocalisation du tissu suivi par une défocalisation. Cela justifierait la périodicité. La valeur théorique de la puissance critique au-delà de laquelle l'autofocalisation du

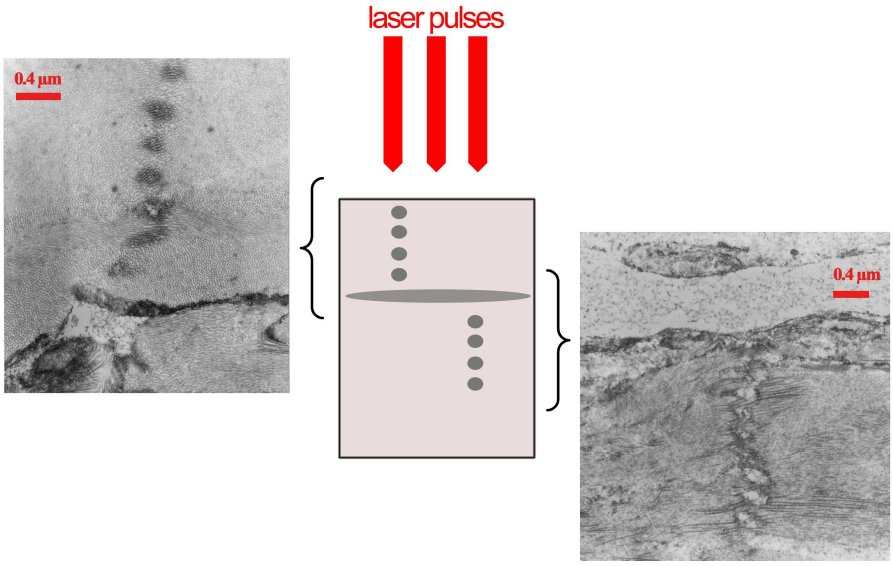

Figure 9.6: Images en MET de modifications tissulaires en dehors du plan lamellaire de focalisation présentant une structure périodique

faisceau se produit est la suivante, en fonction de la longueur d'onde

$$\begin{cases} P_{cr}^{cornea} \approx 10.2\ MW, & \lambda = 1.06\ \mu m \\ P_{cr}^{cornea} \approx 5.8\ MW, & \lambda = 800\ nm \end{cases} \tag{9.1}$$

en considérant un indice de réfraction non-linéaire de la cornée proche de celui de l'eau $n_2^{cornea} \approx n_2^{eau} = 1,2 \times 10^{-16}\ cm^2$/W. Sur la base de nos conditions expérimentales et compte tenu des valeurs de l'énergie seuil théorique et expérimentale, nous avons calculé les puissances crêtes correspondantes pour obtenir le claquage optique (tableau 9.4). Les valeurs sont proches de la puissance critique d'autofocalisation, ce qui renforce notre hypothèse. Cependant, dans la littérature, on reporte des périodes de structure de l'ordre de quelques longueurs d'onde [12], alors que dans notre cas, elle est inférieure à la longueur d'onde. Dans le futur, afin de mieux comprendre le phénomène, il serait intéressant d'effectuer des simulations numériques en prenant en compte le comportement optique non-linéaire de la cornée, accompagnées par des expériences étudiant l'influence de l'ouverture numérique.

	λ=1.06 μm, τ=500 fs, $NA = 0.15$	λ=800 nm, τ=150 fs, $NA = 0.3$	λ=800 nm, τ=150 fs, $NA = 0.5$
P_{th} (correspondant à l'énergie théorique pour le CO)	2.3 MW	1.1 MW	0.4 MW
P_{ex} (correspondant à l'énergie expérimentale pour le CO)	4 MW	1.3 MW	0.8 MW
$P_{ex \cdot 4}$ (correspondant à quatre fois le seuil)	14 MW	5.2 MW	3.2 MW

Table 9.4: Puissances crêtes correspondant à l'énergie théorique et expérimentale pour obtenir le claquage optique (CO) et à quatre fois le seuil lors des incisions à 150 μm

9.4 Dépôt de particules de verre lors de la keratoplastie transfixiante

Nous avons mis en évidence que certaines coupes histologiques et ultrastructurales présentaient des corps solides se déposant sur l'épithélium et sur les berges de l'incision dans le stroma antérieur (figure 9.7, gauche). Cela s'est vérifié lors de découpes transfixiantes, avec le système clinique, indépendamment du protocole choisi. Dans tous les cas, s'agissant de cornées œdémateuses, une énergie supérieure au seuil a été utilisée. Une analyse par la technique de spectroscopie de perte d'énergie d'électrons (EELS)[1] a permis d'en déterminer la composition chimique et a montré que ces particules sont formées d'oxygène et de silicium, c'est à dire de verre (figure 9.7, droite). En observant le cône d'applanation utilisé dans les procédures de kératoplastie avec le laser clinique pour aplatir la cornée, on remarque que la surface du verre en contact avec la cornée pendant la procédure n'est plus polie. Elle présente des gravures correspondantes à la découpe circonférentielle et au marquage des points de suture (figure 9.8). Nous déduisons que les particules de verre proviennent de l'usinage du verre par le laser, que nous attribuons à deux facteurs :

- les protocoles incluent un paramètre appelé "depth into glass" qui définit de combien le laser remonte dans le verre en contact avec la cornée ; cela assure que l'épithélium est entièrement incisé ;

[1] Collaboration avec Fréderic Pailloux et Thierry Cabioc'h du Laboratoire de Physique des Matériaux, Université de Poitiers

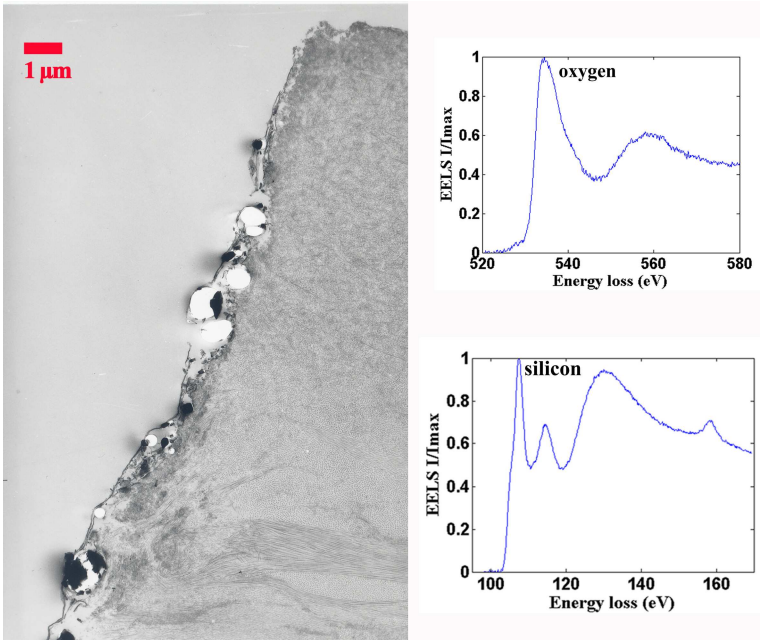

Figure 9.7: Dépôt de corps solides dans la stroma antérieur (gauche). Tracé d'oxygène et de silicium par la technique EELS, indiquant la composition chimiques de particules (droite) (données fournies par Fréderic Pailloux and Thierry Cabioc'h, Laboratoire de Physique des Matériaux, Université de Poitiers)

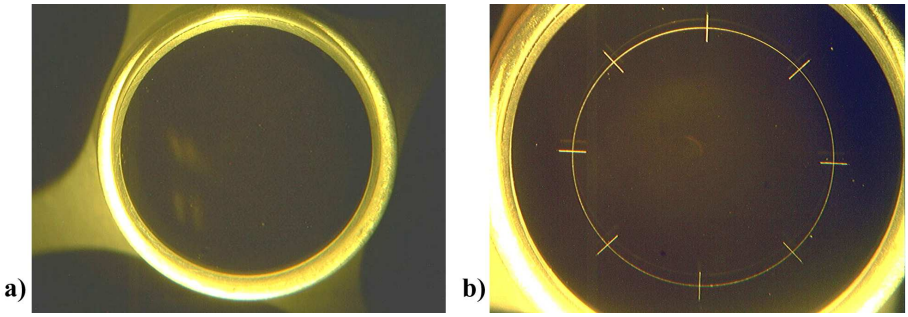

Figure 9.8: Micrographes optiques d'un cône d'applanation avant (a) et après (b) la procédure laser. Le verre en contact avec la cornée a été usiné par le laser

- le verre est un matériau diélectrique et transparent ayant un seuil de claquage optique proche de la cornée. En conséquence, l'énergie utilisée pour rompre les fibres de collagène dans la cornée est suffisante pour usiner la lame de verre. De plus, à cause de l'opacité du tissu, des énergies importantes ont été utilisées, comme indiqué par le fabriquant, ce qui augmente la probabilité de produire des particules, car la région de claquage optique est élargie [2, 116].

Le verre est un matériau inerte biologiquement et, jusqu'à présent, aucune complication liée à la présence de débris de verre dans la cornée n'a été reportée. Cependant, cela pourrait avoir des effets sur la réponse inflammatoire du tissu et le processus de cicatrisation. En absence d'études *in vivo*, il serait préférable d'éviter la formation de ces particules. Nous avons montré, qu'en arrêtant la procédure laser à l'interface verre-cornée, cela est possible.

Chapter 10

Contrôle *in situ* de l'atténuation de la densité d'énergie laser dans une cornée opaque

Dans ce chapitre, nous proposons une méthode innovante de contrôle *in situ* de l'atténuation de la densité d'énergie laser dans une cornéee pathologique, par génération de seconde harmonique. Nous évaluons également l'influence des aberrations sphériques dans cette atténuation. À partir des résultats obtenus, nous montrons qu'il est possible d'améliorer la qualité de découpe dans une cornée pathologique.

10.1 Évaluation de l'atténuation laser

10.1.1 Détermination de la nature du signal non-linéaire

Lorsqu'on focalise un laser femtoseconde dans la cornée à une énergie inférieure au seuil de claquage, on génère une émission non-linéaire. Nous avons utilisé deux méthodes pour déterminer la nature de cette émission : l'analyse spectrale du signal rétro-émis et l'étude de la variation de l'émission non-linéaire en fonction de l'énergie incidente.

La figure 10.1a montre le spectre obtenu en rétro-émission lorsque un faisceau laser à 1,06 μm est focalisé dans la cornée à une énergie inférieure au seuil de disruption. Le pic à 530 nm montre que l'émission non-linéaire est représentée par la génération de seconde harmonique (le pic à 1,06 μm correspond au signal laser résiduel).
La figure 10.1b montre la variation du signal reçu par le photomultiplicateur en fonction de l'énergie incidente (non filtré, avec filtre passe-bande à 530 nm et filtre passe-haut > 660 nm). Il a été obtenu en focalisant le faisceau en un point de la cornée et en augmentant progressivement l'énergie. En analysant le signal obtenu avec filtre passe-bande, on remarque une

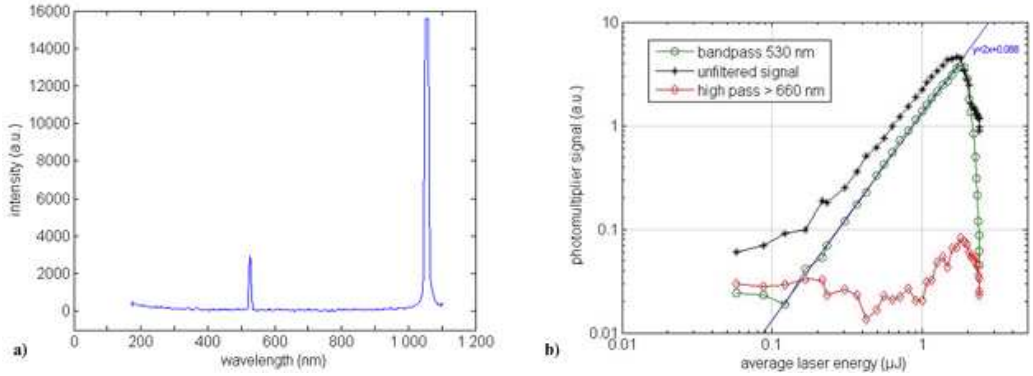

Figure 10.1: a) Spectre du signal retro-émis par la cornée irradiée par un faisceau laser à 1,06 μm. b) Intensité de l'emission optique en fonction de l'énergie laser incidente. Un signal de seconde harmonique est produit

dépendance quadratique, qui confirme qu'il s'agit de la génération de seconde harmonique.

10.1.2 Quantification de l'atténuation laser par GSH

Nous avons utilisé le signal de seconde harmonique pour contrôler l'atténuation de la densité d'énergie en fonction de la profondeur de focalisation d'un faisceau laser dans une cornée pathologique. L'atténuation est dûe a l'œdème du tissu qui en modifie les propriétés optiques, produisant de la diffusion et des aberrations optiques. La figure 10.2 montre le comportement de la SH en fonction de la profondeur de focalisation du laser dans la cornée, à une énergie constante non-destructive et en utilisant un objectif avec ouverture numérique 0,15 (échelle

logarithmique sur la droite, échelle linéaire sur la gauche). On remarque une atténuation expo-

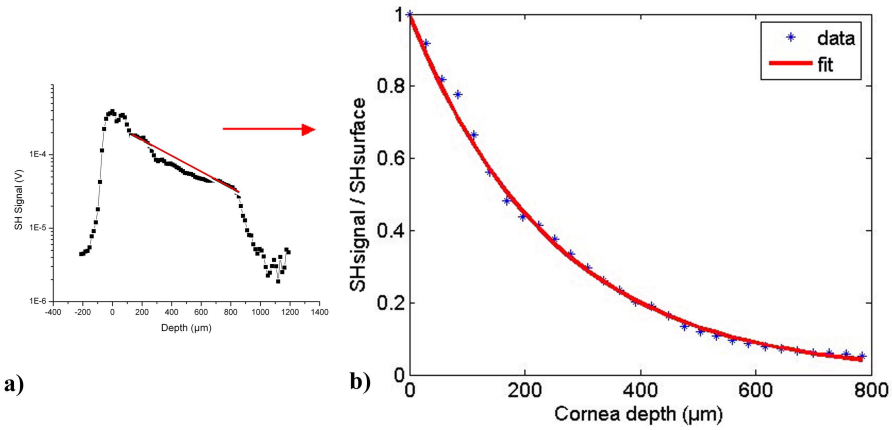

Figure 10.2: Atténuation du signal retro-émis d'une cornée opaque irradiée par un laser Nd:verre à une énergie non-destructive

nentielle. L'intensité de SH peut être exprimée par la formule suivante

$$I_{SH} = [I_0 e^{-\frac{z}{l}}]^2 e^{-\mu z} \tag{10.1}$$

où I_0 est l'intensité laser incidente, l est la profondeur de pénétration à $1/e$ et μ est le coefficient d'atténuation propre à la SH que nous négligeons, en supposant donc que le comportement exponentiel décroissant de la SH est dû essentiellement à l'atténuation du laser. Cette hypothèse est justifiée en considérant que tous les photons diffusés sont récupérés par le photomultiplicateur ayant une large surface de détection. Il a été possible de visualiser en 2D cette atténuation en acquérant le signal dans un plan postérieur-antérieur de 100x200 μm^2 (figure 10.3). L'image obtenue permet également de reconnaître l'anatomie de la cornée quand on la compare à une découpe histologique. Sur une série de 10 cornées, la mesure présentée dans la figure 10.2 a été effectuée à différentes coordonnées latérales, ce qui a permis d'établir une cartographie en 3D de l'atténuation (figure 10.4) (à cause du temps d'acquisition important, seulement 5 à 6 mesures ont été effectuées). En se basant sur la relation 10.1, il est possible de déterminer la profondeur de pénétration du faisceau laser. Les valeurs moyennes obtenues pour les 10 cornées sont présentées dans le tableau 10.1. Le rapport entre l'épaisseur de l'échantillon et la profondeur de pénétration, qui dépendent du degré d'œdème, varie entre 1,8 pour une cornée peu diffusante et 3,8 pour une cornée très diffusante.

En parallèle, nous avons effectué des incisions laser à des énergies de 1 à 6 μJ et une ouverture

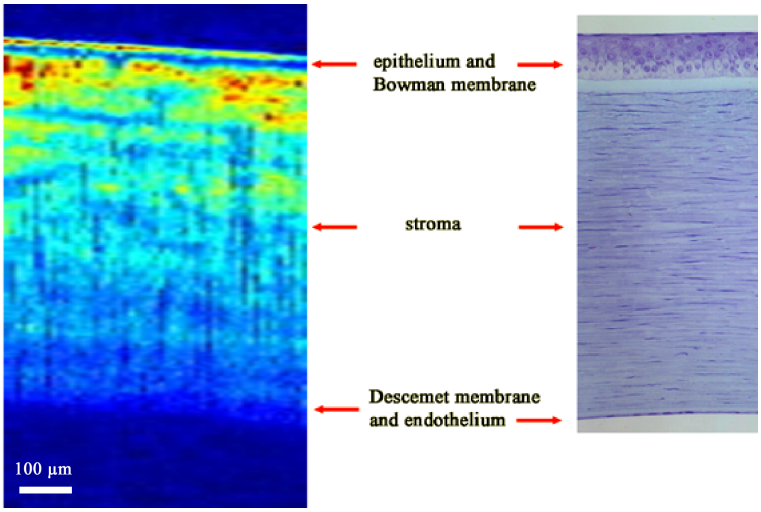

Figure 10.3: Image obtenue par GSH *in situ*. On distingue l'anatomie de la cornée

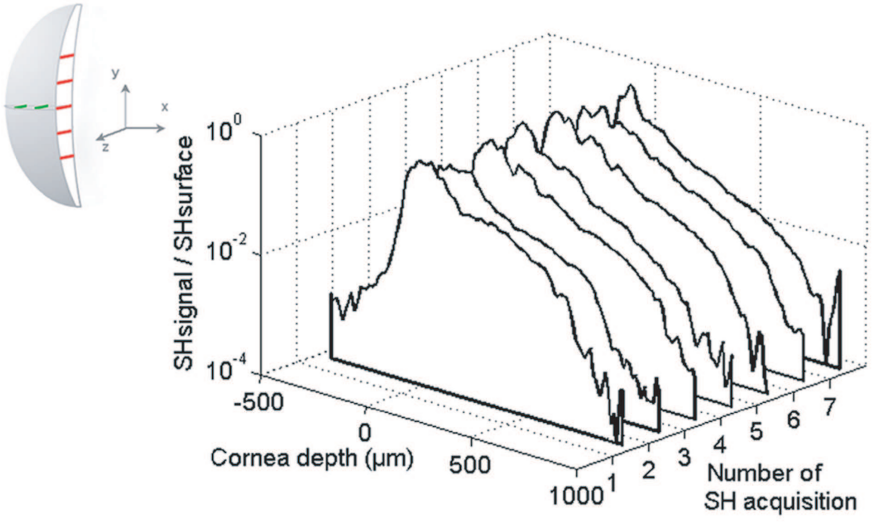

Figure 10.4: Attenuation du signal de SH retro-émis dans le volume d'une cornée à différentes coordonnées latérales

Cornée	1	2	3	4	5	6	7	8	9	10
Epaisseur (μm)	700	750	850	600	900	750	800	1100	1000	1000
Prof. de pénétration (μm)	205	210	299	313	326	337	359	381	388	476
Déviation standard (μm)	13	13	22	27	24	23	32	28	27	29

Table 10.1: Mesure des profondeurs de pénétration du laser dans le volume de dix cornées

numérique de 0,15. La figure 10.5 montre une section histologique de la cornée traitée. On

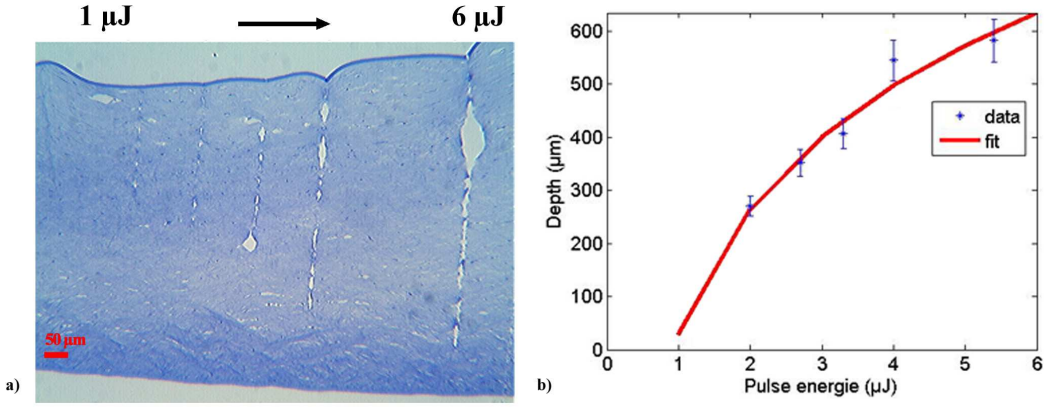

Figure 10.5: a) Section histologique d'une cornée dans laquelle on a effectué des incisions à une énergie de 1 μJ à 6 μJ avec une variation d'environ 1 μJ et $ON = 0,15$; b) Profondeur de pénétration du laser en fonction de l'énergie incidente. Le tracé rouge représente l'ajustement exprimé par $y = \ln(x/342\ \mu m)$

remarque que la longueur d'incision augmente avec l'énergie incidente et cela de façon logarithmique. Une valeur de 340 μm a été trouvée pour la profondeur de pénétration. Cette valeur est en accord avec celles mesurées par GSH. L'analyse histologique *a posteriori* constitue un deuxième moyen de quantification de l'atténuation. Cependant, à la différence de la méthode par GSH, il s'agit d'une approche destructive qui ne peut pas s'appliquer en clinique.
Dans notre étude, nous considérons que la profondeur de pénétration mesurée inclut l'effet combiné de tous les processus contribuant à l'atténuation. Elle est donc donnée par

$$l \approx \frac{1}{\frac{1}{l_{sc}} + \frac{1}{l_{sa}}} \tag{10.2}$$

où l_{sc} et l_{sa} représentent respectivement les profondeurs de pénétration de la diffusion et de l'aberration sphérique. Des simulations ZEMAX, nous déduisons une valeur de 800 μm pour l_{sa} et donc une valeur comprise entre 270 et 800 μm pour l_{sc}. En sachant qu'une cornée transparente a une épaisseur d'environ 550 μm, on peut considérer que dans le premier cas, la diffusion est le facteur dominant dans l'atténuation. Dans le deuxième, la cornée est relativement transparente, car la diffusion et les aberrations contribuent de la même façon à l'atténuation.

10.2 Correction de l'atténuation

Nous avons effectué des simulations avec le logiciel ZEMAX pour évaluer la contribution de l'aberration sphérique à l'atténuation. Pour notre simple système optique, composé d'un faisceau laser focalisé dans la cornée, l'approximation géométrique utilisée par ZEMAX, nous semble suffisante. L'optique de focalisation a été modélisée par un élément paraxial ayant une ouverture numérique équivalente, alors que la cornée a été modélisée par un matériau avec le même indice de réfraction que la cornée. La figure 10.6 montre le calcul de la valeur de Strehl en fonction de la profondeur de pénétration, à différente ouvertures numériques. On peut facile-

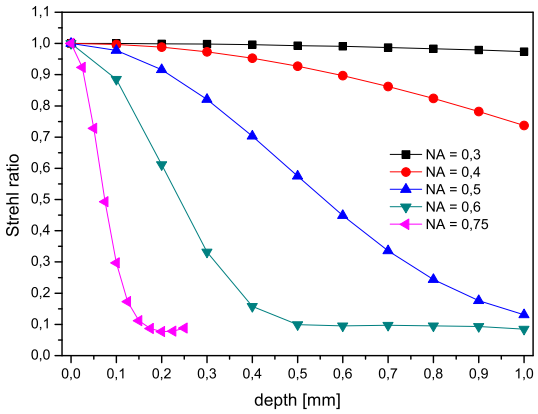

Figure 10.6: Variation du rapport de Strehl à differentes ouvertures numériques en fonction de la profondeur de pénétration dans un matériau avec indice de réfraction 1,37, modélisant la cornée

ment remarquer qu'à des basses ouvertures numériques, l'aberration sphérique ne diminue pas

la rapport de Strehl. En considérant une cornée ayant une épaisseur d'environ 1000 μm, qui correspond à une valeur typique d'une cornée œdémateuse, l'influence de l'aberration sphérique dans la dégradation de la fonction d'appareil devient importante pour des valeurs de l'ouverture numérique >0,5.
En parallèle, nous avons effectué des expériences en utilisant les objectifs de microscopie conçus pour corriger les aberrations sphériques à une profondeur de focalisation donnée dans le matériau transparent. La figure 10.7 montre des incisions laser obtenues à $ON = 0,4$ (a) et $ON = 0,6$ (b), dans une cornée œdémateuse, avec une énergie de 4 fois le seuil. Dans le tableau

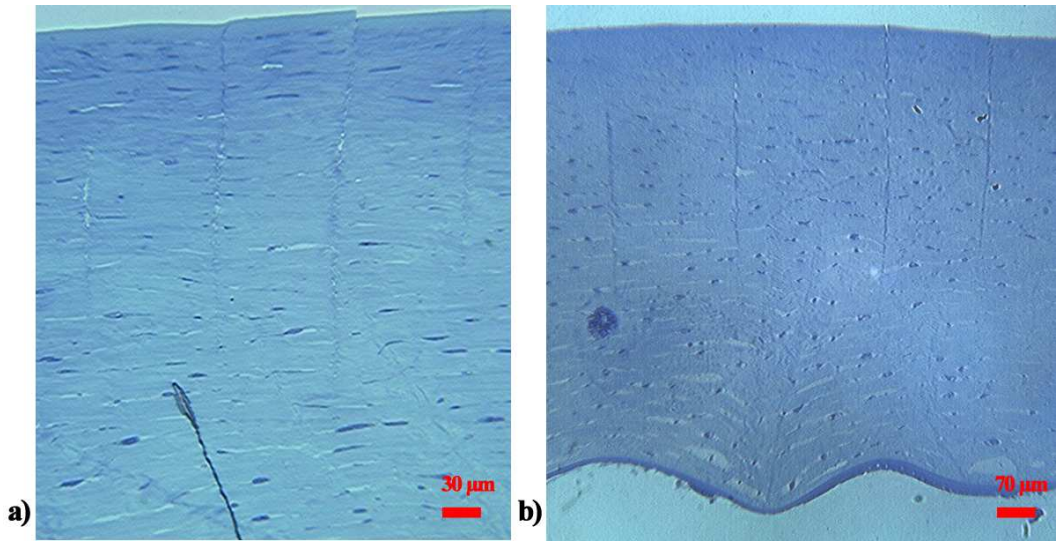

Figure 10.7: Section histologique d'incisions laser dans une cornée œdémateuse obtenues avec $ON = 0,6$ (a) and $ON = 0,4$ (b) et une correction de l'aberration sphérique respectivement à des profondeurs de 0, 300 μm, 450 μm, et 640 μm et 0, 200 μm, 400 μm, et 600 μm (de gauche à droite)

10.2, les profondeurs de correction et les correspondantes longueurs d'incision obtenues sont reportées. À une ouverture numérique de 0,6, en comparant la seconde incision à la première, on remarque qu'en corrigeant plus profondément dans la cornée, la longueur d'incision augmente. Cela est valable jusqu'à une profondeur de correction maximum au-delà de laquelle la longueur de l'incision diminue à nouveau, comme obtenu pour la quatrième incision. On observe une tendance similaire avec $ON = 0,4$, mais de façon beaucoup moins marquée, ce qui confirme qu'à des basses ouvertures numériques, l'aberration sphérique joue un rôle mineur dans l'atténuation. Ces résultats expérimentaux sont en accord avec une simulation numérique par laquelle on a estimé la longueur maximum d'incison en fonction du rapport de Strehl et de

$ON = 0,6$				
profondeur de correction (μm)	0	300	450	640
longueur d'incision obtenue (μm)	250	295	320	220
$ON = 0,4$				
profondeur de correction (μm)	0	200	400	600
longueur d'incision obtenue (μm)	425	420	435	360

Table 10.2: Longueurs d'incision obtenue en focalisant le laser dans la cornée avec les objectifs de microscopie conçus pour corriger les aberrations spheriques

la profondeur de pénétration, en écrivant l'intensité de la forme suivante

$$I(z) \approx I_0 e^{-\frac{z}{l_{sc}} - \frac{|z-z_0|}{l_{sa}}} \tag{10.3}$$

où z_0 est la profondeur de correction des objectifs. Le claquage optique a lieu si l'intensité est supérieure à I_{th}, exprimée par

$$I_0 e^{-\frac{z}{l_{sc}} - \frac{|z-z_0|}{l_{sa}}} > I_{th} \tag{10.4}$$

ou encore

$$\frac{z}{l_{sc}} + \frac{\mid z - z_0 \mid}{l_{sa}} < ln\left(\frac{I_0}{I_{th}}\right) \tag{10.5}$$

On supprimant la valeur absolue, on obtient

$$\begin{cases} z < z_0, & \dfrac{z}{l_{sc}} + \dfrac{z-z_0}{l_{sa}} < ln\left(\dfrac{I_0}{I_{th}}\right) \\ z > z_0, & \dfrac{z}{l_{sc}} - \dfrac{z-z_0}{l_{sa}} < ln\left(\dfrac{I_0}{I_{th}}\right) \end{cases} \tag{10.6}$$

puis

$$\begin{cases} z < z_0, & z < \dfrac{ln\left(\dfrac{I_0}{I_{th}}\right) l_{sa} + z_0}{\left(\dfrac{l_{sa}}{l_{sc}} + 1\right)} \\ z > z_0, & z < \dfrac{ln\left(\dfrac{I_0}{I_{th}}\right) l_{sa} - z_0}{\left(\dfrac{l_{sa}}{l_{sc}} + 1\right)} \end{cases} \tag{10.7}$$

Dans la relation 10.7, beaucoup de paramètres peuvent être changés et nous avons choisi de représenter la profondeur de pénétration associée à l'aberration sphérique en fonction de la profondeur de correction. On considère deux scénarios :

- on fixe $l_{sc} = 350\ \mu$m et on représente un faisceau de courbe, l_{sa} variant entre 300 et 700 μm (figure 10.8);
- on fixe $l_{sa} = 500\ \mu$m et on représente un faisceau de courbes, l_{sc} variant entre 250 et 450 μm (figure 10.9).

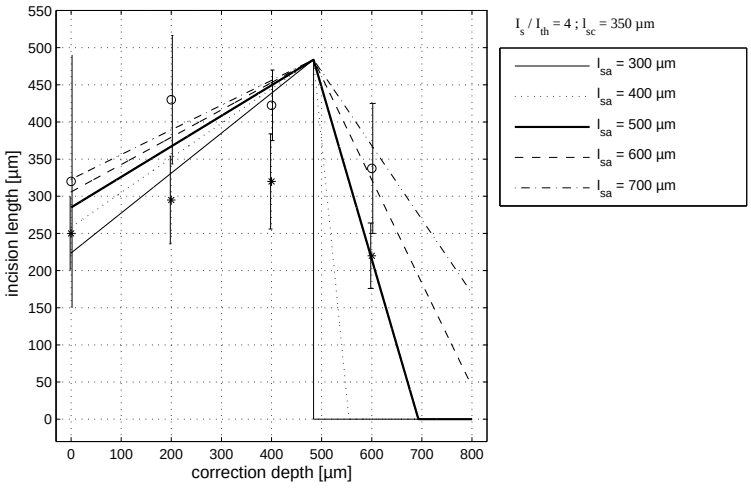

Figure 10.8: Longueur max d'incision en fonction de la profondeur de correction réglée sur l'objectif de microscopie. $l_{sc} = 350\ \mu$m. l_{sa} varie entre 300 et 700 μm. Les étoiles correspondent aux valeurs expérimentaux d'une cornée ; les cercles représentent une valeur expérimentale moyennant deux cornées

On observe que

- à une valeur donnée de l_{sc}, l_{sa}, et I_0/I_{th}, une longueur max d'incision peut être obtenue ;
- cette tendance est amplifiée quand $l_{sa} < l_{sc}$. La variation de l_{sa} ne modifie pas la longueur d'incision max ;
- à une valeur donnée de l_{sa}, la longueur d'incision max augmente en augmentant l_{sa}.

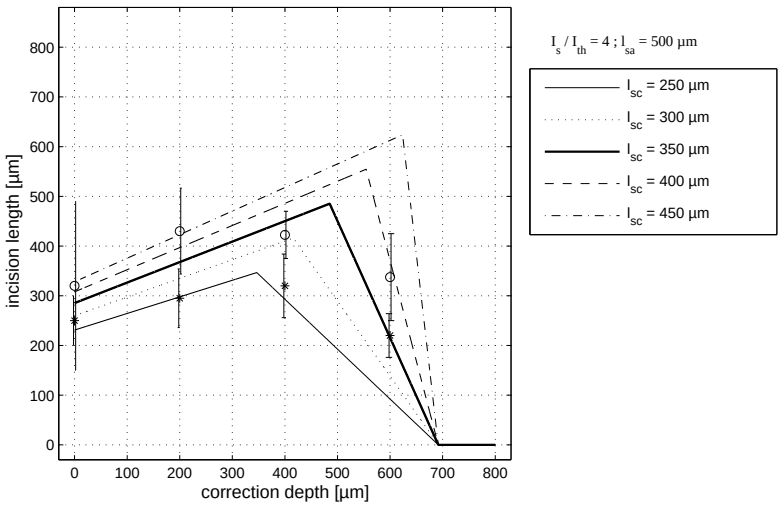

Figure 10.9: Longueur max d'incision en fonction de la profondeur de correction réglée sur l'objectif de microscopie. $l_{sa} = 500\,\mu$m. l_{sc} varie entre 250 to 450 μm. Les étoiles correspondent aux valeurs expérimentales d'une cornée ; les cercles représentent une valeur expérimentale moyennant deux cornées

10.2.1 Compensation de l'atténuation laser

En utilisant la méthode de quantification de l'atténuation par GSH, nous avons déterminé pour une cornée une profondeur de pénétration de $350 \pm 20\ \mu$m. Sur la base de cette valeur, nous avons effectué une incison dans une cornée œdémateuse en augmentant l'énergie selon la relation suivante

$$E = E_{th} e^{\frac{z}{350\mu m}} \tag{10.8}$$

et à une ouverture numérique de 0,15, pour minimiser l'influence de l'aberration sphérique. Nous remarquons que

- les effets du laser sur la cornée sont uniformes sur toute la longueur de l'incision, mis à part un effet de surface, que nous attribuons à des conditions expérimentales limites concernant la durée de l'impulsion proche de la picoseconde pour cette mesure;
- qu'une incision max de 320 μm peut être obtenue, correspondant à l'énergie maximale disponible sur le système laser.

Une incision transfixiante aurait pu être obtenue pour des valeurs très importantes de l'énergie.

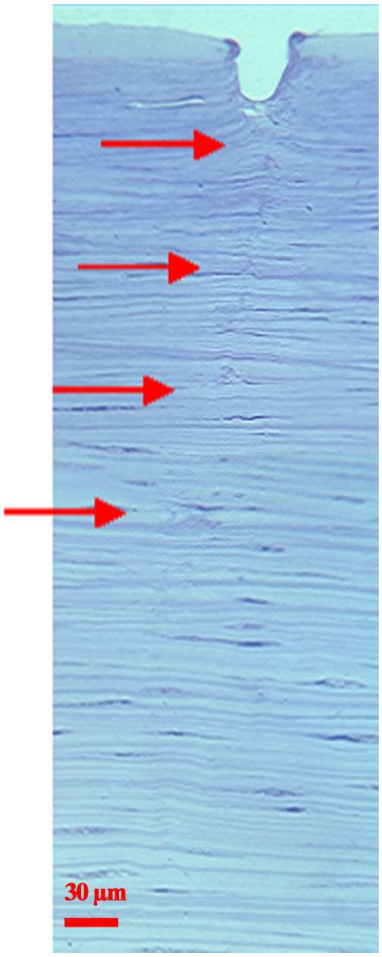

Figure 10.10: Incision dans le stroma moyen et antérieur, obtenue avec une ouverture numérique de 0,5 et une énergie laser variée entre 2 μJ et 5 μJ

10.2.2 Discussion

Nous avons démontré qu'avec la génération de seconde harmonique, il est possible de quantifier de façon non-destructive l'atténuation de la densité d'énergie dans une cornée œdémateuse et que des énergies importantes sont nécessaires pour obtenir des incisions transfixiantes. Cette atténuation est attribuée à la diffusion, mais également à la diminution de la qualité

spatiale du faisceau au point focal lorsque des ouvertures numériques importantes sont utilisées. En effectuant des découpes avec des objectifs de focalisation qui permettent de corriger les aberrations sphériques, mous avons montré que les aberrations peuvent être corrigées jusqu'à une valeur maximale, qui reste inférieure à l'épaisseur d'une cornée diffusante. Il a été également mis en évidence que l'influence de l'aberration sphérique est réduite en diminuant l'ouverture numérique. Cependant, en accord avec des études précédentes, nous avons montré dans le châpitre précédent qu'en focalisant plus fortement, la finesse et la précision de l'incision augmentent et que des effets non-linéaires non désirés sont réduits. Il semble donc nécessaire de trouver un compromis pour le choix de l'ouverture numérique. De basses ouvertures numériques $(ON < 0,3)$ ne sont pas envisageables aussi parce que dans des tissus très diffusants, la densité d'énergie en surface peut être supérieure à celle au point focal dans le volume de la cornée. Définir une limite supérieure est aussi délicat. Pour éviter les effets des aberrations, des objectives à immersion devraient être utilisés, mais il serait difficile d'appliquer cela dans des procédures cliniques. De nos mesures, il résulte qu'une valeur de l'ouverture numérique comprise entre 0,4 et 0,6 serait optimale.

Conclusions et perspectives

La kératoplastie est une opération chirurgicale qui consiste à remplacer un disque de cornée pathologique opaque d'un patient par un disque de cornée saine transparente d'un donneur. La disruption d'un tissu par laser femtoseconde à été largement étudiée et les systèmes laser actuellement présents sur le marché sont très performants dans la découpe de cornées saines. Cependant, leurs performances sont réduites lors du traitement du tissu pathologique, dont les propriétés optiques sont modifiées. Ces modifications ne sont pas prises en compte et le choix des paramètres laser reste qualitatif.
Dans le cadre de cette thèse, une plateforme expérimentale a été développée pour étudier l'interaction laser-tissu en fonction de différents paramètres, pour identifier les limitations techniques auxquelles se heurtent les lasers actuels, et proposer des solutions pour optimiser les processus de découpe du tissu. Les principaux résultats et observations sont les suivants :

- les lentilles d'applanation prévues dans les protocoles cliniques de découpe produisent des corps solides de dimensions microscopiques et nanométriques qui se déposent dans la cornée. Ces particules ont été identifiées par la méthode EELS comme étant des particules de silice provenant de ces mêmes lentilles qui couvrent la cornée et qui sont usinées par le laser. Cet effet est dû à un mauvais préréglage du système et peut être supprimé en modifiant les paramètres ;

- lors de découpes lamellaires (parallèles à la surface de la cornée), en fonction des paramètres lasers, des effets non-linéaires d'autofocalisation peuvent se produire, engendrant des modifications permanentes du tissu. Les lasers cliniques ne contrôlent pas aujourd'hui l'apparition de ce phénomène ;

- lors de la découpe de cornées claires ou pathologiques, un excès d'énergie, même léger,

engendre des effets secondaires importants. Pour assurer une bonne qualité de la chirurgie, il est donc primordial de maîtriser l'énergie déposée dans le tissu. Dans le tissu pathologique, la densité d'énergie du faisceau laser est atténuée lorsque le faisceau est focalisé en profondeur à cause d'effets de diffusion et d'aberrations optiques. Dans les protocoles cliniques de découpe actuellement disponibles, l'énergie de découpe est choisie en fonction de l'expérience du chirurgien et adaptée de façon qualitative au degré d'œdème de la cornée ;

- il est possible de quantifier cette atténuation par une mesure *in situ* du signal non-linéaire de seconde harmonique en utilisant la même source laser. Le libre parcours moyen minimal des photons dans le tissu pathologique observé au cours de nos expériences est de l'ordre de 200 μm (l'épaisseur d'une cornée saine est d'environ 550 μm). À notre connaissance, il s'agit de la première mesure non-invasive *in situ* de ce paramètre. La contribution de l'aberration sphérique dans cette atténuation a également pu être modélisée et quantifiée ;

- les données quantitatives obtenues par mesure de seconde harmonique *in situ* peuvent être utilisées pour ajuster "sur mesure" l'énergie de l'impulsion, minimisant ainsi les effets secondaires et optimisant la qualité de l'intervention chirurgicale.

Les recherches effectuées au cours de cette thèse ont permis de suggérer des voix d'amélioration des systèmes actuels

- quelle que soit la nature exacte du comportement de la diffusion en fonction de la longueur d'onde, il est établi qu'elle pourra être considérablement réduite en utilisant un laser travaillant à une longueur d'onde plus importante que 1,06 μm, typique des systèmes actuels ;

- les aberrations induites par les éventuelles déformations de la cornée peuvent être mesurées et corrigés par un système d'optique adaptative.

L'équipe *Optique-Photonique-Santé* du Laboratoire d'Optique Appliquée travaille actuellement sur un projet de développement d'un système de greffe de cornée automatisée par laser femtoseconde, émettant autour d'une longueur d'onde de 1,6 μm et intégrant un système de correction du front d'onde.

Bibliography

[1] C. L. Arnold, A. Heisterkamp, W. Ertmer, and H. Lubatschowski. Computational model for nonlinear plasma formation in high NA micromachining of transparent materials and biological cells. *Opt. Express*, 15:10303–17, 2007.

[2] C.L. Arnold, A. Heisterkamp, W. Ertmer, and H. Lubatschowski. Streak formation as side effect of optical breakdown during processing the bulk of transparent Kerr media with ultra-short laser pulses. *Appl. Phys. B*, 80:247–53, 2005.

[3] G. B. Benedek. Theory and transparency of the eye. *Appl. Opt.*, 10:459–73, 1971.

[4] P. S. Binder. Flap dimensions created with the Intralase fs laser. *J. Cataract Refract. Surg.*, 30:26–32, 2004.

[5] M. Born and E. Wolf. *Principles of Optics*. Cambridge University Press, 1999.

[6] J. L. Boulnois. Photophysical processes in recent medical laser developments: a review. *Lasers in Medical Science*, 1:47–66, 1986.

[7] L. J. Bour. *Visual optics and instrumentation*, chapter : Polarized light and the eye, pages 310–325. Boca Raton, FL: CRC Press, 1991.

[8] R. W. Boyd. *Nonlinear optics*. Academic Press, 1992.

[9] L. Buratto and E. Bohm. The use of the femtosecond laser in penetrating keratoplasty. *Am. J. Ophthalmol.*, 143:737–42, 2007.

[10] P. J. Campagnola, M. D. Wei, A. Lewis, and L. M. Loew. High-resolution nonlinear optical imaging of live cells by second harmonic generation. *Biophys. J.*, 77:3341–49, 1999.

[11] S. L. Chin, S. A. Hosseini, W. Liu, Q. Luo, F. Théberge, N. Aközbek, A. Becker, V. P. Kandidov, O. G. Kosareva, and H. Schroeder. The propagation of powerful femtosecond laser pulses in optical media: physics, applications, and new challenges. *Can. J. Phys.*, 83:863–905, 2005.

[12] A. Couairon and A. Mysyrowicz. Femtosecond filamentation in transparent media. *Physics Reports*, 441:47–189, 2007.

[13] G. Cox, E. Kable, A. Jones, I. Fraser, F. Manconi, and M. D. Gorrell. Three-dimensional imaging of collagen using second harmonic generation. *Journal of Structural Biology*, 141:53–62, 2003.

[14] A. S. Craig and D. A. Parry. Collagen fibrils of the vertebrate corneal stroma. *J. Ultrastruct. Mol. Struct. Res.*, 74:172–75, 1981.

[15] W. Denk, J. H. Strickler, and W. W. Webb. Two-photon laser scanning fluorescence microscopy. *Science*, 248:73–76, 1990.

[16] F. Docchio, C. A. Sacchi, and J. Marshall. Experimental investigation of optical breakdown thresholds in ocular media under single pulse irradiation with different pulse durations. *Lasers Ophthalmol.*, 1:83–93, 1986.

[17] D. Donate, O. Albert, K. Plamann, J.P. Colliac, P. Sabatier, G. Mourou, P. Denis, C. Burillon, Y. Pouliquen, and J.M. Legeais. Ultrastructural and histologic studies of femtosecond laser incisions in human cornea. *Invest. Ophthalmol. Vis. Sci.*, 46:E–Abstract 4359, 2005.

[18] F. Droun, F. Balembois, and P. Georges. Laser crystals for the production of ultra-short laser pulses. *Ann. Chim. Mat.*, 28:47–72, 2003.

[19] D. Du, X. Liu, G. Korn, J. Squier, and G. Mourou. Laser-induced breakdown by impact ionization in SiO_2 with pulse widths from 7 ns to 150 fs. *Appl. Phys. Lett.*, 64:3071–73, 1994.

[20] D. Du, J. Squier, R. Kurtz, V. Elner, X. Liu, G. Güttmann, and G. Mourou. *Ultrafast Phenomena IX*, chapter Damage Threshold as a Function of Pulse Duration in Biological Tissue, page 254Ű55. Springer-Verlag, New York, 1994.

[21] A. K. Dunn, V. P. Wallace, M. Coleno, M. W. Berns, and B. J. Tromberg. Influence of optical properties on two-photon fluorescence imaging in turbid samples. *Appl. Opt.*, 39:1194–1201, 2000.

[22] D. S. Durrie and G. M. Kezirian. Femtosecond laser versus mechanical keratome flaps in wavefront-guided laser in situ keratomileusis: prospective contralateral eye study. *J. Cataract Refract. Surg.*, 31:120–26, 2005.

[23] R.F. Egerton. *Electron Energy-Loss Spectroscopy in the Electron Microscope*. Springer, 1996.

[24] R. Ell, U. Morgner, F. X. K AÂrtner, J. G. Fujimoto, E. P. Ippen, V. Scheuer, G. Angelow, T. Tschudi, M. J. Lederer, A. Boiko, and B. Luther-Davies. Generation of 5-fs pulses and octave-spanning spectra directly from a Ti:sapphire laser. *Opt. Lett.*, 26:373–75, 2001.

[25] R. A. Farrell and R. L. McCally. *Corneal transparency*, chapter 57 in "Principles and Practice of Ophthalmology. 2nd ed", pages 629–44. Philadelphia, WB Saunders, 2000.

[26] T. Feuk. On the transparency of the stroma in the mammalian cornea. *IEEE Trans. Biomed. Eng.*, 17:1866–90, 1970.

[27] S. Fine and W. P. Hansen. Optical second harmonic generation in biological system. *Appl. Opt.*, 10:2350–53, 1971.

[28] I. Freund and M. Deutsch. Second-harmonic microscopy of biological tissue. *Opt. Lett.*, 11:94–96, 1986.

[29] J. G. Fujimoto, W. Z. Lin, C. A. Puliafito E. P. Ippen, and R. F. Steinert. Time-resolved studies of Nd:YAG laser-induced breakdown. Plasma formation, acoustic wave generation, and cavitation. *Invest. Ophthalmol. Vis. Sci.*, 26:1771–77, 1985.

[30] E. Fukada. Piezoelectric properties of biological macromolecules. *Advan. in Biophys.*, 6:121–55, 1974.

[31] L. Gallais. *Endommagement laser dans les composants optiques : métrologie, analyse statistique et photo-induite des sites initiateurs*. PhD thesis, Université de droit, d'économie et des sciences, Aix Marseille III, 2002.

[32] E. G. Gamaly, A. V. Rode, and B. Luther-Davies. *Ultrafast laser-ablation and film deposition*, chapter 5 in "Pulsed laser deposition of thin films: applications-led growth of functional materials". Robert Eason, 2007.

[33] R. Gauderon, P. B. Lukins, and C. J. R. Sheppard. Simultaneous multichannel nonlinear imaging: combined two-photon excited fluorescence and second-harmonic generation microscopy. *Micron*, 32:685–89, 2001.

[34] D. Giguère, G. Olivié, F. Vidal, S. Toetsch, G. Girard, T. Ozaki, J. C. Kieffer, O. Nada, and I. Brunette. Laser ablation threshold dependence on pulse duration for fused silica and corneal tissues: experiments and modeling. *JOSA A*, 24:1562–68, 2007.

[35] I. K. Gipson and N.C. Joyce. *Principles and Practice of Ophthalmology. 2nd ed*, chapter 56, Anatomy and cell biology of the cornea superficial limbus and conjunctiva, pages 612–29. Philadelphia, WB Saunders, 2000.

[36] M. Gisselberg, J. I. Clark, S. Vaezy, and T. B. Osgood. A quantitative evaluation of Fourier components in transparent and opaque calf cornea. *Am. J. Anat.*, 191:408–18, 1991.

[37] Y. Guo, P. P. Ho, A. Tirksliunas, F. Liu, and R. R. Alfano. Optical harmonic generation from animal tissues by the use of picosecond and femtosecond laser pulses. *Applied Optics*, 32:6810–13, 1996.

[38] T. J. Gyi, K. M. Meek, and G. F. Elliott. Collagen interfibrillar distances in corneal stroma using synchrotron X-ray diffraction: a species study. *Int. J. Biol. Macromol.*, 10:265–69, 1988.

[39] M. Han, G. Giese, and J. F. Bille. Second harmonic generation imaging of collagen fibrils in cornea and sclera. *Opt. Express*, 13:5791–97, 2005.

[40] M. Han, L. Zickler, M. Walter G. Giese, F. H. Loesel, and J. F. Bille. Second-harmonic imaging of cornea after intrastromal femtosecond laser ablation. *J. Biomed. Opt.*, 9:760–66, 2004.

[41] R. W. Hart and R. A. Farrell. Light scattering in the cornea. *J. Opt. Soc. Am.*, 59:766–74, 1969.

[42] A. Heisterkamp, T. Mamom, W. Drommer, W. Ertmer, and H. Lubatschowski. Photodisruption with ultrashort laser pulses for intrastromal refractive surgery. *Laser Physics*, 13:743–48, 2003.

[43] A. Heisterkamp, T. Ripken, T. Mamom, W. Drommer, H. Welling, W. Ertmer, and H. Lubatschowski. Nonlinear side effects of fs pulses inside corneal tissue during photodisruption. *Appl. Phys. B*, 74:419–25, 2002.

[44] M. P. Holzer, T. M. Rabsilber, and G. U. Auffarth. Penetrating keratoplasty using femtosecond laser. *Am. J. Ophthalmol.*, 143:524–26, 2007.

[45] C. Hönninger, F. Morier-Genoud, M. Moser, U. Keller, L. R. Brovelli, and C. Harder. Efficient and tunable diode-pumped femtosecond Yb:glass lasers. *Opt. Lett.*, 23:126–128, 1998.

[46] C. Horvath, A. Braun, H. Liu, T. Juhasz, and G. Mourou. Compact directly diode-pumped femtosecond Nd:glass chirped-pulse-amplification laser system. *Opt. Lett.*, 22:1790–92, 1997.

[47] M. Y. Hu, J. P. McCulley, H. D. Cavanagh, R. W. Bowman, S. M. Verity, V. V. Mootha, and W. M. Petroll. Comparison of the corneal response to laser in situ keratomileusis with flap creation using the FS15 and FS30 femtosecond lasers: clinical and confocal microscopy findings. *J. Cataract. Refract. Surg.*, 33:673–81, 2007.

[48] A. Artola J. I. Belda and J. Alió. Diffuse lamellar keratitis 6 months after uneventful laser in situ keratomileusis. *J. Refract. Surg.*, 19:70–71, 2003.

[49] C. H. Dohlman-B. Kravitt J. N. Goldman, G. B. Benedek. Structural alterations affecting transparency in swollen human corneas. *Invest. Ophthalmol.*, 7:501–19, 1968.

[50] A.P. Joglekar, H. Liu, G.J. Spooner, E. Meyhöfer, G. Mourou, and A.J. Hunt. A study of the deterministic character of optical damage by femtosecond laser pulses and applications to nanomachining. *Appl. Phys. B*, 77:25–30, 2003.

[51] S. C. Jones, P. Braunlich, R. T. Casper, X. A. Shen, and P. Kelly. Recent progress on laser-induced modifications and intrinsic bulk damage of wide-gap optical materials. *Opt. Eng.*, 28:1039–68, 1989.

[52] T. Juhasz, X. H. Hu, L. Turi, and Z. Bor. Dynamics of shock wave and cavitation bubbles generated by picosecond laser pulses in corneal tissue and water. *Lasers Surg. Med.*, 15:91–98, 1994.

[53] T. Juhasz, F. H. Loesel, C. Horvath, R. M. Kurtz, and G. Mourou. Corneal refractive surgery with femtosecond lasers. *IEEE J. Sel. Top. Quantum Electron.*, 5:902–10, 1999.

[54] A. Kaiser, B. Rethfeld, M. Vicanek, and G. Simon. Microscopic processes in dielectrics under irradiation by subpicosecond laser pulses. *Physical Review B*, 61:11437–50, 2000.

[55] F. X. Kartner and U. Keller. Stabilization of solitonlike pulses with a slow saturable absorber. *Opt. Lett.*, 20:16–18, 1995.

[56] L. V. Keldysh. Ionization in the field of a strong electromagnetic wave. *Sov. Phys. JETP*, 20:1307–14, 1965.

[57] G.M. Kezirian and K. G. Stonecipher. Intralase femtosecond laser and mechanical keratomes for laser in situ keratomileusis. *J. Cataract Refract. Surg.*, 30:804–11, 2004.

[58] D. Kopf, F. X. Kartner, U. Keller, and K. J. Weingarten. Diode-pumped mode-locked Nd:glass lasers with an antiresonant Fabry-Perot saturable absorber. *Opt. Lett.*, 20:1169–71, 1995.

[59] M. Lenzner, J. Krüger, S. Sartania, Z. Cheng, Ch. Spielmann, G. Mourou, W. Kautek, and F. Krausz. Femtosecond optical breakdown in dielectrics. *Physical Review Letters*, 80:4076–79, 1998.

[60] D. W. Leonard and K. M. Meek. Refractive indices of the collagen fibrils and extrafibrillar material of the corneal stroma. *Biophysical Journal*, 72:1382–87, 1997.

[61] H. L. Little, H. C. Zweng, and R R. Peabody. Argon laser slit-lamp retinal photocoagulation. *Trans. Am. Acad. Ophthalmol. Otolaryngol.*, 74:85–97, 1970.

[62] F. H. Loesel, M. H. Niemz, J. F. Bille, and T. Juhasz. Laser-induced optical breakdown on hard and soft tissue and its dependence on the pulse duration: experiment and model. *IEEE Journal of Quantum Electronics*, 10:1717–22, 1996.

[63] H. Lubatschowski. *Laser in Medicine: Laser-Tissue Interaction and Applications - A Handbook for Physicists*. John Wiley and Sons, 2005.

[64] H. Lubatschowski, G. Maatz, A. Heisterkamp, U. Hetzel, W. Drommer, H. Welling, and W. Ertmer. Application of ultrashort laser pulses for intrastromal refractive surgery. *Graefe's Archive for Clinical and Experimental Ophthalmology*, 238:33–39, 2000.

[65] M. S. El-Agha H. D. Cavanagh M. S. Chung, J. S. Pepose. Confocal microscopic findings in a case of delayed-onset bilateral diffuse lamellar keratitis after laser in situ keratomileusis. *J. Cataract Refract. Surg.*, 28:1467–70, 2002.

[66] A. P. Forsback P. Saukko-R. Penttinen M. Tommila, J. Jokinen and E. Ekholm. Bioactive glass-derived hydroxyapatite-coating promotes granulation tissue growth in subcutaneous cellulose implants in rats. *Acta Biomater.*, 4:354–61, 2008.

[67] G. Maatz, A. Heisterkamp, H. Lubatschowski, S. Barcikowski, C. Fallnich, H. Welling, and Ertmer. Chemical and physical side effects at application of ultrashort laser pulses for intrastromal refractive surgery. *J. Opt. A: Pure Appl. Opt.*, 2:59–64, 2000.

[68] JH Marburger. Self-focusing: theory. *Prog. Quant. Electron.*, 4:35–110, 1975.

[69] D. M. Maurice. The structure and transparency of the corneal stroma. *J. Physiol.*, 136:263–86, 1957.

[70] K. M. Meek and C. Boote. The organization of collagen in the corneal stroma. *Experimental Eye Research*, 78:503–12, 2004.

[71] K. M. Meek and N. J. Fullwood. Corneal and scleral collagen - a microscopist's perspective. *Micron*, 32:261–72, 2001.

[72] K. M. Meek, D. W. Leonard, C. J. Connon, S. Dennis, and S. Khan. Transparency, swelling and scarring in the corneal stroma. *Eye*, 17:927–36, 2003.

[73] C. Meltendorf, J. Schroeter, R. Bug, T. Kohnen, and T. Deller. Corneal trephination with the femtosecond laser. *Cornea*, 25:1090–92, 2006.

[74] Q. Mohamed, M. C. Gillies, and T. Y. Wong. Management of diabetic retinopathy: a systematic review. *JAMA*, 298:261–72, 2007.

[75] T. Moller-Pedersen. Keratocyte reflectivity and corneal haze. *Exp. Eye Res.*, 78:553–60, 2004.

[76] P. F. Moulton. Spectroscopic and laser characteristics of Ti:Al_2O_3. *J. Opt. Soc. Am. B*, 3:125–33, 1986.

[77] A. S. Neubauer and M. W. Ulbig. Laser treatment in diabetic retinopathy. *Ophthalmologica*, 221:95–102, 2007.

[78] M. H. Niemz. *Laser-Tissue Interactions: Fundamentals and Applications (Biological and Medical Physics, Biomedical Engineering)*. Springer, 2007.

[79] M. H. Niemz, T. Hoppeler, T. Juhasz, and J. F. Bille. Threshold fluence measurements for plasma-mediated ablation in corneal tissue. Laser pulse duration was between 120 fs and 100 ps. *Laser and light in ophthalmology*, 85:149–55, 1993.

[80] D. N. Nikogosyan, A. A. Oraevsky, and V. I. Rupsov. 2-photon ionization and dissociation of liquid water by powerful laser UV-radiation. *Chemical Physics*, 77:131–43, 1983.

[81] T Nishida. *Cornea. 2nd ed*, chapter 1, Cornea: Anatomy and Physiology. Mosby, 2004.

[82] J. Noack and A. Vogel. Laser-induced plasma formation in water at nanosecond to femtosecond time scales: calculation of thresholds, absorption coefficients, and radiant exposure. *IEEE Journal of Quantum Electronics*, 35:1156–67, 1999.

[83] L. T. Nordan, S. G. Slade, R. N. Baker, C. Suarez, T. Juhasz, and R. J. Kurtz. Femtosecond laser flap creation for laser in situ keratomileusis: six-month follow-up of initial U.S. clinical series. *J. Refract. Surg.*, 19:8–14, 2003.

[84] M. Oheim, E. Beaurepaire, E. Chaigneau, J. Mertz, and S. Charpak. Two-photon microscopy in brain tissue: parameters influencing the imaging depth. *J. Neurosci. Meth.*, 111:29–37, 2001.

[85] I. G. Pallikaris, M. E. Papatzanaki, O. Frenschock E. Z. Stathi, and A. Georgiadis. Laser in situ keratomileusis. *Lasers Surg. Med.*, 10:463–68, 1990.

[86] A.-M. Pena, T. Dartigalongue T. Boulesteix, and M.-C. Schanne-Klein. Chiroptical effects in the second harmonic signal of collagens I and IV. *J. Am. Chem. Soc.*, 127:10314–22, 2005.

[87] M. Pessot, P. Maine, and G. Mourou. 1000 times expansion/compression of optical pulses for chirped pulse amplification. *Opt. Commun.*, 62:419–421, 1987.

[88] D. W. Piston, B. R. Masters, and W. W. Webb. Three-dimensionally resolved NAD(P)H cellular metabolic redox imaging of the in situ cornea with two-photon excitation laser scanning microscopy. *J. Microsc.*, 178:20–27, 1995.

[89] C. A. Puliafito and R. F. Steinert. Short-pulsed Nd:YAG laser microsurgery of the eye - Biophysical considerations. *IEEE Journal of Quantum Electronics*, 20:1442–48, 1984.

[90] A. J. Quantock. The cornea is clear - but why? *OT, www.optometry.co.uk*, pages 32–35, 2000.

[91] P. E. Tatham R. A. Farrell, R. L. McCally. Wave-length dependencies of light scattering in normal and cold swollen rabbit corneas and their structural implications. *J. Physiol.*, 233:589–612, 1973.

[92] B. Rethfeld. Free-electron generation in laser-irradiated dielectrics. *Phys. Rev. B*, 73:035101–6, 2006.

[93] S. Roth and I. Freund. Second harmonic generation in collagen. *J. Chem. Phys.*, 15:1637–43, 1979.

[94] S. Roth and I. Freund. Optical second-harmonic scattering in rat-tail tendon. *Biopolymers*, 20:1271–90, 1981.

[95] B. E. A. Saleh and M. C. Teich. *Fundamentals of Photonics*. Hardcover, 2007.

[96] M. A. Sarayba, T. Juhasz, R. S. Chuck, T. S. Ignacio, T. B. Nguyen, P. Sweet, and R M. Kurtz. Femtosecond laser posterior lamellar keratoplasty: a laboratory model. *Cornea*, 24:328–33, 2005.

[97] Z. Sayers, M. H. Koch, S. B. Whitburn, K. M. Meek, G. F. Elliott, and A. Harmsen. Synchrotron X-ray diffraction study of corneal stroma. *J. Mol. Biol.*, 160:593–607, 1982.

[98] C. Schaffer, A. Brodeur, and E. Mazur. Laser-induced breakdown and damage in bulk transparent materials induced by tightly-focused femtosecond laser pulses. *Meas. Sci. Technol.*, 12:1784–94, 2001.

[99] B. Seitz, H. Brünner, A. Viestenz, C. Hofmann-Rummelt, U. Schlötzer-Schrehardt, G.O. Naumann, and A. Langenbucher. Inverse mushroom-shaped nonmechanical penetrating keratoplasty using a femtosecond laser. *Am. J. Ophthalmol.*, 139:941–44, 2005.

[100] B. Seitz, A. Langenbucher, C. Hofmann-Rummelt, U. Schlotzer-Schrehardt, and G. O. Naumann. Nonmechanical posterior lamellar keratoplasty using the femtosecond laser (femto-plak) for corneal endothelial decompensation. *Am. J. Ophthalmol.*, 136:769–72, 2003.

[101] Y. R. Shen. *The principles of nonlinear optics*. John Wiley & Sons, 1992.

[102] A. E. Siegman. *Lasers*. University Science Books, 1990.

[103] H. K. Soong, S. Mian, O. Abbasi, and T. Juhasz. Femtosecond laser-assisted posterior lamellar keratoplasty: initial studies of surgical technique in eye bank eyes. *Ophthalmology*, 12:44–49, 2005.

[104] D. E. Spence, P. N. Kean, and W. Sibbett. 60-fsec pulse generation from a self-mode-locked Ti:sapphire laser. *Opt. Lett.*, 16:42–44, 1991.

[105] R. F. Steinert, T. S. Ignacio, and M. A. Sarayba. Top hat-shaped penetrating keratoplasty using the femtosecond laser. *Am. J. Ophthalmol.*, 143:689–91, 2007.

[106] K. Stonecipher and nad M. Stonecipher T. S. Ignacio. Advances in refractive surgery: microkeratome and femtosecond laser flap creation in relation to safety, efficacy, predictability, and biomechanical stability. *Curr. Opin. Ophthalmol.*, 17:368–72, 2006.

[107] D. Strickland and G. Mourou. Compression of amplified chirped optical pulses. *Opt. Commun.*, 55:447–49, 1985.

[108] M. Strupler, A.-M. Pena, M. Hernest, P.-L. Tharaux, J.-L. Martin, E. Beaurepaire, and M.-C. Schanne-Klein. Second harmonic imaging and scoring of collagen in fibrotic tissues. *Optics Express*, 145:4054–65, 2007.

[109] B. C. Stuart, M. D. Feit, S. Herman, A. M. Rubenchik, B. W. Shore, and M. D. Perry. Nanosecond-to-femtosecond laser-induced breakdown in dielectrics. *Physical Review B*, 53:1749–61, 1996.

[110] B. C. Stuart, M. D. Feit, A. M. Rubenchik, B. W. Shore, and M. D. Perry. Laser-induced damage in dielectrics with nanosecond to subpicosecond pulses. *Phys. Rev. Lett.*, 74:2248–51, 1995.

[111] L. Sudrie. *Propagation non-linéaire des impulsions laser femtosecondes dans la silice*. PhD thesis, Laboratoire d'Optique Appliquée, Université Paris XI Orsay, 2002.

[112] A. C. Tien, S. Backus, H. Kapteyn, M. Murnane, and G. Mourou. Short-pulse laser damage in transparent materials as a function of pulse duration. *Physical Review Letters*, 82:3883–86, 1999.

[113] D. B. Tran, M. A. Sarayba, Z. Bor, Y. J. Duh C. Garufis, C. R. Soltes, T. Juhasz, and R. M. Kurtz. Randomized prospective clinical study comparing induced aberrations with Intralase and Hansatome flap creation in fellow eyes: potential impact on wavefront-guided laser in situ keratomileusis. *J. Cataract Refract. Surg.*, 31:97–105, 2005.

[114] H. C. van de Hulst. *Light scattering by small particles*. Dover, 1981.

[115] A. Vogel, K. Nahen, D. Theisen, R. Birngruber, R. J. Thomas, and B. A. Rockwell. Influence of optical aberrations on laser-induced plasma formation in water and their consequences for intraocular photodisruption. *Appl. Opt.*, 38:3636–43, 1999.

[116] A. Vogel, J. Noack, G. Hüttman, and G. Paltauf. Mechanisms of femtosecond laser nanosurgery of cells and tissues. *Appl. Phys. B*, 81:1015–47, 2005.

[117] A. Vogel, J. Noack, K. Nahen, D. Theisen, S. Busch, U. Parlitz, D.X. Hammer, G.D. Noojin, B.A. Rockwell, and R. Birngruber. Energy balance of optical breakdown in water at nanosecond to femtosecond time scales. *Appl. Phys. B*, 68:271–80, 1996.

[118] A. Vogel and V. Venugopalan. Mechanisms of pulsed laser ablation of biological tissues. *Chem. Rev.*, 103:577–644, 2003.

[119] A. J. Welch, J. H. Torres, and W.F. Cheong. Laser physics and laser-tissue interaction. *Tex Heart Inst J*, 16:141–49, 1989.

[120] W. E. White, F. G. Patterson, R. L. Combs, D. F. Price, and R. L. Shepherd. Compensation of higher-order frequency-dependent phase terms in chirped-pulse amplification systems. *Opt. Lett.*, 18:1343–45, 1993.

[121] A. T. Yeh, N. Nassif, A. Zoumi, and B. J. Tromberg. Selective corneal imaging using combined second-harmonic generation and two-photon excited fluorescence. *Opt. Lett.*, 27:2082–84, 2002.

[122] P. D. Yurchenco and J. C. Schittny. Molecular architecture of basement membranes. *FASEB J.*, 4:1577–90, 1990.

[123] A. Zoumi, A. Yeh, and B. J. Tromberg. Imaging cells and extracellular matrix in vivo by using second-harmonic generation and two-photon excited fluorescence. *P. Natl. Acad. Sci.*, 99:11014–19, 2002.

List of publications

V.Nuzzo, F.Aptel, M.Savoldelli, K.Plamann, D.Donate, and J.-M.Legeais. Histological and ultrastructural characterization of corneal femtosecond laser trephination. Accepted to be published in *Cornea*

V.Nuzzo, K.Plamann, M.Savoldelli, F.Aptel B.Reynier, F.Pailloux, T.Cabioc'h, O.Albert, and J.-M.Legeais. Deposit of glass fragments during femtosecond laser penetrating keratoplasty. *Graefe's Archive for Clinical and Experimental Ophthalmology*, 2008, Sep 23

K.Plamann, V.Nuzzo, D.Peyrot, F.Deloison, M.Savoldelli, and J.-M Legeais. Laser parameters, focusing optics, and side effects in femtosecond laser corneal surgery. *Proc. SPIE* Vol. 6844, 68440W, *Ophthalmic Technologies XVIII*; Fabrice Manns; Per G. Söderberg; Arthur Ho; Bruce E. Stuck; Michael Belkin; Eds., February 2008

V.Nuzzo, K.Plamann, M.Savoldelli, M.Merano, D.Donate, O.Albert, P.F.Gardeazábal Rodríguez, G.Mourou, and J-M.Legeais. In situ Monitoring of Second Harmonic Generation in Human Corneas to Compensate for Femtosecond Laser Pulse Attenuation Applied to Keratoplasty. *Journal of Biomedical Optics*, 2007, 12:064032 (11 pp) (also selected by the *Virtual Journal of Ultrafast Science* - December 2007)

K.Plamann, V.Nuzzo, O.Albert, G.Mourou, M.Savoldelli, F.Dagonet, D.Donate, and J.-M Legeais. Femtosecond laser corneal surgery with in-situ determination of the laser attenuation and ablation threshold by second harmonic generation. *Proc. SPIE* Vol. 6426, 642616, *Ophthalmic Technologies XVII*; Fabrice Manns, Per G. Soederberg, Arthur Ho, Bruce E. Stuck, Michael Belkin M.D.; Eds., March 2007